Thèse de doctorat

Université de Limoges

Université de Limoges
ED 614 . Chimie, Écologie, Géosciences, Agrosciences (CEGA)
EA 7500 – Laboratoire PEIRENE

Thèse pour obtenir le grade de
Docteur de l'Université de Limoges

Chimie Organique

Présentée et soutenu par
Nidia MALDONADO CARMONA

Le 14 Septembre 2021

Acetylated lignin nanoparticles as a new photosensitizer's vehicle for Photodynamic Antimicrobial Chemotherapy (PACT)

Thèse dirigée par Dr. Stéphanie LEROY-LHEZ, Dr. Tan-Sothea OUK et Pr. Maria Miguéns PEREIRA

JURY :

Président du jury
Mme. Fabienne DUMOULIN, Professeur, Medical Engineering Department, Acıbadem Mehmet Ali Aydınlar University

Rapporteurs
M. Kristjan PLAETZER, Professeur, Department of Biosciences, Université de Salzbourg
M. Mathias SENGE, Professeur, School of Chemistry, Trinity College of Dublin

Examinateurs
Mme. Fabienne DUMOULIN, Professeur, Medical Engineering Department, Acıbadem Mehmet Ali Aydınlar University

Invités
M. Nicolas VILLANDIER, Maître de conférences-HDR, Faculté des Sciences et Techniques, Université de Limoges
M. Mário J. F. CALVETE, Maître de conférences-HDR, Coimbra Chemistry Center, Universidade de Coimbra
Mme. Rachida ZERROUKI, Professeur, Faculté des Sciences et Techniques, Université de Limoges

"I am among those who think that science has great beauty. A scientist in his laboratory is not only a technician: he is also a child placed before natural phenomena which impress him like a fairy tale."

Marie Skłodowska-Curie

“Like musicians, like mathematicians—like elite athletes—scientists peak early and dwindle fast. It isn’t creativity that fades, but stamina: science is an endurance sport. To produce that single illuminating experiment, a thousand nonilluminating experiments have to be sent into the trash; it is battle between nature and nerve.”

Siddharta Mukherjee, The Gene: An Intimate History

DEDICATION

To the loving memory of Silvia Guzmán Trampe and Alfonso Troyo Ballina, and to their son Diego and their families; their light still shines upon all of us

To my parents, Reyna and Fermin, for their unmeasurable effort and loving care. For believing in me and pushing me forward, even if that keeps me away from them.

To my parents-in-law, Martha and Pablo, for their support and love, for integrating me in their family, and for giving the best piece of them to me.

To my friends, the new and the old ones, who always cheered for me; thanks for being there through thick and thin: Melissa, Alba, Corina, Diana R., Monet, Berenice, Nelly, Fanny, Dr. Mike, Ricardo, Alexandrina, Juan Carlos, Pedro Pablo, Beltry, Cristofer, Mike, Edgar, Anna, Danny, Jessica, Cristina, Laura, Giani, Dulce, Pablo A., Irazu, Francisco, Aurore, Piotr, Claire, Emma, João, Harry, Dáire, Manu, Zoi, Bhavya, André, Maria Inês, Tiago, Giusi, Marcos, Diana M., Fábio R., Cornelia, Karine, Maxime, Jérémy, Marlène, Ricardo C., Marta P. Thanks for sharing all those good moments with me and making life something special.

To Enrique, for being my partner, my friend, my support and my everything. This is all because of you. Thanks for dreaming with me.

Thank you! Merci beaucoup! ¡Gracias! Obrigadissima!

ACKNOWLEDGEMENTS

I would like to acknowledge the members of the jury, Pr. Mathias Senge, Pr. Kristjan Plaetzer and Pr. Fabienne Dumoulin, for the invested time in the evaluation of my work.

I would also like to acknowledge the coordinator and manager of the project POLYTHEA, Dr. Stéphanie Leroy-Lhez and Aurore Berthier, for giving me a chance to demonstrate my capacities and develop my scientific work in Europe.

Again, I would like to acknowledge Stéphanie, but also Nicolas Villandier, Tan-Sothea Ouk, Mário Calvete and Mariette Pereira, for being my supervisors in this multidisciplinary project, involving so many topics, and which required different expertises for it to be successful. I'm especially happy to have worked under the supervision of Stéphanie, Nicolas and Tan, as they have always been welcoming, supportive and caring. Thanks for being awesome.

I would like to acknowledge Dr. Katarzyna Matczyszyn, and Pr. Krzysztof J. Pawlik, for receiving me for a short secondment in Wrocław, Poland. Also, I would like to thank Dr. Arno Wiehe for similarly receiving me for a one-month secondment in Berlin, Germany. Finally, I would like to acknowledge Dr. Sandra Da Re, from INSERM, for receiving me for a short secondment in Limoges. Thanks for your cooperation and your teachings.

This work would not be possible without the amazing participation of Claude Calliste, with whom I learnt the secrets of EPR. I would also like to acknowledge Dr. Yann Launay, from IRCER (Limoges), whom shed a light on the shape of nanoparticles and their interaction with bacteria. Addtionally, I would like to remark the amazing support from Claire Carrion and Catherine Ouk from BISCEm (Limoges), Dr. Andrzej Żak from the Electron Microscopy Laboratory at Wrocław University of Science and Technology (Wrocław), and from Dr. Johann Bouclé from XLIM (Limoges). Their support has provided me with invaluable skills and learnings, not only in science, but also in life in general.

One of the greatest aspects of POLYTHEA project was the chance to meet several persons that made the work, not only interesting, but enjoyable, and then I acknowledge their presence and the scientific discussions I had with them. First, to my POLYTHEA fellows Emma, Zoi, Dáire, João, Bhavya, Harry, Claire, Piotr and Manuel. Then, to the Limoges students, Guillaume, Zineb, Soukaina, Veronica, Abdechakour, Morag, Dima, Marie, Romain, Victor, Andreia and, especially, to Jérémy. Also, I acknowledge the Coimbra students, Giusi, Andreia, Rafael, Zoi, Diana Margarida, Fábio, Alexander, Dimitri, Iuri, Liliana, Vanessa, Carolina, Vitaliy, and Rui. Finally, I acknowledge the work and support from Marta Piksa, from the Polish Academy of Sciences.

The presentation of this work is the final conjunction of three different laboratories, and this work could not have been achieved without the participation of several people. Then, I acknowledge the participation and support of the personal from the Laboratoire PEIRENE, and especially to Pr. Vincent Sol, Pr. Vincent Chaleix, Pr. Rachida Zerrouki, Frédérique Brégier, Catherine Riou, Sylvie Poirier, Guillaume Marchand, Dorothée Moine, and Michèle Constantin. I also acknowledge the support of the personal from the IUT du Limousin Genie Biologique, especially to Christophe Genin, Karine Grenier, Cornelia Landolt, Naïma Saad, Charlotte Vernisse, Jean Baptiste, and Patrick. I also acknowledge the support of the

personal from the Universidade de Coimbra, especially to Pr. Luis Arnaut, Pr. Sergio Seixas, Ligia, Fábio Schaberle, Estefania, Ana Clara, Sara, Rui, Fábio Rodrigues, and Pedro.

This project has received funding from the European Union's Horizon 2020 research and innovation programme under the Marie Sklodowska-Curie grant agreement n°764837.

DROITS D'AUTEURS

TABLE OF CONTENTS

TABLE OF FIGURES

INTRODUCTION

I. Antimicrobial resistance

Antimicrobial resistance is one of the arising problems of the XXIst century, as it is estimated that every year 700,000 people die, due to infections related to multi-drug resistant microorganisms [1]. Projections indicate that if actions are not taken on this regard, the death toll would increase up to 10 million people per year, in 2050, with developing countries taking the most damage of it [2].

Antimicrobial resistance arise is the result of the ever-growing presence of antibiotics into the environment, which has selected resistant bacteria, and allowed the global spread of the so-called “superbugs”. Recent studies have shown that antibiotic resistance genes (ARGs) are present even in the remote jungles of the Amazon [3], or in the supposedly pristine Arctic region [4]. The quick spread of antibiotic resistance is due to molecular mechanisms resulting from a millennial chemical war at the microscopic level. ARGs can be inherited through generations (vertical transfer) or it can be acquired through other molecular mechanisms (horizontal transfer) as depicted in Figure 1.

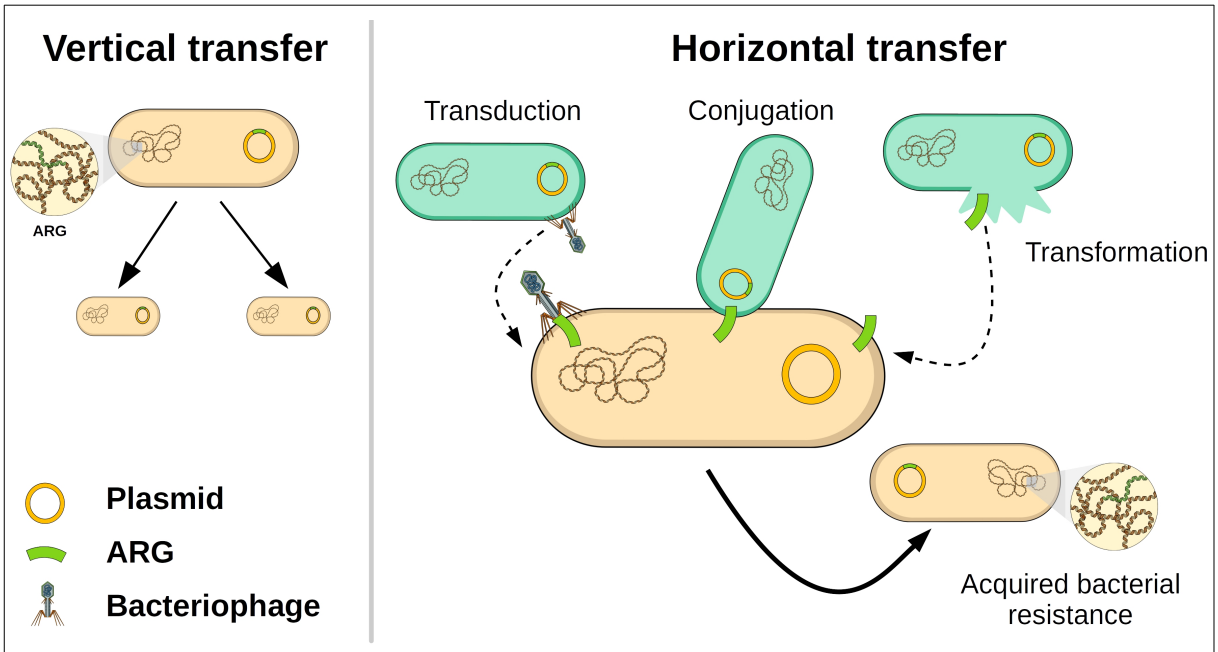

Figure 1: Molecular mechanisms for the transferral of ARGs in bacteria. While ARGs can be transferred through generations (vertical transfer), ARGs can be transferred as well through bacteriophage-driven transduction, bacterial conjugation or acquired as pieces of DNA obtained from dead bacteria (horizontal transfer).

The effective horizontal transfer of ARGs has led to a catastrophic scenario. Several antibiotics, discovered during the last century but discarded due to their acute toxicity, have been brought into the clinical use as “last resource” alternatives. However, alarms are ringing around the world, as even these aggressive alternatives are being decimated by the global spread of specific resistance genes [5].

As a deadly conjunction, the pipelines of development of new antibiotics are barely empty.

Up to December 2020, approximately 43 new antibiotics were in different stages of clinical development, from which only two had reached the application of “new drug” upon the Food and Drugs Administration (FDA). However, from these 43 new molecules, only 24 were expected to have an activity against the World Health Organization’s (WHO) list of critical threat pathogens. Furthermore, only 10 of them received the classification of “new molecules”, posing a high risk of cross-resistance with molecules of similar structure already available [6]. These new molecules, although promising, will be reserved for specific infections and hospital environments, to decelerate the appearance of antibiotics resistance, with most of the population still in contact with antibiotics showing decreasing efficiency.

This dire situation has prompted scientists to look for alternatives [7], especially where systemic antibiotics are not needed, as agriculture and food industry. Traditionally, antibiotics have been acknowledged as “magic bullets”, as they have specific molecular targets and molecular mechanisms, that avoid the host but attack the pathogen. However, this specificity permits that bacterial resistance arise as a consequence of punctual mutations and/or acquisition of resistance genes. Thus, an antibacterial alternative with non-specific molecular target is desirable, with their best examples being cold atmospheric plasma and photodynamic therapy.

II. PhotoDynamic Therapy and Photodynamic Antimicrobial ChemoTherapy

PhotoDynamic Therapy (PDT) is a technique that conjugates photophysics, chemistry and biology for the treatment of cancer cells, resulting in successful clinical treatments, applied for the last 25 years [8]. PDT relies on the conjunction of the “holy trinity”: a photosensitizing molecule, molecular oxygen and light, leading to the production of reactive oxygen species (ROS). These ROS are able to quickly oxidize organic matter, resulting in cellular death. This is useful for several clinical applications, and is currently used against solid tumors [8], cancer [9], rheumatoid arthritis [10], among others.

As PDT, the Photodynamic Antimicrobial ChemoTherapy (PACT) relies on the generation *in situ* of reactive oxygen species, for the annihilation of microorganisms, as bacteria [11], virus [12], yeasts [13], and even parasites [14]. Due to the need of light, PACT can only be used on inanimate surfaces [15] or in the exterior, lumen and cavities of living beings [16], which restricts their width of applications. However, PACT represents an interesting approach, as an ideal photosensitizer will only exert its microbicide effect when irradiated under a certain wavelength, decreasing the chances of microorganisms to generate resistance.

A. Photochemical mechanisms

The production of ROS by PDT and PACT results from the photosensitizer’s excitation when it absorbs a photon. This leads to the promotion of an electron into a higher-energy molecular orbital, resulting in a short-lived excited state whose decay to the ground state can be through fluorescence. However, during the excited singlet state, the electron can undergo spin conversion, leading to the population of the excited triplet state. As this, an intersystem crossing, is a spin-forbidden process, the excited electron goes through a second spin-forbidden conversion, depopulating the triplet state and decaying to the ground state, through phosphorescence, for example. Phosphorescence, as a not-allowed process, usually has a

greater life time (τ_P = 10^{-3} – 1 second), when compared with the fluorescence decay (τ_{Fl} = 10^{-9} – 10^{-6} seconds), and then triplet state photosensitizers are able to interact with the molecules surrounding them (Figure 2) [17].

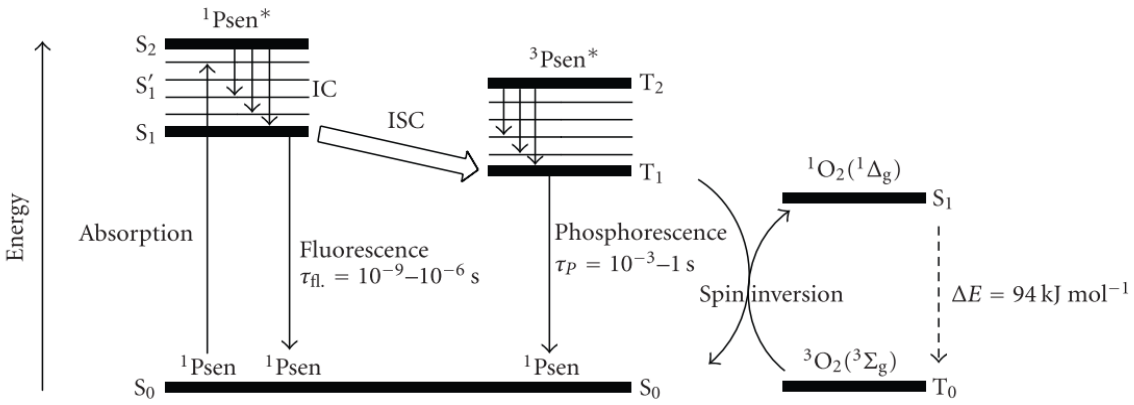

Figure 2 : Modified Jablonsky energy diagram, showing the different excitation states of the photosensitizers (P_{sen}) and the formation of singlet oxygen through Type-II process. Taken from Josefsen and Boyle, 2008 [17].

The ROS that are produced as a consequence of the photosensitizer's exposure to the light, depends on the electron transfer from the excited photosensitizer towards a reducible molecule. If the photosensitizer is in intimate contact with a substrate (i.e., lipids, proteins, nucleic acids), it is susceptible to electron transfer, leading to a chain reaction that produces a high variety of ROS (i.e. $O_2^{\bullet-}$, $OH^{\bullet-}$), with lipids being highly susceptible to it, with this being the Type-I process. However, a specific ROS can be produced if the excited triplet state photosensitizer interacts through energy transfer with ground state molecular oxygen, a spin allowed transition as both are in the same spin state. This Type-II process produces the highly reactive singlet oxygen ($^1O_2$), which is usually related to cell injury and eventual death. But although singlet oxygen is looked forward as an indicative of an efficient photosensitizer, it is important to emphasize that both photodynamic processes can be responsible for cellular death [17].

B. An ideal photosensitizer

Photosensitizers are aromatic molecules, with tetrapyrrolic compounds being the best explored examples. An ideal photosensitizer has been described [17,18] as a molecule which complies with:

- Strong absorption in the visible range (400 – 800 nm),
- Effective ROS producer,
- Suitable photophysical characteristics,
- Have a short and high yielding synthetic route,
- Minimal dark toxicity,
- Simple and stable drug formulation,
- Solubility in biological media.

Tetrapyrrolic compounds are macrocyclic aromatic molecules, structurally related to the natural compounds hemoglobin and chlorophyll. There are several types of tetrapyrrolic compounds (i.e., porphyrins, chlorins, bacteriochlorins, phthalocyanines), and although most of them comply with the chemical and photophysical requirements to be considered good photosensitizers, their solubility and behavior in biological media can be unfavorable (Figure 3). Most of the current research of photosensitizers and their applications in PACT and PDT focuses on the development of new and better photosensitizing molecules, especially for the eradication of Gram-negative bacteria.

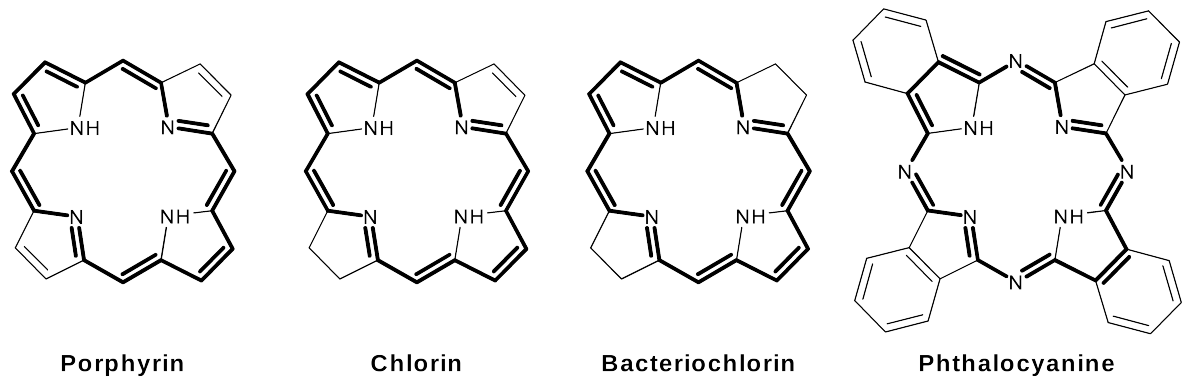

Figure 3: Tetrapyrrolic compounds and their aromatic cores (bold).

Publication 1. “New insights for eradication of Gram-negative bacteria by photodynamic treatment: a still relevant challenge”

[Publication Submitted by June 30th 2021, at Photochemical and Photobiological Sciences]

New insights for eradication of Gram-negative bacteria by photodynamic treatment: a still relevant challenge

Nidia Maldonado-Carmona [1,2], Tan-Sothea Ouk [1], and Stéphanie Leroy-Lhez [1]*

[1]*PEIRENE Laboratory, Faculty of Sciences and Techniques, University of Limoges, Limoges, 87060,France*

[2]*University of Coimbra, Coimbra Chemistry Center, Department of Chemistry, University of Coimbra, Coimbra, 3004-535, Portugal*

Abstract

Antimicrobial resistance is threatening to overshadow last century's medical advances. Previously eradicated infectious diseases are now resurgent as multi-drug resistant strains, especially for Gram-negative strains. Finding new therapeutic solutions is a real challenge for our society. In this framework, Photodynamic Antimicrobial ChemoTherapy relies on the generation of toxic reactive oxygen species in the presence of light, oxygen and a photosensitizer molecule. The reactive species generated represent an alternative to disinfection, as it does not have a specific molecular target, decreasing the potential of resistance development to the antimicrobial treatment. In the last few years this topic has been thoroughly explored, exploring strategies based in single molecules or in conjunction with delivery systems. The present work describes some of the most relevant advances of the last 6 years, focusing on photosensitizers design, formulation and potentiation, aiming for the disinfection of Gram-negative bacteria.

Keywords: disinfection, antibacterial alternatives, photosensitizers, delivery systems

1. Introduction

Although conventional antimicrobial drugs were described as "magic bullets" in the XXIst century, the increase of antimicrobial drug resistance requires a major and rapid intervention, to keep up with the medical advances developed so far [1]. Fighting antimicrobial resistance (AMR) has been recognized as a priority for public health, including food supply [2, 3]. The number of microorganisms exhibiting AMR, especially resistance to multiple antibiotics, has continued to increase in Europe. An estimation has predicted that deaths caused by antimicrobial resistance could rise from approximately 700,000 deaths a year to close to 10 million deaths per year by 2050, with a cumulative cost of 100 trillion US dollars [2, 4]. Alternative and more efficient antimicrobial strategies are urgently needed, especially against "ESKAPE" superbugs (*Enterococcus faecium*, *Staphylococcus aureus*, *Klebsiella pneumoniae*, *Acinetobacter baumannii*, *Pseudomonas aeruginosa*, and *Enterobacter spp*) [5]. In 2017, the World Health Organization (WHO) has published a list of antibiotic-resistant priority pathogens [6], most of which are Gram-negative bacterial pathogens. Due to their distinctive structure, Gram-negative bacteria are more resistant than Gram-positive bacteria, causing significant morbidity and mortality worldwide. Since resistance in Gram-negative bacteria is often mediated by plasmids carrying multiple resistance genes, treatment is frequently restricted to second-line and third-line antibiotics with high toxicity or poor efficacy, which causes patient harm and increases health care costs. The development of novel but still conventional systemic antimicrobial agents, having only a single mode or site of action, will not alleviate the situation. Indeed, it is probably only a matter of time until any such agents will also become ineffective. An improved approach to avoid future development of resistance is to focus on agents/techniques with modes of action that interact with multiple targets on the microorganisms [7]. A suitable therapeutic option for local control and as preventive exposure prior to surgery or anti-cancer therapy is the Photodynamic Antimicrobial ChemoTherapy (PACT) [8].

Photodynamic therapy (PDT) requires the simultaneous use of a chromophore molecule, called photosensitizer (PS), oxygen, and light. Upon light irradiation, the PS (^{0}PS) gets into an excited singlet state (^{1}PS*), which through intersystem crossing, turns into an excited triplet state (^{3}PS*), which can interact with an electron acceptor substrate (Type-I mechanism) or with molecular oxygen (Type-II mechanism), to form highly reactive oxygen species (ROS) such as hydroxyl radicals and cytotoxic singlet oxygen $^1O_2$ (Figure 1). Both mechanisms induce the photooxidation of biomolecules, such as nucleic acids, lipids, and proteins, leading to eventual cell death [9].

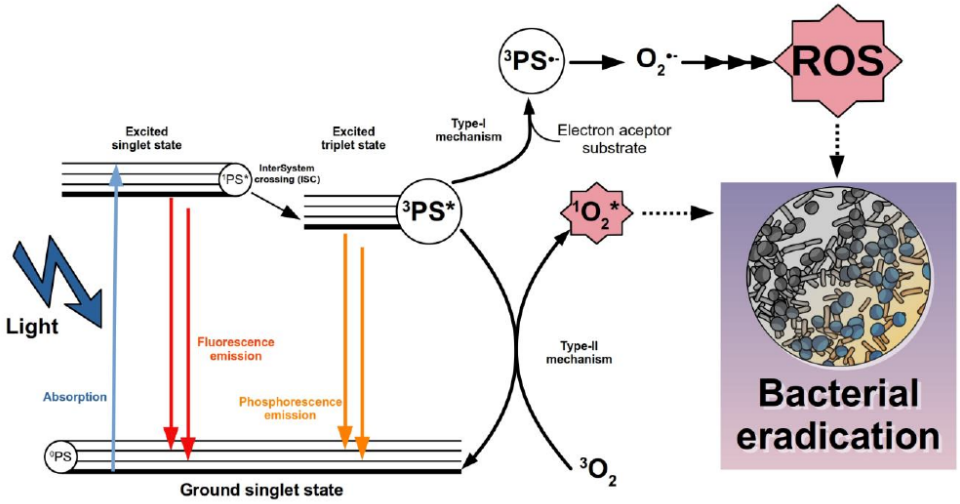

Figure 1: Illustration of the photochemical mechanisms of different reactive oxygen species (ROS) produced during photodynamic action

Although PDT was initially used for the treatment of cancer, and tumors, the emergence of MultiDrug Resistant (MDR) bacteria has conducted to the adaptation of PDT for the treatment of infections [10–13]. In this regard, PACT is a promising approach for the treatment of bacterial infections. Because of the high reactivity of ROS, light-activated PS are able to neutralize, bacteria and bacterial virulence factors, reducing their effectiveness or decreasing their expression. Then, PACT is not only able to decrease the survival of pathogenic bacteria, but also able to decrease the pathogenicity and virulence. The speed of ROS production, and consequently, killing bacteria rate, together with the non-specific molecular target of ROS, is likely to decrease the development of resistance towards PACT [14, 15]. This is just one of the advantages of using PACT as an alternative for bacterial disinfection, as PACT is able to cause localized impact on a site of infection thanks to a local irradiation. However, the necessity of light irradiation could be a double-edged sword, as some physiological environments are unlikely to be reached by light. Nevertheless, there are several potential environments and applications where PACT could replace or complement conventional antimicrobial therapies (Figure 2, [16]).

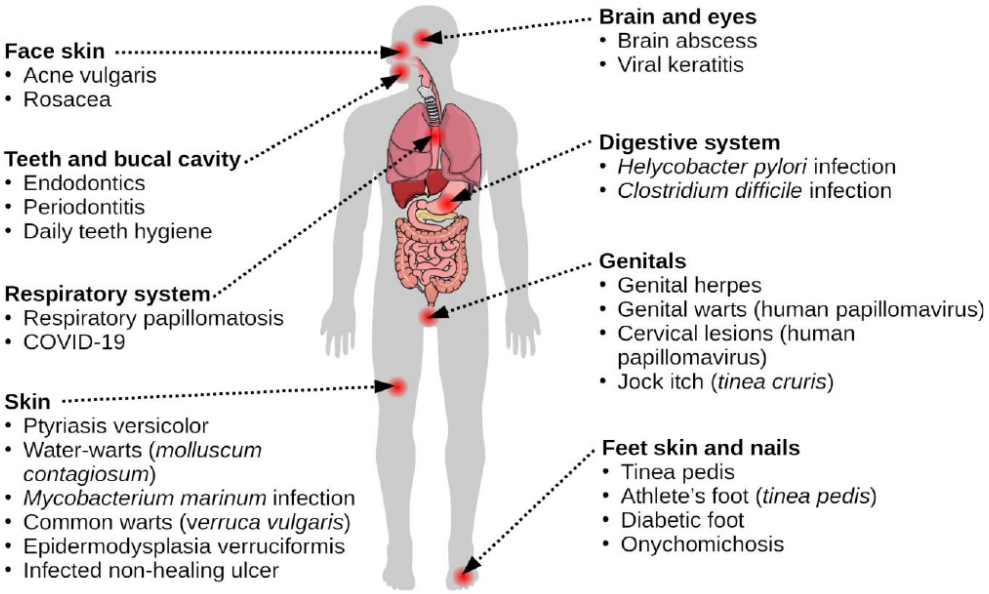

Figure 2: Localized sites of infection, which could be potentially treated by PACT.

Since the development of the initial antibacterial treatments, it was shown that bacteria had different susceptibilities towards chemotherapy, which relies on the physiology of bacteria [17]. Bacteria are usually divided by their capacity to retain crystal violet in their peptidoglycan cell wall, being Gram-positive if bacteria retained the stain and Gram-negative if bacteria did not retain the dye. This test allows microbiologists to differentiate the type of envelopes that bacteria have. Gram-positive bacteria display a thick cell wall constituted by peptidoglycans, which easily retains crystal violet, decorated with teichoic acids and lipids. Meanwhile, Gram-negative bacteria possess two lipidic membranes, separated by a periplasmic space and a thin peptidoglycan layer (Figure 3). The outer membrane is decorated with lipoproteins and negatively-charged lipopolysaccharides (LPS), with Gram-negative bacteria relying on porin channels for the transport of small molecules through the outer membrane. These structures prevent the entry of unknown molecules into bacteria, decreasing their permeability and usually requiring small, polar compounds with cationic charges as antibiotic molecules [18]. Photosensitizers used in PACT are not exempt to these solubility challenges and in the following sections we'll explore some of the emerging alternatives towards Gram-negative disinfection, which, interestingly, not only relies on the presence of cationic charged molecules, but also on delivery systems and the use of adjuvants to favor the permeation into the outer membrane of bacteria.

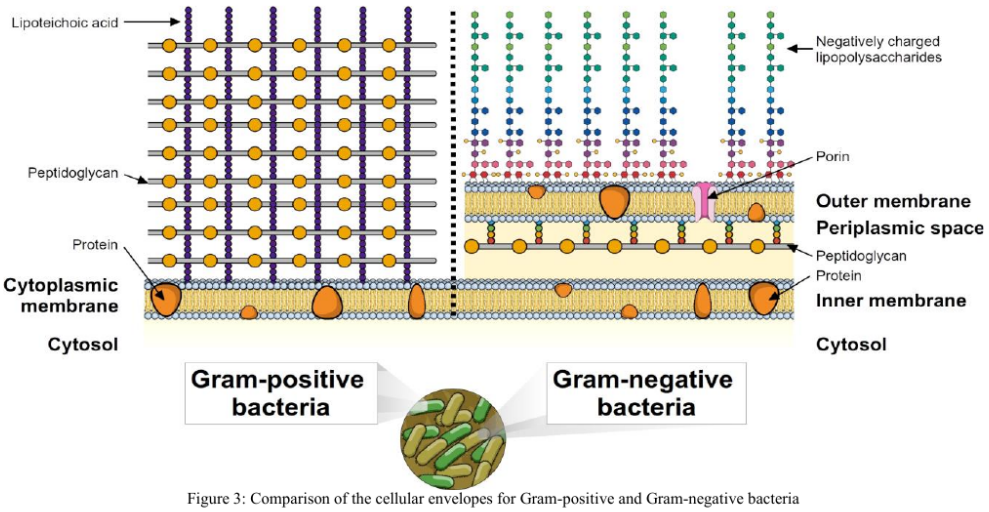

Figure 3: Comparison of the cellular envelopes for Gram-positive and Gram-negative bacteria

2. Photosensitizers structure

Most of the research efforts poured into PACT current pipeline, still explores the effects of structural changes into the efficiency of the photosensitizers. Unlike traditional antibiotic therapies, there are several kinds of molecules with photosensitizing activity that are explored as clinically relevant photosensitizers against bacteria. In the following sections, we will describe several recent examples of synthesized photosensitizers tested against Gram-negative bacteria, grouped by ionic nature and chemical structure. As a side note, through the following sections, whenever the term "efficient eradication" or similar is used, it refers to a decrease of at least 99.9 % of bacterial survival or 3-log reduction. A technical resume of the described examples, along with relevant information (i.e. concentration of the photosensitizer, light source, light fluence, light dose, etc.) are summarized in the Supplementary Material.

2.1 Cationic photosensitizers

Most of the antibacterial pipelines focuses on the development of novel cationic molecules [19], with this trend being valid for PACT as well. This has led to an extensive library of different photosensitizers, with different core structures, as porphyrins, phthalocyanines, chlorins, bacteriochlorins and others (Supplementary Material 1).

2.1.1 Cationic porphyrins

Porphyrin's relative easiness of synthesis and chemical tuning, has provoked a huge number of relevant examples in the use of cationic porphyrins, understandably, relying in the presence of tertiary amines derivatives. One of the best studied examples of cationic porphyrins is **TMPyP** (**1**, Figure 4), from which several applications are found in literature. In one of the most recent examples using **1**, and compared with its zinc(II) derivative **2**, Seeger et al. demonstrated efficient photo-eradication against model *Proteus mirabilis* and *P. aeruginosa*, but also against their respective clinical isolates from canine otitis, as a result of light-driven production of singlet oxygen [20]. Although normally the non-metalated **TMPyP** or its zinc(II) metalated derivative are analyzed, Skwor et al. have devoted to the analysis on the influence of the metalation (Cu^{2+}, Fe^{2+}, Pd^{2+} and Zn^{2+}) in the antibacterial activity, finding that **3**, metalated with Pd, was the most efficient at eradicating *E. coli* [21], this evidencing the upmost importance of the metal used, and consequences on the photo physics of PS. Indeed, whereas copper and iron induce prompt quenching of the excited state, palladium(II) enhances spin-orbit coupling, and thus conversion to the triplet state and ultimately in fine singlet oxygen generation.

The advances obtained through the structural analysis of several cationic porphyrins has led to the conclusion that cationic charge is not only needed, but also an amphiphilic moiety that enhances the cellular uptake. Then, cationic porphyrins **4** and **5**, along their zinc(II) derivatives **6** and **7** (Figure 4), were successfully tested by Calmeiro et al. against *E. coli*, with its antimicrobial activity resulting enhanced by the presence of KI 100 mM (For further details on PACT potentiation effect due to inorganic salts, see Section 4.3, *vide infra*) [22]. Furthermore, a complete family of porphyrins bearing either non-cationic phenyl moieties or methylpyridinium-4-yl moieties (**8** – **12**, Figure 4), were tested against *E. coli* eradication, showing that other parameters, such as the charge number and distribution must be taken into account.

Compound **12** was evidenced to be the most efficient antibacterial treatment [23]. On regard of the efficient results obtained with **12**, it was further used by Marciel et al. for the efficient disinfection of *E. coli* in plasma and blood, with low evidence of hemolytic activity towards erythrocytes [24].

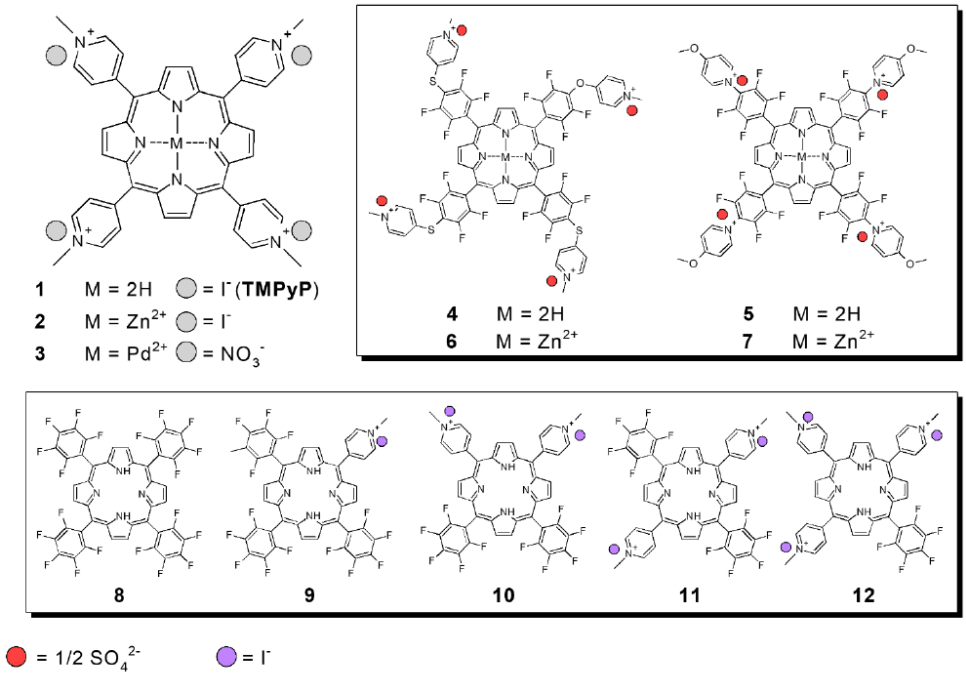

Figure 4: Structure of some cationic porphyrins presented along this work

In another approach, several cationic *o*-pyridil porphyrins (**13** – **16**, Figure 5) were compared, testing the influence of the alkyl's length chain on *E. coli* disinfection, where it was found that the compound **16,** bearing an alkyl chain with eight carbons, decreased the bacterial viability in around 97 %, while compound **13** was only able to reduce bacterial viability by 20 % [25, 26]. These results were compared with similar iron(III)-metalated porphyrins [27], obtaining similar results and bearing the same conclusions: for Gram-negative eradication not only cationic charges are needed, but also lipophilicity is desirable.

As it is unlikely that current research has achieved the ultimate photosensitizer, several works aim to increase the structural diversity of the porphyrinic systems, aiming also for β-substituted porphyrins. Namely, Moura et al. presented three cationic porphyrins (**17** – **20**, Figure 5), bearing imidazole units at a β-pyrrolic position, and analyzed their efficiency against bioluminescent *E. coli,* successfully reducing its bacterial density [28]. Interestingly, **19**, albeit bromine substituted is not the best $^1O_2$ producer, it is one of the most efficient in killing bacteria; furthermore, the most efficient compound in $^1O_2$ generation, **17**, was unable to decrease bacterial survival. In another example, Vinagreiro et al., focused on porphyrins *meta*-substituted with 1-methyl-imidazol-2-yl, synthesizing compounds **21** to **24**, Figure 5. These compounds were tested against model bacteria *E. coli* and *P. aeruginosa*, and given the efficient results obtained with compounds **22** and **24**, they were further successfully tested against multidrug-resistant *A. baumannii, K. pneumoniae* and *E. coli* [29].

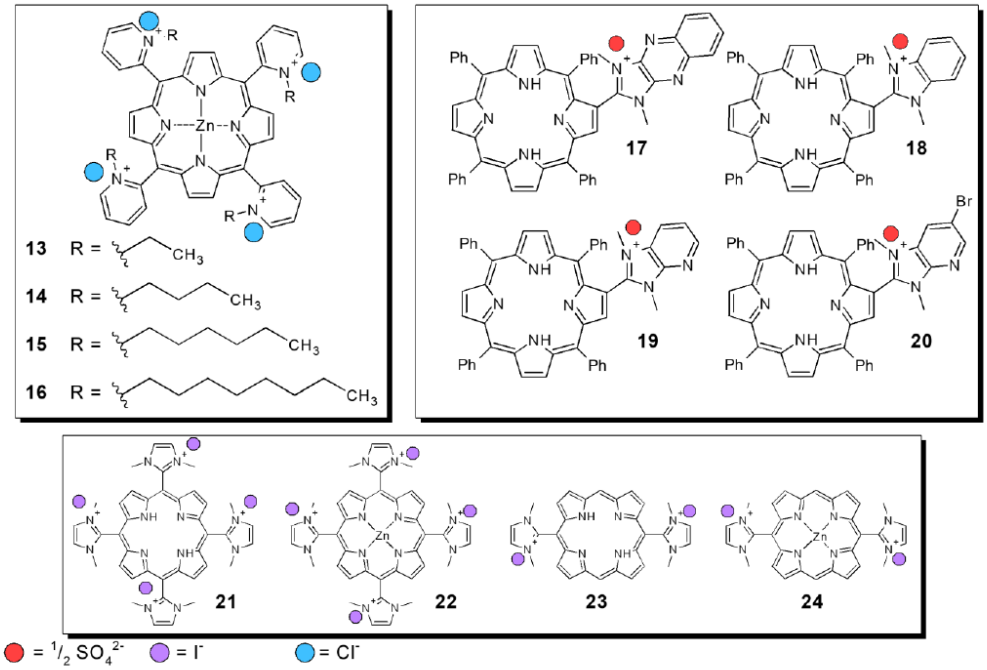

Figure 5: Different structures of cationic porphyrins

2.1.2 Cationic phthalocyanines and subphthalocyanines

Porphyrins are not the only photosensitizers aimed for the eradication of bacteria. Phthalocyanines are widely used against bacteria proliferation, with comprehensive reviews being recently published by Galstyan [30], and by Ribeiro [31]. In the present section we aim to present some of the most representative advances on the use of phthalocyanines against Gram-negative proliferation.

Returning to the previous investigation of Marciel et al. [24], the cationic phthalocyanine **25** (Figure 6), bearing eight cationic charges was used for blood disinfection. When researchers compared the obtained results of **12** (Figure 4) and **25** (Figure 6), although both photosensitizers were able to efficiently decrease the bacterial concentration in PBS, when challenged in complex media (i.e., plasma or complete blood), the cationic porphyrin was more efficient than the cationic phthalocyanine, an effect attributed to the phthalocyanines tendency to aggregate in aqueous media, despite its eight cationic charges [24].

In another approach, Lourenço et al., developed four cationic phthalocyanines, with four to sixteen cationic charges, which were tested against bioluminescent *E. coli* and *E. coli* biofilm, under white and red light. The best results were obtained with the phthalocyanines with 4, 8 and 16 cationic charges (**26 – 29**, Figure 6) under red light irradiation, for both planktonic and biofilm cells. Interestingly, the best result appears to be with the phthalocyanine bearing 8 cationic charges, which could be attributed to the size of the molecule [32]. In a similar effort, Aroso et al. prepared and analyzed the effect of the number of charges, the length of the alkyl chain and the nature of the complexed metal (**30 – 33**, Figure 6). The best antimicrobial effect against *E. coli* and *P. aeruginosa* was found with **30**, a zinc(II) phthalocyanine bearing four cationic charges and a two-carbons alkyl chain, in agreement with previous experiments where “less is more” [33].

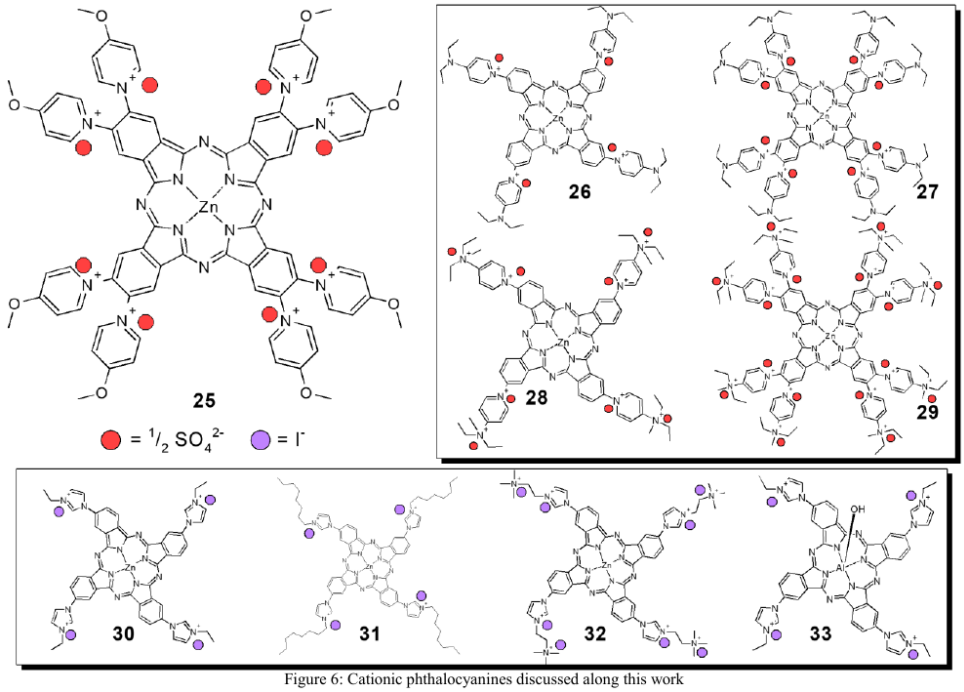

Figure 6: Cationic phthalocyanines discussed along this work

In another example, Mantareva et al., prepared two lutetium(III) acetate cationic phthalocyanines, and tested them against an antibiotic-sensitive strain of *P. aeruginosa*. The phthalocyanines differed in the position of the methylpyridinium-4-yl moieties, being in the non-peripheral (**34**) or peripheral position (**35**, Figure 7). This difference appears to be decisive, as the non-peripheral substituted phthalocyanine was an efficient photobactericide molecule, while the other only showed a modest reduction in bacterial survival [34]. In a related work, Dlugaszewska et al. prepared a magnesium(II) phthalocyanine (**36**, Figure 7), bearing eight cationic moieties in the non-peripheral positions, which was able to eradicate planktonic bacteria of *E. coli*, *P. aeruginosa* and *Serratia marcescens* under near-infrared light irradiation, but failed to eradicate mature biofilm from the same bacteria [35].

Most of the differences found for several phthalocyanine compounds are due to the phthalocyanines tendency to aggregate in aqueous media. To overcome this, Ruiz-Gonzalez et al., prepared four cationic dendrimeric phthalocyanines, bearing either zinc(II) (**37** and **38**) or ruthenium(III) (**39** and **40**, Figure 7). Interestingly, it was found that the zinc-metalated phthalocyanines had a best performance against *E. coli,* under light irradiation at 635 nm [36]. The presence of hydroxyl moieties could prevent the aggregation of the phthalocyanines, as Meerovich et al. proposed with an octa-cholinyl substituted phthalocyanine (**41**, Figure 7), which was able to successfully decrease the bacterial survival of *P. aeruginosa* planktonic cells and biofilm cultures, after red light irradiation [37]. Also, Lin et al. developed a monosubstituted phthalocyanine **42** (Figure 7), which was efficient at the eradication of *E. coli*, needing only 8 µM of the compound to achieve a 5-log reduction [38].

Then, cationic phthalocyanines are a good alternative for photosensitizers against Gram-negative bacteria, as demonstrated through several literature examples. New examples should consider not only the presence of cationic charges, but also the presence of hydrophilic moieties to prevent aggregation in aqueous media, a factor that seems particularly detrimental for these compounds.

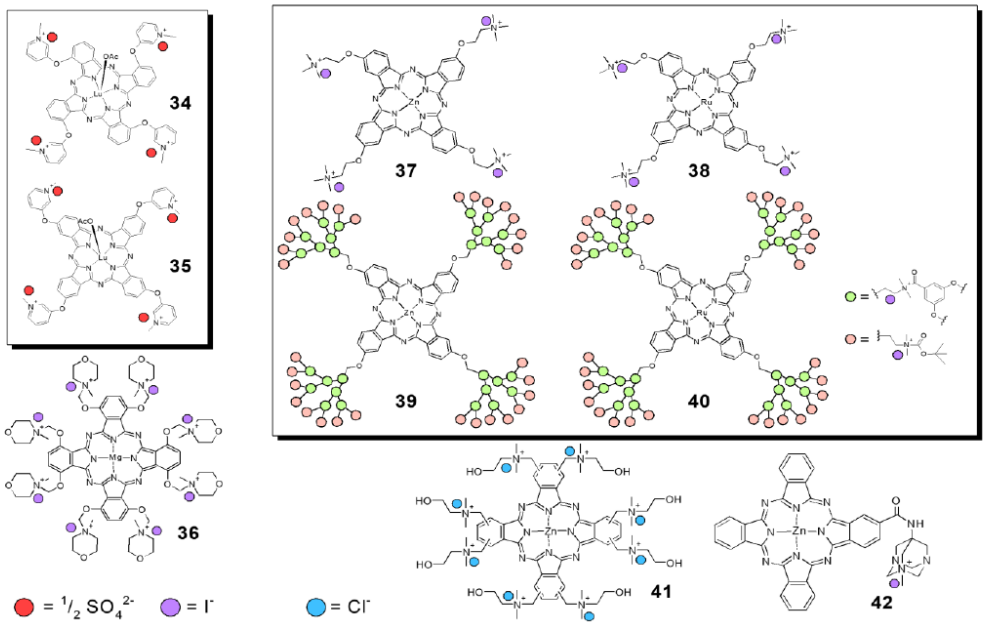

Figure 7: Cationic phthalocyanines presented along this work.

2.1.3 Cationic chlorins and bacteriochlorins

Although less common, there are some examples on the use of cationic chlorins and bacteriochlorins against Gram-negative proliferation. As an example, Meerovich et al., tested two different bacteriochlorins (**43** and **44**, Figure 8) against *P. aeruginosa* planktonic cells and biofilm cultures. Both symmetric bacteriochlorins, were able to efficiently reduce the bacterial survival of planktonic cells, while it required higher concentrations and higher light doses to eradicate biofilm cultures [37]. In the same work, Meerovich et al. compared the efficiency of these bacteriochlorins against the cationic phthalocyanine **41** (Figure 7), evidencing that the bacteriochlorins were more efficient under similar conditions, possibly due to the difference of size, which permits smaller molecules to diffuse easily through Gram-negative membranes. In another example, Ziganshyna et al. tested a commercial bacteriochlorin tetrahydroporphyrin-tetratosylate **45** (Figure 8), against several drug-resistant strains of Gram-negative bacteria, demonstrating a good eradication, although high concentrations and high light doses (from a laser or a LED-source) were used [39].

2.1.4 Cationic BODIPY

Cationic bore-dipyrromethene' (BODIPY) are pyrrolic derivatives which are easily synthesized and chemically tuned, which are under current intense research as efficient photosensitizers for photodynamic therapy [40]. In a recent example, two cationic BODIPY (**46** and **47**, Figure 8) were synthesized and tested against *E. coli* planktonic cells, achieving an efficient eradication. Although structurally different, these two BODIPY's had similar effectivity, but when 50 mM of KI were added to the mixture, the BODIPY with a cholinyl moiety was clearly the most efficient photosensitizer, when irradiated with white light [41]. This compound was later further analyzed by Piskorz et al., whom found that this compound was also effective, under different experimental parameters. Furthermore, they found that the presence of iodine into the β positions (**48**, Figure 8) increased their activity around 10 times [42].

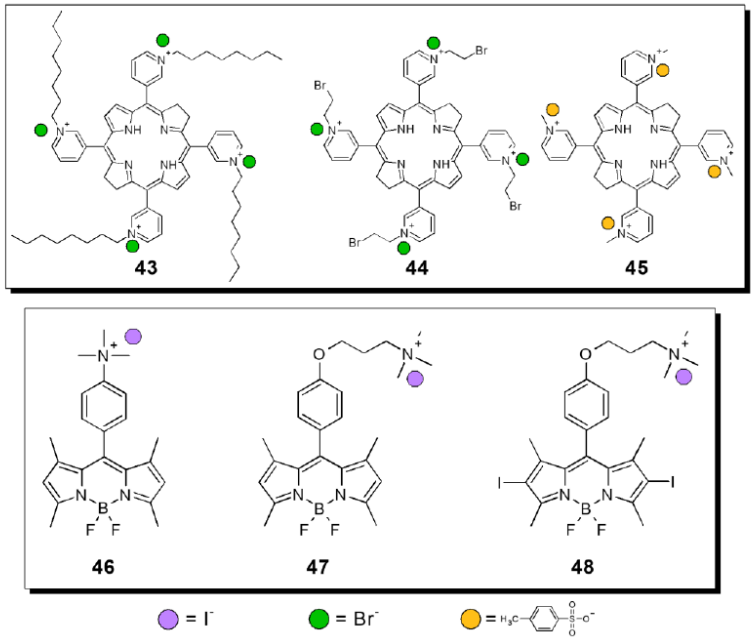

Figure 8. Cationic bacteriochlorins and BODIPYs derivatives

2.1.5 Methylene blue and other dyes

Traditional dyes, as methylene blue, Rose Bengal, erythromicine, etc., were the first photosensitizers. Up to this date **methylene blue** (**MB**, **49**, Figure 9) is still under preclinical use, due to their well-known characteristics and proved safety. Nevertheless, there are still novel applications and exciting results to be found. As an example, dos Anjos et al., used **MB** for the eradication of three strains of *K. pneumoniae*, which were producers of β-lactamase, an enzyme that impedes the proper function of β-lactamic antibiotics. Then, the use of **MB** in sublethal doses decreased the activity of β-lactamase, and, furthermore, possibly reverts the sensitivity of the *K. pneumoniae* strains to β-lactamic antibiotics [43]. In a similar approach, different types of carbapenemases produced strains by *S. marscences, K. pneumoniae* and *Enterobacter aerogenes,* were photodynamically degraded by **MB**, leading to a recovery of the sensitivity to carbapenem [44]. Additionally, there's evidence that **MB** can lead to a modest eradication of several strains of *A. baumannii*, independently of their sensitivity towards carbapenem [45]. Then, **MB** appears as a suitable complement to traditional chemotherapy against drug-resistant bacteria. In another approach, different dyes, as **toluidine blue O (TBO) 50**, **azure A 51** and **new methylene blue 52** (Figure 9), had been tested against *K. pneumoniae*, resulting in efficient photosensitizers against planktonic and mature biofilms [46].

2.1.6 Other cationic photosensitizers

Another kind of photosensitizer are porphycenes, which are isomers of porphyrins. Their unique aromatic structure provides them with different photophysical properties than those observed for the porphyrins. Although the less, there are some examples of cationic porphycenes being used against bacteria, as Ruiz-González et al. research, whom synthesized two porphycenes (**53** and **54**, Figure 9) and tested them against *P. aeruginosa* and *E. coli*, resulting in an efficient eradication of bacteria [47].

Phenalenone derivatives have also acquired recent relevance as photosensitizers. Phenalenone is an oxygenated polycyclic aromatic molecule, bearing a ketone moiety [48]. Previously described toxicity has stalted the development of phenalenone derivatives as photodynamic agents, but some recent studies are overtaking this challenge. As an example, Tabenski et al., synthesized four cationic phenalenone derivatives (**55 – 59**, Figure 9), bearing a quaternary amine, and testing their activity against *E. coli* after blue light irradiation, comparing the obtained result with the reference molecule SAPYR **55**. The results obtained indicated an efficient bacterial eradication, with the best result obtained with an imine-substituted derivative, attributed to a foreseen ability to form hydrogen bonds with glutamate moieties on the bacterial membranes [49]. In a more recent example, Godard et al. prepared a complete library of phenalenone derivatives (**60 –**

75, Figure 9), combining phenalenone's photosensitizing activity with the antimicrobial activity derived from triazolium salts. These compounds were tested against three Gram-negative strains, two strains of *E. coli* and one strain of *P. aeruginosa*. Some of the compounds were active against the three strains, and although the results are modest, the authors discuss about the increased effect on compounds with hydrophobic moieties, which are likely to increase the interaction with the lipidic membranes of Gram-negative organisms [50].

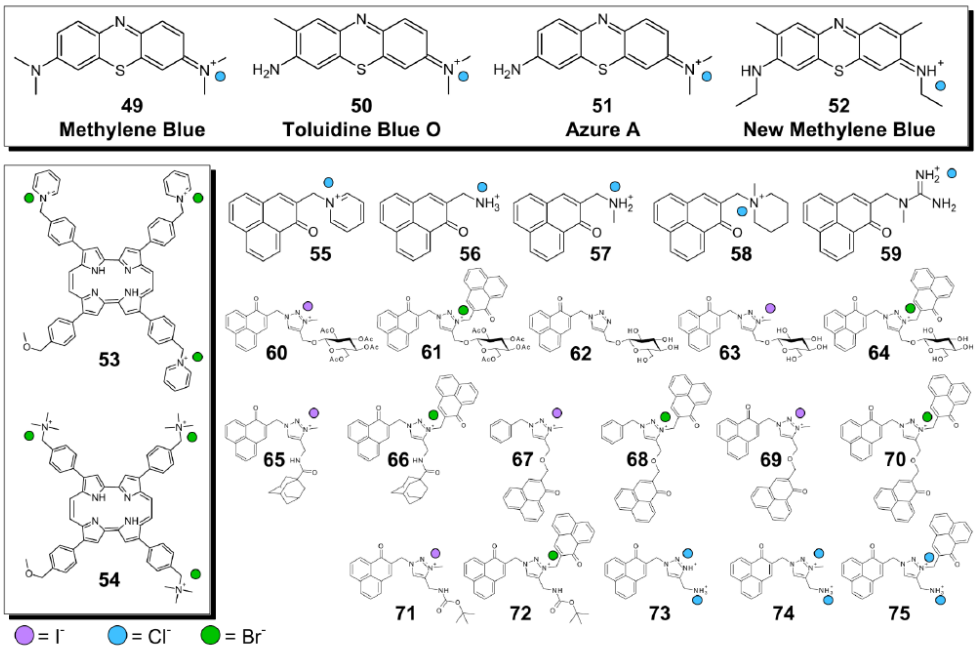

Figure 9. Cationic bacteriochlorins and BODIPYs derivative

One can also cite fullerenes, spherical carbon-based molecules, being just discovered in 1985. Thanks to their particular shape and structure, fullerenes absorb visible light, have a high intersystem crossing yield, and are even able to produce light-driven ROS [51]. Due to their chemical characteristics, fullerenes are highly hydrophobic and tend to aggregate in aqueous media, and then cationic functionalization provides both with increased water availability and targets the membranes of Gram-negative bacteria [52]. Furthermore, their aggregation capacity has been exploited, through the formation of fullerenes nanoparticles and testing them against *E. coli* [53].

2.2 Neutral and anionic photosensitizer

Although most of the current development of new photosensitizers is focused on cationic molecules, there are still some examples where non-cationic molecules are used for efficient bacterial eradication. However, is noteworthy that several of the molecules described along this section are parental molecules of the cationic porphyrins previously described.

2.2.1 Porphyrins

As previously described, Calmeiro et al., prepared several porphyrins, including the non-N-methylated derivatives of **4** and **6**, and tested them against *E. coli* in the presence and absence of KI [22]. Interestingly, while the neutral compounds failed to eradicate bacteria, the addition of KI into the media increased the efficiency of photobactericidal activity up to 3-logs, through the permeabilization of the Gram-negative membranes. Significantly, in another example, Ferreyra et al., prepared a porphyrin (**76**) and a chlorin (**77**, Figure 10)**,** with the porphyrin being able to efficiently eradicate *E. coli*, which despite its lack of cationic charges, was able to be uptaken by bacteria, reaching uptake levels similar as those found for cationic **TMPyP** [54].

2.2.2 Phthalocyanines

Similarly, when neutral phthalocyanines are tested against Gram-negative bacteria, they failed to eradicate bacteria where its cationic counterparts (**42,** Figure 7) succeeded [38]. Recently, Berezin et al., compared the efficiency of a neutral (**78**) and an anionic phthalocyanine (**79**, Figure 10) for *E. coli* eradication, using Tween 80 1% as a membrane disruptor, but also as a de-aggregation agent for the phthalocyanines, which together with the use of EDTA 0.1%, lead to excellent bacterial eradication [55]. Similarly, Biyiklioglu et al., compared the efficiency of a silicon phthalocyanine (**80**) and a boron subphthalocyanine (**81**, Figure 10) against *E. coli*, finding that both eradicate bacteria under white light irradiation, and being the subphthalocyanine the most effective compound, which correlated with subphthalocyanine's superior singlet oxygen production [56].

2.2.3 Chlorins and bacteriochlorins

In a recent example, **chlorin e6 (82**, Figure 10**)** was tested against biofilms made of two or three different bacterial species, namely *Moraxella catarrhalis, Haemophilus influenza* and *Streptococcus pneumoniae*, mimicking the bacterial environment found in otitis media infections. The effectivity of **chlorin e6** against the biofilms depended of the bacterial strains, the concentration, the incubation time and the light dose. Biofilms tend to be resilient communities that are impermeable to small molecules, providing resistance to antimicrobial therapies, and thus, the modest success of **chlorin e6** could be a fundamental stone for the use of photodynamic therapy, in combination with another antimicrobial chemotherapy, for the treatment of persistent otitis media [57]. Returning to the work of Ferreyra et al., they prepared a chlorin (**77**), which was tested against *E. coli*, achieving efficient eradication. When compared with the parental porphyrin **76**, both compounds had similar results against *E. coli* [54].

The lack of efficiency of neutral compounds against Gram-negative bacteria can be deduced as a consequence of the lack of interaction between the compounds and the cellular membrane. Krüger et al., approached this question using the neutral chlorin **chlorophyllin (83**, Figure 10**)**, against *Bacillus cereus*, *E. coli* and a membrane-defective mutant of *E. coli*. This compound could only eradicate bacteria lacking a proper cellular membrane, with the *E. coli* mutant being sensitive to photodynamic eradication [58].

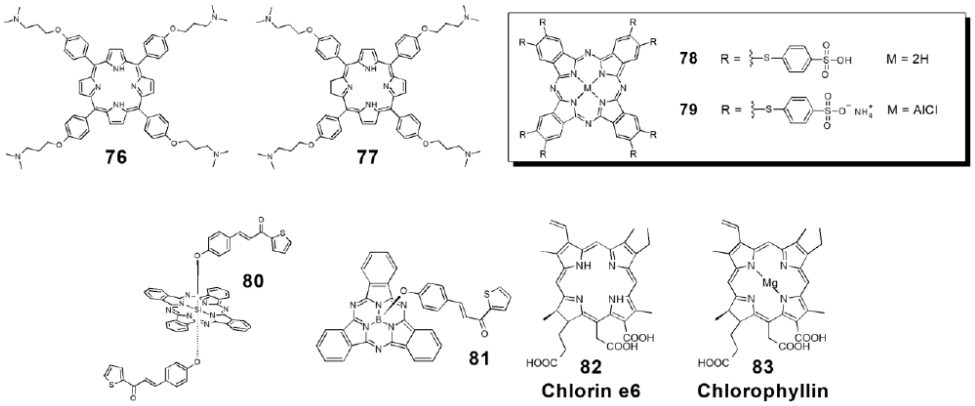

Figure 10. Neutral and anionic porphyrins, chlorins, phthalocyanines and subphthalocyanines

2.2.4 BODIPY and dipyrrinato compounds

Like others example of cationic PS of whom neutral analogs have been also investigated, neutral BODIPYs have been also studied. In the previous example of Piskorz et al., the non-cationic derivatives of **47** and **48** (Figure 8) were only able to reduce bacterial survival at high concentrations, as 50 and 500 μM [42].

In a recent example, Hohlfeld et al. prepared several neutral **BODIPY** compounds as an effort to understand the effect that chemical modifications had on their efficiency on disinfection of bacteria. The tested compounds could be divided in two groups, bearing either a 2,3,5,6-tetrafluorophenyl (**84** to **88**) or a 3-nitrophenyl (**89** to **93**, Figure 11) moiety at the *meso*-position. Further functionalization allowed to assess the effect of different moieties (i.e., amine groups, alkyne groups, hydroxyl groups, etc.) in the eradication of *P. aeruginosa*. The best results were obtained with the **BODIPY**s derivatives bearing a tetrafluorophenyl moiety and an unprotected thio-carbohydrate (glucosyl **87** or galactosyl **88**). Furthermore, the compounds were challenged in the presence of serum 10%, which significantly decreased the efficiency of the photodynamic treatments [59]. In a similar approach, the same researchers prepared several dipyrrinato-iridium complexes (**94** to **101**, Figure 11), and tested them against *P. aeruginosa*, under similar experimental conditions. Several

compounds were found to be effective against bacteria, and, similarly, their efficiency was decreased in the presence of serum 10 % [60].

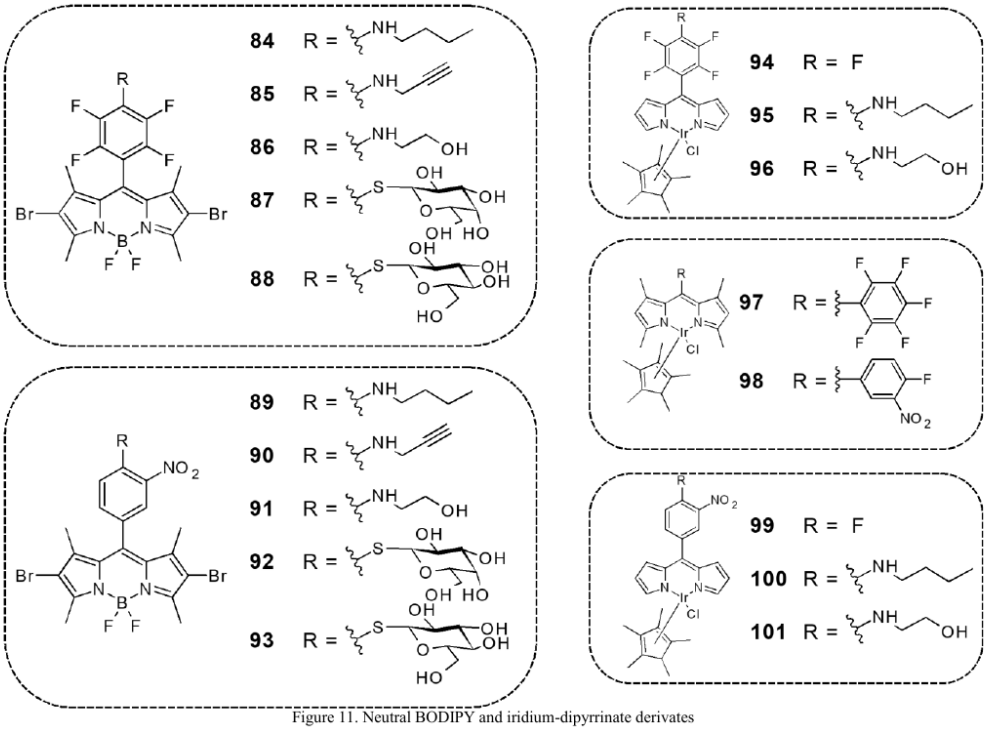

Figure 11. Neutral BODIPY and iridium-dipyrrinate derivates

2.2.5 Other photosensitizers

Erythrosine (102, Figure 12) is an anionic dye photosensitizer, whose efficiency against *A. baumannii* planktonic cells and biofilms has been investigated by Fekrirad and collaborators. Their research achieved an efficient eradication of planktonic bacteria when incubated with 0.01% of acetic acid, and achieved biofilm eradication when **erythrosine** was combined with 0.01% of acetic acid and 12.5 µM chitosan [61]. In a similar approach, Santos et al., increased the efficiency of **Rose Bengal (RB)** and **eosin** (Figure 12) against *Salmonella enterica* serovar Typhimurium, through the addition of KI prior irradiation with green light. The authors attributed this effect to the stabilization of the singlet oxygen with the ion I^-, leading to the formation of peroxyiodide and other radical species [62].

Although generally photosensitizers are perceived as small molecules, some reports indicate that LOV (light-oxygen-voltage receptor) proteins are susceptible to be used as photosensitizers against bacteria [63]. In a most recent report, three different proteins, **SOPP3**, **SuperNova** and **KillerOrange** (Figure 12), originally intended as *in vivo* reporters of oxygen-limited systems, tend to be toxic towards *E. coli*, their heterologous host, when irradiated with light. Several experiments further confirm the toxicity of these proteins against *P. aeruginosa*, representing an interesting system that can easily be expressed together with targeting proteins, as lectine B (LecB), increasing their antibacterial efficiency [64].

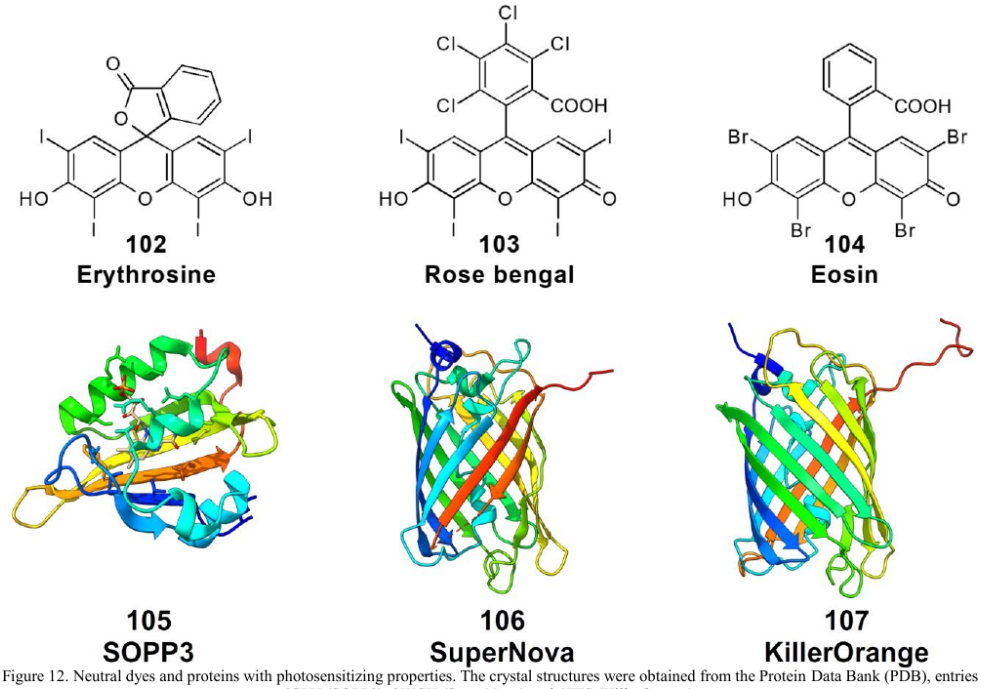

Figure 12. Neutral dyes and proteins with photosensitizing properties. The crystal structures were obtained from the Protein Data Bank (PDB), entries 6GPU (SOPP3), 3WCK (SuperNova) and 4ZFS (KillerOrange).

2.3 Synthetic metallic complexes

As photodynamic applications against microorganisms diversify, more alternatives of different photosensitizers start to appear. We have previously addressed several examples were metals, as iron [27], iridium [60], palladium [21], ruthenium [36], and lutetium [34], are used to form complexes with photosensitizers. However, the use of metals is not limited to the decoration of already stablished photosensitizers.

In a recent example, Hopkins and collaborators prepared a ruthenium(II) and platinum(II) complex (**108**, Figure 13) with phenanthroline, which was then tested against *E. coli* under white light irradiation. The results obtained indicated that the complex acts as a photosensitizer, resulting more efficient than cisplatin, a model platinum complex [65]. Intending to provide an increased bioavailability of the ruthenium complexes, Soliman and collaborators synthesized a ruthenium-polylactic acid complex (**109**, Figure 13), which was used to form nanoparticles. The nanoparticles were fully characterized, but when tested against bacteria, they were uncapable of eradicate Gram-negative bacteria, as *E. coli* and *P. aeruginosa*, explained through the low internalization of the nanoparticles [66]. Similarly, Le Gall et al. prepared several ruthenium polypyridiyl complexes (**110** - **126**, Figure 13). Then, although their binding to *E. coli* and *P. aeruginosa* was demonstrated through luminescence, the compounds were unable to decrease bacterial survival of Gram-negative bacteria [67]. In order to increase the binding between the ruthenium complexes and bacteria, another approach has been taken by Pierce et al. This group of researchers attached buforin II, an antimicrobial peptide, to a ruthenium complex (**127**, Figure 13), and then tested it against several model strains, successfully photoeradicating the model *E. coli*, but also against clinical isolates of drug-resistant *P. aeruginosa, E. coli, A. baumannii* and *K. pneumoniae* [68].

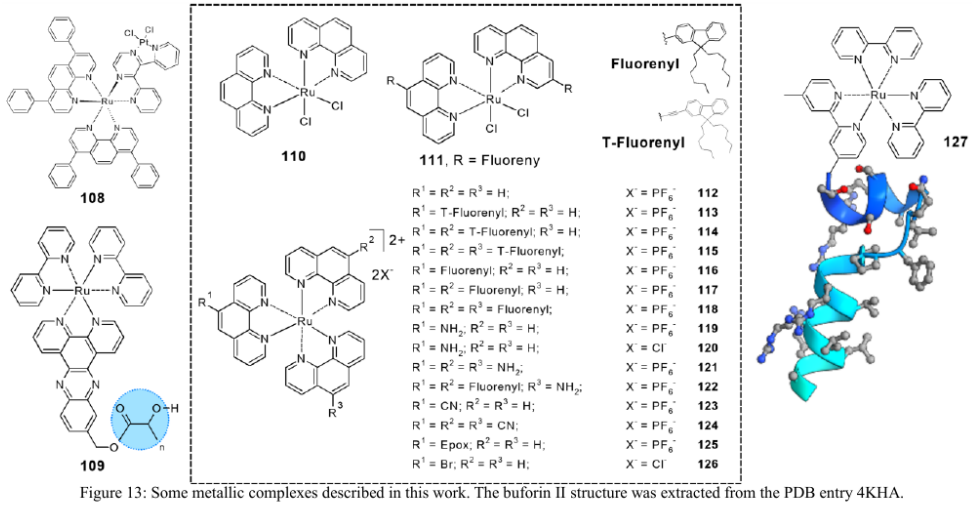

Figure 13: Some metallic complexes described in this work. The buforin II structure was extracted from the PDB entry 4KHA.

3. Materials with photosensitizing properties and delivery systems

As previously stated, AMR is a huge health concern for governments and scientists, with an imperative need for stronger policies, encouraging the development of novel technologies to fight microbial proliferation. One ever-growing topic is the development of self-disinfecting surfaces, as microbial contamination in surfaces, at hospital and food processing environments, can provide a platform for the proliferation and dissemination of bacterial biofilms into our communities. The development of materials with self-disinfecting properties, can be achieved with photosensitizing molecules, and additionally addressing the low aqueous solubility of several photosensitizers. Several examples of photosensitizing materials use either carbon-based or inorganic scaffolds, with all the systems having assets and drawbacks; an efficient antimicrobial material should indeed exhibit a good equilibrium between stability, preserved photophysical properties of PS, bactericidal efficiency and safety towards the host.

3.1 Materials based on biopolymers and carbon-based molecules

During the past decades, in line with the emergence of green chemistry, and due to their low cost and renewability, bio-sourced polymers have appeared as alternative drug formulations and scaffolds. As for PACT applications, an interesting review about the use of bio sourced polymers has recently been written [69], but the ever-growing interest of bio-sourced polymers makes a difficult task to pace up with the literature. Thus, in the following sections we present some of the most recent advances of materials based on biopolymers.

3.1.1 Cellulose materials

Among all the biopolymers, cellulose, a major structural compound in plants, is particularly used. Indeed, this natural polysaccharide, is constituted of a linear chain of several hundred to many thousands of β(1 → 4) linked D-glucose units, with a large amount of hydroxyl groups available, which can undergo a large range of chemical modifications that give rise to different materials. These properties permit cellulose to be addressed as an alternative raw material for different PS formulations.

For example, some studies reported the development of antibacterial cellulosic fabrics. The study published last year by Fayyaz et al. evaluated the photodynamic activity of three different tetracationic porphyrins, and their zinc derivatives (**1**, **2**, **128-131**, Figure 14) were impregnated on cellulosic fabrics, and tested against *E. coli* and *P. aeruginosa* [70]. Not only, all the modified fabrics displayed a photo-antibacterial activity against all strains investigated, but also, accordingly to the washing and thermal stability of the materials, these fabrics could be efficiently used for biomedical textile applications. In another study, Nzambe Ta Keki et al. investigated a neutral metalated porphyrin (**132**, Figure 14) covalently attached onto Kraft pulp fibers [71]. The authors clearly demonstrated here that their system was efficient towards Gram-negative bacteria, with an observed decrease greater than 4-log of bacterial count, after light irradiation.

More recently, a new strategy to obtain cellulose-fibers-based materials has been developed, such as electrospun cellulose microfibers developed by Wang et al [72]. Indeed, electrospinning is a simple and inexpensive polymer

formulation method, which can be applied to both natural and artificial polymers, accommodates a wide variety of photosensitizers and allow to generate materials with favorable features, such as high surface area-to-mass ratio, or a wide range of morphologies and high porosity. Thus, the authors investigated porous cellulose diacetate electrospun microfibers loaded with **protoporphyrin-IX** (**PPIX**, **133**) as photosensitizer as active systems against *E. coli*. The different characterizations of the obtained material shown not only that the PS was uniformly distributed on the microfibers, but also that due to the pores size and shape, it was less prone to promote *E. coli* adhesion. However, the modest antimicrobial photodynamic efficiency against *E. coli* could be improved, once again, through the addition of 100 mM KI, enabling up to 6-log of bacterial reduction.

Through these examples, the authors have also emphasized the importance of the morphology of the material as well as its capacity to adhere to bacteria, while ROS generation by the photosensitizer must be keep high. Those parameters are even more important for materials without cationic charges, which are recognized as important factor for the interaction with Gram-negative bacterial membranes. Similar kind of observations have been done for chitosan-based photo-antibacterial materials.

3.1.2 Chitosan-based materials

Chitosan is a polymer derivated from chitin, a polymer that composes the shells of shrimps and insects. This polymer is composed of β-(1→4) glucosamine and N-acetyl glucosamine monomers. Indeed, this polysaccharide has evidenced its suitability for PACT application, due to its low toxicity, biodegradability, bacterial association, film-forming ability, and intrinsic antimicrobial activity due, to its numerous pendant amino groups. Castro et al. have, for example, investigated the antibacterial efficacy of **12** derivatives (**134** and **135**, Figure 14), conjugated to chitosan (films) or TiO_2 (powder), against *E. coli* [73]. The PS immobilization on chitosan was less efficient than on TiO_2, and the interaction of PS with chitosan was evidenced by UV-visible absorption spectra shift. Moreover, **12** showed the same $^1O_2$ production in solution and immobilized on chitosan, probably due to aggregation-driven attenuation or increased photostablility of the immobilized PS. The antibacterial efficiency of the systems was found to be linked to their singlet oxygen production, which relies on both PS structure and PS-material interaction, being decreased for both chitosan and TiO_2 materials.

Chitosan, in its polycationic form, can be formulated as a hydrogel. Hydrogels are cross-linked polymer chains, swollen with water, which can be loaded with small molecules, either through entrapment or grafting through its amino groups. Bayat and Karimi have used these properties to prepare different chitosan hydrogels. In a first example, they associated a zinc phthalocyanine/colistin conjugate **136** (Figure 14) and chitosan, increasing the bioavailability of the phthalocyanine, while also providing a targeting moiety [74]. Additionally, they observed enhanced PACT efficiency against *P. aeruginosa*, resulting from the synergy of the photodynamic effect and the antibacterial agent targeting, which has been observed previously by Sol's group [75]. The second hydrogel contained a zinc phthalocyanine **137** (Figure 14)**,** difloxacin and chitosan, producing $^1O_2$ with good efficiency, under visible light irradiation, resulting in a good candidate for PACT applications [76]. More recently, another study analyzed a hydrogel bearing a silicon phthalocyanine **138** (Figure 14), published by Strokov and Galstyan. When analyzed, the hydrogel kept the phthalocyanine's photophysical features, namely absorption and emission wavelength, fluorescence quantum yield, while showing an increased $^1O_2$ production. This led to an efficient *E. coli* eradication*,* probably due to the stronger interaction with bacteria cells and the enhanced singlet oxygen production of the material [77]. In another example, Yin *et al*., demonstrated that eradication of drug-resistant bacteria *E. coli*, can be achieved through incorporation of upconverting nanoparticles (UCNPs) doped with **MB** in chitosan hydrogel [78]. Their most efficient system (UCNPs@MB:QCS 2:100) against *E. coli* achieved up to 95% of bacteria killing efficiency, after 20 minutes of 980 nm irradiation at 1 W/cm^2.

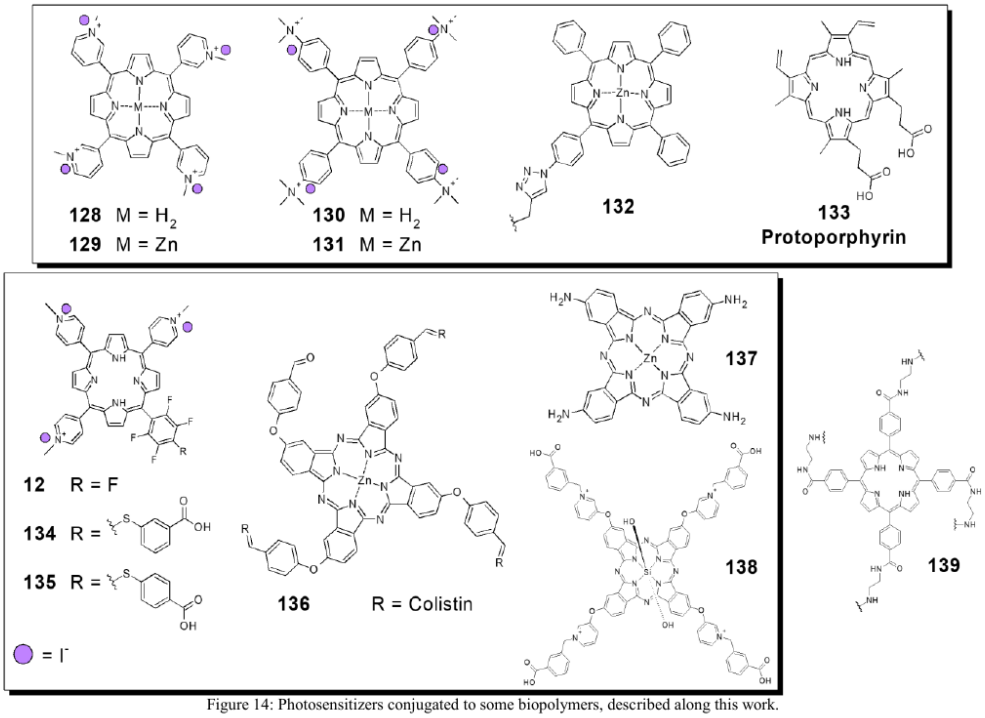

Figure 14: Photosensitizers conjugated to some biopolymers, described along this work.

3.1.3 Other biopolymers materials

A recent study published by Kumari et al., deals with the self-assembly of a DNA-Porphyrin (**139**, Figure 14) hybrid nanonetwork [79]. In this work, the DNA-porphyrin hybrid nanonetwork was less efficient than the free porphyrins to inactivate *E. coli* strains, probably due to the negatively charged DNA backbone, which would prevent the uptake of the scaffold. However, the systems also showed reduced toxicity towards mammalians cells, that is a great asset for future applications.

Another very interesting natural biopolymer is protein keratin. Wool keratin has demonstrated to have great potential in regenerative medicine, but bacteria colonization and biofilm formation should be prevented. Ferroni et al. associated wool keratin 3D scaffolds with encapsulated **Azure A** (Figure 9), in order to form photo-activable porous sponges [80]. The obtained materials exhibited good efficiency against *P. aeruginosa* under light irradiation, and no toxicity towards mammalian skin cells, while possessing a suitable 3D structure, pore size and degradation rate, resulting in a suitable candidate for tissue engineering.

3.1.4 Micelles, liposomes, vesicles and microemulsions

Lipidic materials are able to spontaneously form self-assembled micelles and liposomes, which have been widely exploited in therapeutic applications [81]. For example, Rout et al. investigated the use of eucalyptus oil microemulsion as a carrier for delivering **TBO** (Figure 9) [82]. They evidenced that, in addition to a synergic antibacterial effect against *P. aeruginosa*, this formulation increased the permeation characteristics, as the penetration into the viable layers of the skin was improved for the encapsulated PS, when compared with the free **TBO**; additionally, **TBO**'s stability was enhanced.

In another study, Sharma et al. described cationic vesicles encapsulating **MB** against *E. coli* [83]. These vesicles are made with hexadecyl pyridinium cuprate as cationic component, and sodium oleate as the anionic one, with different ratios. The ratio 70:30 in the cationic and anionic components demonstrated a complete eradication of bacteria within 5 min of irradiation, with the enhanced vesicles attachment being the key factor for the improved efficiency. Moreover, the role of the metal was also evidenced, demonstrating enhanced $^1O_2$ generation. **MB** has also been encapsulated in cationic liposomal formulations containing dimethyldioctadecylammonium chloride, dipalmitoylphosphatidycholine and cholesterol, by Boccalini et al. [84]. **MB**-loaded liposomes showed a higher efficiency, in both terms of bacterial toxicity

against *E. coli* and penetration into the bacterial biofilm, compared to the free **MB**. Moreover, an enhanced inactivation of lipopolysaccharides, a major pro-inflammatory endotoxin of Gram-negative bacteria, was also observed. More recently, Pourhajibagher et al. encapsulated **curcumin** (**140**, Figure 15) in silver sulfadiazine nanoliposomes, developing a photoactivable antimicrobial system, efficient against *A. baumannii* [85]. These systems showed negligible toxicity against eukaryotic cells, while efficiently photoeradicating *A. baumannii*. In another example, Sobotta and collaborators, encapsulated two chlorins (**141** and **142**, Figure 15) inside lipidic vesicles and tested them against *E. coli*. However, at the highest concentrations tested, the treatments were unable to decrease the bacterial survival of *E. coli* further than 2.23 log, while demonstrating efficiency eradication of Gram-positive bacteria [86].

In addition to liposomes, vesicles and microemulsions, PS can also be encapsulated in micelles, as evidenced by Wang et al. in 2021, whom prepared **chlorin-e6** polyethyleneimine-based micelles, with enhanced photodynamic inactivation of *E. coli* [87]. The $^1O_2$ generation production of **chlorin-e6** was preserved inside the micelle, while the water solubility of the PS was improved without the need of any organic solvents. The authors also evidenced that cellular uptake was enhanced when chlorin-e6 was transported through micelles, with both enhanced uptake and singlet oxygen production, leading to the high antibacterial efficiency observed.

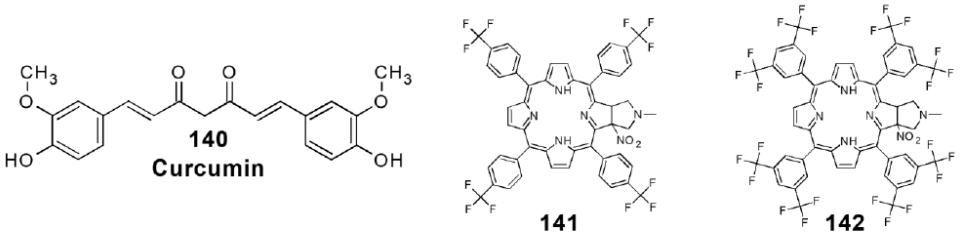

Figure 15: Photosensitizers associated to some lipidic systems, described along this work.

3.1.5 Other systems

More recently, Contreras et al. have also investigated Photodynamically Active Fibers (PAFs) based on poly(L-lactide)co-(glycolide) and poly(ε-caprolactone) loaded with **MB** [88]. Moreover, The **MB**-encapsulated electrospun fibers showed a good structure stability, as well as a controlled released of **MB** over 3 weeks. In addition, up to 2.5-log viability reduction was observed for *E. coli* under light irradiation. Moreover, dark toxicity was drastically reduced compared to free **MB**. Electrospun fibers containing poly(ε-caprolactone) were used to develop innovative membranes, that were associated to a metal-organic framework (MOF), loaded with **RB [89]**. The authors combined all the assets of the different components for their molecular system: poly(ε-caprolactone) allowed the membrane formation, while MOF, with their intrinsic porous structure, provided high chemical and thermal stability. After visible light irradiation, these hybrid nanofibrous membranes exhibited excellent ROS generation and antimicrobial activity against *E. coli*.

Another interesting approach, is the one developed by Castro et al. They developed two systems based on 2-hydroxyethyl methacrylate, and **8** (Figure 1), either as a copolymer or as a porphyrin-loaded polymer [90]. The obtained co-polymer was more efficient in terms of $^1O_2$ generation, than the **1**-loaded polymer, probably due to the dispersion of the porphyrin on the polymer net, avoiding PS aggregation. Moreover, a reduction of approximately 99.9% of *E. coli* was observed in the case of the co-polymer, which could be reused at least three times, without losing its efficiency. The porphyrin-loaded polymer was more efficient than the free PS against *E. coli,* while requiring higher concentrations than for the co-polymer treatment (co-polymer > loaded polymer > free porphyrin). This example perfectly illustrates the primordial importance of PS formulation.

3.2 Inorganic and hybrid materials

As previously described, in addition to formulation to reach the highest photoactivable efficiency of PS, scientists consider other factors when designing photo-activable materials. As an example, they aim for the development of environment-friendly systems, which would be economic, reusable, recyclable and cost-benefit permissive. This can be obtained through the use of inorganic solid matrices as scaffolds for PS molecules.

3.2.1 Magnetic nanoparticles

This could be addressed, for example, by immobilization of the PS on magnetic nanoparticles, which can be visualized and guided in water and organic solvents, by means of an external magnetic field [91]. As an example, Scanone et al. have, developed silica-coated Fe_3O_4 nanoparticles grafted with either a **8** [91] or BODIPY derivatives **143** and **144**

(Figure 16) [92]. They particularly investigated the charge effect of the whole system and nicely evidenced that the most efficient against *E. coli*, was the one that exhibited the most positive ζ-potential and the highest $^1O_2$ quantum yield. Indeed, the authors observed a 4-log reduction of *E. coli* after 30 min of irradiation (visible light; 90 mW/cm^2). Moreover, the system could be reused at least three times without losing its efficiency. This example illustrates the importance of an equilibrium between stability, charge and ROS generation, for systems used in PACT applications. In the latter study, with BODIPY derivatives, the authors investigated the impact of heavy atom, bromine, on ROS production and the overall efficiency of the photo-activable antimicrobial material. Their bromine substituted system reached a reduction of 5 logs in *E. coli* survival after 15 min of irradiation, versus 1.7 logs in the same conditions, for the non-brominated system.

Super Paramagnetic Iron Oxide Nanoparticles (SPIONs) had been also used for antimicrobial materials. Indeed, they are well-known as effective PhotoThermal Therapy (PTT) agents that could be associated with PS in order to reach combined PTT-PDT systems [93]. In this line, Bilici *et al*. investigated the bactericidal effect of **indocyanine green** (**ICG**, **145**, Figure 16) grafted on 3-amino-propyltrimethosilane coated SPIONs against *E. coli, K. pneumoniae,* and *P. aeruginosa*, particularly focusing in the influence of the charge on cellular uptake. Interestingly, the system without **ICG** exhibited a positive ζ-potential, whereas, when loaded with **ICG**, ζ-potential was negative; nevertheless, the cell internalization studies for both systems did not shown significant difference. Efficiency against bacteria was dependent of the strains, with **ICG**-loaded one being the most efficient. In another approach, Fe_3O nanoparticles for PTT-PDT combined applications were developed by Zhang et al., using chitosan coating and an anionic porphyrin, **TCPP 146** (Figure 16), with the introduction of metal nodes preventing the self-aggregation of the porphyrin and improving $^1O_2$ generation [94]. By using both PTT and PDT, the authors reached a 98% of *E. coli* reduction of bacterial survival, while PTT or PDT only reached 45% and 42%, respectively.

3.2.2 Titanium oxide nanoparticles

Titanium oxide (TiO_2) nanoparticles are nanomaterials with interesting APDT applications, thanks to their low toxicity, high stability and excellent biocompatibility, as already underlined in the work of Castro et al. [73]. One can also cite the work of Sułek et al., who investigated visible-light-activated TiO_2 based materials, modified by tetra sulfonated porphyrin derivatives (**147** – **150**, Figure 16), and formulated as transparent colloidal solutions [95, 96]. However, although only 1-2 log decrease in survival of *E. coli* was monitored after 20 J/cm^2 of blue light (420 nm), the authors improved their efficiency of the systems with KI potentiation, leading to a reduction of up to 5 logs.

In another example, Ozturk et al., developed TiO_2 based nanomaterials loaded with a subphthalocycanine **151** (Figure 16), showed promising results against *E. coli* [97]. They evidenced that their system had inhibitory and bactericidal effects on *E. coli* at 10 and 20 J/cm^2 light doses, respectively. The systems combined the activities of both TiO_2 (intrinsic) and subphthalocycanines (light-activated), while preventing PS aggregation. Unfortunately, no photophysical data of the PS was measured, preventing a comparison with Sułek's system in order to propose a structure-activity relationship.

3.2.3 Mesoporous Silica nanoparticles or supports

Another material currently used in biomedical application are silica nanoparticles. In this framework, while aiming to improve antimicrobial systems and bacteria cell wall interaction, as well as developing a theranostic materials, Grüner et al. have fully described UCNP, coated with a mesoporous silica shell, loaded with a silicon phthalocyanine (**152**, Figure 16). Moreover, they further functionalized their nanoparticles with (3-aminopropyl)triethoxysilane and CH_3I, HOOC-TEG-COOH, or HOOC-TEG-NH_2 and CH_3I. These complex systems were analyzed for their efficiencies at photo-inactivating *E. coli* [98]. The intrinsic toxicity of UCNP was enhanced by the mesoporous shell of the particles, which improved binding of the particles to the bacterial membrane. A synergic effect was observed, with *E. coli* eradication being dependent on the number of cationic charges incorporated into the systems, permitting the binding to the bacterial membrane, and promoting its disorganization. Tang et al. described as well a very smart system that combined silicon nanoparticles, loaded with **chlorine-e6** as PS, and glucose polymer, to promote their transport through the ATP-binding cassette transporter [99]. Their systems showed an antibacterial efficiency up to 96% against *P. aeruginosa* under.

In another example, Sun et al. developed a complex platform for bactericide applications associating a polymeric matrix made up with poly(ε-caprolactone) and the vegetal-protein zein, coating **MB**-loaded mesoporous silica nanoparticles [100]. Moreover, with further surface modification with trichloro-(1H,1H,2H,2H-heptadecafluorodecyl)silane, their nanocomposite exhibited enhanced surface hydrophobicity and bacterial repellency. Indeed, thanks to the synergistic effects of PACT and anti-bacterial adhesion, the hybrid nanomaterials showed 97% of disinfection, lower than for the PS alone, for *E. coli* upon visible light irradiation (660nm; 20 min). Another nanohybrid material, combining the effect of different materials has recently been described by Kuthati et al. [101]. In this study, the authors associated **curcumin** as PS with silver nanoparticles, immobilized on copper-impregnated mesoporous silica

nanoparticles. Their whole system exhibited a positive ζ potential, up to +35 mV, that allowed good binding, and efficient membrane disorganization, resulting in efficient disinfectant materials against *E. coli*.

3.2.4 Silver NP

Currently, photosensitizers have been combined with silver nanoparticles (AgNPs), as the silver bactericidal effect is widely known. In this field, AgNPs exhibit a pronounced antimicrobial effect, especially against Gram-negative bacteria, being a potential complement to PACT. The mechanism of AgNPs bactericidal effect rely in the destruction of bacterial membranes thanks to the Ag^+ ions. Moreover, the conjunction of PS and AgNPs has resulted in a synergistic effect the bactericide effect of the Ag^+ and ROS. Several examples can be found in the literature, using **TMPyP** [102] or **MB** [103] as PS. Similar observations were made with PS-AgNPs immobilized in fabrics [104]. In this study, Chen et al. hypothesized that the strong electric field around the silver nanoparticles can promote the optical absorption of the PS and singlet oxygen generation , as already observed by other groups. Recently, Macia et al. have proposed an improvement of this interaction between AgNPs and PS, comparing the effect of the shape, in **RB**-decorated silica-coated silver nanocubes ($Ag@SiO_2$-RB Ncs) or silver nanospheres ($Ag@SiO_2$-RB Nss) [105]. They evidenced that the intrinsic electromagnetic hotspots produced by the lightning-rod effect in anisotropic metal nanoparticles, permitted a better bactericidal efficiency. A viability decrease of *E. coli* of 6-log was observed in the case of $Ag@SiO_2$-RB NCs, compared to a 4-log in the case of RB-$Ag@SiO_2$ NSs, whereas their hydrodynamic diameters and ζ-potential were within the same range.

3.2.5 Graphene quantum dots

In another example, AgNPs were combined with Graphene Quantum Dots (GQD) [106]. GQDs are zero-dimension carbon nanomaterials that exhibit excellent photoluminescence, water dispersibility, biocompatibility, and low cytotoxicity properties, as well as the capacity to photo-generate ROS. In this study, the authors aimed to combined both photodynamic and photothermal effects, finding an increased ROS generation by the GQD in the conjugate, which could be attributed to GQDs stabilization onto AgNPs surface. Furthermore, the antibacterial effect against *E. coli* was enhanced, when compared to the free GQDs, resulting from the synergistic effect of enhanced PDT, efficient PTT, and the unique properties of AgNPs.

GQDs can also be used as a two-photon PS, leading to an efficient elimination of *E. coli,* after ultra-low-energy (800 nm) irradiation from a femtosecond laser during only 15 s [107]. In order to further improve the specificity and the antibacterial efficiency of their GQD, the authors coated them with lipopolysaccharides, a major component of the outer membrane of *E. coli*. More recently, Huang et al. also modified GQD surfaces in order to enhance their efficiency in PACT. Indeed, they developed spermidine co-doped polymeric GQDs, that could be photoactivated by very short LED irradiation (1 min.), in order to accelerate wound healing and thus reduce the risk of recurrent infections [108]. They evidenced that their positively charged materials could directly interact with the cell membrane of bacteria, thereby disrupting the membrane's integrity, but have not observed a significant photothermal effect on the inactivation of bacteria, as the temperature during the irradiation, just increased from 25 to 30 °C.

GQDs have also been combined with organic PS, such as **MB** [109] or as **TCPP**-loaded zirconium-based metal-organic framework [110]. In the first example, the sulfur doped GQDs improved the singlet oxygen generation of MB, by increasing both the lifetime of the triplet state of methylene blue and the efficiency of internal system crossing from singlet-MB to triplet-MB, increasing the bactericidal efficiency against *E. coli* [109]. In the second example, the authors developed a novel textile material, with GQDs being grafted onto cotton fiber surface, via amide bond after chemical modification, and the MOF being synthesized *in situ*. They achieved an enhanced $^1O_2$ generation, thanks to Förster resonance energy transfer (FRET), from GQDs to MOF, and due to the singlet oxygen diffusion through the MOF's porous structure. Furthermore, their material was able to achieve 6-log reduction of inactivation of *E. coli* and *P. aeruginosa* [110].

3.2.6 Carbone quantum dots

As GQD, Carbon quantum Dots (CQDs), represent a promising alternative for photodynamic applications. CQDs are mostly prepared by bottom-up synthetic strategies and have spherical shape of up to 10 nm, whereas GQDs are typically derived from graphene/graphite, or other graphitic 3D material, by top-down synthetic approaches [111]. Knoblauch et al., has recently studied brominated CQDs, and evidenced that they were able to generate ROS, via both type I and type II mechanisms, which led to growth inhibition of *E. coli* [112]. Unfortunately, the authors also observed dark toxicity, due to the pH-triggered release of reactive nitrogen species, both under dark and UV exposed conditions. In addition, it is noteworthy to mention that, once again, this material exhibits negative ζ-potential, while still being

efficient against bacterial proliferation. Nie et al. also recently published two studies focused on CQDs synthesized from citric acid and 1,5-diaminonaphthalene in ethanol, using a one-pot solvothermal method, either used as such [113] or trapped in polyacrylonitrile electrospun nanofibers [114]. In both cases, materials were more efficient against Gram-negative *E. coli,* than against the Gram-positive *S. aureus*. The authors hypothesized this can be due to the physical interaction between the CQDs and the bacteria, which was favored by the rod-shaped *E. coli* whereas, *S. aureus* tends to form grape-like clusters, preventing ROS diffusion towards bacteria residing within the interior of these clusters. These systems exhibited positive ζ-potential and were able to produce only singlet oxygen as ROS.

3.2.7 Other carbon-based materials

Single Wall Carbon Nanotubes (SWCNT) and Multiple Wall Carbon Nanotubes (MWCNT) have also been successfully used as antimicrobial materials against Gram-negative strains, having attracted attention in drug delivery, especially as vectors in PACT or PDT. The potential broad-spectrum antimicrobial action of carbon nanotubes also enhances their efficacy of antibacterial therapy [115]. In recent studies, **RB** conjugated to MWCNT [116] or **MB** conjugated to SWCNT [115], evidenced an enhanced photodynamic efficiency against *E. coli*, disregard the charge of the PS, and due to a greater interaction with bacteria. In the same line, Yu et al. reported in 2019 a supramolecular self-assembly of a polycationic porphyrin (**153**, Figure 16) and graphene nanoribbons, grafted with poly(ethylene oxide) chains to afford excellent dispersibility in aqueous solution [117]. Their new nanocomposite combined both PDT and PTT photo-activable at 660 nm and 808 nm, respectively, for the treatment of bacterial infection. It was demonstrated to be efficient against a wide range of bacterial strains, including *E. coli* and *P. aeruginosa,* while being photostable and with minimal toxicity against human cells.

It is noteworthy to underline that **MB** has been loaded in non-natural hydrogels, with good results towards bacteria, as the polyacrylamide hydrogel grafted with cationic phenothiazinium derivatives, developed by Spagnul et al. [118].

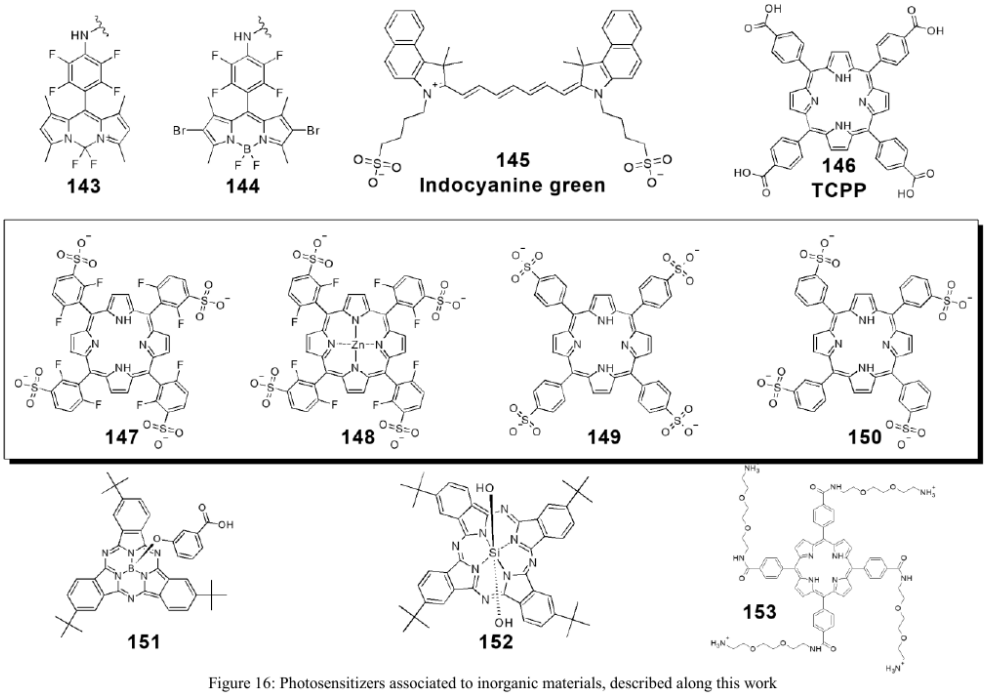

Figure 16: Photosensitizers associated to inorganic materials, described along this work

4. Strategies for PACT potentiation

Along this work we have described several improvements in the development of photosensitizing molecules, systems and scaffolds. Noteworthy, several of these strategies failed by themselves, and researchers craftily overcame

these difficulties through the use of potentiation strategies and targeting methods. These methods are further discussed in the following sections, shedding light on these strategies.

4.1 Potentiation with antibiotics

In previous sections, we have discussed the conjugation of photosensitizers with some well-known antimicrobial molecules, as colistin [74] and difloxacin [76]. This conjugation can increase the target selectivity and, eventually, the efficacy of disinfection, by disturbing the membrane integrity of microorganisms.

Another strategy, is the conjugation of PS with well-known antibiotics. As an example, Nonell and co-workers demonstrated the use of gentamicin as a targeting unit in a covalent conjugation strategy [119]. Their conjugate (**154**, Figure 17) showed a significant eradication of *E. coli* strains at sub-micromolar concentrations.

Recently, the use of Verapamil, a small molecule acting as a multi-drug resistance modulator, demonstrated to have an incidence on PS uptake. Verapamil inhibits the activity of the Multidrug and Toxic compound efflux (MATE) pumps, by binding to their active site. Sułek et al. have demonstrated that verapamil influences porphyrin penetration into Gram-negative bacteria [120]. Consequently, an enhanced photodynamic effect (up to 2 log-reduction of bacterial growth) was obtained against *E. coli* with **TMPyP** and two sulfonated porphyrin, **TPPS** and **Cl_2TPPS** (Figure 17). Furthermore, De Aguiar Coletti et al. have tested the synergistic effect of the combination Verapamil/MB on biofilms of *S. aureus* and *E. coli* [121]. For *E. coli* biofilm, the combination of 215 µg/mL of verapamil and 200 µg/mL of **MB**, and a light dose of 44 J/cm^2 enhanced the biofilm reduction by 3.4 log.

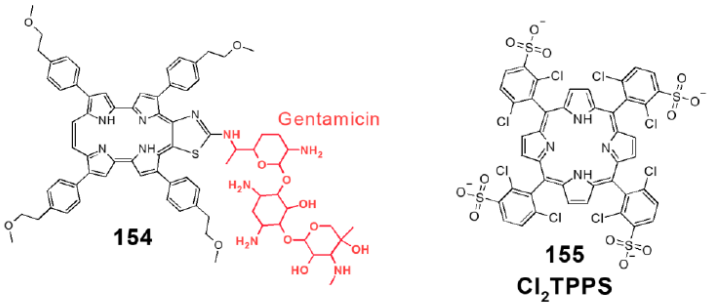

Figure 17: Some of the photosensitizers potentiated with antibiotics, described along this work

4.2 Potentiation with oligopeptides and aminoacids

Others authors have used antimicrobial peptides (AMPs) for targeting bacterial cell membranes by electrostatic interactions, resulting to disruption of membrane integrity. As an example, polymyxins are non-ribosomal lipopeptides, used for the treatment of infections caused by Gram-negative bacteria, with colistin being one member of this family [122]. Colistin conjugation to PS has demonstrated an increase in the PS uptake by Gram-negative bacteria [123]. In recent years, Le Guern et al. have developed several conjugates with polymyxin B (**156** - **158**, Figure 18), obtaining enhanced antimicrobial activity against Gram-negative bacteria [75, 124, 125]. Indeed, a cationic porphyrin was attached to a polymyxin B derivative, using thiol-maleimide click chemistry, and the obtained conjugate presented an enhanced PACT efficacy against *P. aeruginosa* and *E. coli*. Similarly, the previously described **137,** bears three colistin molecules via imine formation [74], being embedded into chitosan hydrogels, and resulting in efficient eradication of *P. aeruginosa*. Additionally, other authors have developed a probe associating MB and polymyxin B, as a theranostic agent for bacterial infections [126, 127].

Previously, we have described the use of AMPs as targeting moieties against bacteria, taking advantage of their own antimicrobial activity. However, these are not the only examples using amino acids and oligopeptides as targeting molecules. As an example, **PPIX** was bound to the $(KLAKLAK)_2$ peptide (**159**, Figure 18) [128], presenting an excellent activity against both *S. aureus* and *E. coli*. In another example, the AMP Aurein 1.2 was concomitantly used with **MB**, **chlorin-e6** and **curcumin**, and tested as a disinfection treatment against several bacterial strains, showing modest results against *E. coli* bacteria, contrasting with the excellent results obtained against Gram-positive strains [129].

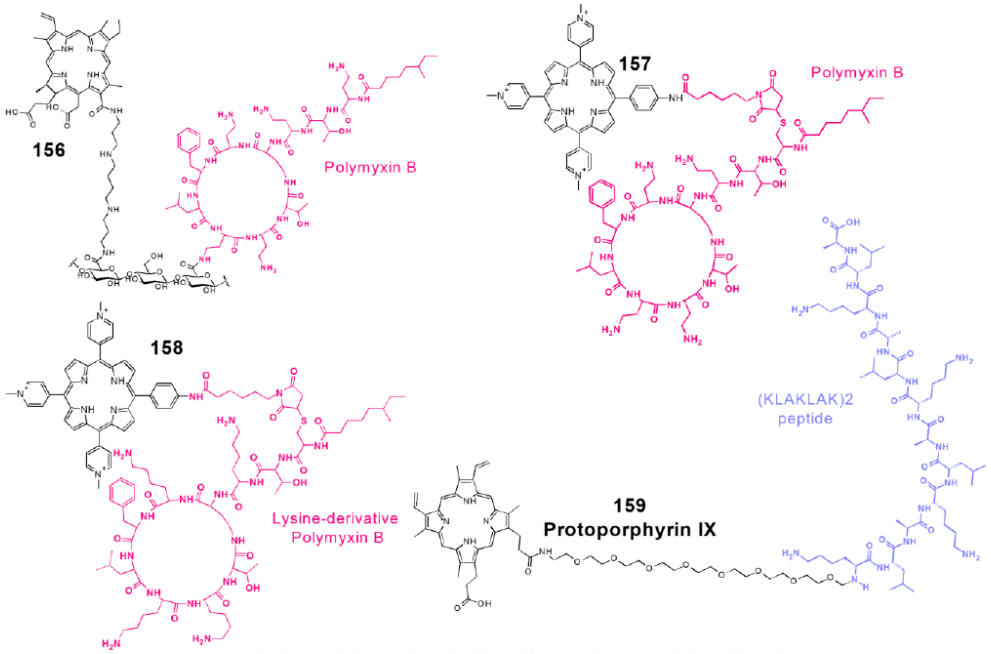

Figure 18: Photosensitizers conjugated with peptides or AMPs, presented along this work

4.3 Potentiation by potassium iodide and inorganic salts

The use of inorganic salts as potentiation agents in PDT and PACT has been previously described [130]. It must be highlighted the widely explored role of potassium iodide as a potentiator in PACT, with several examples being described along this work [22, 41, 62]. In a relevant example, Wen et al., demonstrated that **RB**, a photosensitizer mostly inactive against Gram-negative bacteria, efficiently eradicates *E. coli* and *P. aeruginosa* when complemented with KI. Furthermore, they provided insight into the mechanistic of this potentiation, being found that anionic iodine (I^-) is released as a function of irradiation, when **RB** is present. Then, the authors hypothesized that I^- reacts with singlet oxygen, forming the radical iodide and the superoxide anion, forming a cascade of reactive oxygen species that lead to bacterial death [131]. Then, PACT potentiation with this cheap, non-toxic, widely available inorganic salt, is likely to be further explored in the years to come.

5. Conclusions

Infectious diseases caused by Gram-negative bacteria are still a concern challenge in daily life, but PACT is an effective alternative against bacterial proliferation. Challenges presented, as low internalization and binding towards Gram-negative bacteria, have been addressed with the use of cationic compounds, lipophilic moieties, and delivery and potentiation systems. Currently, there are not active clinical trials for Gram-negative infection related diseases, but this panorama is likely to change in the next few years, given the increasing rate of publication of articles related to photodynamic disinfection, with our particular interest in Gram-negative bacteria.

We conclude that further efforts need to be poured into this topic, as the results are already promising and fruitful. Then, not only Scientifics, but also politicians, should focus in the devotion of more resources and politics, inverting the current trend and leading to an ever-growing pipeline of antibacterial alternatives.

6. Declarations

Funding. This project has received funding from the European Union's Horizon 2020 research and innovation programme under the Marie Sklodowska-Curie grant agreement n°764837.

Conflicts of interests. The authors declare no conflict of interest.

Acknowledgements. The authors would like to acknowledge Dr. Nicolas Villandier for the revision and correction of this manuscript.

Author's contributions. Conceptualization: S.L.-L.; Funding acquisition: S.L.-L.; Investigation: N.M.-C.; T.-S.O., S.L.-L.; Project administration: S.L.-L.; Software: N.M.-C.; Supervision: S.L.-L.; Visualization: N.M.-C.; T.-S.O., S.L.-L.; Writing – original draft: N.M.-C.; T.-S.O., S.L.-L.; Writing – review and editing: N.M.-C.; T.-S.O., S.L.-L.

7. References

1. Talebi Bezmin Abadi A, Rizvanov AA, Haertlé T, & Blatt NL (2019) World Health Organization Report: Current Crisis of Antibiotic Resistance. *Bionanoscience* 9:778–788 . https://doi.org/10.1007/s12668-019-00658-4
2. O'Neill Commission, & O'Neill Commission (2016) Tackling Drug-Resistant Infections Globally: Final Report and Recommendations the Review on Antimicrobial Resistance Chaired By Jim O'Neill
3. Capita R, & Alonso-Calleja C (2013) Antibiotic-Resistant Bacteria: A Challenge for the Food Industry. *Crit Rev Food Sci Nutr* 53:11–48 . https://doi.org/10.1080/10408398.2010.519837
4. Jasovský D, Littmann J, Zorzet A, & Cars O (2016) Antimicrobial resistance—a threat to the world's sustainable development. *Ups J Med Sci* 121:159–164 . https://doi.org/10.1080/03009734.2016.1195900
5. Venter H (2019) Reversing resistance to counter antimicrobial resistance in the World Health Organisation's critical priority of most dangerous pathogens. *Biosci Rep* 39:1–12 . https://doi.org/10.1042/BSR20180474
6. World Health Organization (2017) WHO publishes list of bacteria for which new antibiotics are urgently needed. In: World Heal. Organ. https://www.who.int/news/item/27-02-2017-who-publishes-list-of-bacteria-for-which-new-antibiotics-are-urgently-needed. Accessed 8 Jun 2021
7. Mulani MS, Kamble EE, Kumkar SN, Tawre MS, & Pardesi KR (2019) Emerging Strategies to Combat ESKAPE Pathogens in the Era of Antimicrobial Resistance: A Review. *Front Microbiol* 10: . https://doi.org/10.3389/fmicb.2019.00539
8. Wainwright M (2019) Photoantimicrobials and PACT: what's in an abbreviation? *Photochem Photobiol Sci* 18:12–14 . https://doi.org/10.1039/C8PP00390D
9. Alves E, Faustino MAF, Neves MGPMS, Cunha A, Tome J, & Almeida A (2014) An insight on bacterial cellular targets of photodynamic inactivation. *Future Med Chem* 6:141–164 . https://doi.org/10.4155/fmc.13.211
10. Wainwright M (1998) Photodynamic antimicrobial chemotherapy (PACT). *J Antimicrob Chemother* 42:13–28 . https://doi.org/10.1093/jac/42.1.13
11. Pucci MJ, & Dougherty TJ (2016) Editorial overview: Antimicrobials: fighting bacterial infections in the 21st century — thinking outside of the box. *Curr Opin Microbiol* 33:v–vii . https://doi.org/10.1016/j.mib.2016.08.002
12. Almeida A (2020) Photodynamic Therapy in the Inactivation of Microorganisms. *Antibiotics* 9: . https://doi.org/10.3390/antibiotics9040138
13. Wainwright M, Maisch T, Nonell S, Plaetzer K, Almeida A, Tegos GP, & Hamblin MR (2017) Photoantimicrobials—are we afraid of the light? *Lancet Infect Dis* 17:e49–e55 . https://doi.org/10.1016/S1473-3099(16)30268-7
14. Kashef N, & Hamblin MR (2017) Can microbial cells develop resistance to oxidative stress in antimicrobial photodynamic inactivation? *Drug Resist Updat* 31:31–42 . https://doi.org/10.1016/j.drup.2017.07.003
15. Maisch T (2015) Resistance in antimicrobial photodynamic inactivation of bacteria. *Photochem Photobiol Sci* 14:1518–1526 . https://doi.org/10.1039/C5PP00037H
16. Kharkwal GB, Sharma SK, Huang Y-Y, Dai T, & Hamblin MR (2011) Photodynamic therapy for infections: Clinical applications. *Lasers Surg Med* 43:755–767 . https://doi.org/10.1002/lsm.21080
17. Masi M, Réfregiers M, Pos KM, & Pagès JM (2017) Mechanisms of envelope permeability and antibiotic influx and efflux in Gram-negative bacteria. *Nat Microbiol* 2: . https://doi.org/10.1038/nmicrobiol.2017.1

18. Richter MF, Drown BS, Riley AP, Garcia A, Shirai T, Svec RL, & Hergenrother PJ (2017) Predictive compound accumulation rules yield a broad-spectrum antibiotic. *Nature* 545:299–304 . https://doi.org/10.1038/nature22308

19. Cieplik F, Deng D, Crielaard W, Buchalla W, Hellwig E, Al-Ahmad A, & Maisch T (2018) Antimicrobial photodynamic therapy–what we know and what we don't. *Crit Rev Microbiol* 44:571–589 . https://doi.org/10.1080/1040841X.2018.1467876

20. Seeger MG, Ries AS, Gressler LT, Botton SA, Iglesias BA, & Cargnelutti JF (2020) In vitro antimicrobial photodynamic therapy using tetra-cationic porphyrins against multidrug-resistant bacteria isolated from canine otitis. *Photodiagnosis Photodyn Ther* 32:101982 . https://doi.org/10.1016/j.pdpdt.2020.101982

21. Skwor TA, Klemm S, Zhang H, Schardt B, Blaszczyk S, & Bork MA (2016) Photodynamic inactivation of methicillin-resistant Staphylococcus aureus and Escherichia coli: A metalloporphyrin comparison. *J Photochem Photobiol B Biol* 165:51–57 . https://doi.org/10.1016/j.jphotobiol.2016.10.016

22. Calmeiro JMD, Gamelas SRD, Gomes ATPC, Faustino MAF, Neves MGPMS, Almeida A, Tomé JPC, & Lourenço LMO (2020) Versatile thiopyridyl/pyridinone porphyrins combined with potassium iodide and thiopyridinium/methoxypyridinium porphyrins on E. coli photoinactivation. *Dye Pigment* 181:108476 . https://doi.org/10.1016/j.dyepig.2020.108476

23. Simões C, Gomes MC, Neves MGPMS, Cunha Â, Tomé JPC, Tomé AC, Cavaleiro JAS, Almeida A, & Faustino MAF (2016) Photodynamic inactivation of Escherichia coli with cationic meso -tetraarylporphyrins – The charge number and charge distribution effects. *Catal Today* 266:197–204 . https://doi.org/10.1016/j.cattod.2015.07.031

24. Marciel L, Teles L, Moreira B, Pacheco M, Lourenço LM, Neves MG, Tomé JP, Faustino MA, & Almeida A (2017) An effective and potentially safe blood disinfection protocol using tetrapyrrolic photosensitizers. *Future Med Chem* 9:365–379 . https://doi.org/10.4155/fmc-2016-0217

25. Thomas M, Craik JD, Tovmasyan A, Batinic-Haberle I, & Benov LT (2015) Amphiphilic cationic Zn-porphyrins with high photodynamic antimicrobial activity. *Future Microbiol* 10:709–724 . https://doi.org/10.2217/fmb.14.148

26. Alenezi K, Tovmasyan A, Batinic-Haberle I, & Benov LT (2017) Optimizing Zn porphyrin-based photosensitizers for efficient antibacterial photodynamic therapy. *Photodiagnosis Photodyn Ther* 17:154–159 . https://doi.org/10.1016/j.pdpdt.2016.11.009

27. Tovmasyan A, Batinic-Haberle I, & Benov L (2020) Antibacterial activity of synthetic cationic iron porphyrins. *Antioxidants* 9:1–14 . https://doi.org/10.3390/antiox9100972

28. Moura NMM, Esteves M, Vieira C, Rocha GMSRO, Faustino MAF, Almeida A, Cavaleiro JAS, Lodeiro C, & Neves MGPMS (2019) Novel β-functionalized mono-charged porphyrinic derivatives: Synthesis and photoinactivation of Escherichia coli. *Dye Pigment* 160:361–371 . https://doi.org/10.1016/j.dyepig.2018.06.048

29. Vinagreiro CS, Zangirolami A, Schaberle FA, Nunes SCC, Blanco KC, Inada NM, da Silva GJ, Pais AACC, Bagnato VS, Arnaut LG, & Pereira MM (2020) Antibacterial Photodynamic Inactivation of Antibiotic-Resistant Bacteria and Biofilms with Nanomolar Photosensitizer Concentrations. *ACS Infect Dis* 6:1517–1526 . https://doi.org/10.1021/acsinfecdis.9b00379

30. Galstyan A (2021) Turning Photons into Drugs: Phthalocyanine-Based Photosensitizers as Efficient Photoantimicrobials. *Chem – A Eur J* 27:1903–1920 . https://doi.org/10.1002/chem.202002703

31. Ribeiro CPS, & Lourenço LMO (2021) Overview of cationic phthalocyanines for effective photoinactivation of pathogenic microorganisms. *J Photochem Photobiol C Photochem Rev* 48:100422 . https://doi.org/10.1016/j.jphotochemrev.2021.100422

32. Lourenço LMO, Rocha DMGC, Ramos CI V., Gomes MC, Almeida A, Faustino MAF, Almeida Paz FA, Neves MGPMS, Cunha Â, & Tomé JPC (2019) Photoinactivation of Planktonic and Biofilm Forms of Escherichia coli

through the Action of Cationic Zinc(II) Phthalocyanines. *ChemPhotoChem* 3:251–260 . https://doi.org/10.1002/cptc.201900020

33. Aroso RT, Calvete MJF, Pucelik B, Dubin G, Arnaut LG, Pereira MM, & Dąbrowski JM (2019) Photoinactivation of microorganisms with sub-micromolar concentrations of imidazolium metallophthalocyanine salts. *Eur J Med Chem* 184:111740 . https://doi.org/10.1016/j.ejmech.2019.111740

34. Mantareva V, Kussovski V, Durmuş M, Borisova E, & Angelov I (2016) Photodynamic inactivation of pathogenic species Pseudomonas aeruginosa and Candida albicans with lutetium (III) acetate phthalocyanines and specific light irradiation. *Lasers Med Sci* 31:1591–1598 . https://doi.org/10.1007/s10103-016-2022-8

35. Dlugaszewska J, Szczolko W, Koczorowski T, Skupin-Mrugalska P, Teubert A, Konopka K, Kucinska M, Murias M, Düzgüneş N, Mielcarek J, & Goslinski T (2017) Antimicrobial and anticancer photodynamic activity of a phthalocyanine photosensitizer with N-methyl morpholiniumethoxy substituents in non-peripheral positions. *J Inorg Biochem* 172:67–79 . https://doi.org/10.1016/j.jinorgbio.2017.04.009

36. Ruiz-González R, Setaro F, Gulías Ò, Agut M, Hahn U, Torres T, & Nonell S (2017) Cationic phthalocyanine dendrimers as potential antimicrobial photosensitisers. *Org Biomol Chem* 15:9008–9017 . https://doi.org/10.1039/C7OB02270K

37. Meerovich GA, Akhlyustina E V, Tiganova IG, Lukyanets EA, Makarova EA, Tolordava ER, Yuzhakova OA, Romanishkin ID, Philipova NI, Zhizhimova YS, Romanova YM, Loschenov VB, & Gintsburg AL (2020) Novel Polycationic Photosensitizers for Antibacterial Photodynamic Therapy. In: Donelli G (ed) Advances in Microbiology, Infectious Diseases and Public Health: Volume 14. Springer International Publishing, Cham, pp 1–19

38. Lin H, Chen J, Zhang Y, Ulla A, Liu J, & Lin F (2018) Enhanced anti-microbial effect through cationization of a mono-triazatricyclodecane substituted asymmetric phthalocyanine. *J Inorg Biochem* 189:192–198 . https://doi.org/10.1016/j.jinorgbio.2018.10.001

39. Ziganshyna S, Guttenberger A, Lippmann N, Schulz S, Bercker S, Kahnt A, Rüffer T, Voigt A, Gerlach K, & Werdehausen R (2020) Tetrahydroporphyrin-tetratosylate (THPTS) -based photodynamic inactivation of critical multidrug-resistant bacteria in vitro. *Int J Antimicrob Agents* 55:105976 . https://doi.org/doi.org/10.1016/j.ijantimicag.2020.105976

40. Durantini AM, Heredia DA, Durantini JE, & Durantini EN (2018) BODIPYs to the rescue: Potential applications in photodynamic inactivation. *Eur J Med Chem* 144:651–661 . https://doi.org/10.1016/j.ejmech.2017.12.068

41. Reynoso E, Quiroga ED, Agazzi ML, Ballatore MB, Bertolotti SG, & Durantini EN (2017) Photodynamic inactivation of microorganisms sensitized by cationic BODIPY derivatives potentiated by potassium iodide. *Photochem Photobiol Sci* 1524–1536 . https://doi.org/https://doi.org/10.1039/c7pp00204a

42. Piskorz J, Porolnik W, Kucinska M, Dlugaszewska J, Murias M, & Mielcarek J (2021) BODIPY-Based Photosensitizers as Potential Anticancer and Antibacterial Agents: Role of the Positive Charge and the Heavy Atom Effect. *ChemMedChem* 16:399–411 . https://doi.org/10.1002/cmdc.202000529

43. dos Anjos C, Sellera FP, Ribeiro MS, Baptista MS, Pogliani FC, Lincopan N, & Sabino CP (2020) Antimicrobial blue light and photodynamic therapy inhibit clinically relevant β-lactamases with extended-spectrum (ESBL) and carbapenemase activity. *Photodiagnosis Photodyn Ther* 32:102086 . https://doi.org/10.1016/j.pdpdt.2020.102086

44. Feng Y, Palanisami A, Ashraf S, Bhayana B, & Hasan T (2020) Photodynamic inactivation of bacterial carbapenemases restores bacterial carbapenem susceptibility and enhances carbapenem antibiotic effectiveness. *Photodiagnosis Photodyn Ther* 30:101693 . https://doi.org/10.1016/j.pdpdt.2020.101693

45. Mello MM De, Barros PP De, Bernardes RDC, Alves SR, Ramanzini NP, Figueiredo-godoi LMA, Carolina A, Prado C, Olavo A, Jorge C, & Junqueira JC (2019) Antimicrobial photodynamic therapy against clinical isolates

of carbapenem-susceptible and carbapenem-resistant Acinetobacter baumannii. *Lasers Med Sci* 34:1755–1761 . https://doi.org/10.1007/s10103-019-02773-w

46. Misba L, Zaidi S, & Khan AU (2017) A comparison of antibacterial and antibiofilm efficacy of phenothiazinium dyes between Gram positive and Gram negative bacterial biofilm. *Photodiagnosis Photodyn Ther* 18:24–33 . https://doi.org/10.1016/j.pdpdt.2017.01.177

47. Ruiz-González R, Agut M, Reddi E, & Nonell S (2015) A Comparative Study on Two Cationic Porphycenes: Photophysical and Antimicrobial Photoinactivation Evaluation. *Int J Mol Sci* 16:27072–27086 . https://doi.org/10.3390/ijms161125999

48. Godard J, Brégier F, Arnoux P, Myrzakhmetov B, Champavier Y, Frochot C, & Sol V (2020) New Phenalenone Derivatives: Synthesis and Evaluation of Their Singlet Oxygen Quantum Yield. *ACS Omega* 5:28264–28272 . https://doi.org/https://doi.org/10.1021/acsomega.0c04172

49. Tabenski I, Cieplik F, Tabenski L, Regensburger J, Hiller K, Buchalla W, Maisch T, & Späth A (2016) The impact of cationic substituents in phenalen-1-one photosensitizers on antimicrobial photodynamic efficacy. *Photochem Photobiol Sci* 15:57–68 . https://doi.org/10.1039/C5PP00262A

50. Godard J, Gibbons D, Leroy-Lhez S, Williams RM, Villandier N, Ouk T-S, Brégier F, & Sol V (2021) Development of Phenalenone-Triazolium Salt Derivatives for aPDT: Synthesis and Antibacterial Screening. *Antibiotics* 10:626 . https://doi.org/10.3390/antibiotics10060626

51. Hamblin MR (2018) Fullerenes as photosensitizers in photodynamic therapy: pros and cons. *Photochem Photobiol Sci* 17:1515–1533 . https://doi.org/10.1039/C8PP00195B

52. Huang L, Wang M, Dai T, Sperandio FF, Huang Y-Y, Xuan Y, Chiang LY, & Hamblin MR (2014) Antimicrobial photodynamic therapy with decacationic monoadducts and bisadducts of [70]fullerene: in vitro and in vivo studies. *Nanomedicine* 9:253–266 . https://doi.org/10.2217/nnm.13.22

53. Yin R, Wang M, Huang Y-Y, Landi G, Vecchio D, Chiang LY, & Hamblin MR (2015) Antimicrobial photodynamic inactivation with decacationic functionalized fullerenes: Oxygen-independent photokilling in presence of azide and new mechanistic insights. *Free Radic Biol Med* 79:14–27 . https://doi.org/10.1016/j.freeradbiomed.2014.10.514

54. Ferreyra DD, Reynoso E, Cordero P, Spesia MB, Alvarez MG, Milanesio ME, & Durantini EN (2016) Synthesis and properties of 5,10,15,20-tetrakis[4-(3-N,N-dimethylaminopropoxy)phenyl] chlorin as potential broad-spectrum antimicrobial photosensitizers. *J Photochem Photobiol B Biol* 158:243–251 . https://doi.org/10.1016/j.jphotobiol.2016.02.021

55. Berezin DB, Makarov V V, Znoyko SA, Mayzlish VE, & Kustov A V (2020) Aggregation of water soluble octaanionic phthalocyanines and their photoinactivation antimicrobial effect in vitro. *Ital Oral Surg* 30:621–623 . https://doi.org/10.1016/j.mencom.2020.09.023

56. Biyiklioglu Z, Ozturk I, Arslan T, Tunçel A, Ocakoglu K, Hosgor-Limoncu M, & Yurt F (2019) Synthesis and antimicrobial photodynamic activities of axially {4-[(1E)-3-oxo-3-(2-thienyl)prop-1-en-1-yl]phenoxy} groups substituted silicon phthalocyanine, subphthalocyanine on Gram-positive and Gram-negative bacteria. *Dye Pigment* 166:149–158 . https://doi.org/10.1016/j.dyepig.2019.03.010

57. Bair KL, Shafirstein G, & Campagnari AA (2020) In vitro Photodynamic Therapy of Polymicrobial Biofilms Commonly Associated With Otitis Media Bacteria and Culture Conditions. *Front Microbiol* 11:1–9 . https://doi.org/10.3389/fmicb.2020.558482

58. Krüger M, Richter P, Strauch S, Nasir A, Burkovski A, Antunes C, Meißgeier T, Schlücker E, Schwab S, & Lebert M (2019) What an Escherichia coli Mutant Can Teach Us About the Antibacterial Effect of Chlorophyllin. *Microorganisms* 7:59 . https://doi.org/10.3390/microorganisms7020059

59. Hohlfeld BF, Gitter B, Flanagan KJ, Kingsbury CJ, Kulak N, Senge MO, & Wiehe A (2020) Exploring the relationship between structure and activity in BODIPYs designed for antimicrobial phototherapy. *Org Biomol Chem* 18:2416–2431 . https://doi.org/10.1039/d0ob00188k

60. Hohlfeld BF, Gitter B, Kingsbury CJ, Flanagan KJ, Steen D, Wieland GD, Kulak N, Senge MO, & Wiehe A (2020) Dipyrrinato-Iridium(III) Complexes for Application in Photodynamic Therapy and Antimicrobial Photodynamic Inactivation. *Chem - A Eur J* 27: . https://doi.org/10.1002/chem.202004776

61. Fekrirad Z, Darabpour E, & Kashef N (2021) Eradication of Acinetobacter baumannii Planktonic and Biofilm Cells Through Erythrosine - Mediated Photodynamic Inactivation Augmented by Acetic Acid and Chitosan. *Curr Microbiol* 78:879–886 . https://doi.org/10.1007/s00284-021-02350-x

62. Santos AR, Batista AFP, Gomes ATPC, Neves M da GPMS, Faustino MAF, Almeida A, Hioka N, & Mikcha JMG (2019) The remarkable effect of potassium iodide in eosin and rose bengal photodynamic action against salmonella typhimurium and staphylococcus aureus. *Antibiotics* 8: . https://doi.org/10.3390/antibiotics8040211

63. Wingen M, Potzkei J, Endres S, Casini G, Rupprecht C, Fahlke C, Krauss U, Jaeger K-E, Drepper T, & Gensch T (2014) The photophysics of LOV-based fluorescent proteins – new tools for cell biology. *Photochem Photobiol Sci* 13:875–883 . https://doi.org/10.1039/C3PP50414J

64. Hilgers F, Bitzenhofer NL, Ackermann Y, Burmeister A, Grünberger A, Jaeger KE, & Drepper T (2019) Genetically encoded photosensitizers as light-triggered antimicrobial agents. *Int J Mol Sci* 20:1–20 . https://doi.org/10.3390/ijms20184608

65. Hopkins SL, Stepanyan L, Vahidi N, Jain A, Winkel BSJ, & Brewer KJ (2017) Visible light induced antibacterial properties of a Ru(II)–Pt(II) bimetallic complex. *Inorganica Chim Acta* 454:229–233 . https://doi.org/10.1016/j.ica.2016.06.006

66. Soliman N, Sol V, Ouk T-S, Thomas CM, & Gasser G (2020) Encapsulation of a Ru(II) Polypyridyl Complex into Polylactide Nanoparticles for Antimicrobial Photodynamic Therapy. *Pharmaceutics* 12:961 . https://doi.org/10.3390/pharmaceutics12100961

67. Le Gall T, Lemercier G, Chevreux S, Tücking KS, Ravel J, Thétiot F, Jonas U, Schönherr H, & Montier T (2018) Ruthenium(II) Polypyridyl Complexes as Photosensitizers for Antibacterial Photodynamic Therapy: A Structure–Activity Study on Clinical Bacterial Strains. *ChemMedChem* 13:2229–2239 . https://doi.org/10.1002/cmdc.201800392

68. Pierce S, Jennings MP, Juliano SA, & Angeles-Boza AM (2020) Peptide–Ruthenium Conjugate as an Efficient Photosensitizer for the Inactivation of Multidrug-Resistant Bacteria. *Inorg Chem* 59:14866–14870 . https://doi.org/10.1021/acs.inorgchem.0c02491

69. Maldonado-Carmona N, Ouk T-SS, Calvete MJFF, Pereira MM, Villandier N, & Leroy-Lhez S (2020) Conjugating biomaterials with photosensitizers: advances and perspectives for photodynamic antimicrobial chemotherapy. *Photochem Photobiol Sci* 19:445–461 . https://doi.org/10.1039/c9pp00398c

70. Fayyaz F, Rassa M, & Rahimi R (2021) Antibacterial Photoactivity and Thermal Stability of Tetra-cationic Porphyrins Immobilized on Cellulosic Fabrics. *Photochem Photobiol* 97:385–397 . https://doi.org/10.1111/php.13353

71. Nzambe Ta keki JK, Ouk T-S, Zerrouki R, Faugeras P-A, Sol V, & Brouillette F (2016) Synthesis and photobactericidal properties of a neutral porphyrin grafted onto lignocellulosic fibers. *Mater Sci Eng C* 62:61–67 . https://doi.org/10.1016/j.msec.2016.01.028

72. Wang T, Ke H, Chen S, Wang J, Yang W, Cao X, Liu J, Wei Q, Ghiladi RA, & Wang Q (2021) Porous protoporphyrin IX-embedded cellulose diacetate electrospun microfibers in antimicrobial photodynamic inactivation. *Mater Sci Eng C* 118:111502 . https://doi.org/10.1016/j.msec.2020.111502

903 73. Castro KADF, Moura NMM, Ferreira RI, Almeida A, & Neves MGPMS (2019) New Materials Based on
904 Cationic Porphyrins Conjugated to Chitosan or Titanium Dioxide : Synthesis , Characterization and
905 Antimicrobial E ffi cacy. *Int J Mol Sci* 20:2522 . https://doi.org/10.3390/ijms20102522

906 74. Bayat F, & Karimi AR (2019) Design of photodynamic chitosan hydrogels bearing phthalocyanine-colistin
907 conjugate as an antibacterial agent. *Int J Biol Macromol* 129:927–935 .
908 https://doi.org/10.1016/j.ijbiomac.2019.02.081

909 75. Le Guern F, Ouk T-S, Grenier K, Joly N, Lequart V, & Sol V (2017) Enhancement of photobactericidal activity
910 of chlorin-e6-cellulose nanocrystals by covalent attachment of polymyxin B. *J Mater Chem B* 5:6953–6962 .
911 https://doi.org/10.1039/C7TB01274H

912 76. Bayat F, Karimi AR, & Adimi T (2020) Design of nanostructure chitosan hydrogels for carrying zinc
913 phthalocyanine as a photosensitizer and difloxacin as an antibacterial agent. *Int J Biol Macromol* 159:598–606 .
914 https://doi.org/10.1016/j.ijbiomac.2020.05.086

915 77. Strokov K, & Galstyan A (2020) Chitosan-Silicon Phthalocyanine Conjugate as Effective Photo- Functional
916 Hydrogel for Tracking and Killing of Bacteria. *European J Org Chem* 7327–7332 .
917 https://doi.org/10.1002/ejoc.202001363

918 78. Yin M, Li Z, Zhou L, Dong K, Ren J, & Qu X (2016) A multifunctional upconverting nanoparticle incorporated
919 polycationic hydrogel for near-infrared triggered and synergistic treatment of drug-resistant bacteria.
920 *Nanotechnology* 27:125601 . https://doi.org/10.1088/0957-4484/27/12/125601

921 79. Kumari R, Khan MI, Bhowmick S, Sinha KK, Das N, & Das P (2017) Self-assembly of DNA-porphyrin hybrid
922 molecules for the creation of antimicrobial nanonetwork. *J Photochem Photobiol B Biol* 172:28–35 .
923 https://doi.org/10.1016/j.jphotobiol.2017.05.010

924 80. Ferroni C, Sotgiu G, Sagnella A, Varchi G, Guerrini A, Giuri D, Polo E, Orlandi VT, Marras E, Gariboldi M,
925 Monti E, & Aluigi A (2016) Wool Keratin 3D Scaffolds with Light-Triggered Antimicrobial Activity.
926 *Biomacromolecules* 17:2882–2890 . https://doi.org/10.1021/acs.biomac.6b00697

927 81. Osorno LL, Brandley AN, Maldonado DE, Yiantsos A, Mosley RJ, & Byrne ME (2021) Review of
928 contemporary self-assembled systems for the controlled delivery of therapeutics in medicine. *Nanomaterials*
929 11:1–28 . https://doi.org/10.3390/nano11020278

930 82. Rout B, Liu C, & Wu W (2016) Enhancement of photodynamic inactivation against Pseudomonas aeruginosa
931 by a nano-carrier approach. *Colloids Surfaces B Biointerfaces* 140:472–480 .
932 https://doi.org/10.1016/j.colsurfb.2016.01.002

933 83. Sharma B, Kaur G, & Chaudhary GR (2020) Optimization and utilization of single chain metallocatanionic
934 vesicles for antibacterial photodynamic therapy (aPDT) against E. coli. *J Mater Chem B* 8:9304–9313 .
935 https://doi.org/10.1039/D0TB01551B

936 84. Boccalini G, Conti L, Montis C, Bani D, Bencini A, Berti D, Giorgi C, Mengoni A, & Valtancoli B (2017)
937 Methylene blue-containing liposomes as new photodynamic anti-bacterial agents. *J Mater Chem B* 5:2788–
938 2797 . https://doi.org/10.1039/C6TB03367A

939 85. Pourhajibagher M, Partoazar A, Alaeddini M, Etemad-Moghadam S, & Bahador A (2020) Photodisinfection
940 effects of silver sulfadiazine nanoliposomes doped-curcumin on Acinetobacter baumannii : a mouse model.
941 *Nanomedicine* 15:437–452 . https://doi.org/10.2217/nnm-2019-0315

942 86. Sobotta L, Sniechowska J, Ziental D, Dlugaszewska J, & Potrzebowski MJ (2019) Chlorins with
943 (trifluoromethyl)phenyl substituents – Synthesis, lipid formulation and photodynamic activity against bacteria.
944 *Dye Pigment* 160:292–300 . https://doi.org/10.1016/j.dyepig.2018.08.004

945 87. Wang Q, Zhang D, Feng J, Sun T, Li C, Xie X, & Shi Q (2021) Enhanced photodynamic inactivation for Gram-
946 negative bacteria by branched polyethylenimine-containing nanoparticles under visible light irradiation. *J*
947 *Colloid Interface Sci* 584:539–550 . https://doi.org/10.1016/j.jcis.2020.09.106

88. Contreras A, Raxworthy MJ, Wood S, & Tronci G (2020) Hydrolytic Degradability, Cell Tolerance and On-Demand Antibacterial Effect of Electrospun Photodynamically Active Fibres. *Pharmaceutics* 12:711 . https://doi.org/10.3390/pharmaceutics12080711

89. Qian S, Song L, Sun L, Zhang X, Xin Z, & Yin J (2020) Journal of Photochemistry & Photobiology A : Chemistry Metal-organic framework / poly (ε -caprolactone) hybrid electrospun nanofibrous membranes with effective photodynamic antibacterial activities. *J Photochem Photobiol A Chem* 400:112626 . https://doi.org/10.1016/j.jphotochem.2020.112626

90. Castro KADF, Moura NMM, Simões MMQ, Cavaleiro JAS, Faustino M do AF, Cunha Â, Almeida Paz FA, Mendes RF, Almeida A, Freire CSR, Vilela C, Silvestre AJD, Nakagaki S, & Neves M da GPMS (2019) Synthesis and characterization of photoactive porphyrin and poly(2-hydroxyethyl methacrylate) based materials with bactericidal properties. *Appl Mater Today* 16:332–341 . https://doi.org/10.1016/j.apmt.2019.06.010

91. Scanone AC, Gsponer NS, Alvarez MG, Heredia DA, Durantini AM, & Durantini EN (2020) Magnetic Nanoplatforms for in Situ Modification of Macromolecules: Synthesis, Characterization, and Photoinactivating Power of Cationic Nanoiman-Porphyrin Conjugates. *ACS Appl Bio Mater* 3:5930–5940 . https://doi.org/10.1021/acsabm.0c00625

92. Scanone AC, Santamarina SC, Heredia DA, Durantini EN, & Durantini AM (2020) Functionalized Magnetic Nanoparticles with BODIPYs for Bioimaging and Antimicrobial Therapy Applications. *ACS Appl Bio Mater* 3:1061–1070 . https://doi.org/10.1021/acsabm.9b01035

93. Bilici K, Atac N, Muti A, Baylam I, Dogan O, Sennaroglu A, Can F, & Yagci Acar H (2020) Broad spectrum antibacterial photodynamic and photothermal therapy achieved with indocyanine green loaded SPIONs under near infrared irradiation. *Biomater Sci* 8:4616–4625 . https://doi.org/10.1039/d0bm00821d

94. Zhang Y, Ma J, Wang D, Xu C, Sheng S, Cheng J, Bao C, Li Y, & Tian H (2020) Fe-TCPP@CS nanoparticles as photodynamic and photothermal agents for efficient antimicrobial therapy. *Biomater Sci* 8:6526–6532 . https://doi.org/10.1039/D0BM01427C

95. Sułek A, Pucelik B, Kobielusz M, Łabuz P, Dubin G, & Dąbrowski JM (2019) Surface Modification of Nanocrystalline TiO2 Materials with Sulfonated Porphyrins for Visible Light Antimicrobial Therapy. *Catalysts* 9:821 . https://doi.org/10.3390/catal9100821

96. Sułek A, Pucelik B, Kuncewicz J, Dubin G, & Dąbrowski JM (2019) Sensitization of TiO2 by halogenated porphyrin derivatives for visible light biomedical and environmental photocatalysis. *Catal Today* 335:538–549 . https://doi.org/10.1016/j.cattod.2019.02.070

97. Ozturk I, Tunçel A, Ince M, Ocakoglu K, Hoşgör-Limoncu M, & Yurt F (2018) Antibacterial properties of subphthalocyanine and subphthalocyanine-TiO 2 nanoparticles on Staphylococcus aureus and Escherichia coli. *J Porphyr Phthalocyanines* 22:1099–1105 . https://doi.org/10.1142/S1088424618501122

98. Grüner MC, Arai MS, Carreira M, Inada N, & De Camargo ASS (2018) Functionalizing the mesoporous silica shell of upconversion nanoparticles to enhance bacterial targeting and killing via photosensitizer-induced antimicrobial photodynamic therapy. *ACS Appl Bio Mater* 1:1028–1036 . https://doi.org/10.1021/acsabm.8b00224

99. Tang J, Chu B, Wang J, Song B, Su Y, Wang H, & He Y (2019) Multifunctional nanoagents for ultrasensitive imaging and photoactive killing of Gram-negative and Gram-positive bacteria. *Nat Commun* 10:4057 . https://doi.org/10.1038/s41467-019-12088-7

100. Sun J, Fan Y, Zhang P, Zhang X, Zhou Q, Zhao J, & Ren L (2020) Journal of Colloid and Interface Science Self-enriched mesoporous silica nanoparticle composite membrane with remarkable photodynamic antimicrobial performances. *J Colloid Interface Sci* 559:197–205 . https://doi.org/10.1016/j.jcis.2019.10.021

101. Kuthati Y, Kankala RK, Busa P, Lin SX, Deng JP, Mou CY, & Lee CH (2017) Phototherapeutic spectrum expansion through synergistic effect of mesoporous silica trio-nanohybrids against antibiotic-resistant gram-

negative bacterium. *J Photochem Photobiol B Biol* 169:124–133 . https://doi.org/10.1016/j.jphotobiol.2017.03.003

102. Malá Z, Žárská L, Bajgar R, Bogdanová K, Kolář M, Panáček A, Binder S, & Kolářová H (2021) The application of antimicrobial photodynamic inactivation on methicillin-resistant S. aureus and ESBL-producing K. pneumoniae using porphyrin photosensitizer in combination with silver nanoparticles. *Photodiagnosis Photodyn Ther* 33:102140 . https://doi.org/10.1016/j.pdpdt.2020.102140

103. Parasuraman P, R. Y T, Shaji C, Sharan A, Bahkali AH, Al-Harthi HF, Syed A, Anju VT, Dyavaiah M, & Siddhardha B (2020) Biogenic Silver Nanoparticles Decorated with Methylene Blue Potentiated the Photodynamic Inactivation of Pseudomonas aeruginosa and Staphylococcus aureus. *Pharmaceutics* 12:709 . https://doi.org/10.3390/pharmaceutics12080709

104. Chen J, Yang L, Chen J, Liu W, Zhang D, Xu P, Dai T, Shang L, Yang Y, Tang S, Zhang Y, Lin H, & Chen Z (2019) Composite of silver nanoparticles and photosensitizer leads to mutual enhancement of antimicrobial e ffi cacy and promotes wound healing. *Chem Eng J* 374:1373–1381 . https://doi.org/10.1016/j.cej.2019.05.184

105. Macia N, Bresoli-Obach R, Nonell S, & Heyne B (2019) Hybrid Silver Nanocubes for Improved Plasmon-Enhanced Singlet Oxygen Production and Inactivation of Bacteria. *J Am Chem Soc* 141:684–692 . https://doi.org/10.1021/jacs.8b12206

106. Yu Y, Mei L, Shi Y, Zhang X, Cheng K, Cao F, Zhang L, Xu J, Li X, & Xu Z (2020) Ag-Conjugated graphene quantum dots with blue light-enhanced singlet oxygen generation for ternary-mode highly-efficient antimicrobial therapy. *J Mater Chem B* 8:1371–1382 . https://doi.org/10.1039/C9TB02300C

107. Kuo W-S, Chang C-Y, Chen H-H, Hsu C-LL, Wang J-Y, Kao H-F, Chou LC-S, Chen Y-C, Chen S-J, Chang W-T, Tseng S-W, Wu P-C, & Pu Y-C (2016) Two-Photon Photoexcited Photodynamic Therapy and Contrast Agent with Antimicrobial Graphene Quantum Dots. *ACS Appl Mater Interfaces* 8:30467–30474 . https://doi.org/10.1021/acsami.6b12014

108. Huang H, Anand A, Lin C, Lin H, Lin Y, Harroun SG, & Huang C (2021) LED irradiation of halogen / nitrogen-doped polymeric graphene quantum dots triggers the photodynamic inactivation of bacteria in infected wounds. *Carbon N Y* 174:710–722 . https://doi.org/10.1016/j.carbon.2020.11.092

109. Kholikov K, Ilhom S, Sajjad M, Smith ME, Monroe JD, San O, & Oguz A (2018) Photodiagnosis and Photodynamic Therapy Improved singlet oxygen generation and antimicrobial activity of sulphur- doped graphene quantum dots coupled with methylene blue for photodynamic therapy applications. *Photodiagnosis Photodyn Ther* 24:7–14 . https://doi.org/10.1016/j.pdpdt.2018.08.011

110. Nie X, Wu S, Mensah A, Wang Q, Huang F, & Wei Q (2020) FRET as a novel strategy to enhance the singlet oxygen generation of porphyrinic MOF decorated self-disinfecting fabrics. *Chem Eng J* 395:125012 . https://doi.org/10.1016/j.cej.2020.125012

111. Lim CS, Hola K, Ambrosi A, Zboril R, & Pumera M (2015) Graphene and carbon quantum dots electrochemistry. *Electrochem commun* 52:75–79 . https://doi.org/10.1016/j.elecom.2015.01.023

112. Knoblauch R, Harvey A, Ra E, Greenberg KM, Lau J, Hawkins E, & Geddes CD (2021) Antimicrobial carbon nanodots: photodynamic inactivation and dark antimicrobial effects on bacteria by brominated carbon nanodots. *Nanoscale* 13:85–99 . https://doi.org/10.1039/D0NR06842J

113. Nie X, Jiang C, Wu S, Chen W, Lv P, & Wang Q (2020) Journal of Photochemistry & Photobiology , B : Biology Carbon quantum dots : A bright future as photosensitizers for in vitro antibacterial photodynamic inactivation. *J Photochem Photobiol B Biol* 206:111864 . https://doi.org/10.1016/j.jphotobiol.2020.111864

114. Nie X, Wu S, Mensah A, Lu K, & Wei Q (2020) Carbon quantum dots embedded electrospun nanofibers for efficient antibacterial photodynamic inactivation. *Mater Sci Eng C* 108:110377 . https://doi.org/10.1016/j.msec.2019.110377

115. Parasuraman P, Anju VT, Sruthil Lal S, Sharan A, Busi S, Kaviyarasu K, Arshad M, Dawoud TMS, & Syed A (2019) Synthesis and antimicrobial photodynamic effect of methylene blue conjugated carbon nanotubes on E. coli and S. aureus. *Photochem Photobiol Sci* 18:563–576 . https://doi.org/10.1039/C8PP00369F

116. VT A, Paramanantham P, SB SL, Sharan A, Alsaedi MH, Dawoud TMS, Asad S, & Busi S (2018) Antimicrobial photodynamic activity of rose bengal conjugated multi walled carbon nanotubes against planktonic cells and biofilm of Escherichia coli. *Photodiagnosis Photodyn Ther* 24:300–310 . https://doi.org/10.1016/j.pdpdt.2018.10.013

117. Yu Z, Li X, Xu F, Hu X, Yan J, Kwon N, Chen G, Tang T, Dong X, Mai Y, Chen D, Yoon J, He X, & Tian H (2020) A Supramolecular-Based Dual-Wavelength Phototherapeutic Agent with Broad-Spectrum Antimicrobial Activity Against Drug-Resistant Bacteria. *Angew Chemie Int Ed* 59:3658–3664 . https://doi.org/10.1002/anie.201913506

118. Spagnul C, Greenman J, Wainwright M, Kamil Z, & Boyle RW (2016) Synthesis, characterization and biological evaluation of a new photoactive hydrogel against Gram-positive and Gram-negative bacteria. *J Mater Chem B* 4:1499–1509 . https://doi.org/10.1039/C5TB02569A

119. Nieves I, Hally C, Viappiani C, Agut M, & Nonell S (2020) A porphycene-gentamicin conjugate for enhanced photodynamic inactivation of bacteria. *Bioorg Chem* 97:103661 . https://doi.org/10.1016/j.bioorg.2020.103661

120. Sułek A, Pucelik B, Kobielusz M, Barzowska A, & Dąbrowski JM (2020) Photodynamic inactivation of bacteria with porphyrin derivatives: Effect of charge, lipophilicity, ros generation, and cellular uptake on their biological activity in vitro. *Int J Mol Sci* 21:1–34 . https://doi.org/10.3390/ijms21228716

121. de Aguiar Coletti TMSF, de Freitas LM, Almeida AMF, & Fontana CR (2017) Optimization of Antimicrobial Photodynamic Therapy in Biofilms by Inhibiting Efflux Pump. *Photomed Laser Surg* 35:378–385 . https://doi.org/10.1089/pho.2016.4246

122. Rabanal F, & Cajal Y (2017) Recent advances and perspectives in the design and development of polymyxins. *Nat Prod Rep* 34:886–908 . https://doi.org/10.1039/C7NP00023E

123. Richter P, Krüger M, Prasad B, Gastiger S, Bodenschatz M, Wieder F, Burkovski A, Geißdörfer W, Lebert M, & Strauch SM (2019) Using colistin as a trojan horse: Inactivation of gram-negative bacteria with chlorophyllin. *Antibiotics* 8:1–23 . https://doi.org/10.3390/antibiotics8040158

124. Le Guern F, Sol V, Ouk C, Arnoux P, Frochot C, & Ouk TS (2017) Enhanced Photobactericidal and Targeting Properties of a Cationic Porphyrin following the Attachment of Polymyxin B. *Bioconjug Chem* 28:2493–2506 . https://doi.org/10.1021/acs.bioconjchem.7b00516

125. Le Guern F, Ouk TS, Ouk C, Vanderesse R, Champavier Y, Pinault E, & Sol V (2018) Lysine Analogue of Polymyxin B as a Significant Opportunity for Photodynamic Antimicrobial Chemotherapy. *ACS Med Chem Lett* 9:11–16 . https://doi.org/10.1021/acsmedchemlett.7b00360

126. Akram AR, Chankeshwara S V., Scholefield E, Aslam T, McDonald N, Megia-Fernandez A, Marshall A, Mills B, Avlonitis N, Craven TH, Smyth AM, Collie DS, Gray C, Hirani N, Hill AT, Govan JR, Walsh T, Haslett C, Bradley M, & Dhaliwal K (2018) In situ identification of Gram-negative bacteria in human lungs using a topical fluorescent peptide targeting lipid A. *Sci Transl Med* 10: . https://doi.org/10.1126/scitranslmed.aal0033

127. Ucuncu M, Mills B, Duncan S, Staderini M, Dhaliwal K, & Bradley M (2020) Polymyxin-based photosensitizer for the potent and selective killing of Gram-negative bacteria. *Chem Commun* 56:3757–3760 . https://doi.org/10.1039/D0CC00155D

128. Zhang A-N, Wu W, Zhang C, Wang Q-Y, Zhuang Z-N, Cheng H, & Zhang X-Z (2019) A versatile bacterial membrane-binding chimeric peptide with enhanced photodynamic antimicrobial activity. *J Mater Chem B* 7:1087–1095 . https://doi.org/10.1039/C8TB03094D

129. De Freitas LM, Lorenzón EN, Santos-Filho NA, Zago LHDP, Uliana MP, De Oliveira KT, Cilli EM, & Fontana CR (2018) Antimicrobial Photodynamic therapy enhanced by the peptide aurein. *Sci Rep* 8:1–15 . https://doi.org/10.1038/s41598-018-22687-x

130. Hamblin MR, & Abrahamse H (2018) Inorganic Salts and Antimicrobial Photodynamic Therapy: Mechanistic Conundrums? *Molecules* 23:3190 . https://doi.org/10.3390/molecules23123190

131. Wen X, Zhang X, Szewczyk G, El-Hussein A, Huang Y-Y, Sarna T, & Hamblin MR (2017) Potassium Iodide Potentiates Antimicrobial Photodynamic Inactivation Mediated by Rose Bengal in In Vitro and In Vivo Studies. *Antimicrob Agents Chemother* 61:1–15 . https://doi.org/10.1128/AAC.00467-17

New insights for eradication of Gram-negative bacteria by photodynamic treatment: a still relevant challenge

Nidia Maldonado-Carmona [1,2], Tan-Sothea Ouk [1], and Stéphanie Leroy-Lhez [1]*

[1]*PEIRENE Laboratory, Faculty of Sciences and Techniques, University of Limoges, Limoges, 87060,France*

[2]*University of Coimbra, Coimbra Chemistry Center, Department of Chemistry, University of Coimbra, Coimbra, 3004-535, Portugal*

Section 2.1. Cationic photosensitizers

Reference	Photosensitizer	Counterion	Bacteria strains	Pre-treatment incubation time	Photodynamic bactericide concentration [Viability reduction]	Light source [Wavelength of emission]	Light fluence	Light dose
[20]	**1**	I^-	*Proteus mirabillis* ATTC 29906	ND	5 µM [3 log reduction]	White LED-light [400 – 800 nm]	25 mW/cm²	90 J/cm²
			P. mirabillis SBP 65/18	ND	5 µM [3 log reduction]			90 J/cm²
			P. aeruginosa ATTC 25853	ND	5 µM [3 log reduction]			90 J/cm²
			P. aeruginosa SBP 65/18	ND	5 µM [3 log reduction]			90 J/cm²
	2	I^-	*P. mirabillis* ATTC 29906	ND	5 µM [3 log reduction]	White LED-light [400 – 800 nm]	25 mW/cm²	90 J/cm²
			P. mirabillis SBP 65/18	ND	5 µM [3 log reduction]			135 J/cm²
			P. aeruginosa ATTC 25853	ND	5 µM [3 log reduction]			135 J/cm²
			P. aeruginosa SBP 65/18	ND	5 µM [3 log reduction]			135 J/cm²
[21]	**3**	NO_3^-	*E. coli* ATCC 11775	5 minutes	10 µM [4 log reduction]	Blue LED-light [405 nm]	60 mW/cm²	20 J/cm²
[22]	**4**	I^-	*E. coli*	10 minutes	1 µM [~7 log reduction]	White light	25 mW/cm²	90 J/cm²
	5	SO_4^{-2}	*E. coli*	10 minutes	1 µM [~2 log reduction]			90 J/cm²
	6	I^-	*E. coli*	10 minutes	1 µM [~1 log reduction]			90 J/cm²
	7	SO_4^{-2}	*E. coli*	10 minutes	1 µM [~7 log redcution]			90 J/cm²
[23]	**9**	I^-	*E. coli* ATCC 13706	15 minutes	5 µM [no log reduction]	White light [380 – 700 nm]	40 mW/cm²	648 J/cm²
	10	I^-	*E. coli* ATCC 13706	15 minutes	5 µM [~3 log reduction]			216 J/cm²
	11	I^-	*E. coli* ATCC 13706	15 minutes	5 µM [~4 log reduction]			144 J/cm²
	12	I^-	*E. coli* ATCC 13706	15 minutes	5 µM [~6 log reduction]			144 J/cm²
	1	I^-	*E. coli* ATCC 13706	15 minutes	5 µM [~4 log reduction]			144 J/cm²
[24]	**12**	I^-	*E. coli* ATCC 13706	10 minutes [PBS]	5 µM [~6 log reduction]	White light [400 – 800 nm]	150 mW/cm²	135 J/cm²
				10 minutes [Plasma]	5 µM [~3 log reduction]			270 J/cm²
				10 minutes [whole blood]	5 µM [~4 log reduction]			1620 J/cm²

Section 2.1. Cationic photosensitizers

Reference	Photosensitizer	Counterion	Bacteria strains	Pre-treatment incubation time	Photodynamic bactericide concentration [Viability reduction]	Light source [Wavelength of emission]	Light fluence	Light dose
[25]	**13**	Cl^-	*E. coli* GC4468	30 minutes	1 µM [10% MTT reduction]	Incandescent lamp	35 mW/cm²	42 J/cm²
	14	Cl^-	*E. coli* GC4468	30 minutes	1 µM [25% MTT reduction]			42 J/cm²
	15	Cl^-	*E. coli* GC4468	30 minutes	1 µM [95% MTT reduction]			42 J/cm²
	16	Cl^-	*E. coli* GC4468	30 minutes	1 µM [95% MTT reduction]			42 J/cm²
[26]	**15**	Cl^-	*E. coli* GC4468	30 minutes	1 µM [30% MTT reduction]	Incandescent lamp	33 mW/cm²	39.6 J/cm²
[26]	**16**	Cl^-	*E. coli* GC4468	30 minutes	1 µM [95% MTT reduction]	Incandescent lamp	33 mW/cm²	39.6 J/cm²
[28]	**17**	SO_4^{2-}	Bioluminiscent *E. coli*	15 minutes	20 µM [no bioluminescent reduction]	Fluorescent lamps [380-700 nm]	2.5 mW/cm²	36 J/cm²
	18	SO_4^{2-}	Bioluminiscent *E. coli*	15 minutes	20 µM [~3 log bioluminescent reduction]			13.5 J/cm²
	19	SO_4^{2-}	Bioluminiscent *E. coli*	15 minutes	20 µM [~3 log bioluminescent reduction]			13.5 J/cm²
	20	SO_4^{2-}	Bioluminiscent *E. coli*	15 minutes	20 µM [~3 log bioluminescent reduction]			22.5 J/cm²
[29]	**21**	I^-	*E. coli* ATCC25922	60 minutes	10 nM [~3 log reduction]	Blue LED light [415 nm]	4 mW/cm²	1.62 J/cm²
			P. aeruginosa ATCC 27853	60 minutes	10 nM [~3 log reduction]			
			E. coli ATCC25922	60 minutes	10 nM [~4 log reduction]			
			P. aeruginosa ATCC 27853	60 minutes	10 nM [~5 log reduction]			
	22	I^-	*A. baumannii* 141HUC	60 minutes	100 nM [~3 log reduction]			1.36 J/cm²
			E. coli 189	60 minutes	100 nM [~3 log reduction]			
			K. pneumoniae	60 minutes	100 nM [~4 log reduction]			
			E. coli ATCC25922	60 minutes	100 nM [~2 log reduction]			
	24	I^-	*P. aeruginosa* ATCC 27853	60 minutes	100 nM [~4 log reduction]			1.08 J/cm²
			A. baumannii 141HUC	60 minutes	100 nM [~2 log reduction]			
			E. coli 189	60 minutes	1 µM [~4 log reduction]			
			K. pneumoniae (kp)	60 minutes	1 µM [~4 log reduction]			
[24]	**25**	SO_4^{-2}	*E. coli* ATCC 13706	10 minutes [PBS]	20 µM [~3 log reduction]	Red light [620 – 750 nm]	150 mW/cm²	810 J/cm²
				10 minutes [Plasma]	20 µM [~2.5 log reduction]			2430 J/cm²
				10 minutes [whole blood]	20 µM [~2 log reduction]			2430 J/cm²

Section 2.1. Cationic photosensitizers

Reference	Photosensitizer	Counterion	Bacteria strains	Pre-treatment incubation time	Photodynamic bactericide concentration [Viability reduction]	Light source [Wavelength of emission]	Light fluence	Light dose
[32]	**26**	SO_4^{2-}	Bioluminiscent *E. coli*	15 minutes	20 µM [~1 log reduction]	White light Lumacare [620 – 750 nm]	150 mW/cm^2	270 J/cm^2
			Bioluminiscent *E. coli*		20 µM [~1 log reduction]	Red light Lumacare [400 - 800 nm]	150 mW/cm^2	270 J/cm^2
	27	SO_4^{2-}	Bioluminiscent *E. coli*	15 minutes	20 µM [~2 log reduction]	White light Lumacare [620 – 750 nm]	150 mW/cm^2	270 J/cm^2
	27	SO_4^{2-}	Bioluminiscent *E. coli*	15 minutes	20 µM [~2 log reduction]	Red light Lumacare [400 - 800 nm]	150 mW/cm^2	270 J/cm^2
[32]	**28**	SO_4^{2-}	Bioluminiscent *E. coli*	15 minutes	20 µM [~2.5 log reduction]	White light Lumacare [620 – 750 nm]	150 mW/cm^2	270 J/cm^2
			Bioluminiscent *E. coli*	15 minutes	20 µM [~3 log reduction]	Red light Lumacare [400 - 800 nm]	150 mW/cm^2	180 J/cm^2
			Bioluminiscent *E. coli* [Biofilm]	15 minutes	20 µM [~2 log reduction]			270 J/cm^2
	29	SO_4^{2-}	Bioluminiscent *E. coli*	15 minutes	20 µM [~1.5 log reduction]	White light Lumacare [620 – 750 nm]	150 mW/cm^2	270 J/cm^2
			Bioluminiscent *E. coli*	15 minutes	20 µM [~5.5 log reduction]	Red light Lumacare [400 - 800 nm]	150 mW/cm^2	180 J/cm^2
			Bioluminiscent *E. coli* [Biofilm]	15 minutes	20 µM [~2 log reduction]			270 J/cm^2
[33]	**30**	I^-	*E. coli*	2 hours	0.1 µM [7 log reduction]	White light 150W Optical illuminator (OSH150)	ND	10 J/cm^2
			P. aeruginosa	2 hours	0.1 µM [7 log reduction]			10 J/cm^2
	31	I^-	*E. coli*	2 hours	10 µM [7 log reduction]			10 J/cm^2
			P. aeruginosa	2 hours	10 µM [7 log reduction]			10 J/cm^2
	32	I^-	*E. coli*	2 hours	0.1 µM [7 log reduction]			10 J/cm^2
			P. aeruginosa	2 hours	5 µM [3 log reduction]			10 J/cm^2
[34]	**33**	I^-	*E. coli*	2 hours	1 µM [~4 log reduction]			10 J/cm^2
			P. aeruginosa	2 hours	20 µM [3 log reduction]			10 J/cm^2
	34	SO_4^{2-}	*P. aeruginosa* 1390	15 minutes	12.5 µM [3.8 log reduction]	Red LED light [665 nm]	60 mW/cm^2	50 J/cm^2
	35	SO_4^{2-}	*P. aeruginosa* 1390	15 minutes	30 µM [no log reduction]			50 J/cm^2
[35]	**36**	I^-	*E. coli* ATCC 25922	11 minutes	100 µM [5.56 log reduction]	LED Multichip Emitters [735 nm]	3.15 mW/cm^2	2.079 J/cm^2
			P. aeruginosa NCTC 6749	11 minutes	100 µM [5.09 log reduction]			2.079 J/cm^2
			Serratia marcescens ATCC 8100	11 minutes	100 µM [5.29 log reduction]			2.079 J/cm^2
[36]	**37**	I^-	*E. coli* CECT 101	30 minutes	5 µM [~3.5 log reduction]	LED lamp [635 ± 15 nm]	ND	10 J/cm^2
	38	I^-	*E. coli* CECT 101	30 minutes	5 µM [~6 log reduction]			30 J/cm^2
	39	I^-	*E. coli* CECT 101	30 minutes	10 µM [~3.5 log reduction]			30 J/cm^2

Section 2.1. Cationic photosensitizers

Reference	Photosensitizer	Counterion	Bacteria strains	Pre-treatment incubation time	Photodynamic bactericide concentration [Viability reduction]	Light source [Wavelength of emission]	Light fluence	Light dose
[36]	**40**	I^-	*E. coli* CECT 101	30 minutes	10 µM [~1.5 log reduction]	LED lamp [635 ± 15 nm]	ND	60 J/cm^2
[37]	**41**	Cl^-	*P. aeruginosa* 32	30 minutes	3 µM [~3.5 log reduction]	LED light SPD-M-685 (BIOSPEC, Russia) [685 nm]	ND	20 J/cm^2
			P. aeruginosa 32 [biofilm]	60 minutes	125 µM [~3.2 log reduction]			100 J/cm^2
[38]	**42**	I^-	*E. coli* DH5α pAKlux2.1	15 minutes	8 µM [5 log reduction]	LED-light [660 nm]	42.5 mW/cm^2	12.7 J/cm^2
[37]	**43**	Br^-	*P. aeruginosa* 32	30 minutes	1 µM [~4 log reduction]	LED light SPD-M-685 (BIOSPEC, Russia) [685 nm]	NA	20 J/cm^2
			P. aeruginosa 32 [biofilm]	60 minutes	125 µM [~3 log reduction]			100 J/cm^2
	44	Br^-	*P. aeruginosa* 32	30 minutes	1 µM [~5 log reduction]			20 J/cm^2
			P. aeruginosa 32 [biofilm]	60 minutes	125 µM [~4 log reduction]			100 J/cm^2
[39]	**45**	Tetratosylate	ESBL-producing *E. coli*	4 minutes	200 µM [~3 log reduction]	Laser light (NTC laser, NOVI, USA) [760 nm]	2.5 W/cm^2	594 J/cm^2
			ESBL-producing and fluoroquinolone-resistant *K. pneumoniae*	4 minutes	200 µM [5 log reduction]	LED (Roithner Lasertechnik GmbH, Austria) [760 nm]	0.18 W/cm^2	1166 J/cm^2
			Carbapenem-resistant *K. pneumoniae*	4 minutes	200 µM [~3 log reduction]	Laser light (NTC laser, NOVI, USA) [760 nm]	2.5 W/cm^2	594 J/cm^2
				4 minutes	200 µM [6 log reduction]	Laser light (NTC laser, NOVI, USA) [760 nm]	2.5 W/cm^2	594 J/cm^2
				4 minutes	200 µM [6 log reduction]	LED (Roithner Lasertechnik GmbH, Austria) [760 nm]	0.18 W/cm^2	1166 J/cm^2
			Carbapenem-resistant *P. aeruginosa*	4 minutes	200 µM [6 log reduction]	Laser light (NTC laser, NOVI, USA) [760 nm]	2.5 W/cm^2	594 J/cm^2
[40]	**46**	I^-	*E. coli* EC7	30 minutes	5 µM [~2.5 log reduction]	Novamat 130 AF slide projector [350 – 800 nm]	70 mW/cm^2	63 J/cm^2
				30 minutes + KI 50 mM	5 µM [~3.5 log reduction]			63 J/cm^2
	47	I^-	*E. coli* EC7	30 minutes	5 µM [~2.5 log reduction]			63 J/cm^2
				30 minutes + KI 50 mM	5 µM [~7.5 log reduction]			63 J/cm^2
[41]	**47**	I^-	*Escherichia coli* ATCC 25922	20 minutes	50 µM [3.1 log reduction]	InGan-based High Power LED multi-chip Emitters [525 nm]	ND	10.8 J/cm^2
	48	I^-	*Escherichia coli* ATCC 25922		5 µM [>5.3 log reduction]			16.99 J/cm^2
[43]	**49**	Cl^-	*K. pneumoniae* KPBr-1	ND	100 µM [3 log reduction]	Red LED probe [660 nm]	100 mW/cm^2	16.53 J/cm^2
			K. pneumoniae ICBKPS3.2		100 µM [3 log reduction]			16.71 J/cm^2
			K. pneumoniae ATCC 700603		100 µM [3 log reduction]			

Section 2.1. Cationic photosensitizers

Reference	Photosensitizer	Counterion	Bacteria strains	Pre-treatment incubation time	Photodynamic bactericide concentration [Viability reduction]	Light source [Wavelength of emission]	Light fluence	Light dose
[46]	**50**	Cl^-	*K. pneumoniae* ATCC 700603	10 minutes	10 µM [~3 log reduction]	Laser [630 nm]	130 mW/cm²	39 J/cm²
			K. pneumoniae ATCC 700603 [biofilm]	30 minutes	50 µM [~3 log reduction]			100 J/cm²
	51	Cl^-	*K. pneumoniae* ATCC 700603	10 minutes	10 µM [~3 log reduction]			39 J/cm²
			K. pneumoniae ATCC 700603 [biofilm]	30 minutes	50 µM [~3 log reduction]			100 J/cm²
	52	Cl^-	*K. pneumoniae* ATCC 700603	10 minutes	10 µM [~3 log reduction]			39 J/cm²
[46]	**52**	Cl^-	*K. pneumoniae* ATCC 700603 [biofilm]	30 minutes	50 µM [~3 log reduction]	Laser [630 nm]	130 mW/cm²	100 J/cm²
[47]	**53**	Br	*P. aeruginosa* ATCC25668	30 minutes	15 µM [~3.5 log reduction]	Waldmann PDT1200 [600 – 750 nm]	ND	100 J/cm²
	54	Br	*E. coli* CECT 101	30 minutes	5 µM [~3.5 log reduction]	LED-based lamp [635 nm]		60 J/cm²
			P. aeruginosa ATCC25668	30 minutes	20 µM [~5.5 log reduction]	Waldmann PDT1200 [600 – 750 nm]		100 J/cm²
[49]	**55**	Cl^-	*E. coli* ATCC 25922	10 seconds	10 µM [~6 log reduction]	Blue emitting neon tube [400 – 450 nm]	20 mW/cm²	1.2 J/cm²
	56	Cl^-	*E. coli* ATCC 25922	10 seconds	10 µM [~6 log reduction]			
	57	Cl^-	*E. coli* ATCC 25922	10 seconds	10 µM [~3 log reduction]			
	58	Cl^-	*E. coli* ATCC 25922	10 seconds	10 µM [~3 log reduction]			
	59	Cl^-	*E. coli* ATCC 25922	10 seconds	5 µM [~3 log reduction]			
[50]	**60**	I^-	*E. coli* CIP54.8T	ND	100 µM [MIC]	White LED visible light [390 – 700 nm]	4.83 mW/cm²	25 J/cm²
			E. coli CIP53.126	ND	200 µM [MIC]			
			P. aeruginosa CIP76.110	ND	200 µM [MIC]			
	61	Br	*E. coli* CIP53.126	ND	200 µM [MIC]			
			P. aeruginosa CIP76.110	ND	200 µM [MIC]			
	62	-	*E. coli* CIP54.8T	ND	>200 µM [MIC]			
			E. coli CIP53.126	ND	>200 µM [MIC]			
			P. aeruginosa CIP76.110	ND	>200 µM [MIC]			
	63	I^-	*E. coli* CIP54.8T	ND	>200 µM [MIC]			
			E. coli CIP53.126	ND	>200 µM [MIC]			
			P. aeruginosa CIP76.110	ND	>200 µM [MIC]			

Section 2.1. Cationic photosensitizers								
Reference	**Photosensitizer**	**Counterion**	**Bacteria strains**	**Pre-treatment incubation time**	**Photodynamic bactericide concentration [Viability reduction]**	**Light source [Wavelength of emission]**	**Light fluence**	**Light dose**
[50]	**64**	Br^-	*E. coli* CIP54.8T	ND	>200 µM [MIC]	White LED visible light [390 – 700 nm]	4.83 mW/cm^2	25 J/cm^2
			E. coli CIP53.126	ND	>200 µM [MIC]			
			P. aeruginosa CIP76.110	ND	200 µM [MIC]			
	65	I^-	*E. coli* CIP54.8T	ND	50 µM [MIC]			
			E. coli CIP53.126	ND	25 µM [MIC]			
			P. aeruginosa CIP76.110	ND	200 µM [MIC]			
	66	Br^-	*E. coli* CIP54.8T	ND	ND			
	66	Br^-	*E. coli* CIP53.126	ND	ND			
			P. aeruginosa CIP76.110	ND	ND			
	67	I^-	*E. coli* CIP54.8T	ND	200 µM [MIC]			
			E. coli CIP53.126	ND	100 µM [MIC]			
			P. aeruginosa CIP76.110	ND	>200 µM [MIC]			
	68	Br^-	*E. coli* CIP54.8T	ND	>200 µM [MIC]			
			E. coli CIP53.126	ND	>200 µM [MIC]			
			P. aeruginosa CIP76.110	ND	>200 µM [MIC]			
	69	I^-	*E. coli* CIP54.8T	ND	100 µM [MIC]			
			E. coli CIP53.126	ND	50 µM [MIC]			
			P. aeruginosa CIP76.110	ND	100 µM [MIC]			
	70	Br^-	*E. coli* CIP54.8T	ND	200 µM [MIC]			
			E. coli CIP53.126	ND	100 µM [MIC]			
			P. aeruginosa CIP76.110	ND	200 µM [MIC]			
	71	I^-	*E. coli* CIP54.8T	ND	100 µM [MIC]			
			E. coli CIP53.126	ND	50 µM [MIC]			
			P. aeruginosa CIP76.110	ND	>200 µM [MIC]			
	72	Br^-	*E. coli* CIP54.8T	ND	>200 µM [MIC]			
			E. coli CIP53.126	ND	>200 µM [MIC]			
			P. aeruginosa CIP76.110	ND	25 µM [MIC]			

Section 2.1. Cationic photosensitizers								
Reference	**Photosensitizer**	**Counterion**	**Bacteria strains**	**Pre-treatment incubation time**	**Photodynamic bactericide concentration [Viability reduction]**	**Light source [Wavelength of emission]**	**Light fluence**	**Light dose**
[50]	**73**	Cl^-	*E. coli* CIP54.8T	ND	100 µM [MIC]	White LED visible light [390 – 700 nm]	4.83 mW/cm²	25 J/cm²
			E. coli CIP53.126	ND	50 µM [MIC]			
			P. aeruginosa CIP76.110	ND	12.5 µM [MIC]			
	74	Cl^-	*E. coli* CIP54.8T	ND	>200 µM [MIC]			
			E. coli CIP53.126	ND	>200 µM [MIC]			
			P. aeruginosa CIP76.110	ND	200 µM [MIC]			
	75	Cl^-	*E. coli* CIP54.8T	ND	>200 µM [MIC]			
			E. coli CIP53.126	ND	>200 µM [MIC]			
			P. aeruginosa CIP76.110	ND	>200 µM [MIC]			
	55	Cl^-	*E. coli* CIP54.8T	ND	200 µM [MIC]			
			E. coli CIP53.126	ND	>200 µM [MIC]			
			P. aeruginosa CIP76.110	ND	50 µM [MIC]			

Section 2.2. Neutral and anionic photosensitizers							
Reference	**Photosensitizer**	**Bacteria strains**	**Pre-treatment incubation time**	**Photodynamic bactericide concentration**	**Light source [Wavelength of emission]**	**Light fluence**	**Light dose**
[22]	**4b**	Bioluminescent *E. coli*	10 minutes	1 µM [no log reduction]	White light	25 mW/cm²	90 J/cm²
			10 minutes + 100 mM KI	1 µM [7 log reduction]			
	6b	Bioluminescent *E. coli*	10 minutes	1 µM [no log reduction]			
			10 minutes + 100 mM KI	1 µM [7 log reduction]			
	5b	Bioluminescent *E. coli*	10 minutes	1 µM [no log reduction]			
			10 minutes + 100 mM KI	1 µM [7 log reduction]			
	7b	Bioluminescent *E. coli*	10 minutes	1 µM [no log reduction]			
			10 minutes + 100 mM KI	1 µM [7 log reduction]			
[54]	**76**	*E. coli* EC7	30 minutes	1 µM [~4 log reduction]	Novamat 130 AF slide projector [350 – 800 nm]	90 mW/cm²	81 J/cm²
	77	*E. coli* EC7	30 minutes	1 µM [~6 log reduction]			
[38]	**42b**	*E. coli* DH5α pAKlux2.1	15 minutes	8 µM [no log reduction]	LED-light [660 nm]	42.5 mW/cm²	12.7 J/cm²

Section 2.2. Neutral and anionic photosensitizers

Reference	Photosensitizer	Bacteria strains	Pre-treatment incubation time	Photodynamic bactericide concentration	Light source [Wavelength of emission]	Light fluence	Light dose
[55]	**78**	*E. coli* M-17	30 minutes + Tween 80 1%	50 µM [no log reduction]	Light diode panel [740 nm]	0.1 W/cm^2	40 J/cm^2
			30 minutes + Tween 80 1% and disodium EDTA 0.1%	50 µM [6 log reduction]			
	79	*E. coli* M-17	30 minutes + Tween 80 1% and disodium EDTA 0.1%	500 µM[no detected reduction]			
[56]	**80**	*E. coli* ATCC 25922	30 minutes	64 µg/mL [3 log reduction]	White LED>light	12.6 mW/cm^2	20 J/cm^2
	81	*E. coli* ATCC 25922	30 minutes	64 µg/mL [3 log reduction]			10 J/cm^2
[42]	**47b**	*E. coli* ATCC 25922	20 minutes	500 µM [1.7 log reduction]	InGan-based High Power LED multi-chip Emitters [505 nm]	ND	10.8 J/cm^2
	48b	*E. coli* ATCC 25922	20 minutes	500 µM [>5.4 log reduction]			
[59]	**84**	*P. aeruginosa* ATCC 27853	30 minutes	100 µM [1.5 log reduction]	White light KL 2500 LCD	ND	100 J/cm^2
			30 minutes + 10% serum	100 µM [no log reduction]			
	85	*P. aeruginosa* ATCC 27853	30 minutes	100 µM [0.5 log reduction]			
			30 minutes + 10% serum	100 µM [no log reduction]			
	86	*P. aeruginosa* ATCC 27853	30 minutes	100 µM [1 log reduction]			
			30 minutes + 10% serum	100 µM [0.5 log reduction]			
	87	P. aeruginosa ATCC 27853	30 minutes	100 µM [3 log reduction]			
			30 minutes + 10% serum	100 µM [~0.8 log reduction]			
	88	*P. aeruginosa* ATCC 27853	30 minutes	100 µM [3.5 log reduction]			
			30 minutes + 10% serum	100 µM [no log reduction]			
	89	*P. aeruginosa* ATCC 27853	30 minutes	100 µM [no log reduction]			
			30 minutes + 10% serum	100 µM [1 log reduction]			
	90	*P. aeruginosa* ATCC 27853	30 minutes	100 µM [1 log reduction]			
			30 minutes + 10% serum	100 µM [no log reduction]			
	91	*P. aeruginosa* ATCC 27853	30 minutes	100 µM [no log reduction]			
			30 minutes + 10% serum	100 µM [no log reduction]			
	92	*P. aeruginosa* ATCC 27853	30 minutes	100 µM [2 log reduction]			
			30 minutes + 10% serum	100 µM [0.8 log reduction]			
	93	*P. aeruginosa* ATCC 27853	30 minutes	100 µM [1 log reduction]			
			30 minutes + 10% serum	100 µM [no log reduction]			

Section 2.2. Neutral and anionic photosensitizers

Reference	Photosensitizer	Bacteria strains	Pre-treatment incubation time	Photodynamic bactericide concentration	Light source [Wavelength of emission]	Light fluence	Light dose
[60]	**94**	*P. aeruginosa* ATCC 27853	30 minutes	10 µM [>6.5 log reduction]	White light KL 2500 LCD	ND	100 J/cm^2
			30 minutes + 10% serum	100 µM [1 log reduction]			
	95	*P. aeruginosa* ATCC 27853	30 minutes	10 µM [~3 log reduction]			
			30 minutes + 10% serum	100 µM [0.5 log reduction]			
	96	*P. aeruginosa* ATCC 27853	30 minutes	100 µM [1.5 log reduction]			
			30 minutes + 10% serum	100 µM [no log reduction]			
	97	*P. aeruginosa* ATCC 27853	30 minutes	100 µM [no log reduction]			
			30 minutes + 10% serum	100 µM [no log reduction]			
	98	*P. aeruginosa* ATCC 27853	30 minutes	100 µM [no log reduction]			
		P. aeruginosa ATCC 27853	30 minutes + 10% serum	100 µM [no log reduction]			
	99	*P. aeruginosa* ATCC 27853	30 minutes	10 µM [>6.5 log reduction]			
			30 minutes + 10% serum	100 µM [no log reduction]			
	100	*P. aeruginosa* ATCC 27853	30 minutes	10 µM [>6.5 log reduction]			
			30 minutes + 10% serum	100 µM [no log reduction]			
	101	*P. aeruginosa* ATCC 27853	30 minutes	100 µM [>6.5 log reduction]			
			30 minutes + 10% serum	100 µM [no log reduction]			
[61]	**102**	*A. baumannii* ATCC BAA747	15 minutes + 0.01% acetic acid	50 µM [~7 log reduction]	Green laser diode [530 nm]	45 mW	40 J/cm^2
		A. baumannii ATCC BAA747 [biofilm]	15 minutes + 0.01 % acetic acid + chitosan 12.5 µM	100 µM [~3.8 log reduction]			80 J/cm^2
		A. baumanii AB1	15 minutes + 0.01% acetic acid	50 µM [~7 log reduction]			40 J/cm^2
		A. baumanii AB1 [biofilm]	15 minutes + 0.01 % acetic acid + chitosan 12.5 µM	100 µM [~5.5 log reduction			80 J/cm^2
		A. baumannii AB2	15 minutes + 0.01% acetic acid	50 µM [~7 log reduction]			40 J/cm^2
		A. baumannii AB2 [biofilm]	15 minutes + 0.01 % acetic acid + chitosan 12.5 µM	100 µM [~3.2 log reduction]			80 J/cm^2
[62]	**103**	*Salmonella enterica* ATCC 14028	10 minutes	50 µM [~3 log reduction]	Green LED array [530 ± 40 nm]	10 mW/cm^2	9 J/cm^2
			10 minutes + KI 100 mM	0.10 µM [>7.5 log reduction]			9 J/cm^2
			10 minutes	100 µM [1 log reduction]			9 J/cm^2
	104	*Salmonella enterica* ATCC 14028	10 minutes + KI 50 mM	0.10 µM [>7.5 log reduction]			9 J/cm^2

Section 2.3. Synthetic metallic complexes							
Reference	**Photosensitizer**	**Bacteria strains**	**Pre-treatment incubation time**	**Photodynamic bactericide concentration**	**Light source [Wavelength of emission]**	**Light fluence**	**Light dose**
[65]	**108**	*E. coli* JM109	ND	5 µM [~95% growth inhibition]	Luxeon 5W LED [520 nm]	4.18 x 10^{17} photons/s	ND
[66]	**109**	*P. aeruginosa* CIP76.110	4 hours	50 µM [no log reduction]	White visible LED light	4.83 mW/cm²	25 J/cm²
		E. coli CIP54.8T		50 µM [no log reduction]			
[68]	**127**	*E. coli* MG 1655	ND	1 µM [MIC]	Blue light [470 nm]	12 mW/cm²	8.6 J/cm²
		P. aeruginosa AR 0229	ND	2 µM [MIC]			
		E. coli AR 0114	ND	0.5 µM [MIC]			
		A. baumannii Naval-17	ND	0.5 µM [MIC]			
		K. pneumoniae AR 0113	ND	4 µM [MIC]			

Section 3.1. Materials based on biopolymers and carbon-based molecules								
Reference	**Material**	**Photosensitizer**	**Bacteria strains**	**Pre-treatment incubation time**	**Photodynamic bactericide concentration**	**Light source [Wavelength of emission]**	**Light fluence**	**Light dose**
[70]	Cellulose fabrics [impregnation]	**1**	*E. coli*	20 minutes	100 µM [100% inactivation]	100 Watt tungsten lamp	~0.36 mW/cm²	1.296 J/cm²
			P. aeruginosa		100 µM [100% inactivation]			1.296 J/cm²
		2	*E. coli*		100 µM [100% inactivation]			1.296 J/cm²
			P. aeruginosa		100 µM [100% inactivation]			1.296 J/cm²
		128	*E. coli*		100 µM [100% inactivation]			1.296 J/cm²
			P. aeruginosa		100 µM [100% inactivation]			1.296 J/cm²
		129	*E. coli*		100 µM [100% inactivation]			1.944 J/cm²
			P. aeruginosa		100 µM [100% inactivation]			1.296 J/cm²
		130	*E. coli*		100 µM [60% inactivation]			1.944 J/cm²
			P. aeruginosa		100 µM [50% inactivation]			1.944 J/cm²
		131	*E. coli*		100 µM [40% inactivation]			1.944 J/cm²
			P. aeruginosa		100 µM [100% inactivation]			1.944 J/cm²
[71]	Kraft pulp fibers [grafting]	**132**	*P. aeruginosa* CIP76.110	ND	ND [~4 log reduction]	Luxeon Star White [400- 800 nm]	0.16 mW/cm²	9.5 J/cm²
[72]	Electrospun cellulose microfibers	**133**	*E. coli* 8099	30 minutes	ND [~1 log reduction]	Xe lamp [420 nm]	65 mW/cm²	117 J/cm²
				30 minutes + KI 25 mM	ND [> 6 log reduction]			

Section 3.1. Materials based on biopolymers and carbon-based molecules

Reference	Material	Photosensitizer	Bacteria strains	Pre-treatment incubation time	Photodynamic bactericide concentration	Light source [Wavelength of emission]	Light fluence	Light dose
[73]	Chitosan films [impregnation]	**12**	*E. coli* Top 10 pHK724	60 minutes	3 µM [~4 log reduction]	PAR radiation lamp [380 – 700 nm]	3 mW/cm^2	16.2 J/cm^2
	Chitosan films [impregnation]	**134**	*E. coli* Top 10 pHK724	60 minutes	3 µM [no log reduction]			16.2 J/cm^2
	TiO_2 [nanoparticles]		*E. coli* Top 10 pHK724	60 minutes	10 µM [~2 log reduction]			32.4 J/cm^2
	Chitosan films [impregnation]	**135**	*E. coli* Top 10 pHK724	60 minutes	3 µM [no log reduction]			16.2 J/cm^2
	TiO_2 [nanoparticles]		*E. coli* Top 10 pHK724	60 minutes	10 µM [~2 log reduction]			32.4 J/cm^2
[74]	Chitosan hydrogels [crosslinking]	**136**	*P. aeruginosa* ATCC 27853	ND	ND [4.69 log reduction]	Laser light [660 nm]	ND	ND
[77]	Chitosan hydrogels [crosslinking]	**138**	*E. coli* Nissle1917	15 minutes	0.2 mg/mL [~5 log reduction]	Red LED lamp [660 nm]	5 W/cm^2	63 J/cm^2
	Chitosan hydrogels [additive]			15 minutes + 0.4 mg/mL chitosan	10 µM [~3 log reduction]			1200 J/cm^2
[78]	Chitosan hydrogels [impregnation of UCNP@MB)	**49 MB**	*E. coli* ATCC55244	ND	ND [95% reduction]	Infrared light [980 nm]	1 W/cm^2	
[79]	DNA hybri nanonetwork [crosslinking]	**139**	*E. coli* BK-21	ND	600 nM [30 % reduction]	Incandescent white ligt	ND	ND
[80]	Wool keratin [crosslinkng]	**51 Azure A**	*P. aeruginosa* PAO1	ND	1 mg [~6 log reduction]	500 W halogen-tungsten lamp	48 mW/cm^2	345.6 J/cm^2
[82]	Eucalyptus oil [microemulsion]	**50 TBO**	*P. aeruginosa* BCRC 12154	ND	0.1 µg/mL [~2.2 log reduction]	IP65 LED light	0.674 mW/cm^2	0.61 J/cm^2
[83]	Hexadecyl pyridinium trichloro cupreate [vesicles]	**49 MB**	*E. coli* MTCC 40	30 minutes	ND [1.90 log reduction]	Red-light [664 nm]	24 mW/cm^2	44.64 J/cm^2
[84]	Dipalmitylphosphatidylcholine, cholesterol and dimethyldioctadecyl-ammonium [liposomes]	**49 MB**	*E. coli* S17-1	10 minutes	0.02% [~1 log reduction]	Diode laser [630 nm]	26.3 mW/cm^2	1.578 J/cm^2
[85]	Silver sulfadiazine [nanoliposomes]	**140**	*A. baumannii*	5 minutes	0.5 mg/mL [~100 % reduction]	Blue LED light DY400-4 [450 nm]	ND	300 – 420 J/cm^2
			A. baumannii [biofilm]	5 minutes	0.5 mg/mL [76.4 % reduction]			
			A. baumannii [antibacterial *in vivo* model, mouse]	5 minutes	0.5 mg/mL [68.5 % reduction]			

Section 3.1. Materials based on biopolymers and carbon-based molecules								
Reference	**Material**	**Photosensitizer**	**Bacteria strains**	**Pre-treatment incubation time**	**Photodynamic bactericide concentration**	**Light source [Wavelength of emission]**	**Light fluence**	**Light dose**
[86]	1-palmitoyl-2-oleoyl-sn-glycero-3-phosphocholine and N-[1-(2,3-dioleoyloxy)propyl]-N,N,N-trimethylammonium chloride [vesicles]	**141**	*E. coli* ATCC 25922	20 minutes	100 µM [0.11 log decrease]	High Power LED MultiChip Emitters [max 640 nm]	ND	30 J/cm²
			P. aeruginosa ATCC 6749		100 µM [no log decrease]			
		142	*E. coli* ATCC 25922		100 µM [2.23 log decrease]			
			P. aeruginosa ATCC 6749		100 µM [no log decrease]			
[87]	Polyethyleneimine and octanoyl chloride [micelles]	**82 Chlorin e6**	*E. coli* ATCC 8739	30 minutes	2.195 µg/mL [MIC]	LED light [630 nm]	30 mW/cm²	5.4 J/cm²
[88]	Poly(L-lactide)co-(glycolide) and poly(ε-caprolactone) [Fibers]	**49 MB**	*E. coli* 11,954	2 hours	ND [~2.5 log reduction]	ND	120 mW/cm²	215 J/cm²
[89]	Zeolitic imidazolate framework-8 and poly (ε-caprolactone [nanofibers]	**103 RB**	*E. coli*	ND	ND [~100 % reduction]	Visible light lamp [515 nm]	1.8 mW/cm²	3.24 J/cm²
[90]	2-hydroxyethyl methacrylate [non-covalent binding]	**8**	Bioluminescent *E. coli*	15 minutes	40 µM [~2 log reduction]	White halogen light [400 – 800 nm]	156 mW/cm²	702 J/cm²
	2-hydroxyethyl methacrylate [covalent binding]	**8**	Bioluminescent *E. coli*		10 µM [~2 log reduction]			

Section 3.2. Inorganic and hybrid materials								
Reference	**Material**	**Photosensitizer**	**Bacteria strains**	**Pre-treatment incubation time**	**Photodynamic bactericide concentration**	**Light source [Wavelength of emission]**	**Light fluence**	**Light dose**
[91]	Iron oxide magnetic nanoparticles [grafting]	**8**	*E. coli* EC7	30 minutes	2 µM [~1.9 log reduction]	Visible light	90 mW/cm²	162 J/cm²
	Iron oxide magnetic cationic nanoparticles [grafting]			30 minutes	2 µM [~3 log reduction]			
[92]	Iron oxide magnetic nanoparticles [grafting]	**143**	*E. coli* EC7	30 minutes	3 µM [~1.7 log reduction]	Cole-Parmer Illuminator 150 W halogen lamp [480 – 550 nm]	0.5 mW/cm²	4.5 J/cm²
	Iron oxide magnetic nanoparticles [grafting]	**144**			3 µM [~5 log reduction]			4.5 J/cm²

Section 3.2. Inorganic and hybrid materials

Reference	Material	Photosensitizer	Bacteria strains	Pre-treatment incubation time	Photodynamic bactericide concentration	Light source [Wavelength of emission]	Light fluence	Light dose
[93]	Super paramagnetic iron oxide nanoparticles	**145 ICG**	*E. coli* ATCC 25922	ND	25 µg/mL [~11 log reduction]	Laser [808 nm]	3 W/cm^2	1793 J/cm^2
			E. coli ATCC 25922 [biofilm]		25 µg/mL [~3 log reduction]			
			K. pneumoniae ATCC 70083		25 µg/mL [~11 log reduction]			
			K. pneumoniae ATCC 70083[biofilm]		25 µg/mL [~6.5 log reduction]			
[93]	Super paramagnetic iron oxide nanoparticles [grafting]	**145 ICG**	*P. aeruginosa* ATCC 700829	ND	25 µg/mL [~11 log reduction]	Laser [808 nm]	3 W/cm^2	1793 J/cm^2
			P. aeruginosa ATCC 700829 [biofilm]		25 µg/mL [~3 log reduction]			
[94]	Chitosan coated iron oxide magnetic nanoparticles [grafting]	**146 TCPP**	*E. coli*	30 minutes	100 µg/mL [98% reduction]	Laser irradiation [635 nm]	1 W/cm^2	ND
[95]	Nanocrystalline TiO_2 nanoparticles [grafting]	**147**	*E. coli* K12	2 hours	0.1 mg/mL [~4 log reduction]	Blue-LED light [420 nm]	ND	10 J/cm^2
			E. coli K12	2 hours + KI 100 mM	0.01 g/mL [~3 log reduction]			
			E. coli K12	2 hours + H_2O_2 100 mM	0.01 g/mL [~3 log reduction]			
		148	*E. coli* K12	2 hours	1 mg/mL [~2.5 log reduction]			
			E. coli K12	2 hours + KI 100 mM	0.01 g/mL [~1 log reduction]			
			E. coli K12	2 hours + H_2O_2 100 mM	0.01 g/mL [~5.5 log reduction]			
		149	*E. coli* K12	2 hours	1 mg/mL [~1 log reduction]			
			E. coli K12	2 hours + KI 100 mM	0.5 g/mL [~5 log reduction]			
			E. coli K12	2 hours + H_2O_2 100 mM	0.01 g/mL [~6 log reduction]			
[96]	Nanocrystalline TiO_2 nanoparticles [grafting]	**147**	*E. coli* K12	2 hours	0.1 g/L [~0.5 log reduction]	Blue-LED light [420 nm]	ND	20 J/cm^2
			E. coli K12	2 hours + 50 mM KI	0.1 g/L [~1.5 log reduction]	Green-LED light [530 nm]	ND	20 J/cm^2
			E. coli K12	2 hours + 50 mM KI	0.1 g/L [~6 log reduction]	Blue-LED light [420 nm]	ND	20 J/cm^2
			E. coli K12	2 hours + 50 mM KI	0.1 g/L [~6 log reduction]	Green-LED light [530 nm]	ND	20 J/cm^2
		148	*E. coli* K12	2 hours	0.1 g/L [~2 log reduction]	Blue-LED light [420 nm]	ND	20 J/cm^2
			E. coli K12	2 hours	0.1 g/L [~2 log reduction]	Green-LED light [530 nm]	ND	20 J/cm^2
			E. coli K12	2 hours + 50 mM KI	0.1 g/L [~6 log reduction]	Blue-LED light [420 nm]	ND	20 J/cm^2
			E. coli K12	2 hours + 50 mM KI	0.1 g/L [~6 log reduction]	Green-LED light [530 nm]	ND	20 J/cm^2

Section 3.2. Inorganic and hybrid materials

Reference	Material	Photosensitizer	Bacteria strains	Pre-treatment incubation time	Photodynamic bactericide concentration	Light source [Wavelength of emission]	Light fluence	Light dose
[96]	Nanocrystalline TiO_2 nanoparticles [grafting]	**150**	*E. coli* K12	2 hours	0.1 g/L [~1 log reduction]	Blue-LED light [420 nm]	ND	20 J/cm^2
			E. coli K12	2 hours	0.1 g/L [~2 log reduction]	Green-LED light [530 nm]	ND	20 J/cm^2
			E. coli K12	2 hours + 50 mM KI	0.1 g/L [~6 log reduction]	Blue-LED light [420 nm]	ND	20 J/cm^2
			E. coli K12	2 hours + 50 mM KI	0.1 g/L [~6 log reduction]	Green-LED light [530 nm]	ND	20 J/cm^2
[97]	TiO_2 nanoparticles [grafting]	**151**	*E. coli* ATCC 25922	30 minutes	16 µg/mL [~3 log reduction]	LED light source	12.6 mW/cm^2	30 J/cm^2
[98]	(3-aminopropyl) triethoxysilane upconverting nanoparticles [functionalization]	**152**	*E. coli* ATCC 25922	ND	2 mg/mL [> 8 log reduction]	LED device [660 nm]	ND	108 J/cm^2
					2 mg/mL [> 6.5 log reduction]	Laser [976 nm]	0.4 W/cm^2	720 J/cm^2
[100]	Mesoporous silica nanoparticles embedded membranes and functionalized with THFS [doping]	**49 MB**	*E. coli*	3 hours	ND [~83% reduction]	Visible light [660 nm]	3.2 mW/cm^2	3.84 J/cm^2
	Mesoporous silica nanoparticles embedded membranes [doping]				ND [~95% reduction]			
[101]	Silver nanoparticles, copper impregnated mesoporous silica coated [encapsulation]	**140 curcumin**	*E. coli*	10 minutes	20 µg/mL [> 7.5 log reduction]	Blue light	240 mW/cm^2	72 J/cm^2
[103]	Biogenic silver nanoparticles [doping]	**49 MB**	*P. aeruginosa* PAO1	2 hours	125 µg/mL [5 log reduction]	Diode laser [660 nm]	467.1 mW/cm^2	84.1 J/cm^2
			P. aeruginosa PAO1 [biofilm]		125 µg/mL [60% inhibition]			
[104]	Silver nanoparticles/Cellulose fabric [immbolization]	-	*E. coli* DH5α pAKlux2.1	10 minutes	ND [~3.5 log reductio]	Red LED light [660 nm]	75 mW/cm^2	45 J/cm^2
			E. coli ATCC 8739		ND [~4 log reduction]			
[105]	Silver nanocubes [grafting]	**103 RB**	*E. coli* ATCC25922	30 minutes	1.1 µM [~6 log reduction]	Green LED exposure panel [520 nm]	ND	ND
	Silver nanospheres [grafting]				1.1 µM [~4 log reduction]			
[106]	Ag- conjugated graphene quantum dots	-	*E. coli*	No incubation	0.3 µg/mL [~90% reduction]	Blue light [450 nm]	14.2 mW/cm^2	8.52 J/cm^2
[107]	Graphene quantum dots	-	*E. coli*	ND	0.5 µg/mL [~100 % reduction]	Femtosecond laser [800 nm]	2.64 mW	264 nJ/pixel
[108]	Cl/nitrogen-doped polymeric graphene quantum dots	-	*E. coli*	1 hour	0.005 µg/mL [MIC]	LED light	35 mW/cm^2	2.1 J/cm^2
	Br/nitrogen-doped polymeric graphene quantum dots	-	*E. coli*	1 hour	0.008 µg/mL [MIC]			

Section 3.2. Inorganic and hybrid materials

Reference	Material	Photosensitizer	Bacteria strains	Pre-treatment incubation time	Photodynamic bactericide concentration	Light source [Wavelength of emission]	Light fluence	Light dose
[108]	Unitrogen-doped polymeric graphene quantum dots	-	*E. coli*	1 hour	0.05 µg/mL [MIC]	LED light	35 mW/cm^2	2.1 J/cm^2
[109]	Graphene quantum dots	**49 MB**	*E. coli*	ND	ND [~99% reduction]	Red LED light [660 nm]	ND	ND
[110]	Graphene quantum dots immobilized in cotton fabrics	**146 TCPP**	*E. coli* ATCC-8099	1 hour	ND [~6 log reduction]	500 W Xenon lamp [> 420 nm]	ND	ND
			P. aeruginosa CMCC (B) 10104	1 hour	ND [~6 log reduction]	500 W Xenon lamp [> 420 nm]		
[112]	Brominated carbon nanodots	-	*E. coli*	ND	0.4 M [~ 4 log reduction]	Entela Blak-Ray Long Wave UV lamp [365 nm]	3 mW	4 J/cm^2
			E. coli	ND	0.4 M [~ 1 log reduction]	White light [572 nm]	ND	300 J/cm^2
[113]	Carbon quantum dots	-	*E. coli* 8099	ND	0.25 mg/mL [> 6 log reduction]	Xenon arc lamp 500 W [> 420 nm]	65 mW/cm^2	234 J/cm^2
			K. pneumoniae ATCC 2146	ND	5 mg/mL [0.95 log reduction[	LC122 PDT light [400 – 700 nm]	ND	ND
			A. baumannii ATCC 1605	ND	1 mg/mL [1.5 log reduction]			
[114]	Carbon quantum dots embedded into electrospun nanofi	-	*E. coli* ATCC 8099	60 minutes	0.6% [> 6 log reduction]	Xenon arc lamp 500 W [> 420 nm]	ND	ND
			P. aeruginosa CMCC (B) 10104	60 minutes	0.6% [> 6 log reduction]			
[116]	Single wall carbon nanotubes	**103 RB**	*E. coli* MCC 2412	3 hours	50 µg/mL [~5.5 log reduction]	50 mW green laser [520 nm]	2.81 mW/cm^2	1674.7 J/cm^2
			E. coli MCC 2412 [biofilm]	3 hours	50 µg/mL [~65% reduction]			
[115]	Multiple wall carbon nanotubes	**49 MB**	*E. coli* MCC 2412	3 hours	50 µg/mL [~4 log reduction]	Red diode laser [670 nm]	325 mW/cm^2	58.49 J/cm^2
			E. coli MCC 2412 [biofilm]	3 hours	50 µg/mL [~65% reduction]			
[117]	Graphene nanoribbons	**153**	*P. aeruginosa* ATCC 27853	ND	50 µg/mL : 40 µM [~ 90% reduction]	[808 nm]	1 W/cm^2	900 J/cm^2
			A. baumannii ATCC 19606	ND	30 µg/mL : 40 µM [~ 90% reduction]	[808 nm]	1 W/cm^2	450 J/cm^2
			E. coli ATCC 2592	ND	30 µg/mL : 40 µM [~ 90% reduction]	[808 nm]	1 W/cm^2	450 J/cm^2
			K. pneumoniae ATCC13883	ND	30 µg/mL : 40 µM [~ 90% reduction]	[808 nm]	1 W/cm^2	450 J/cm^2
[118]	Polyacrylamide-base hydrogel [grafting]	**49 MB**	*E. coli* DH5α pGLITE	ND	ND [~2.25 log reduction]	150 W white light	14.5 mW/cm^2	21.8 J/cm^2

Page intentionally left in blank

III. Formulation of photosensitizers

One approach to improve the bioavailability of photosensitizers in aqueous media, is the formulation of photosensitizers, aiming for a better distribution in aqueous and even solid media. One of the main problems found for photosensitizers, and specially tetrapyrrolic compounds, is their aggregation in water media, which in turn may decrease the triplet-state quantum yield, consequently decreasing the ROS production [19].

The formulation of photosensitizers has been extensively studied in the last two decade. It is important to mention that PDT and PACT applications require different types of formulations. Normally, PDT formulations target tumor and cancer cells, and it is desirable to provide a slow release of the photosensitizer in the desired area [20]. However, PACT formulations aim for wide bioavailability, low dark toxicity, while targeting several types of microorganisms [21].

Formulations aiming for PACT can be divided in two great branches: water-dispersible formulations and coating formulations. Water dispersible formulations aim for the disinfection of aqueous media, as water sources [22], milk and dairy products [23], blood [24], and even for their applications in skin [25] and corporal cavities [16,26]. On the other hand, coating formulations aim to protect, disinfect or control microbial proliferation on surfaces, as personal equipment protection [15] or even food [27].

Latest concerns on the overuse of plastics [28] and their impact in our life and environment had arisen [29], especially after the COVID-19 outbreak, as single-use plastics are widely used as preventive measurements against the disease spread [30]. This current trend to decrease the use of petroleum-derived resources has boost the use of biosourced polymers as drug delivery systems. Several types of formulations had been used for PACT applications, working as delivery systems, but also as synergistic systems that enhance antimicrobial applications.

Publication 2. “Conjugating biomaterials with photosensitizers: Advances and perspectives for photodynamic antimicrobial chemotherapy” [31]

Photochemical & Photobiological Sciences

ROYAL SOCIETY OF CHEMISTRY

PAPER

View Article Online
View Journal | View Issue

Cite this: *Photochem. Photobiol. Sci.*, 2020, **19**, 445

Conjugating biomaterials with photosensitizers: advances and perspectives for photodynamic antimicrobial chemotherapy

Nidia Maldonado-Carmona,[a,b] Tan-Sothea Ouk,[a] Mário J. F. Calvete,[b] Mariette M. Pereira,[b] Nicolas Villandier[a] and Stephanie Leroy-Lhez *[a]

Received 27th September 2019,
Accepted 5th February 2020

DOI: 10.1039/c9pp00398c

rsc.li/pps

Antimicrobial resistance is threatening to overshadow last century's medical advances. Previously eradicated infectious diseases are now resurgent as multi-drug resistant strains, leading to expensive, toxic and, in some cases, ineffective antimicrobial treatments. Given this outlook, researchers are willing to investigate novel antimicrobial treatments that may be able to deal with antimicrobial resistance, namely photodynamic therapy (PDT). PDT relies on the generation of toxic reactive oxygen species (ROS) in the presence of light and a photosensitizer (PS) molecule. PDT has been known for almost a century, but most of its applications have been directed towards the treatment of cancer and topical diseases. Unlike classical antimicrobial chemotherapy treatments, photodynamic antimicrobial chemotherapy (PACT) has a non-target specific mechanism of action, based on the generation of ROS, working against cellular membranes, walls, proteins, lipids and nucleic acids. This non-specific mechanism diminishes the chances of bacteria developing resistance. However, PSs usually are large molecules, prone to aggregation, diminishing their efficiency. This review will report the development of materials obtained from natural sources, as delivery systems for photosensitizing molecules against microorganisms. The present work emphasizes on the biological results rather than on the synthesis routes to prepare the conjugates. Also, it discusses the current state of the art, providing our perspective on the field.

1. Introduction

One of the most serious uprising threats to human health is antimicrobial resistance, in which microorganisms are able to survive a chemotoxic treatment to which they were previously sensitive. The best known examples for antimicrobial resistance are bacteria which, due to their genomic plasticity, are able to easily spread antimicrobial resistance in a short lapse of time.[1]

Since the discovery and development of antibiotics, antimicrobial resistance (AMR) has been present. Indeed, it has been recently found that, previous to the release of ampicillin into the market, several *Salmonella enterica* serotype Typhimurium strains were already resistant to ampicillin.[2] This is associated with the non-clinical use of penicillin as a livestock growth-promotor in the 1950s, a practice that continues to date. All the non-clinical antibiotic (mis)uses have led to an unaware selection and spread of more resistant bacteria over time. This was not immediately addressed as a problem, as during the 1960–1980s the development and discovery of several antibiotics was in vogue.[3] However, at the end of the so-called "golden age", the pipeline of new antibiotics was tightening, leading to a decrease in the discovery rate of more effective antibiotics, while AMR steadily kept the pace[4,5] (Fig. 1).

In more recent years, alarms have sounded as more virulent strains are present in daily life. There is special concern regarding the ESKAPE group of bacteria (*Enterococcus faecium*, *Staphylococcus aureus*, *Klebsiella pneumoniae*, *Acinetobacter baumannii*, *Pseudomonas aeruginosa*, and *Enterobacter* species), which are prevalent as intranosocomial infections and represent a threat to modern medicine, especially to immunosuppressed, cancer and/or transplant patients.[6] The uprise of multidrug resistant bacteria is a step backwards to human health, as bacteria previously defeated are coming back, as the exemplifying case of extensively drug resistant tuberculosis, nowadays clinically untreatable.[7] Furthermore, AMR also involves fungi[8] and parasites,[9] both resulting in massive economical losses. It is estimated that, if AMR is continuously neglected, the cost of inaction by 2050 would be the astounding sum of 100 trillion USD, and around 10 million deaths every year.[10] As

[a]*University of Limoges, Laboratory PEIRENE, 87060 Limoges CEDEX, France. E-mail: stephanie.lhez@unilim.fr*
[b]*Department of Chemistry, University of Coimbra, Rua Larga 3004-535, Coimbra, Portugal*

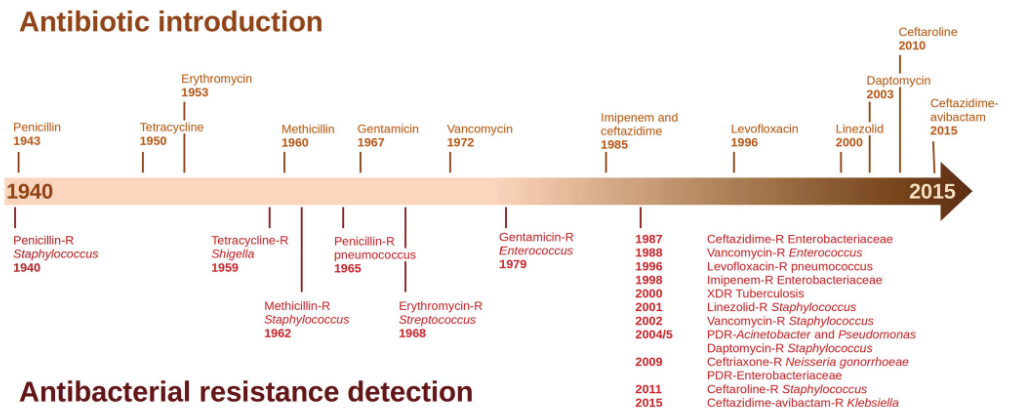

Fig. 1 Schematic illustration of the nearly concurrent detection of AMR shortly after antimicrobial therapy development.[5]

a consequence, the WHO (World Health Organization) has issued several recommendations,[11] including to seek for new treatments with low resistance development and sanitation as a measure to prevent further infections.[10,11] This modern health challenge is addressed by several research groups.

Photodynamic antimicrobial chemotherapy: a light at the end of the tunnel

Photodynamic therapy (PDT) can be briefly described as the light excitation of a nontoxic chromophore (PS) that forms a long-lived excited triplet state (^{3}PS*). ^{3}PS* can in turn interact with surrounding molecules, generally with molecular oxygen, to generate highly reactive and cytotoxic reactive oxygen species (ROS), such as hydroxyl radicals and singlet oxygen. There are two mechanisms that permit ROS formation.[12] The Type I mechanism involves photoinduced electron transfer between a substrate and ^{3}PS*, generating radical ions that easily react with oxygen, and in turn will generate ROS such as superoxide anions or hydroxyl radicals. In addition, the Type II mechanism involves photoinduced triplet–triplet energy transfer between molecular oxygen and ^{3}PS*, generating a singlet oxygen molecule, which readily reacts with other substrates producing ROS.[13]

PDT has been developed since the beginning of the XXth century, mainly against cancer cells.[14–16] Up to 2018, 7 photosensitizers had been approved for their clinical usage for anticancer therapy. Furthermore, new photosensitizers are currently under clinical trial, mainly against cancer, *e.g.* redaporfin for head and neck cancer,[17] but photosensitizers are also investigated for other applications, such as Photrex as a treatment against age-related macular degeneration, and Fotosan as a disinfection agent on carious lesions.[18,19] PDT and cancer are not the purpose of this review but for further scope of its current state, several reviews have been recently written.[20,21]

As previously stated, AMR is a huge health concern for governments and scientists. One of the main reasons that enables microorganisms to easily overcome antimicrobials is antimicrobial specificity. Most antimicrobials have specific molecular mechanisms, *e.g.* β-lactam antibiotics inhibit cell wall synthesis, while aminoglucosides interfere with protein synthesis.[22] Small changes in the bacterial targets increase the resistance against antimicrobials; thus, antimicrobial treatments with non-specific targets are more difficult for the bacteria to overcome. Photodynamic antimicrobial chemotherapy (PACT)[23] relies on the same principles mentioned for PDT, but is focused on microorganisms. Singlet oxygen and/or other ROS species, generated by PACT mechanisms, are able to oxidize sensitive biomacromolecules, such as proteins, DNA, RNA, lipids and other cellular components (Fig. 2).

This is particularly pernicious for bacteria, as, unlike eukaryotic cells, their DNA is not separated from the cytoplasm. Also, as PACT needs the simultaneous use of three

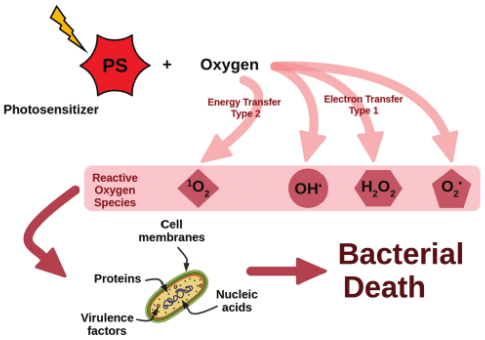

Fig. 2 Schematic representation of the PACT mechanism.

components (PS, light and oxygen), the chemotoxic stimuli can only be intentionally provoked and then selection and resistance can only be driven under controlled and desired circumstances.[24] In addition, there is evidence that suggests that PACT exacerbates the innate immunological response, acting as an immunomodulator by recruiting neutrophils and prolonging the antimicrobial effect of PACT.[25]

Although promising, PDT and PACT need photosensitizers with particular characteristics such as: (a) water-solubility, (b) optimal photophysical properties, (c) minimal side effects, (d) no aggregation, (e) high triplet state formation yield, (f) resistance to photobleaching and (g) small size for membrane permeation.[12] Also, for PDT, it is desirable that the PS molecules have strong absorption between 600 and 800 nm, which is the optical window where tissues are more transparent to a deep penetration of light. However, since PACT is intended for external light exposition, the optical window that can be used is increased and so does the variety of photosensitizers used. Most of the PSs have an aromatic core and mainly are tetrapyrrolic compounds, such as porphyrins, porphins, bacteriochlorins, phthalocyanins, porphycens, *etc*.[13,26] Nevertheless, these suitable properties are often counterbalanced by their inherent low solubility or high aggregation tendency, which is deleterious for a good therapeutic antimicrobial effect, as recently demonstrated.[27]

Conjugates and biomaterials

To address the low water-solubility and PS aggregation issue, several types of formulations have been designed, including nanoparticles, nanofibers, films and suspensions. For this purpose, several raw materials have been used as suitable conjugates for PSs. However, some inorganic materials, although widely used, seem to have negative properties when used on *in vivo* systems. As an example, carbon-based nanoparticles have demonstrated platelet aggregation and vascular thrombosis, while 10 nm silver nanoparticles demonstrated acute toxicity *in vivo*.[28,29] Given the high fabrication costs and side effects of many inorganic composites, biopolymeric conjugates have appeared as relevant alternatives. Most biopolymers are composed of carbohydrates, such as cellulose, cyclodextrin, alginate and chitosan, but there are other materials which do not have sugar on their backbones, such as lignin, poly(3-hydroxybutyrate) and polylactic acid (Fig. 3). One attractive feature of these materials is their wide availability and low cost, as usually they are renewable by-products from agriculture and forestry feedstock.[30] Furthermore, as they are natural compounds, they are easily degraded and non-harmful for therapeutic, biologic and environmental purposes. Also, one of the advantages of using biomaterials is their diluting effect. Indeed, grafting molecules to a material backbone decreases the risk of intramolecular interactions and thus aggregation, potentiating their biological activity.[31]

In recent years, some reviews have been written about the use of conjugates for PDT purposes. Mesquita and collaborators have recently reviewed the synthesis of several conjugates for PACT.[32] Meanwhile, Almeida-Marrero and collaborators wrote a review about conjugates with biopolymers for PDT.[33] Therefore, this present review aims to focus on the biological significance of biopolymeric conjugates, targeted as PACT agents.

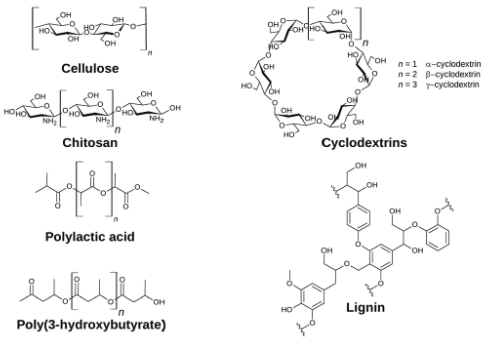

Fig. 3 Chemical structures of different biomaterials used as drug carriers for PACT.

2. Cellulose based conjugates

Cellulose is a natural polysaccharide and it is the major structural compound in plants, mainly found in wood pulp. It is constituted of a linear chain of several hundred to many thousands of β(1 → 4) linked D-glucose units, with a large amount of hydroxyl groups available. Although linear, the presence of hydroxyl groups permits H-bond formation, giving cellulose a fibroid-like shape that confers physical resistance and interesting physical–chemical properties.[34] Also, the abundance of hydroxyl groups enables chemical modifications that give rise to different materials. These properties permit cellulose to be addressed as an alternative raw material for different PS formulations.

Cellulose films

Films have been designed as covers for surfaces when developing self-sterilizing surfaces for PACT. It has been, for example, previously demonstrated that PS entrapped inside films could retain their antimicrobial activity.

Classic PSs, Rose Bengal (RB) and toluidine blue-O (TBO) have been conjugated in a cellulose acetate film, with excellent results against the Gram negative bacterium *Escherichia coli* (eradication 99.6000%) but also against *S. aureus* (99.6000%), methicillin resistant *S. aureus* (MRSA) (100.0000%), *Clostridium difficile* (100.0000%), *Candida albicans* (88.0000%) and even against the bacteriophage ΦX174 (91.0000%). This result is remarkable, as no dark toxicity is observed and the light conditions are those found at hospitals (fluorescent white light, 3700 lx), fulfilling the purpose of self-sterilizing covers under non-special conditions (Fig. 4).[35]

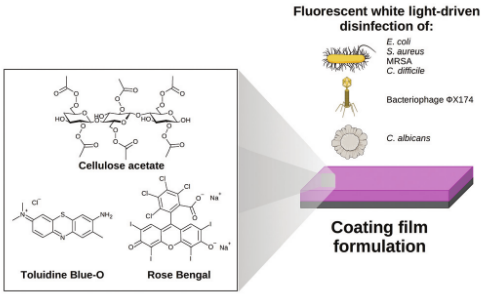

Fig. 4 A coating film formulation was developed with two commonly used photosensitizers, being able to eradicate different kinds of organisms.[35]

Another interesting example of a composite is cellulose laurate. Krausz and co-workers have indeed covalently attached to the hydroxyl moieties of this modified cellulose two different porphyrins, one among them is the natural and endogenous protoporphyrin IX (PpIX), obtaining a plastic and lipophilic film. Indeed, PpIX is an endogenous photosensitizer that is omnipresent in most living cells. It has been used as a PDT agent against cancers due to its lipophilic character and accumulation in tumorous tissues.[36] These violet films were tested against *E. coli* and *S. aureus* bacteria under Tungsten bulb irradiation (146.88 J cm^{-2}), with good phototoxicity and low dark toxicity. The results demonstrated an almost complete eradication. For this work, the authors discussed that the good results obtained could be due to steric hindrance provoked by the cellulose laurate, which permitted a better distribution of the PS on the films, avoiding aggregation.[37,38]

Cellulose fibers

Cellulose fibers, whether as fabrics or as paper sheets incorporating PACT photosensitizers, would also represent an advantage in nosocomial environments, protecting patients and health care providers from pathogenic bacteria.

This approach has been widely studied by the Krausz and Sol research team. The authors developed several porphyrins, with a neutral, cationic or anionic nature, comparing their antibacterial effectiveness when grafted onto cellulosic nanofiber fabric. The results indicated that the grafted fabrics were only effective against *S. aureus* (eradication of 93.7000%), meanwhile *E. coli* remained unaffected by the photodynamic treatment (white LED light, 9.5 J cm^{-2}), regardless of the porphyrin nature (Fig. 5).[39,40] Through a similar approach, the same research group grafted a cationic porphyrin on cellulose fibers, intending to form paper sheets. These paper sheets demonstrated the capacity to eradicate *S. aureus* and *E. coli* up to 100.0000%, under the same light conditions.[41] Later, they also successfully eradicated *S. aureus* and *P. aeruginosa* 100.0000% when they grafted a neutral porphyrin onto lignocellulosic fibers and exposed them to similar light conditions.[42]

This approach was also followed by another research group, wherein porphyrin and boron-dipyrromethene derivatives (BODIPY) were grafted to cellulose fibers, producing paper sheets that were tested against several bacteria and viruses.[43] The porphyrins tested had different ionic charges, being cationic, neutral and anionic. Meanwhile, the BODIPY derivatives were either unsubstituted or substituted with iodine. These materials were all tested under a non-coherent light source (118 J cm^{-2}). The obtained results indicated that the most effective microbial reduction was found with the cationic porphyrin, which nicely correlates to a similar grafting on cellulose nanocrystals[44,45] (*vide infra*). Also, they found a significant decrease of bacterial survival with the paper sheets grafted with the iodine BODIPY derivative. The effectiveness trend of the treatments was found to be cationic porphyrin > iodine substituted BODIPY > unsubstituted BODIPY. However, the anionic and neutral porphyrins did not exert any significant effect.[43] As a more recent example, this research group grafted a cationic porphyrin (Por^{+}) and a zinc-substituted cat-

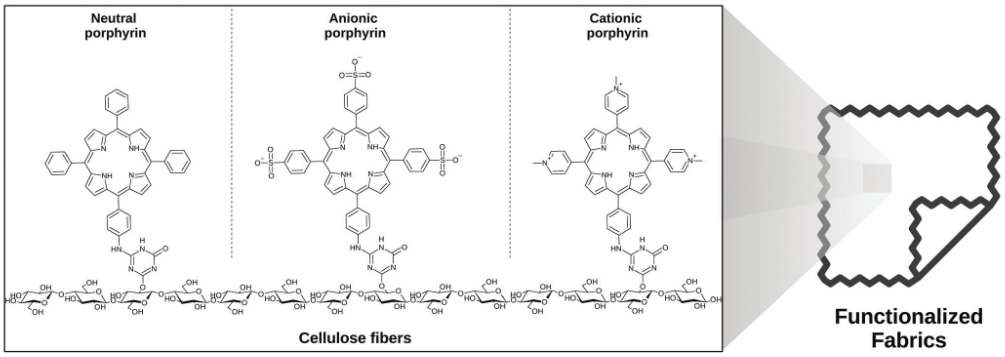

Fig. 5 Grafting of different porphyrins onto cellulosic fibers, developing functionalized fabrics.

ionic porphyrin (Zn-Por^{+}) onto two kinds of cellulose fibers: nanofibrillated cellulose (NFC) and cellulose paper (Pap). The NFC conjugates were finely ground and could be dispersed in aqueous solution and were able to eradicate multidrug-resistant *A. baumannii* (>99.9900% eradication), MRSA (99.9999% eradication) and vancomycin-resistant *E. faecium* (99.9999% eradication), under a 400–700 nm light source and around 234 J cm^{-2}. Also, under similar light conditions the NFC conjugates completely eradicated dengue-1 and vesicular stomatitis viruses, displaying a wide range activity against bacteria and viruses. Furthermore, the grafted porphyrins onto paper were also able to completely eradicate the same bacteria under the same light conditions.[46]

In some recent approaches, PpIX was used as a photosensitizer when grafted onto different cellulosic backbones. In a first report, zinc PpIX was grafted onto regenerated cellulose nanofibers, which were later pressed in the shape of a thin film. This formulation allowed a greater loading capacity (412 nmol mg^{-1}) when compared with previous studies on cellulose fibers (12.4 nmol mg^{-1})[43] and cellulose nanocrystals (160 nmol mg^{-1}).[45] These materials were tested under a Xenon lamp, with a fluence of 500 W for 30 minutes, against *S. aureus* and *E. coli.* A bacterial eradication of 99.9990% for *S. aureus* and 99.0000% for *E. coli* was found. Also, the antibacterial effect was not diminished after 5 hours of light under the same experimental conditions, providing evidence of increased photostability, which is of upmost importance in PACT.[47] In the second approach, PpIX was grafted on a bacterial cellulose nanofiber surface.[48] Bacterial cellulose is a biomaterial that is produced by *Acetobacter xylinum*, which represents a biocompatible and renewable biopolymer that can be easily modified and scaled up. PpIX was grafted to it through an amine spacer with different chain lengths (4, 10 and 14 atoms) to elucidate the differences of antimicrobial activity depending on this parameter. Interestingly, it was found that PpIX grafted onto bacterial cellulose through a 10 atom linker provided the best efficiency, when exposed to a Xenon lamp with a fluence of 500 W for 30 minutes. Also, in this configuration, it was more effective against *E. coli* (99.9990%) than against *S. aureus* (98.5000%), an interesting result, as usually it is observed that Gram positive bacteria are more sensitive than Gram negative ones. This result was supported by singlet oxygen generation, where the most efficient producer of singlet oxygen is also the conjugate bearing the 10 atom spacer.[48] These results were complementary to a third approach where PpIX was grafted onto cotton cellulosic fabrics. These materials allowed to reach an approximated 99.9% of bacterial annihilation for *S. aureus*, meanwhile only ~90.0000% for *E. coli*, when exposed to white light irradiation (9.5 J cm^{-2}).[49] The differences between these results help to remark the importance of a suitable conjugated matrix to deliver the photosensitizer and achieve improved results in PACT.

Some researchers had proposed that the use of several mechanisms of action at the same time diminishes the chance of bacterial antibiotic resistance, and may eventually restore the sensitivity of drug resistant strains.[50] Thus, some studies report the application of PACT in conjunction with another proved antibacterial treatment. In a recent example, Zn(II)-β-carboxy phthalocyanine (CPZ) was covalently attached to ε-polylysine (EPL), a cationic antimicrobial agent, previously coated onto a cellulose fabric. These fabrics were then tested against *E. coli*, *S. aureus* and MRSA under red light irradiation (90 J cm^{-2}). Under these conditions, it was demonstrated that a high antibacterial capacity was able to eradicate bacteria up to 99.0000%, 98.0000% and 99.0000%, respectively. Interestingly, these results are only found in the case of the CPZ–EPL conjugated material, as cellulose and EPL or cellulose and CPZ were only able to kill ~80% of bacteria, proving the synergistic effect of the conjugation of two different systems with different mechanisms of action.[51]

Although most PACT studies are related to porphyrins and phthalocyanines as photosensitizers, there are some remarkable exceptions that need to be taken in account. As an example, Zhuo and collaborators used two anthraquinone dye-like compounds, which were easily attached to cotton fibers through commercially available dyeing processes. These materials were tested against *E. coli* and *S. aureus* and irradiated with UVA light (108 J cm^{-2}). The results demonstrated excellent bacterial eradication, with 99.9000% of dead bacteria. It is important to remark that this dose of UVA light by itself was unable to reduce the bacterial population. Also, the antibacterial effect is maintained even after 5 washes. A slight diminishment was observed only after 10 washes, evidence that those materials were effective and resistant enough to be used as potential antibacterial and reusable clothes.[52] In another remarkable example, anthraquinone 2-carboxylic acid (AQ-COOH) and titanium oxide (TiO_2) were grafted onto cotton fabrics through a common industrial process used for dyeing fabrics. These grafted cotton fabrics (TiO_2/AQ-COOH) were tested against *Pseudomonas fluorescens* under UVA and white light irradiation and were able to diminish the bacterial count by 99.9000% and 99.9900%, respectively. In addition, the authors also compared the antibacterial effect of fibers containing exclusively one component (TiO_2 or AQ-COOH) and no bacterial depletion was found, thus, the pair TiO_2/AQ-COOH is needed to achieve the desired antibacterial effect.[53]

Cellulose nanocrystals

Cellulose nanocrystals (CNC) are obtained from the acid hydrolysis of cellulose fibers, which results in defect-free, rod-like crystals.[54] Due to their high molecular strength and chemically modifiable surface, CNC have been targeted for the development of delivery systems.

As mentioned above, the development of a dual antimicrobial therapy appeared to be a strategy to avoid antimicrobial resistance. Le Guern *et al.*, for example, have developed a CNC conjugated with chlorin e6 (Ce6) and the antimicrobial peptide polymyxin B. This conjugate was tested against *S. aureus*, *Staphylococcus epidermidis*, *E. coli* and *P. aeruginosa* under white LED light irradiation (43.2 J cm^{-2}). The conjugate completely eradicated the three bacterial strains. The approach is especially interesting as it provided a

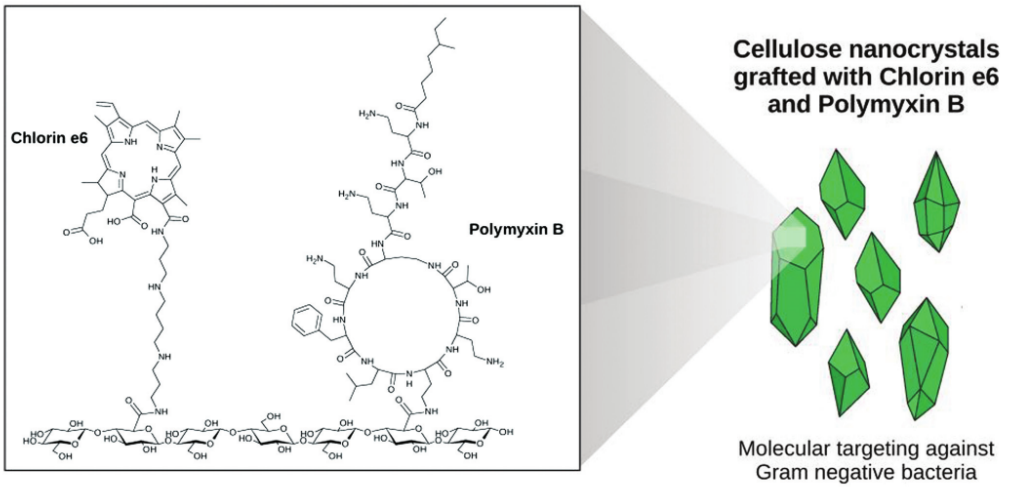

Fig. 6 Cellulose nanocrystals grafted with Chlorin e6 and Polymyxin B demonstrated their effectivity against Gram negative bacteria, due to the molecular targeting provided by Polymyxin B.

targeting PACT system towards Gram negative bacteria as polymyxin B is a well-known Gram negative-targeted compound (Fig. 6).[55]

Another relevant example was described by the Ghiladi research group, who grafted cellulose nanocrystals with cationic zinc-porphyrin (TMPyP) through a click-chemistry approach. The nanocrystals obtained so far were tested against several bacteria, as *E. coli*, *S. aureus*, MRSA, *A. baumannii*, multidrug resistant *A. baumannii* and against *Mycobacterium smegmatis*, under white light illumination (108 J cm^{-2}). In this work, the incubation time prior light exposure was also evaluated, finding it to be crucial for proper bacterial eradication against *P. aeruginosa*. As an example, the survival of *P. aeruginosa* drops from ~40% to 0.1% by increasing the dark incubation time from 5 to 60 minutes.[44,45] The incubation time before light irradiation is an important parameter, as it has been described that bacterial uptake happens quickly, mainly through electrostatic binding and passive diffusion. Meanwhile, mammalian cells uptake PS molecules through endocytosis, which is a slow process that can take several hours. Thus, incubating for a prolonged time may harm mammalian cells rather than bacterial cells in a complex environment.[56]

A different advancement has been developed through the design of two cationic phthalocyanines (Pc^+) and its non-covalent attachment to CNC. The conjugated Pc^+-CNC were tested against *E. coli*, *S. aureus* and *C. albicans*, under red light irradiation (64 J cm^{-2}). The composite Pc^+-CNC was able to efficiently eradicate the microorganisms tested. Also it was evidenced that the Pc^+-CNC was more effective than the non conjugated Pc^+. The authors addressed this improvement as a result of diminished aggregation of the Pc^+ compounds when attached to the cellulose backbone.[57]

Soluble-cellulose conjugates

Several authors have described that the modification of the conjugating materials is almost as relevant as the chemical nature of the photosensitizer that has been grafted on it. For example, recently Jia *et al.* developed a material with both a photosensitizer (PpIX) and a cationic group (γ-butyrobetaine hydrochloride) grafted on microcrystalline cellulose (Fig. 7). This conjugated material prevented the aggregation of the photosensitizer and was water-soluble, promising a highly efficient conjugate for PACT. Indeed, this formulation was shown to be capable to efficiently eradicate *E. coli* and *S. aureus* after 3 minutes of exposure, whether under sunlight or weak light exposure (7.2 J cm^{-2}). More importantly, this approach was tested as a spray for covering surfaces, such as masks, gloves and clothing, eradicating up to 99.9000% of *E. coli* and *S. aureus* under sunlight.[31]

3. Cyclodextrin materials

Cyclodextrins (CDs) are a family of cyclic oligosaccharides, obtained from the enzymatic degradation of starch by the cycloamylose glucanotransferase, found in bacteria such as *Bacillus macerans*. These molecules are formed by 6, 7 or 8 glucopyranose monomers linked by α-1,4 bonds, forming α-, β- and γ-cyclodextrins, respectively. The cyclic form of CD generates a three-dimensional toroid, with the hydroxyl groups being outside the inner macrocycle. Thus, the inner macro-

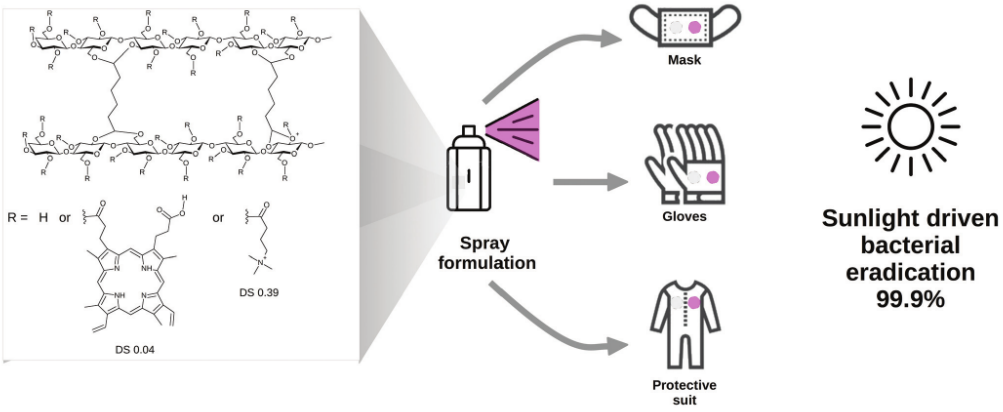

Fig. 7 A remarkable example of cellulose as a vehicle. In this example, PpIX and γ-butyrobetaine hydrochloride were grafted on microcrystalline cellulose.[31]

cycle has a lipophilic microenvironment, where non-polar molecules can be entrapped (Fig. 8). In addition to these naturally found cyclodextrins, different modified CD materials have been developed, increasing the potential of CD as drug vehicles.[58,59] The low toxicity and good biocompatibility of CD makes them excellent conjugating materials for PSs in PACT application.[60] Therefore, in the present review, several recent examples of CD as vehicles for PSs are described below.

Although less threatening than antibacterial resistance, antifungal resistance is a real danger to world health. An interesting approach addressed this problem through the encapsulation of a fluconazole-porphyrin (F-Por) conjugate in a β-cyclodextrin βCD solution, intended to work as a double mechanism of the action conjugate. This system (F-Por/βCD) was tested under light irradiation (white light, 90 mW cm^{-2}) and it was able to arrest the growth of fresh cells of *C. albicans*. However, a better effect was observed when the porphyrin and fluconazole were not covalently linked, but still used βCD as a nano carrier for the non-water soluble PS. This unexpected result underlined that the attachment between the PS and the fungicide is not necessary to achieve a good result for this conjugate. This can be positively addressed, as it allows the use of two complementary therapies (fluconazole and PACT) without numerous and tedious synthesis steps.[62]

Natural compounds have always been in the spotlight of antimicrobial research. Curcumin, extracted from *Curcuma longa*, is a polyphenolic compound that has been used as a good photosensitizer for PDT.[63,64] However, its high lipophilic nature makes it necessary to develop vehicles for non-water soluble PSs. The Tønnesen research group has made some

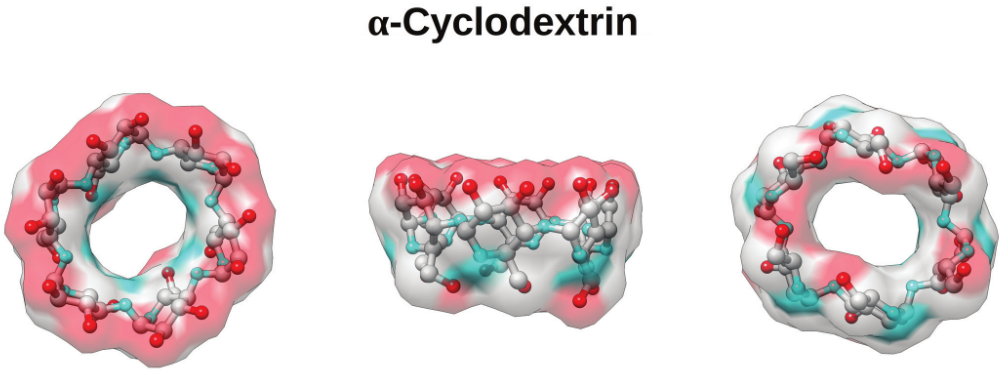

Fig. 8 Tridimensional structure of α-cyclodextrin with its surface. The hydroxyl groups are depicted in red; ether groups in blue; carbon groups in gray. The crystalline structure was obtained from an experimental crystal structure.[61]

interesting advances in this subject, through the formulation of PS conjugates with CD derivatives. They developed lyophilized solutions of curcumin with methyl-β-cyclodextrin as a vehicle, and a mixture of different biopolymers (hydroxypropyl methyl cellulose or hyaluronic acid) to stabilize and favor the lyophilization. The lyophilized powders demonstrated a high hydration and recovery capacity, as well as a high antimicrobial capacity against *Enterococcus faecalis* and *E. coli*. In the case of the Gram positive bacteria, as little as 0.5 μM was enough to completely eradicate bacteria under blue light irradiation (32 J cm^{-2}).[65] Also, through a formulation with hydroxypropyl-β-cyclodextrin (HPβCD), they achieve a supersaturated solution which completely eradicated *E. coli* under similar light conditions.[66] However, no difference was observed between the ethanolic curcumin solution and the CD formulations containing curcumin, when comparing their antibacterial efficiencies. Still, the authors demonstrated the thermostability, photostability and easiness of solubilization of the CD conjugate, which represents an advantage when compared to the ethanolic curcumin solution. Also, through a lyophilized formulation, solvent usage is avoided.[65,66]

Through a different approach, HPβCD was covalently bound to polypropylene fibers (PP), yielding a fabric with a potential low-elution activity. 5,10,15,20-Tetrakis(4-sulfonatophenyl)-21*H*,23*H*-porphine (TPPS), an anionic porphyrin, was encapsulated on the PP/HPβCD conjugate. Then, the material was characterized, focusing on its potential controlled release of porphyrin. The results showed that TPPS was slowly released in aqueous media. Also, this material was able to kill 99.9800% of *S. aureus* cells, but was unable to diminish the bacterial population of *P. aeruginosa*, under halogen lamp irradiation (5 J cm^{-2}).[67]

Recently, a Ce6 photosensitizer grafted on a α-cyclodextrin (αCD) was used to encapsulate polyethylene glycol 1000 (PEG) bound to the antimicrobial peptide Magainin I (M1). The whole supraconjugate αCD–Ce6/PEG-M1 (Fig. 9) enabled the formation of a micelle-like structure, with M1 facing outwards, thus allowing specific bacterial targeting. Micelles were able to kill and destroy bacterial biofilms of *P. aeruginosa* and MRSA above 99.9999%, under laser irradiation (660 nm). This result was rather interesting, as bacterial biofilms are known to be particularly difficult to eradicate. Moreover, under similar conditions, the micelles were unable to kill NIH3T3 cells or human umbilical vein endothelial cells (HUVEC), resulting in less toxicity than the αCD–Ce6 conjugate. The results of this research were promising against bacterial biofilms and similar targeted approaches would be beneficial for human health.[68]

Similarly, delivery systems have been developed for RB. Indeed, even as RB is a well-known PS, it is rarely used without a conjugating system, due to the intrinsic low intracellular uptake ability of RB. However, there is a described decrease in RB's singlet oxygen production when the molecule is covalently attached to another macromolecule. In order to avoid this, RB has been recently encapsulated in αCD. The conjugate was evaluated against *Streptococcus mutans*, a bacterial strain commonly found in teeth, with a total eradication of the bacterial population after a brief time of blue light irradiation (3.5 J cm^{-2}). Also, in order to achieve total eradication, RB alone required a concentration 32 times higher than the conjugate RB/αCD (2 μM and 0.062 μM, respectively).[69]

4. Chitosan materials

Chitosan is the de-acetylated derivative of chitin, one of the most abundant biopolymers in nature and the most abundant amino-polysaccharide polymer. Chitin is usually found on the exoskeleton of insects, crustaceans and also on the cell wall of fungi. Normally, chitin is obtained as a waste from the food industry, from shrimp and crab shells, a renewable resource. Chitosan is a polycationic linear chain of *N*-acetyl-D-glucosamine and β-1,4-linked D-glucosamine, containing multiple hydroxyl and amine moieties, allowing several chemical modifications and grafting of photosensitizers. Therefore, chitosan is often used as a drug carrier, particularly for PACT, as its own antibacterial activity has been described.[70]

There are two different approaches described with chitosan in the literature: solubilized chitosan formulations or macro-

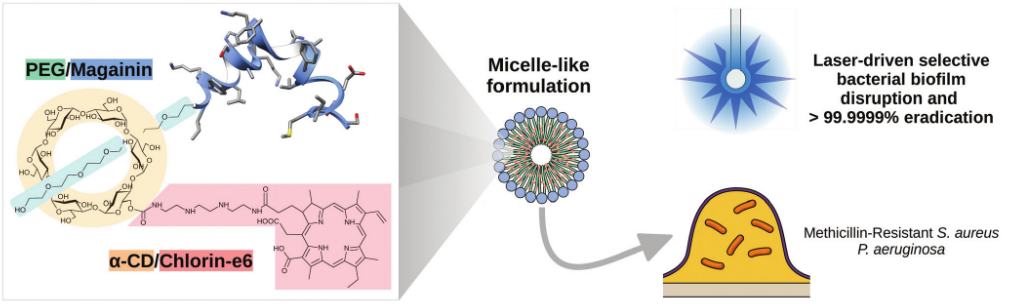

Fig. 9 The supramolecular conjugate αCD–Ce6/PEG-M1. Micelle-like structures were formed and tested against *P. aeruginosa* and MRSA, eradicating both bacteria.[68]

molecular chitosan formulations. Some relevant examples for both are shown below.

Soluble chitosan formulations

Fundamental research on the usage of chitosan for PACT applications was made by Tsai and collaborators in 2011. They tested two PSs, hematoporphyrin micelles and toluidine blue O (TBO), under white LED light irradiation (20 J cm^{-2}). They described that the addition of chitosan (0.25%) before or after PACT increases the bacterial death at least 1000 times, being able to eradicate several strains of both Gram positive and negative bacteria.[71] This finding was also replicated on *C. albicans*, where an increase in the antimicrobial and antibiofilm effect of TBO was observed when chitosan was added to the medium in a similar fashion.[72] After this groundbreaking discovery, chitosan nanoparticles charged with erythrosine were designed and tested against *S. mutans*, *P. aeruginosa* and *C. albicans*. In accordance to the previous results, the PACT effect was enhanced in the presence of chitosan in planktonic cells or in bacterial biofilms.[73] Later, they proved that the addition of chitosan to the treatment inhibited cell recovery after PACT. Apparently chitosan synergic behavior was probably related to cell wall disruption, due to the chitosan cationic charges.[74]

During the same period, different approaches have been developed. A formulation of methylene blue (MB) complimented with chitosan was able to kill *Helicobacter pylori* through the rupture of its cell membrane and further DNA damage after irradiation with white light (7.5 J cm^{-2}) (Fig. 10).[75] This group also exhibited an increase in antibacterial activity against *C. difficile*, a pernicious and resilient gastric bacterium, using a combination of tetracycline and chitosan. Although tetracycline *per se* is an antibiotic, it can also behave as a PS when activated with UVA light (2.5 mW). The concomitant treatment of tetracycline, chitosan and UVA successfully diminished bacterial survival up to 1000 times when compared with the treatment using only light or tetracycline.[76]

Although most of the examples of the usage of chitosan have been done *in vitro*, some remarkable examples should be emphasized. As an example, in an *ex vivo* approach, chitosan and MB were tested against *E. faecalis* in human teeth root canals irradiated with red light (100 mW). It was observed that concomitant treatment is more effective than the individual treatments and single light irradiation. Therefore, these results open up the scope for *in vivo* approximations.[77]

Macromolecular chitosan formulations

Several formulations, including chitosan in the shape of nanoparticles and films, are also available in the literature. Particularly, Kishen's research team had focused on chitosan nanoparticle formulations devised for dental usage. They have successfully tested chitosan nanoparticles with rose bengal (CsRB) against *E. faecalis* and *P. aeruginosa*,[78] *E. faecalis* biofilm,[79] and against a multispecies biofilm.[80] Besides, they also created a cross-link conjugate between chitosan and rose bengal against *E. faecalis* planktonic cells.[81] All these tests were done under similar irradiation conditions, with red light at a fluence of 40 J cm^{-2}.

Also, this research team focused on the *in vivo* difficulties of PACT implementation. They evaluated the interference of the oral cavity tissue components with CsRB, finding different efficiencies as those found in *in vitro* experiments.[82] Besides, they analyzed the efficiency of PACT to destroy *Clostridium histolyticum* collagenase, a virulence factor which facilitates bacterial colonization, finding that CsRB were able to destroy and inhibit bacterial colonization.[83] Nevertheless, the CsRB conjugate was also able to destroy endotoxins and lipopolysaccharides from *P. aeruginosa*, which would diminish the virulence of bacteria. At the same time, CsRB have shown no toxicity against macrophages, demonstrating the safety for *in vivo* treatments.[84]

Another approach against oral cavity infections was achieved with chitosan nanoparticles loaded with the dye indocyanine green (CNP/ICG). As a first approach, CNP/ICG were irradiated with a laser (805 nm, 20 W) and demonstrated good bacterial capacity to kill *Porphyromonas gingivalis*, pathogenic bacteria associated with periodontitis, the infection of the supporting tissue of teeth. Also, they demonstrated that CNP/ICG was able to attach to *P. gingivalis* and other periodontal pathogens, such as *Aggregatibacter actinomycetemcomitans*

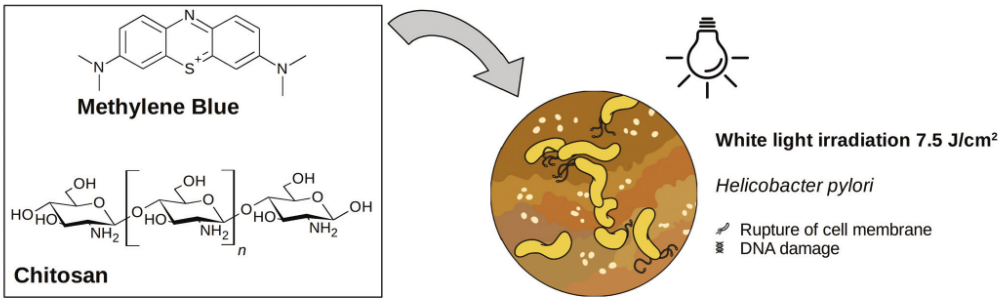

Fig. 10 A soluble formulation of chitosan and MB was formulated for the eradication of *H. pylori*.

and *Fusobacterium nucleatum.*[85] In a more recent study, CNP/ICG was tested against *A. actinomycetemcomitans* and the treatment diminished the viability, bacterial metabolism and biofilm generation. The diminishment of biofilm generation was found to be a consequence of a diminished expression of *fieF*, a gene encoding a virulence factor necessary for biofilm formation. Besides, CNP/ICG has low toxicity on human gingival fibroblast cells under the working conditions. Thus, CNP/ICG may represent a promising *in vivo* treatment against periodontitis.[86]

Another research analyzed the concomitant effect of chitosan nanoparticles and MB. For that purpose, sub-lethal concentrations of both components were tested against *S. aureus*, *P. aeruginosa*, MRSA and multidrug resistant *P. aeruginosa* under laser irradiation (650 nm, 22.93 J cm^{-2}). The authors concluded that the concomitant treatment yielded better results than the chitosan and MB separately. In addition, they also observed low toxicity on human fibroblast cells under the working conditions.[87]

Through another approach, chitosan films were prepared with four different *meta*-substituted porphyrins entrapped in them. The films diminished bacteria survival under white light irradiation (864 J cm^{-2}) and demonstrated a good capacity to inhibit *Listeria inocua* biofilm formation, a model for the pathogenic bacteria *Listeria monocytogenes.* Moreover, the chitosan films were less prone to bacterial attachment than the glass slide control. If bacteria are unable to attach to the surface, they cannot start surface colonization and further biofilm formation. Thus, chitosan films improve the protection of surface coatings through avoidance of the formation of biofilms.[88]

PDT has also been used in other fields, such as agriculture and the food industry, especially for foodborne decontamination. As a good example, a formulation of chlorophyllin and chitosan was used on strawberries as a film coating.[89] Both chitosan and chlorophyllin are FDA (Food and Drug Administration) approved alimentary supplements. The coated strawberries were edible and, when exposed to blue light irradiation (38 J cm^{-2}), demonstrated the total eradication of *S. enterica* serovar *Typhimurium*, a pathogen usually found in strawberries and a pathogenic agent of enterogastritis. Besides, the coating diminished the presence of naturally found molds and yeasts, increasing the shelf life of strawberries (Fig. 11).

Very recently, Sun *et al.* reported a study on carboxymethyl chitosan (CMC) nanoparticles loaded with ammonium methylbenzene blue (a 4,8-bis(2-sulfo-*p*-toluidino)-1,5-dihydroxyanthraquinone; AMB) as a PS. These nanoparticles (CMC-AMB) demonstrated a pH responsive release of the AMB, releasing it mostly under acidic pH. Later, these nanoparticles were tested against *S. aureus*, MRSA, *E. coli* and *P. aeruginosa*, being able to eradicate them under laser irradiance (650 nm, 60.6 J cm^{-2}), either as planktonic cells or as biofilms. They also extended the studies and through an *in vivo* rabbit model approach, the researchers observed a significant reduction of *S. aureus* infection.[90]

5. Other biomaterials

Although there are plenty of biomaterials surrounding us, not all of them have been used in the pharmaceutical industry. Therefore, the use of biomaterials on narrow topics like PACT is even less common and it is mandatory that future research involves the use of these biomaterials. Below, we present some non-traditional biomaterials as supports for photosensitizers to be used in PACT systems, as well as some relevant examples available in the literature.

Nucleic acid aptamers

Aptamers (Apt) are single-strand nucleic acid molecules which spontaneously bend into secondary and tertiary structures. These tridimensional structures bind to molecular targets with high affinity, and thus, aptamers are known as "chemical antibodies". However, unlike antibodies, their production is easier and they can easily be subject to chemical modifications, in order to attach drugs and further functionalize the molecule. Also, aptamers are heat resistant and, even if they go through a denaturation process, they easily recover their functional shape.[91] As aptamers can recognize and attach to a defined

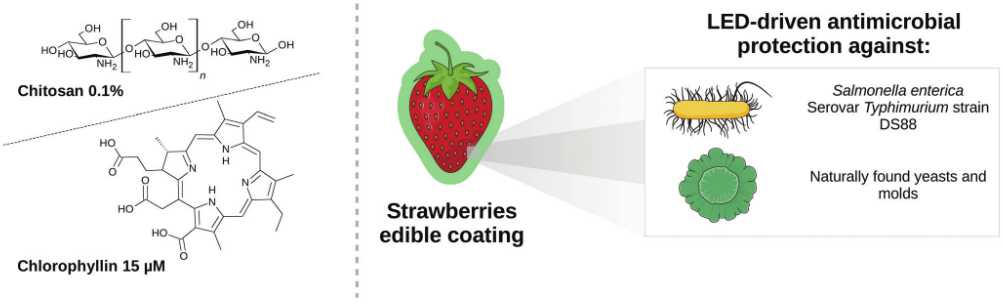

Fig. 11 Chitosan and chlorophyllin on a coating formulation to extend the shelf-life of strawberries.

molecular target, they can behave as targeted drug vehicles. A conjugate system that exploits aptamers for PACT was recently developed. This system is based on iron oxide magnetic nanoparticles, functionalized with Ce6 and with species-identifiable aptamers (Fe_3O_4-Ce6-Apt), which had specific affinity for *E. coli* and *S. aureus*. With this bioconjugate, it was possible to enrich, detect, quantify and eliminate bacterial contamination in blood samples, without side effects observed in the red blood cells. These nanoparticles are likely to be used for early sepsis diagnosis, overcoming the standard method. Sepsis diagnosis usually takes around 2 days to achieve a confident diagnosis, however with Fe_3O_4-Ce6-Apt after 4 hours this same result can be achieved (Fig. 12).[92]

Exopolysaccharides

Exopolysaccharides (EPS) are high molecular weight polymers produced by bacteria. The production of EPS responds to bacterial needs and may work as surface adherents, as a bacterial immunological system, and as structural blockages.[93] The FDA has approved some EPS for human use, especially those generated from lactic acid bacteria, such as *Lactobacillus* genera. In a recent approach, RB was encapsulated inside EPS-605-NH_2 nanoparticles. EPS-605-NH_2 was isolated from *Lactobacillus plantarum* LCC-605, a strain isolated from fermented food Fuyuan Pickles with a high capacity to produce EPS.[94] With this formulation, a concentration of 8 μM and 0.5 μM was needed to completely eradicate *E. coli* and *S. aureus* under a white light irradiation of 3 J cm^{-2}. Besides, these nanoparticles demonstrated low toxicity against Alveolar type II cells (AT II) and also demonstrated a low hemolytic activity. Then, the conjugate demonstrated its safety and efficiency and it is proposed as an alternative for further *in vivo* studies.[95]

Alginates

Alginates are polysaccharides formed by monomers of mannuronic acid and guluronic acid. These molecules represent up to 44% of the dry weight of marine brown seaweeds. Due to their plastic properties, alginates represent a renewable alternative to petrol plastics. Also, they are currently used in medical devices, such as drug delivery systems, wound plasters, and as a potential replacement for cartilage.[96] In a recent example, alginate foams were loaded with curcumin and a dispersant agent PEG 400 and/or HPβCD was used. The obtained foams were easy to handle and hydrate, being suitable for wound dressings. When irradiated under blue light (9.7 J cm^{-2}) and tested against bacteria, they demonstrated low phototoxicity against *E. coli* (eradication 81%) but were able to completely eradicate *E. faecalis*.[97]

Proteins

β-Lactoglobulins (βLG) are proteins from the lipocalin family that bind and transport small ligands, serving several biological roles. It has been demonstrated that their high affinity for small molecules may be useful to be used as drug-carriers.[98]

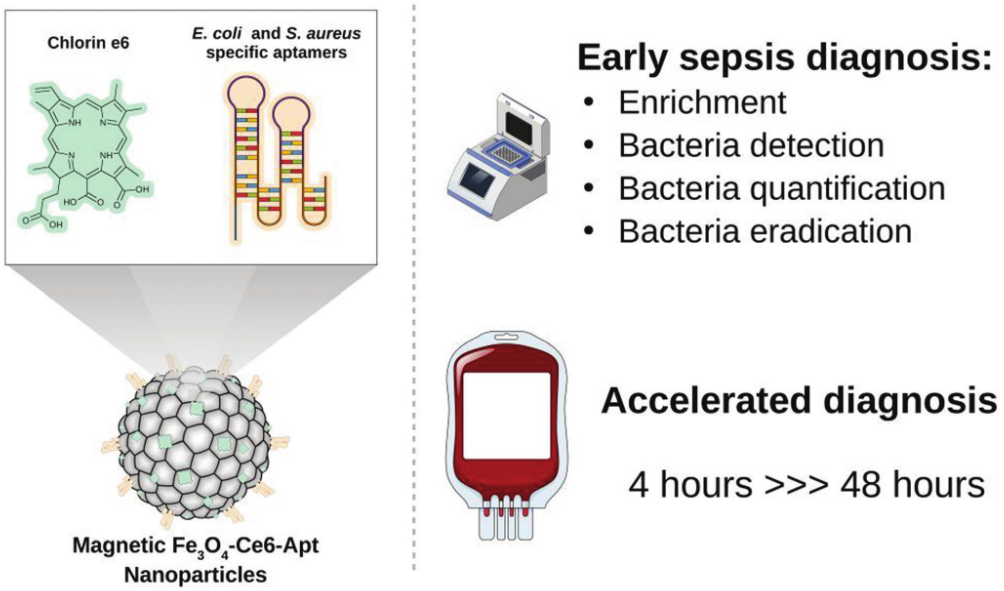

Fig. 12 Magnetic Fe_3O_4 nanoparticles, functionalized with Ce6 and species-identifiable aptamers, were designed for multiple purposes on blood sepsis diagnosis.

As an example, Hypericin (Hyp), a natural occurring photosensitizer, was stabilized with β-lactoglobulin and formed a soluble conjugate (βLG-Hyp). It was demonstrated that the conjugate βLG-Hyp is fluorescent and produces singlet oxygen in aqueous media, in contrast to hypericin in aqueous media. However, when the formulation was tested against *S. aureus*, both Hyp and βLG-Hyp were able to reduce bacterial survival under green light irradiation (37 J cm^{-2}). Furthermore, the Hyp was more effective than βLG; however, dimethyl sulfoxide is added to the tested media, so the authors discussed about the probable usage of βLG-Hyp as a dairy disinfectant, with the advantage of a solvent-free formulation.[99]

Polylactic acid

Lactic acid is an organic molecule which is generated through feedstock waste fermentation. These molecules can be polymerized and form polylactic acid (PLA), which has interesting properties that have been studied for more than three decades. One of the main advantages of PLA is that it is easily hydrolyzed on monomeric lactic acid under compost conditions. Also, PLA has really good biocompatibility and is used as a degradable matrix on wound dressings, suture materials, and bone fixation devices, and as drug delivery systems, such as nano and microparticles, microspheres, *etc*.[100] As an example, recently, curcumin was encapsulated in polylactic acid nanoparticles, with an anionic (Cur-PLA^{-}) or cationic nature (Cur-PLA^{+}). These nanoparticles were tested against planktonic cells of *S. mutans*, *C. albicans* and MRSA, with Cur-PLA^{+} being able to completely eradicate these microorganisms under blue light irradiation (43.2 J cm^{-2}). However, when these nanoparticles were tested against microbial biofilms with one or more species, they failed to diminish the bacterial count.[101]

Poly(3-hydroxybutyrate)

Poly(3-hydroxybutyrate) (PHB) is a polymer from the family of polyhydroxyalkanoates, which are polyesters produced by microorganisms. When extracted from the cellular media, these polymers have thermoplastic and elastomeric properties. Thus, they have been studied over the last 30 years as an environmentally friendly alternative plastic. Research has been focused on its usage in medical devices and tissue replacements, and it has also received some interest as a drug delivery system.[102] Ol'khov and Karpova developed delivery systems based on fibers of PHB loaded with iron(III)-tetraphenylporphyrin. Although the materials were meticulously characterized, non-biological tests were done. However, the authors pinpoint that these formulations may be suitable for antimicrobial and antineoplastic purposes and it is likely that we will hear soon about this topic.[103,104]

Lignin

After cellulose, lignin is the second most abundant biopolymer. Besides its natural abundance, lignin is a subproduct of the paper industry, resulting in around 10^7 tons per year of extracted lignin. However, lignin is mostly regarded as a waste product, often used to produce energy. Only recently, research on lignin as a valuable raw material has taken off.[105]

To the best of our knowledge, only one work regarding PACT and lignin has been published in the last 10 years, even if some reviews on the use of lignin as biomaterials for drug release have been recently published.[106,107] In this single work, silver and gold nanoparticles were coated with different types of lignin. Then, these nanoparticles were tested against planktonic cells of *E. coli* and *S. aureus*, successfully achieving total bacterial eradication under white light irradiation (28.08 J cm^{-2}). Also, a diminishment of 60% on the biofilm formation of *S. aureus* was observed. Besides, under the experimental conditions, the nanoparticles did not induce cytotoxicity against 3T3 fibroblasts. Thus, lignin appears as an appropriate material and more likely we will see an increase in research about this material applied to PACT.[108]

Also, recently, it was described that acetylated lignin displays photosensitizer properties. This observation was made after comparing the singlet oxygen and superoxide anion production of raw kraft lignin (KLi) and an acetylated derivative (AcLi). Only AcLi produced ROS under white halogen light

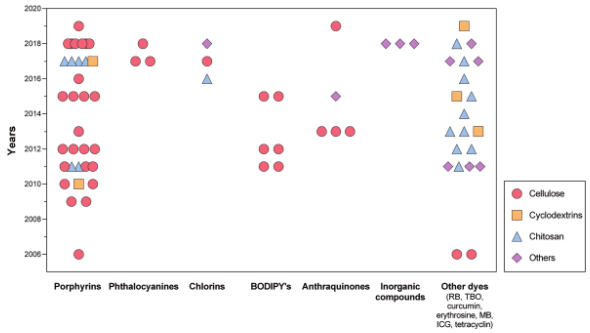

Fig. 13 Distribution of different formulations and conjugates used for PACT from the last 15 years; each point represents a developed conjugate.

exposure (270 μE s^{-1} m^{-2}). Thus, AcLi can work as a photosensitizer and this discovery increases the window of opportunities that lignin provides as a raw material for PACT.[109]

6. Conclusions

Over the last few years, the development of biomaterials for PACT application has received increased attention. Several examples have been described in this review and most likely different research groups are currently working on novel conjugates that aim to further develop materials for PACT that are safe for human usage but also environmentally friendly.

Although several examples have been shown, the most prolific research is focused on cellulose and porphyrin conjugates (Fig. 13). However, we can predict an increase in the usage of new biomaterials, such as lignin. Also, it is more likely that naturally occurring compounds, such as curcumin or hypericin, become more relevant in the PACT field, as some natural compounds are easy to extract, achieving good yields and purity. The field of bioconjugates is widening and, most likely, exciting novel research will soon appear. It should not surprise us that in the next few years an PACT material gets commonly used in hospitals and food packaging.

Conflicts of interest

There are no conflicts to declare.

References

1 Z. Baharoglu, G. Garriss and D. Mazel, Multiple Pathways of Genome Plasticity Leading to Development of Antibiotic Resistance, *Antibiotics*, 2013, **2**, 288–315.
2 A. Tran-Dien, S. Le Hello, C. Bouchier and F. X. Weill, Early transmissible ampicillin resistance in zoonotic Salmonella enterica serotype Typhimurium in the late 1950s: a retrospective, whole-genome sequencing study, *Lancet Infect. Dis.*, 2018, **18**, 207–214.
3 D. Lyddiard, G. L. Jones and B. W. Greatrex, Keeping it simple: Lessons from the golden era of antibiotic discovery, *FEMS Microbiol. Lett.*, 2016, **363**, 1–3.
4 J. Davies, Antibiotic resistance and the golden age of microbiology, *Upsala J. Med. Sci.*, 2014, **119**, 65–67.
5 CDC, About Antibiotic Resistance|Antibiotic/Antimicrobial Resistance|CDC, https://www.cdc.gov/drugresistance/about.html, (accessed 6 January 2020).
6 L. B. Rice, Federal Funding for the Study of Antimicrobial Resistance in Nosocomial Pathogens: No ESKAPE, *J. Infect. Dis.*, 2008, **197**, 1079–1081.
7 Z. F. Udwadia, S. Jain, C. Rodrigues and A. Mehta, XDR tuberculosis in India: what's in a name?, *Lancet Infect. Dis.*, 2007, **7**, 441–442.
8 M. C. Fisher, N. J. Hawkins, D. Sanglard and S. J. Gurr, Worldwide emergence of resistance to antifungal drugs challenges human health and food security, *Science*, 2018, **360**, 739–742.
9 H. P. de Koning, Drug resistance in protozoan parasites, *Emerging Top. Life Sci.*, 2017, **1**, 627–632.
10 O'Neill Commission, Tackling Drug-Resistant Infections Globally: Final Report and Recommendations the Review on Antimicrobial Resistance Chaired By Jim O'Neill.
11 M. Chan, Global Action Plan on Antimicrobial Resistance, *Geneva*, 2015.
12 S. Callaghan and M. O. Senge, The good, the bad, and the ugly – controlling singlet oxygen through design of photosensitizers and delivery systems for photodynamic therapy, *Photochem. Photobiol. Sci.*, 2018, **17**, 1490–1514.
13 L. B. Josefsen and R. W. Boyle, Photodynamic Therapy and the Development of Metal-Based Photosensitisers, *Met.-Based Drugs*, 2008, **2008**, 1–23.
14 C. Yang, Y. Chen, W. Guo, Y. Gao, C. Song, Q. Zhang, N. Zheng, X. Han and C. Guo, Bismuth Ferrite-Based Nanoplatform Design: An Ablation Mechanism Study of Solid Tumor and NIR-Triggered Photothermal/Photodynamic Combination Cancer Therapy, *Adv. Funct. Mater.*, 2018, **28**, 1–13.
15 F. Dandash, D. Y. Léger, C. Fidanzi-Dugas, S. Nasri, F. Brégier, R. Granet, W. Karam, M. Diab-Assaf, V. Sol and B. Liagre, In vitro anticancer activity of new gold(III) porphyrin complexes in colon cancer cells, *J. Inorg. Biochem.*, 2017, **177**, 27–38.
16 P. Figueiredo, K. Lintinen, A. Kiriazis, V. Hynninen, Z. Liu, T. Bauleth-Ramos, A. Rahikkala, A. Correia, T. Kohout, B. Sarmento, J. Yli-Kauhaluoma, J. Hirvonen, O. Ikkala, M. A. Kostiainen and H. A. Santos, In vitro evaluation of biodegradable lignin-based nanoparticles for drug delivery and enhanced antiproliferation effect in cancer cells, *Biomaterials*, 2017, **121**, 97–108.
17 European Patent Office, *Eur. Pat. Off*, WO 2016/178191, 2016.
18 R. Baskaran, J. Lee and S.-G. Yang, Clinical development of photodynamic agents and therapeutic applications, *Biomater. Res.*, 2018, **22**, 1–8.
19 C. Frochot and S. Mordon, Update of the situation of clinical photodynamic therapy in Europe in the 2003–2018 period, *J. Porphyrins Phthalocyanines*, 2019, **23**, 347–357.
20 D. van Straten, V. Mashayekhi, H. de Bruijn, S. Oliveira and D. Robinson, Oncologic Photodynamic Therapy: Basic Principles, Current Clinical Status and Future Directions, *Cancers*, 2017, **9**, 19.
21 J. M. Dąbrowski and L. G. Arnaut, Photodynamic therapy (PDT) of cancer: from local to systemic treatment, *Photochem. Photobiol. Sci.*, 2015, **14**, 1765–1780.
22 *Goodman & Gilman's The Pharmaceutical Basis of Therapeutics*, ed. L. L. Brunton, B. A. Chabner and B. C. Knollmann, McGraw Hill Medical, New York, 12th edn, 2011.
23 M. Wainwright, T. Maisch, S. Nonell, K. Plaetzer, A. Almeida, G. P. Tegos and M. R. Hamblin, Photoantimicrobials—are we afraid of the light?, *Lancet Infect. Dis.*, 2017, **17**, e49–e55.

24 T. G. S. Denis, L. Huang, T. Dai and M. R. Hamblin, Analysis of the bacterial heat shock response to photodynamic therapy-mediated oxidative stress, *Photochem. Photobiol.*, 2011, **87**, 707–713.
25 M. Tanaka, P. Mroz, T. Dai, L. Huang, Y. Morimoto, M. Kinoshita, Y. Yoshihara, K. Nemoto, N. Shinomiya, S. Seki and M. R. Hamblin, Photodynamic Therapy Can Induce a Protective Innate Immune Response against Murine Bacterial Arthritis via Neutrophil Accumulation, *PLoS One*, 2012, **7**, e39823.
26 L. G. Arnaut, *Design of porphyrin-based photosensitizers for photodynamic therapy*, Elsevier Inc., 1st edn, 2011, vol. 63.
27 D. Liu, L. Li, J. Chen, Z. Chen, L. Jiang, C. Yuan and M. Huang, Dissociation of zinc phthalocyanine aggregation on bacterial surface is key for photodynamic antimicrobial effect, *J. Porphyrins Phthalocyanines*, 2018, **22**, 1–10.
28 A. Radomski, P. Jurasz, D. Alonso-Escolano, M. Drews, M. Morandi, T. Malinski and M. W. Radomski, Nanoparticle-induced platelet aggregation and vascular thrombosis, *Br. J. Pharmacol.*, 2005, **146**, 882–893.
29 K. Ogawa, M. Sone, T. Toyoda, Y. Mizuta, J. Akagi and Y.-M. Cho, Size-dependent acute toxicity of silver nanoparticles in mice, *J. Toxicol. Pathol.*, 2017, **31**, 73–80.
30 A. K. Mohanty, M. Misra, L. T. Drzal, S. E. Selke, B. R. Harte and G. Hinrichsen, in *Natural Fibers, Biopolymers, and Biocomposites*, ed. A. K. Mohanty, M. Misra and L. T. Drzal, CRC Press, Boca Raton, 2005, p. 896.
31 R. Jia, W. Tian, H. Bai, J. Zhang, S. Wang and J. Zhang, Sunlight-Driven Wearable and Robust Antibacterial Coatings with Water-Soluble Cellulose-Based Photosensitizers, *Adv. Healthcare Mater.*, 2019, **8**, 1801591.
32 M. Q. Mesquita, C. J. Dias, M. G. P. M. S. Neves, A. Almeida and M. F. Faustino, Revisiting Current Photoactive Materials for Antimicrobial Photodynamic Therapy, *Molecules*, 2018, **23**, 2424.
33 V. Almeida-Marrero, E. van de Winckel, E. Anaya-Plaza, T. Torres and A. de la Escosura, Porphyrinoid biohybrid materials as an emerging toolbox for biomedical light management, *Chem. Soc. Rev.*, 2018, **47**, 7369–7400.
34 D. Klemm, B. Heublein, H.-P. Fink and A. Bohn, Cellulose: Fascinating Biopolymer and Sustainable Raw Material, *Angew. Chem., Int. Ed.*, 2005, **44**, 3358–3393.
35 V. Decraene, J. Pratten and M. Wilson, Cellulose Acetate Containing Toluidine Blue and Rose Bengal Is an Effective Antimicrobial Coating when Exposed to White Light, *Appl. Environ. Microbiol.*, 2006, **72**, 4436–4439.
36 M. Sachar, K. E. Anderson and X. Ma, Protoporphyrin IX: the Good, the Bad, and the Ugly, *J. Pharmacol. Exp. Ther.*, 2016, **356**, 267–275.
37 M. Krouit, R. Granet, P. Branland, B. Verneuil and P. Krausz, New photoantimicrobial films composed of porphyrinated lipophilic cellulose esters, *Bioorg. Med. Chem. Lett.*, 2006, **16**, 1651–1655.
38 M. Krouit, R. Granet and P. Krausz, Photobactericidal films from porphyrins grafted to alkylated cellulose – synthesis and bactericidal properties, *Eur. Polym. J.*, 2009, **45**, 1250–1259.
39 C. Ringot, V. Sol, M. Barrière, N. Saad, P. Bressollier, R. Granet, P. Couleaud, C. Frochot and P. Krausz, Triazinyl Porphyrin-Based Photoactive Cotton Fabrics: Preparation, Characterization, and Antibacterial Activity, *Biomacromolecules*, 2011, **12**, 1716–1723.
40 C. Ringot, N. Saad, R. Granet, P. Bressollier, V. Sol and P. Krausz, Meso -functionalized aminoporphyrins as efficient agents for photo-antibacterial surfaces, *J. Porphyrins Phthalocyanines*, 2010, **14**, 925–931.
41 J.-P. Mbakidi, K. Herke, S. Alvès, V. Chaleix, R. Granet, P. Krausz, S. Leroy-Lhez, T.-S. Ouk and V. Sol, Synthesis and photobiocidal properties of cationic porphyrin-grafted paper, *Carbohydr. Polym.*, 2013, **91**, 333–338.
42 J. K. Nzambe Ta keki, T.-S. Ouk, R. Zerrouki, P.-A. Faugeras, V. Sol and F. Brouillette, Synthesis and photobactericidal properties of a neutral porphyrin grafted onto lignocellulosic fibers, *Mater. Sci. Eng., C*, 2016, **62**, 61–67.
43 B. L. Carpenter, F. Scholle, H. Sadeghifar, A. J. Francis, J. Boltersdorf, W. W. Weare, D. S. Argyropoulos, P. A. Maggard and R. A. Ghiladi, Synthesis, Characterization, and Antimicrobial Efficacy of Photomicrobicidal Cellulose Paper, *Biomacromolecules*, 2015, **16**, 2482–2492.
44 B. L. Carpenter, E. Feese, H. Sadeghifar, D. S. Argyropoulos and R. A. Ghiladi, Porphyrin-Cellulose Nanocrystals: A Photobactericidal Material that Exhibits Broad Spectrum Antimicrobial Activity, *Photochem. Photobiol.*, 2012, **88**, 527–536.
45 E. Feese, H. Sadeghifar, H. S. Gracz, D. S. Argyropoulos and R. A. Ghiladi, Photobactericidal Porphyrin-Cellulose Nanocrystals: Synthesis, Characterization, and Antimicrobial Properties, *Biomacromolecules*, 2011, **12**, 3528–3539.
46 D. R. Alvarado, D. S. Argyropoulos, F. Scholle, B. S. T. Peddinti and R. A. Ghiladi, A facile strategy for photoactive nanocellulose-based antimicrobial materials, *Green Chem.*, 2019, **21**, 3424–3435.
47 J. Dong, R. A. Ghiladi, Q. Wang, Y. Cai and Q. Wei, Protoporphyrin-IX conjugated cellulose nanofibers that exhibit high antibacterial photodynamic inactivation efficacy, *Nanotechnology*, 2018, **29**, 265601.
48 J. Dong, R. A. Ghiladi, Q. Wang, Y. Cai and Q. Wei, Protoporphyrin IX conjugated bacterial cellulose via diamide spacer arms with specific antibacterial photodynamic inactivation against Escherichia coli, *Cellulose*, 2018, **25**, 1673–1686.
49 C. Ringot, N. Saad, F. Brégier, P. Bressollier, E. Poli, V. Chaleix, T. S. Ouk and V. Sol, Antibacterial activity of a photosensitive hybrid cellulose fabric, *Photochem. Photobiol. Sci.*, 2018, **17**, 1780–1786.
50 L. Li, S. Kromann, J. E. Olsen, S. W. Svenningsen and R. H. Olsen, Insight into synergetic mechanisms of tetracycline and the selective serotonin reuptake inhibitor, ser-

traline, in a tetracycline-resistant strain of Escherichia coli, *J. Antibiot.*, 2017, **70**, 944–953.
51 J. Chen, W. Wang, P. Hu, D. Wang, F. Lin, J. Xue, Z. Chen, Z. Iqbal and M. Huang, Dual antimicrobial actions on modified fabric leads to inactivation of drug-resistant bacteria, *Dyes Pigm.*, 2017, **140**, 236–243.
52 J. Zhuo and G. Sun, Antimicrobial Functions on Cellulose Materials Introduced by Anthraquinone Vat Dyes, *ACS Appl. Mater. Interfaces*, 2013, **5**, 10830–10835.
53 R. Rahal, M. Le Bechec, R. Guyoneaud, T. Pigot, H. Paolacci and S. Lacombe, Bactericidal activity under UV and visible light of cotton fabrics coated with anthraquinone-sensitized TiO2, *Catal. Today*, 2013, **209**, 134–139.
54 Y. Habibi, L. A. Lucia and O. J. Rojas, Cellulose Nanocrystals : Chemistry, Self-Assembly, and Applications, *Chem. Rev.*, 2010, **110**, 3479–3500.
55 F. Le Guern, T.-S. Ouk, K. Grenier, N. Joly, V. Lequart and V. Sol, Enhancement of photobactericidal activity of chlorin-e6-cellulose nanocrystals by covalent attachment of polymyxin B, *J. Mater. Chem. B*, 2017, **5**, 6953–6962.
56 M. R. Hamblin and T. Dai, Can surgical site infections be treated by photodynamic therapy?, *Photodiagn. Photodyn. Ther.*, 2010, **7**, 134–136.
57 E. Anaya-Plaza, E. van de Winckel, J. Mikkilä, J. M. Malho, O. Ikkala, O. Gulías, R. Bresolí-Obach, M. Agut, S. Nonell, T. Torres, M. A. Kostiainen and A. de la Escosura, Photoantimicrobial Biohybrids by Supramolecular Immobilization of Cationic Phthalocyanines onto Cellulose Nanocrystals, *Chem. – Eur. J.*, 2017, **23**, 4320–4326.
58 G. Tiwari, R. Tiwari and A. Rai, Cyclodextrins in delivery systems: Applications, *J. Pharm. BioAllied Sci.*, 2010, **2**, 72.
59 G. Crini, Review: A history of cyclodextrins, *Chem. Rev.*, 2014, **114**, 10940–10975.
60 E. Fenyvesi, EMA Review on Cyclodextrins as Excipients, *CycloLab – Cyclodext. News*, 2015, vol. **29**, pp. 1–17.
61 S. Buedenbender and G. E. Schulz, Structural Base for Enzymatic Cyclodextrin Hydrolysis, *J. Mol. Biol.*, 2009, **385**, 606–617.
62 S. J. Mora, M. P. Cormick, M. E. Milanesio and E. N. Durantini, The photodynamic activity of a novel porphyrin derivative bearing a fluconazole structure in different media and against Candida albicans, *Dyes Pigm.*, 2010, **87**, 234–240.
63 M. Cozzolino, P. Delcanale, C. Montali, M. Tognolini, C. Giorgio, M. Corrado, L. Cavanna, P. Bianchini, A. Diaspro, S. Abbruzzetti and C. Viappiani, Enhanced photosensitizing properties of protein bound curcumin, *Life Sci.*, 2019, **233**, 116710.
64 A. E. Kamel, M. Fadel and D. Louis, Curcumin-loaded nanostructured lipid carriers prepared using Peceol™ and olive oil in photodynamic therapy: development and application in breast cancer cell line, *Int. J. Nanomed.*, 2019, **14**, 5073–5085.
65 K. O. Wikene, A. B. Hegge, E. Bruzell and H. H. Tønnesen, Formulation and characterization of lyophilized curcumin solid dispersions for antimicrobial photodynamic therapy (aPDT): studies on curcumin and curcuminoids LII, *Drug Dev. Ind. Pharm.*, 2014, **41**, 969–977.
66 A. B. Hegge, M. Vukicevic, E. Bruzell, S. Kristensen and H. H. Tønnesen, Solid dispersions for preparation of phototoxic supersaturated solutions for antimicrobial photodynamic therapy (aPDT), *Eur. J. Pharm. Biopharm.*, 2013, **83**, 95–105.
67 M. A. Castriciano, R. Zagami, M. P. Casaletto, B. Martel, M. Trapani, A. Romeo, V. Villari, M. T. Sciortino, L. Grasso, S. Guglielmino, L. M. Scolaro and A. Mazzaglia, Poly(carboxylic acid)-Cyclodextrin/Anionic Porphyrin Finished Fabrics as Photosensitizer Releasers for Antimicrobial Photodynamic Therapy, *Biomacromolecules*, 2017, **18**, 1134–1144.
68 Y. Gao, J. Wang, D. Hu, Y. Deng, T. Chen, Q. Jin and J. Ji, Bacteria-Targeted Supramolecular Photosensitizer Delivery Vehicles for Photodynamic Ablation Against Biofilms, *Macromol. Rapid Commun.*, 2019, **40**, 1800763.
69 F. J. R. Alexandrino, E. M. Bezerra, R. F. Da Costa, L. R. L. Cavalcante, F. A. M. Sales, T. S. Francisco, L. K. A. Rodrigues, D. H. A. de Brito, N. M. P. S. Ricardo, S. N. Costa, P. de Lima-Neto, I. L. Barroso-Neto, E. W. S. Caetano and V. N. Freire, Rose Bengal incorporated to α-cyclodextrin microparticles for photodynamic therapy against the cariogenic microorganism Streptococcus mutans, *Photodiagn. Photodyn. Ther.*, 2019, **25**, 111–118.
70 D. Elieh-Ali-Komi and M. R. Hamblin, Chitin and Chitosan: Production and Application of Versatile Biomedical Nanomaterials, *Int. J. Adv. Res.*, 2016, **4**, 411–427.
71 T. Tsai, H.-F. Chien, T.-H. Wang, C.-T. Huang, Y.-B. Ker and C.-T. Chen, Chitosan Augments Photodynamic Inactivation of Gram-Positive and Gram-Negative Bacteria, *Antimicrob. Agents Chemother.*, 2011, **55**, 1883–1890.
72 H.-F. Chien, C.-P. Chen, Y.-C. Chen, P.-H. Chang, T. Tsai and C.-T. Chen, The Use of Chitosan to Enhance Photodynamic Inactivation against Candida albicans and Its Drug-Resistant Clinical Isolates, *Int. J. Mol. Sci.*, 2013, **14**, 7445–7456.
73 C. P. Chen, C. T. Chen and T. Tsai, Chitosan nanoparticles for antimicrobial photodynamic inactivation: Characterization and in vitro investigation, *Photochem. Photobiol.*, 2012, **88**, 570–576.
74 C. H. Lin, H. F. Chien, M. H. Lin, C. P. Chen, M. Shen and C. T. Chen, Chitosan inhibits the rehabilitation of damaged microbes induced by photodynamic inactivation, *Int. J. Mol. Sci.*, 2018, **19**, 2598.
75 S. S. Choi, H. K. Lee and H. S. Chae, Synergistic in vitro photodynamic antimicrobial activity of methylene blue and chitosan against Helicobacter pylori 26695, *Photodiagn. Photodyn. Ther.*, 2014, **11**, 526–532.
76 S. Choi, H. Lee, J. Yu and H. Chae, In vitro augmented photodynamic bactericidal activity of tetracycline and chitosan against Clostridium difficile KCTC5009 in the

planktonic cultures, *J. Photochem. Photobiol., B*, 2015, **153**, 7–12.
77 F. Camacho-Alonso, E. Julián-Belmonte, F. Chiva-García and Y. Martínez-Beneyto, Bactericidal Efficacy of Photodynamic Therapy and Chitosan in Root Canals Experimentally Infected with Enterococcus faecalis : An In Vitro Study, *Photomed. Laser Surg.*, 2017, **35**, 184–189.
78 A. Shrestha and A. Kishen, Polycationic Chitosan-Conjugated Photosensitizer for Antibacterial Photodynamic Therapy, *Photochem. Photobiol.*, 2012, **88**, 577–583.
79 A. Shrestha, M. R. Hamblin and A. Kishen, Photoactivated rose bengal functionalized chitosan nanoparticles produce antibacterial/biofilm activity and stabilize dentin-collagen, *Nanomedicine*, 2014, **10**, 491–501.
80 A. Shrestha and A. Kishen, Antibiofilm Efficacy of Photosensitizer-functionalized Bioactive Nanoparticles on Multispecies Biofilm, *J. Endod.*, 2014, **40**, 1604–1610.
81 A. Shrestha, M. R. Hamblin and A. Kishen, Characterization of a conjugate between rose bengal and chitosan for targeted antibiofilm and tissue stabilization effects as a potential treatment of infected dentin, *Antimicrob. Agents Chemother.*, 2012, **56**, 4876–4884.
82 A. Shrestha and A. Kishen, The Effect of Tissue Inhibitors on the Antibacterial Activity of Chitosan Nanoparticles and Photodynamic Therapy, *J. Endod.*, 2012, **38**, 1275–1278.
83 A. Persadmehr, C. D. Torneck, D. G. Cvitkovitch, V. Pinto, I. Talior, M. Kazembe, S. Shrestha, C. A. McCulloch and A. Kishen, Bioactive Chitosan Nanoparticles and Photodynamic Therapy Inhibit Collagen Degradation In Vitro, *J. Endod.*, 2014, **40**, 703–709.
84 A. Shrestha, M. Cordova and A. Kishen, Photoactivated Polycationic Bioactive Chitosan Nanoparticles Inactivate Bacterial Endotoxins, *J. Endod.*, 2015, **41**, 686–691.
85 A. Nagahara, A. Mitani, M. Fukuda, H. Yamamoto, K. Tahara, I. Morita, C.-C. Ting, T. Watanabe, T. Fujimura, K. Osawa, S. Sato, S. Takahashi, Y. Iwamura, T. Kuroyanagi, Y. Kawashima and T. Noguchi, Antimicrobial photodynamic therapy using a diode laser with a potential new photosensitizer, indocyanine green-loaded nanospheres, may be effective for the clearance of Porphyromonas gingivalis, *J. Periodontal Res.*, 2013, **48**, 591–599.
86 M. Pourhajibagher, A. R. Rokn, M. Rostami-Rad, H. R. Barikani and A. Bahador, Monitoring of Virulence Factors and Metabolic Activity in Aggregatibacter Actinomycetemcomitans Cells Surviving Antimicrobial Photodynamic Therapy via Nano-Chitosan Encapsulated Indocyanine Green, *Front. Phys.*, 2018, **6**, 1–10.
87 E. Darabpour, N. Kashef and S. Mashayekhan, Chitosan nanoparticles enhance the efficiency of methylene blue-mediated antimicrobial photodynamic inactivation of bacterial biofilms: An in vitro study, *Photodiagn. Photodyn. Ther.*, 2016, **14**, 211–217.
88 K. A. D. F. Castro, N. M. M. Moura, A. Fernandes, M. A. F. Faustino, M. M. Q. Simões, J. A. S. Cavaleiro, S. Nakagaki, A. Almeida, Â. Cunha, A. J. D. Silvestre, C. S. R. Freire, R. J. B. Pinto and M. G. P. M. S. Neves, Control of Listeria innocua biofilms by biocompatible photodynamic antifouling chitosan based materials, *Dyes Pigm.*, 2017, **137**, 265–276.
89 I. Buchovec, V. Lukseviciute, A. Marsalka, I. Reklaitis and Z. Luksiene, Effective photosensitization-based inactivation of Gram (−) food pathogens and molds using the chlorophyllin–chitosan complex: towards photoactive edible coatings to preserve strawberries, *Photochem. Photobiol. Sci.*, 2016, **15**, 506–516.
90 L. Sun, W. Jiang, H. Zhang, Y. Guo, W. Chen, Y. Jin, H. Chen, K. Du, H. Dai, J. Ji and B. Wang, Photosensitizer-Loaded Multifunctional Chitosan Nanoparticles for Simultaneous in Situ Imaging, Highly Efficient Bacterial Biofilm Eradication, and Tumor Ablation, *ACS Appl. Mater. Interfaces*, 2019, **11**, 2302–2316.
91 H. Y. Kong and J. Byun, Nucleic Acid Aptamers: New Methods for Selection, Stabilization, and Application in Biomedical Science, *Biomol. Ther.*, 2013, **21**, 423–434.
92 J. Wang, H. Wu, Y. Yang, R. Yan, Y. Zhao, Y. Wang, A. Chen, S. Shao, P. Jiang and Y. Q. Li, Bacterial species-identifiable magnetic nanosystems for early sepsis diagnosis and extracorporeal photodynamic blood disinfection, *Nanoscale*, 2018, **10**, 132–141.
93 T. Ignatova-Ivanova, in *Immunotherapy - Myths, Reality, Ideas, Future*, ed. K. Metodiev, InTech, 2017, vol. i, pp. 345–354.
94 C. Li, L. Zhou, H. Yang, R. Lv, P. Tian, X. Li, Y. Zhang, Z. Chen and F. Lin, Self-Assembled Exopolysaccharide Nanoparticles for Bioremediation and Green Synthesis of Noble Metal Nanoparticles, *ACS Appl. Mater. Interfaces*, 2017, **9**, 22808–22818.
95 C. Li, F. Lin, W. Sun, F.-G. Wu, H. Yang, R. Lv, Y.-X. Zhu, H.-R. Jia, C. Wang, G. Gao and Z. Chen, Self-Assembled Rose Bengal-Exopolysaccharide Nanoparticles for Improved Photodynamic Inactivation of Bacteria by Enhancing Singlet Oxygen Generation Directly in the Solution, *ACS Appl. Mater. Interfaces*, 2018, **10**, 16715–16722.
96 C. Zhang, P. L. Show and S. H. Ho, Progress and perspective on algal plastics – A critical review, *Bioresour. Technol.*, 2019, **289**, 121700.
97 A. B. Hegge, T. Andersen, J. E. Melvik, E. Bruzell, S. Kristensen and H. H. Tønnesen, Formulation and Bacterial Phototoxicity of Curcumin Loaded Alginate Foams for Wound Treatment Applications: Studies on Curcumin and Curcuminoides XLII, *J. Pharm. Sci.*, 2011, **100**, 174–185.
98 R. W. Hesselink and J. B. C. Findlay, Expression, characterization and ligand specificity of lipocalin-1 interacting membrane receptor (LIMR), *Mol. Membr. Biol.*, 2013, **30**, 327–337.
99 B. Rodríguez-Amigo, P. Delcanale, G. Rotger, J. Juárez-Jiménez, S. Abbruzzetti, A. Summer, M. Agut, F. J. Luque, S. Nonell and C. Viappiani, The complex of hypericin with

β-lactoglobulin has antimicrobial activity with potential applications in dairy industry, *J. Dairy Sci.*, 2015, **98**, 89–94.
100 M. S. Singhvi, S. S. Zinjarde and D. V. Gokhale, Polylactic acid: synthesis and biomedical applications, *J. Appl. Microbiol.*, 2019, **127**, 1612–1626.
101 J. K. Trigo Gutierrez, G. C. Zanatta, A. L. M. Ortega, M. I. C. Balastegui, P. V. Sanitá, A. C. Pavarina, P. A. Barbugli and E. G. de O. Mima, Encapsulation of curcumin in polymeric nanoparticles for antimicrobial Photodynamic Therapy, *PLoS One*, 2017, **12**, e0187418.
102 Q. Wu, Y. Wang and G. Q. Chen, Medical application of microbial biopolyesters polyhydroxyalkanoates, *Artif. Cells, Blood Substitutes, Biotechnol.*, 2009, **37**, 1–12.
103 S. G. Karpova, A. A. Ol'khov, N. G. Shilkina, P. M. Tyubaeva, A. A. Popov and A. L. Iordanskii, Investigation of biodegradable composites of poly(3-hydroxybutyrate) ultrathin fibers modified by a complex of iron(III) with tetraphenylporphyrin, *Polym. Sci., Ser. A*, 2017, **59**, 342–351.
104 A. A. Ol'khov, S. G. Karpova, A. V. Lobanov, P. M. Tyubaeva, L. I. Gol'tsova, E. L. Kucherenko and A. L. Iordanskii, Ultrathin Poly(3-hydroxybutyrate) Fibers Modified with the Iron(III) Complex of Tetraphenylporphyrin, *Fibre Chem.*, 2017, **49**, 217–221.
105 S. Beisl, A. Friedl and A. Miltner, Lignin from Micro- to Nanosize: Applications, *Int. J. Mol. Sci.*, 2017, **18**, 2367.
106 M. Witzler, A. Alzagameem, M. Bergs, B. El Khaldi-Hansen, S. E. Klein, D. Hielscher, B. Kamm, J. Kreyenschmidt, E. Tobiasch and M. Schulze, Lignin-derived biomaterials for drug release and tissue engineering, *Molecules*, 2018, **23**, 1–22.
107 M. H. Sipponen, H. Lange, C. Crestini, A. Henn and M. Österberg, Lignin for Nano- and Microscaled Carrier Systems: Applications, Trends, and Challenges, *ChemSusChem*, 2019, **12**, 2038.
108 D. M. Rocca, J. P. Vanegas, K. Fournier, M. C. Becerra, J. C. Scaiano and A. E. Lanterna, Biocompatibility and photo-induced antibacterial activity of lignin-stabilized noble metal nanoparticles, *RSC Adv.*, 2018, **8**, 40454–40463.
109 G. Marchand, C. A. Calliste, R. M. Williams, C. McLure, S. Leroy-Lhez and N. Villandier, Acetylated Lignins: A Potential Bio-Sourced Photosensitizer, *ChemistrySelect*, 2018, **3**, 5512–5516.

Page intentionally left in blank

PhD Objectives

The project POLYTHEA received funding from the European Comission, under the Marie Skłodowska-Curie grant agreement n° 764837. This project motto was “How light can save lives” and was focused on the life-sciences applications of photosensitizers, and their formulations. Each of the ten developed projects were carried out in two or more european locations, as France, Portugal, Ireland, Poland, Switzerland, Greece, Netherlands, Germany and Scotland. The work presented in this thesis was developed in France and Portugal, with secondments in Poland and Germany, with the common goal to develop antibacterial photodynamic formulations.

Antimicrobial resistance arise has boost the research for disinfectant alternatives, as Photodynamic Antimicrobial ChemoTherapy which relies on *in situ* produced reactive oxygen species (ROS). The production of ROS is driven by the interaction of light and a photosensitizing molecule. However, usually photosensitizing molecules have bioavailability problems in aqueous media, which formulation research has taken as a challenge. In addition, the use of biopolymers as raw materials for drug delivery has increased, as a response to global efforts to decrease the use of petroleum-derived products.

In this work, it was projected the use of biopolymers as raw materials for the formulation of photosensitizers. The developed formulations were fully characterized, in their physical, and photophysical characteristics. Also, their bactericide activity against Gram-positive and Gram-negative bacteria was analyzed. Once demonstrated the efficiency of the proposed formulation system, it was analyzed the effect of different types of photosensitizers inside the formulation, demonstrating the universality of the proposed formulation.

This PhD thesis is presented as a collection of the different peer-reviewed publications obtained along the three years of the project. Thus, a short introduction for each research paper is presented, and then the accepted publications are introduced.

RESULTS

I. Acetylated lignin nanoparticles: a prospective vehicle for photosensitizers

From the several materials available from biological sources, lignin is a material that has not been used for the formulation of photosensitizers, despite its high abundance in the nature. Lignin is the second most abundant biopolymer, being a mayor constituent of tree trunks and then extracted as a by-product of the paper industry, which produces around 55-70 million tons each year [32]. However, from this massive amount of biomass obtained, around 98 % is burnt for energy generation, while only the remaining 2 % is used as added-value products, finding applications as binder, filler, additive, dispersant, adsorbent, surfactant or as precursor for carbon materials [33]. This situation contrasts with the potential that lignin has, as its chemical structure can be easily modified [34] to tune its solubility, providing with interesting applications, as pH responsive polymeric nanoparticles [35,36], antibacterial food packages [37], water purification applications [38], anion-exchange resins [39], and as drug delivery systems [40]. Remarkably, in the last few years lignin has attracted interest from researchers, and this has been reflected in the number of publications per year (Figure 4).

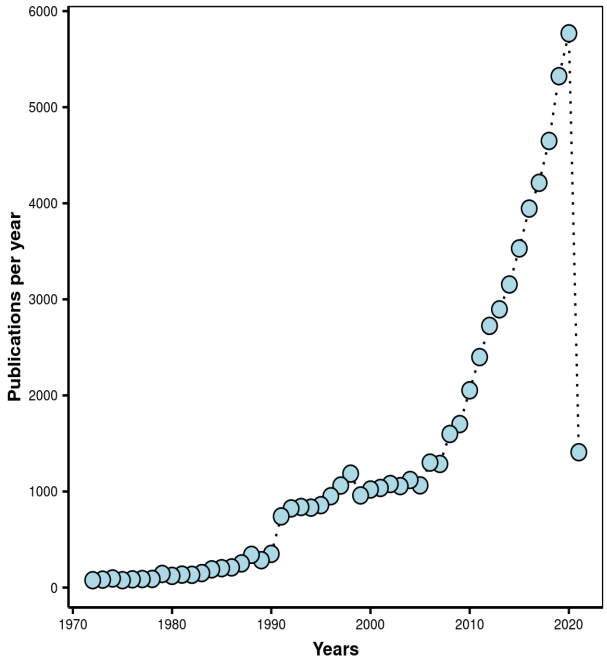

Figure 4: Publications related to the term "lignin". For the creation of this figure, the word "lignin" was searched in Web of Science [accessed April 14th, 2021]

Although the use of lignin as a raw material for biomedical applications has gained importance in the last ten years, there are only some examples of lignin as a raw material for photodynamic applications. This is likely due to the well-known antioxidant activity of lignin [41], which would prevent the formation of ROS into the media. One of the latest research published at the laboratory PEIRENE demonstrated that the acetylation of the hydroxyl moieties in Kraft lignin led to the photodynamic production of singlet oxygen [32]. This observation quickly led to the presumption that acetylated lignin could work as a carrier

system for photosensitizing molecules.

In **Publication 3**, the formation of acetylated lignin nanoparticles is explored, comparing different lignin sources, their acetylation substitution degrees, and their chemical properties. Furthermore, these lignins were used as raw materials for the preparation of nanoparticles, through two different methods, and their physical properties were characterized. The dynamics of nanoparticles formation was studied *in silico*, resulting in the first approximation of lignin nanoparticles simulation through antisolvent addition. Furthermore, the encapsulation of 5,10,15,20-tetrakis(4-hydroxyphenyl)-21H,23H-porphine (**THPP**) was modeled *in silico*, complementing the experimental results obtained. The **THPP**-loaded acetylated lignin nanoparticles (**THPP@AcLi)** were physically characterized, resulting in a stable formulation with potential antibacterial applications.

Publication 3. "Acetylated lignin nanoparticles as a possible vehicle for photosensitizing molecules" [42]

Nanoscale Advances

ROYAL SOCIETY OF CHEMISTRY

PAPER

View Article Online
View Journal | View Issue

Check for updates

Cite this: *Nanoscale Adv.*, 2020, **2**, 5648

Acetylated lignin nanoparticles as a possible vehicle for photosensitizing molecules†

Guillaume Marchand,[a] Gabin Fabre,[b] Nidia Maldonado-Carmona,[c] Nicolas Villandier[c] and Stéphanie Leroy-Lhez *[c]

Received 28th July 2020
Accepted 12th October 2020

DOI: 10.1039/d0na00615g

rsc.li/nanoscale-advances

Lignins are underused and abundant bio-sourced polymers with various potential applications. An attractive one is the development of nanoparticles for bioactive compound delivery. Here, we optimized the synthesis of hydrodispersible nanoparticles of acetylated lignin by comparing different lignin sources, degrees of acetylation and preparation methods. The formation of acetylated lignin nanoparticles in various solvents was probed by both experiments and, for the first time, a molecular dynamics simulation. We showed that dialysis is more suitable to obtain these nanoparticles than anti-solvent addition. The encapsulation of hydrophobic photosensitizing porphyrin in these nanoparticles was also demonstrated and rationalized at the molecular level, together with experiments, docking and molecular dynamics simulations. As acetylated lignin has been demonstrated to exhibit photosensitizing activity, the encapsulation of bioactive compounds in lignin nanoparticles opens the doors to a broad range of potential applications.

Introduction

Lignocellulosic biomass is an abundant renewable resource, mainly composed of cellulose, hemicelluloses and lignins. It appears to be a very interesting alternative to fossil resources for the production of biofuels and bio-based chemicals.[1–5]

Lignins are aromatic heteropolymers, derived mainly from radical polymerization of three monolignols: *p*-coumaryl, coniferyl and sinapyl alcohols.[6] They are the second most abundant renewable resource in nature, after cellulose, and comprise 25–30% of the non-fossil organic molecules on Earth.[7] They are mostly obtained or produced as a byproduct of pulping and in the paper-making industry. Of the 55–70 million tons produced annually, only 1–2% is used for the production of value-added products,[8] despite the fact that lignins exhibit low cytotoxicity, are biodegradable and have antioxidant, antimicrobial, anti-inflammatory and UV-blocking properties.[9–12] Lignins have the potential to be used in the treatment of obesity, diabetes, thrombosis, viral infections and cancer.[13] These biological activities convinced research teams to prepare micro- and nano-particles for bioactive compound delivery from unmodified or functionalized lignins. The materials obtained have found various applications in environmental science and medicine.[14–16] For example, in combination with other drugs, the biopolymer seems to be a good candidate for the development of solutions to fight against antimicrobial resistance.[17]

One alternative to increase the added value of products obtained from lignins is to modify them chemically. These modifications are generally carried out on the aromatic rings or aliphatic and phenolic hydroxyl groups present in the chemical structure of lignins.[18–20] Moreover, they can influence the physicochemical properties of lignins. As was reported in our previous work, acetylated lignins exhibit promising photosensitizing behavior in view of their ability to generate reactive oxygen species.[21] However, the various observations were made under organic solvent conditions. For this purpose, nanoparticles were prepared from two sources of softwood kraft acetylated lignins, named **AcKL-1** and **AcKL-2**, respectively, and through two different methods: by addition of an anti-solvent and by dialysis. Molecular dynamics simulations of lignin nanoparticles highlighted their solvent-dependent conformation, in correlation with experimental results. The influence of different experimental parameters on the final structure of these nano-objects as well as their stability was also studied. In order to enlarge the scope of their applications, the ability of these biologically sourced nanoparticles to encapsulate a bioactive molecule was also studied, both experimentally, and by docking and molecular dynamics simulations.

Experimental section

Reagents and solvents

Deionized water (resistivity ≥ 18 MΩ cm) used for the experiments conducted in this work was obtained from a Millipore

[a]*PEIRENE EA7500, Université de Limoges, Faculté de Pharmacie, 2 rue du Docteur Marcland, 87025 Limoges Cedex, France*
[b]*UMR 1248 INSERM, Université de Limoges, Faculté de Pharmacie, 2 rue du Docteur Marcland, 87025 Limoges Cedex, France*
[c]*PEIRENE EA7500, Université de Limoges, Faculté des Sciences, 123 rue du Albert Thomas, 87025 Limoges Cedex, France. E-mail: stephanie.lhez@unilim.fr*

† Electronic supplementary information (ESI) available: ESI1 includes supplementary experimental information, and ESI2 is a video of the molecular dynamics observations of nanoparticle formation. See DOI: 10.1039/d0na00615g

water purification system. Other reagents, except lignins and solvents, were purchased from various suppliers: Alfa Aesar, Sigma-Aldrich, and Fisher and were used without further purification.

Origin of kraft lignins KL-1 and KL-2

Both kraft lignins, **KL-1** and **KL-2**, are derived from softwoods. They were industrially precipitated from alkaline black liquors by acidification. **KL-1** was obtained from the supplier Sigma-Aldrich (supplier reference: 80068-05-1) and **KL-2** was generously donated by the Université du Québec à Trois-Rivières. The lignins were employed without prior purification.

Total acetylation of kraft lignins KL-1 and KL-2

Biopolymers were acetylated according to the method described by Marchand *et al.*[21] The two materials obtained from acetylation of **KL-1** and **KL-2** were named **AcKL-1** and **AcKL-2**, respectively.

Preparation of acetylated lignin nanoparticles

Two sets of nanoparticles were prepared from totally acetylated lignins, **AcKL-1** and **AcKL-2**, respectively. Each set of nanoparticles was prepared according to two different methods: either by dialysis (**NP-1** and **NP-2**) or by addition of an anti-solvent (**NP-1′** and **NP-2′**). Nanoparticles were also prepared by dialysis from partially acetylated materials $\mathbf{Ac_7KL\text{-}2}$, $\mathbf{Ac_{35}KL\text{-}2}$ and $\mathbf{Ac_{59}KL\text{-}2}$. The influence of different experimental parameters on the final structure of these nano-objects, as well as their stability, was studied.

Anti-solvent addition. The preparation was based on the work of Qian *et al.*[24] Acetylated lignins **AcKL-1** and **AcKL-2** were firstly dissolved in tetrahydrofuran (THF) at a concentration of 1 g L^{-1}. The solution was then stirred for 20 minutes and left to stand for three days in order to allow a good dispersion of the polymer, and thus a good subsequent structuring of the nanoparticles. Afterwards, two volumes of ultrapure water were added under magnetic stirring to the acetylated lignin solution at a flow rate of 18 mL h^{-1}. After water addition, the solution was filtered using a Millipore nylon filter (porosity 0.45 μm), and seven volumes of ultrapure water were added. The solution was finally left stirring in the open air overnight to allow the THF to evaporate.

Dialysis. The preparation by dialysis was based on various nanoparticle preparations already reported in the literature.[25–27] A fixed amount of acetylated or partially acetylated lignin (1 to 4 g L^{-1}) was first dissolved in a water-miscible organic solvent. The polymer solution was then introduced into a dialysis membrane with a porosity of 12 000 to 14 000 Da and dialyzed against 10 L of distilled water for 24 hours under low mechanical stirring. The nanoparticle solution was then centrifuged at 2740 × *g* for 20 min, and the supernatant was removed. This operation was repeated twice, and the nanoparticles were then dispersed into a fixed volume of water.

^{31}P NMR spectroscopy

^{31}P NMR analyses were performed at room temperature on a Bruker DPX 500 NMR spectrometer. The method described by Granata and Argyropoulos[23] was used. Cyclohexanol was used as an internal standard and chromium(III) acetylacetonate as a relaxation agent. NMR tubes were provided with coaxial inserts filled with 85% H_3PO_4 and all chemical shifts were reported relative to the signal of phosphoric acid.

FTIR spectroscopy

FT-IR spectra were obtained using a Frontier PerkinElmer spectrometer in the attenuation total reactance analysis mode. Spectra were collected between 600 and 4000 cm^{-1} after placing the pure product on a diamond crystal plate.

UV-Visible absorption spectroscopy

Acquisitions of UV-Visible absorption spectra were carried out between 300 and 800 nm on a Specord 210 Lambda double-beam spectrophotometer from Analytik Jena, using a 10 mm quartz cell.

Partial acetylation of kraft lignin KL-2

KL-2 was partially acetylated under stirring for 48 h at 25 °C in a mixture consisting of 10 mL of anhydrous pyridine and an equal volume of acetic anhydride, as described in the work of Buono *et al.*[22] At the end of the reaction, modified lignins were precipitated by the addition of ten volumes of distilled water, washed under vacuum with cold water and finally dried at 105 °C for 48 hours. FTIR and ^{31}P NMR analyses of the products showed clear signs of partial acetylation (see ESI1, Fig. S1 and S2†). More specifically, the study of the ^{31}P NMR spectra of partially acetylated lignins, after their functionalization, according to the method described by Granata and Argyropoulos,[23] allowed us to determine that 7, 35 and 59% of the hydroxyl groups of the respectively named $\mathbf{Ac_7KL\text{-}2}$, $\mathbf{Ac_{35}KL\text{-}2}$ and $\mathbf{Ac_{59}KL\text{-}2}$ lignins had been acetylated (see Tables 1, S1 and S2†).

Dynamic light scattering

Acquisitions of nanoparticle size distributions were performed on a Malvern Zetasizer Nano-ZS instrument. Measurements were carried out using a He–Ne laser at 663 nm, a wavelength where lignin absorbance is considered negligible,[40,41] thus avoiding any interactions that may lead to measurement errors. Three measurements, for lignins, were made on each sample at 20 °C using a light scattering angle of 173° and a refractive index of 1.59. The obtained DLS raw data were fit to a Gaussian model, excluding the values with less than 1% presence. The obtained data were validated through the analysis of their R square coefficient and through the analysis of the residuals with a D'Agostino & Pearson Omnibus K2 test. With this statistical approach, we obtained the mean size (geometrical mean) and the standard deviation (σ), which allowed us to approximate the range where 95% of the nanoparticles could be found (2σ).

Transmission electron microscopy

Analyses were carried out on two microscopes: a JEOL 100CX2 of 100 kV and a JEM-2100F of 200 kV. Immediately after ultrasonic

Table 1 Synthesis of partially acetylated lignins

Acetylated lignins	Starting material KL-2 (g)	Acetic anhydride (mL)	Acetic anhydride (eq.)	Pyridine (mL)	Mass yield (%)	Resulting acetylation rate (%)
Ac_7KL-2	2	0.180	0.22	10	95	7
Ac_{35}KL-2	2	0.472	0.57	10	96	35
Ac_{59}KL-2	2	0.700	0.85	10	103	59

dispersion, a drop of solution containing the material to be observed was deposited, on a 400 mesh copper grid with a 12 nm thick carbon membrane before analysis. No prior metallation of the samples was performed.

Scanning electron microscopy

Analyses were carried out on a ZEISS LEO1530VP. A drop of solution containing the material to be observed was deposited and dried on a sample holder. Prior platinum metallation of the samples was performed using an Agar Sputter Coater.

Acetylated lignin model preparation

For the investigation by computational chemistry, nine lignin models were used based on the work of Petridis *et al.*[28,29] The nine different lignin models all showed 61 guaiacyl units, but the models ranged from 0 to 6 branch points, representing the interunit-linkage of softwood lignin. All free hydroxyl groups were acetylated. Bonded and van der Waals parameters for the acetyl moiety were taken from the acetylated N-terminus (residue ACED in CHARMM36 (ref. 30)). Partial charges for the methyl part of the acetyl were also taken from residue ACED, while charges for the ester moiety were taken from an acetylated glycerol headgroup (residue GLYC, CHARMM36). In order to construct the coordinates for the different polymers, single units were added one by one using psfgen 1.6.4, a VMD[31] plugin. In order to prevent steric clashes by unit addition, in between each addition a short (10 ps) molecular dynamics (MD) simulation was run in a vacuum, in which the last unit added (in position N) was pulled away for the unit in position N − 4 along the polymer chain, with a force of 500 kJ mol^{-1} nm^{-1}. Thus, most of the polymer structure could relax while units were added at the tip of a branch of four residues, with enough empty space to avoid steric clashes during addition. All lignin models were further relaxed by simulated annealing MD simulations, in which the lignin was solvated in water molecules (TIP3P model[32]). The temperature of the lignin was linearly increased from 0 to 480 K in 1 ns, while the water was heated from 0 to 300 K. This cycle was repeated 100 times.

Encapsulation of THPP

The encapsulation of 5,10,15,20-tetrakis(4-hydroxyphenyl) porphyrin (**THPP**) was performed by dialysis. **AcKL-2** lignin was dissolved in acetone at a concentration of 2 g L^{-1} in the presence of the porphyrin at a concentration of 0.2 g L^{-1}. Acetone was chosen for these nanoparticle preparations because **THPP** is not soluble in THF. The solution obtained was then dialyzed against distilled water for 24 hours. The amount of porphyrin encapsulated in the nanoparticles was evaluated as follows: nanoparticles were centrifuged (2750 × *g*, 20 minutes) and washed with distilled water, and then, the nanoparticles were suspended in a fixed volume of water. A known volume of nanoparticles was dissolved in a known volume of acetone, to release the encapsulated molecules by destroying the structure of the nano-objects. The quantity of **THPP** was calculated in the acetone solution, and then extrapolated to the originally encapsulated THPP in the lignin nanoparticles, through UV-Visible absorption spectroscopy, by monitoring the absorbance at 419 nm. The concentration of **THPP** encapsulated in **NP-THPP** was then evaluated using the molar extinction coefficient of **THPP** (388 500 L mol^{-1} cm), calculated from standard solutions of **THPP** in acetone, with **THPP** concentrations ranging from 7.7×10^{-7} to 2.7×10^{-6} mol L^{-1}.

Docking calculations

In order to investigate possible preferential binding sites of **THPP** on the surface of lignin, docking calculations were performed using Autodock Vina.[33] For each lignin model, 1000 snapshots were taken at regular intervals during the 100 ns heating simulations. **THPP** was then docked on the whole polymer for each of these snapshots, with an exhaustiveness factor of 20. The energy range from the most to the least favorable poses was set to 5 kcal mol^{-1}.

Free molecular dynamics simulations

Free MD simulations were performed using Gromacs 5.1.[34] They were integrated using a 2 fs time step and the leap-frog Verlet scheme. Cutoffs for coulombic and van der Waals interactions were set to 1.2 nm, and particle mesh Ewald was used for long-range interactions. A switch function was used for van der Waals interactions between 0.9 and 1.0 nm. Temperature and pressure were kept constant at 298 K and 1 atm (isotropically). Periodic boundary conditions were used in every dimension. Bond constraints were handled by LINCS.[35] After an energy minimization using the steepest-descent algorithm, a 200 ps equilibration simulation was run with the v-rescale thermostat (τ_T = 0.1 ps) and Berendsen barostat (τ_p = 1.0 ps, compressibility = 4.5×10^{-5} bar^{-1}). Then, production MD simulations were run with identical parameters, except for the barostat which was Parrinello–Rahman with τ_p = 5.0 ps.

The CHARMM force field for lignin and the TIP3P model were used for lignin and water. THF and acetone parameters were taken from the CHARMM36 force field.[30] **THPP** topology was obtained with the CgenFF program.[36,37]

Dialysis MD simulations

Dialysis was simulated by gradually replacing the initial solvent (acetone) with water during MD simulations. For this purpose, 100 cubic systems of solvent mixtures were prepared, in which the molar ratio of organic solvent (i) varied gradually from 0 to 100%. The volume V of each system was 27 nm^3. The initial number of water molecules ($N_{H_2O,i}$) in each mixture was determined according to eqn (1), based on experimentally determined densities for water–acetone mixtures (ρ_i).

$$N_{H_2O,i} = \frac{N_A \times V \times \rho_i}{M_{H_2O} + \frac{i}{1-i} \times M_{acetone}} \quad (1)$$

where N_A is the Avogadro constant, and M_{H_2O} and $M_{acetone}$ the molar weights of water and acetone, respectively. The densities (ρ_i) of the acetone–water mixtures were respectively fitted from ref. 38 to eqn (2) with $R^2 = 0.999$ and 0.996.

$$\rho_i = 173.21i^2 - 385.62i + 1000 \quad (2)$$

For each mixture, a 10 ns NPT simulation was performed and convergence of the density was ensured.

For the dialysis MD simulation, one unfolded lignin model was initially solvated with 100% acetone, along with 2 **THPP** molecules randomly placed in the solvent. The size of the dodecahedron box was adjusted so that the shortest distance between the lignin or **THPP** molecules to the edge of the box was 1.0 nm. During dialysis, every 5 ns, the solvent was removed, and the volume of the box was readjusted as mentioned above; this ensured that lignin did not interact with itself in the event of an unfolding, and allowed us to save computational time when lignin folded on itself. Then, the system was re-solvated in the next solvent mixture, *i.e.*, with 1% (mol/mol) less acetone. The thermostat and barostat during dialysis were identical to those in equilibration MD simulations.

Results and discussion

Solvent dependent conformation of lignin

To assess the behavior of acetylated lignin in water or in THF, free MD simulations were performed in those two solvents. First, the initial structures for the 9 acetylated lignin models were taken at the end of the simulated annealing simulations in water. After 100 ns of free MD simulation in water, the lignin models remained folded in small nanoparticles with an average diameter of 4.6 nm. This folding mimics the formation of NPs observed experimentally. Then, the water was stripped from the last structure of the free MD simulation, the lignin was resolvated in THF, and simulated for 100 ns (200 ns for L0a-acetyl).

For all these simulations, the solvent accessible surface area (SASA) was calculated and convergence was reached after 30 to 50 ns. SASA was averaged from 50 ns to the end of the simulations in water and in THF (Fig. S3†). It increased significantly in THF (152 ± 20 nm^2) compared to simulations in water (107 ± 5 nm^2). This indicates that acetylated lignin tends to form "crumpled globules" in water, and not in THF where it is soluble and unfolds. This is in good correlation with the previously reported behavior of native (non-acetylated) lignin.[39]

Additionally, no correlation was found between the number of branches in the lignin polymer (from 0 to 6 in 61 guaiacyl units) and SASA in either solvent (Fig. S4†). On the contrary, there was no significant difference between either SASA in water. This suggests that lignin adopts conformations of maximum packing in this solvent, where the SASA is minimized and thus it is independent of branching.

Determination of critical water concentration

Preparation of nanoparticles from acetylated lignin is based on the hydrophobicity of the modified lignins. During a gradual addition of water to a solution of lignins in a water-miscible organic solvent, the proportion of the organic solvent decreases. As a consequence, the lignin molecules begin to associate in the form of spheres to minimize hydrophobic interactions, until the formation of nanometric size particles, when the solvent is mainly composed of water. This progressive association can be demonstrated by measuring the intensity of the light scattered by an organic solution of lignins as a function of the volume of water added. The results obtained for **AcKL-1** and **AcKL-2** initially dissolved in THF are presented in Fig. 1. As the graph shows, for the two acetylated lignin solutions, the intensity of the scattered light increases suddenly from a water proportion of 30%, which is a sign that the polymer chains begin to aggregate. It should also be noted that the intensity of the scattered light increases more rapidly in the case of **AcKL-2** than **AcKL-1**, signifying that the association of lignins takes place more slowly in the latter case. This proportion of water, from which nanoparticles begin to form, is defined as the critical water concentration (CWC).[40] This concentration, although the same for the two lignins studied, is 10% lower than the one obtained by Qian *et al.*[24] These results are not surprising because Qian *et al.* used a lignin with a molar weight of 4200 g

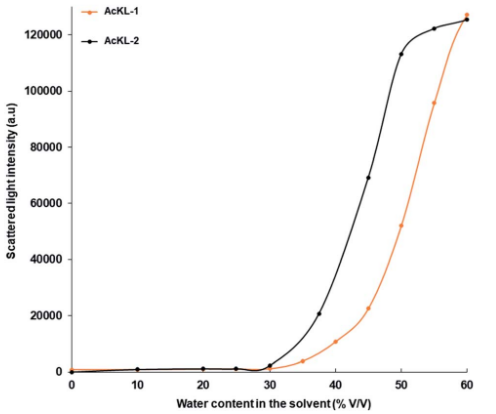

Fig. 1 Evolution of the scattered light intensity by acetylated lignin solutions in THF as a function of the quantity of added water.

mol^{-1} against lignins that are 13 100 and 9900 g mol^{-1} for **AcKL-1** and **AcKL-2**, respectively, and it has been previously described that the CWC of a polymer solution is a function of it molar mass.

The CWC was also evaluated with dialysis MD simulation, starting from 100% acetone. A decrease of the SASA was observed after the solvent mixture was 93% water (% mol_{water}/$mol_{acetone}$), which is equivalent to 76% water (% v_{water}/$v_{acetone}$) (Fig. S4†). The higher CWC compared to experimental results shown in Fig. 1 could be explained by the difference of solvent (THF *vs.* acetone) or by the difference of polymer molar mass.

Preparation of acetylated lignin nanoparticles

Nanoparticles were prepared from two sources of softwood kraft acetylated lignins, **AcKL-1** and **AcKL-2**, according to two different methods: by addition of an anti-solvent and by dialysis.

Anti-solvent addition. This method of preparation is based on the work of Qian *et al.*[24] and consists in a gradual addition of water to a THF solution of acetylated lignins. Nanoparticles were made according to this method, from acetylated lignins **AcKL-1** and **AcKL-2**, and respectively named **NP-1′** and **NP-2′**. For each source of lignin, preparations were made in ten replicates. The size distribution of the obtained nano-objects was then estimated for each case by DLS spectroscopy. Also, transmission electron microscopy analyses complemented these observations. Analysis of the size distribution of **NP-1′** and **NP-2′** (Fig. 2 and Table S3†) showed that both nanoparticles were obtained with mean sizes of 60.54 nm and 80.02 nm, while the distribution of 95% of the nanoparticle population (D_{95}) is found between 24.9 and 96.18 nm, and 30.18 and 129.86 nm, respectively. Thus, we can observe a slight variation in the mean size, depending on the starting material used. These observations were confirmed by transmission electron microscopy analysis. These results should be qualified in view of the low repeatability observed during the various preparations. Indeed, regardless of the starting material used, large standard deviations from the average particle diameters were observed.

Dialysis. This method of preparation consists in dissolving acetylated lignin in a water-miscible solvent such as THF or acetone, and in dialyzing the lignin solution against water. During this process, the organic solvent is gradually exchanged with water, resulting in the aggregation of acetylated polymer chains and thus leading to the formation of nanoparticles, as was described by molecular dynamics simulations. Nanoparticles were made according to this method from acetylated lignins **AcKL-1** and **AcKL-2** and respectively named **NP-1** and **NP-2**. Five preparations were made for each source of lignin. The size distributions of the nanoparticles obtained were estimated for each case by DLS spectroscopy (Fig. 2). The obtained mean sizes correspond to 157 nm and 163.3 nm, respectively, while their D_{95} is found to be between 45.82 and 268.18, and 52.18 and 274.42 nm, respectively. These observations were confirmed by transmission electron microscopy analysis (Fig. 2).

The two previously described methods have been compared, in order to choose the more suitable one for the preparation of nanoparticles, and especially to study their ability for drug encapsulation.

Although nanoparticles obtained by anti-solvent addition could be of smaller size than those obtained by dialysis, this first method has many disadvantages compared to dialysis, the first of them being that there is a high variance found between the samples (Fig. 2 and Table S1†). Indeed, the sizes observed

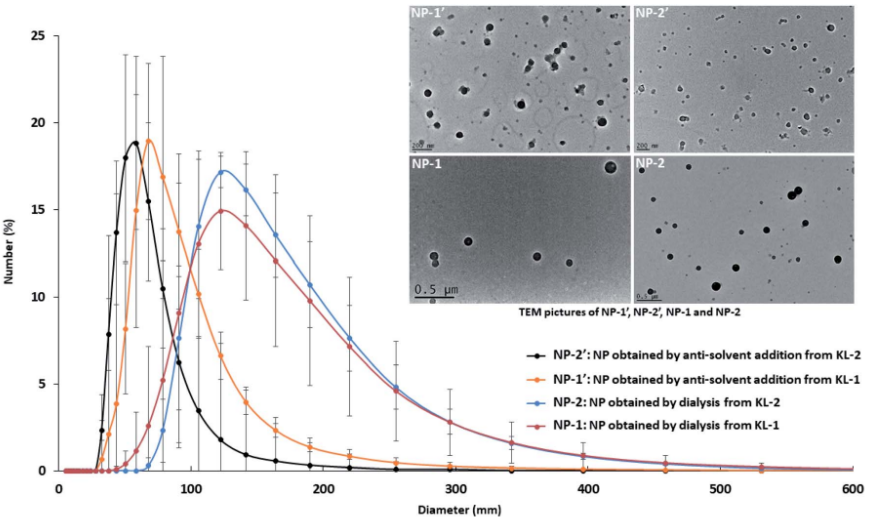

Fig. 2 Size distribution of NP-1′, NP-2′, NP-1 and NP-2. Inset: TEM pictures of NP-1′, NP-2′, NP-1 and NP-2.

for nanoparticles produced by the anti-solvent method vary significantly between the different syntheses, while the size of the nanoparticles obtained by dialysis is more constant. Therefore, this latter method allows us to work on populations of nanoparticles having relatively constant sizes.

SEM pictures (Fig. 3) confirm these observations and clearly show that several populations of nanoparticles, with different morphologies, were obtained by the anti-solvent method, while the ones obtained by dialysis are relatively similar in their shape, size and morphology.

In addition, the anti-solvent method involved a filtration step, in which a large proportion of the nanoparticles were retained on the filter. This provoked a mass concentration of lignin nanoparticles, not only too low, but also too complex to determine. This method therefore does not seem appropriate for the production of nanoparticles for biological activity measurements, where nano-objects have to be in sufficient and known quantity. Conversely, dialysis not only allowed the preparation of nanoparticles in sufficient quantity, but also the estimation of the mass concentration in solution. Indeed, no significant loss of material was observed by this method of preparation. To ensure this, **NP-2** solutions were lyophilized, and the mass of each residue was determined. These masses were found to be substantially identical to the masses of lignins initially introduced into the dialysis membranes since the observed mass loss is less than 1% (Table S4†).

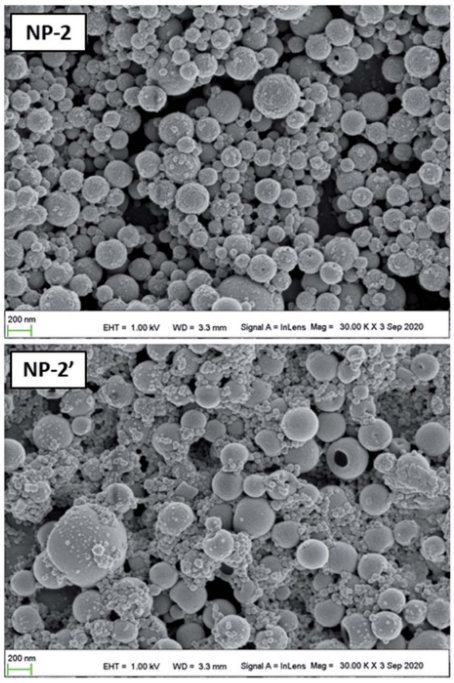

Fig. 3 SEM pictures of **NP-2** and **NP-2'**.

Finally, the production of nanoparticles by dialysis has the advantage of being, experimentally, the simpler of the two methods. Indeed, it requires fewer steps than the anti-solvent method. Moreover, it is not necessary to leave the acetylated lignin solution for three days before the nanoparticle preparation step as various tests have shown that only twenty minutes of stirring is necessary for a good future structuring of the nanoparticles.

In conclusion, dialysis, by making it possible to obtain nanoparticles in a simple and repeatable manner, appeared to be the most suitable method for the preparation of nanoparticles of acetylated lignins.

Stability of lignin nanoparticles prepared by dialysis

In order to test the stability and endurance of the acetylated lignin nanoparticles, we subjected them to several treatments. One of the key steps in the preparation of lignin nanoparticles is their centrifugation to collect and concentrate them. During this step, nanoparticles are subjected to high centrifugal forces. It is therefore fundamental to know if the nanoparticles can endure this stage. Transmission electron microscopy observations showed that no degradation of acetylated lignin nanoparticles was observed after centrifugation up to 10 000 $\times$ g. Furthermore, TEM pictures (Fig. S5†) showed that nanoparticles keep their spherical shape after this step. The stability of nanoparticles was also evaluated over time. The size distribution of **NP-2** was measured regularly by DLS spectroscopy for 36 days. The analysis of the results did not reveal any degradation of the nanoparticles over this period. Considering the advantages outlined in previous paragraphs and the stability that **NP-2** demonstrated during and after centrifugation and over time, dialysis was retained as the method of choice for the preparation of acetylated lignin nanoparticles in the rest of this work.

Separation of nanoparticle populations by centrifugation

We have demonstrated so far the feasibility of our method for the preparation of acetylated lignin nanoparticles. However, the obtained nanoparticles have a heterogeneous distribution of sizes, which could diminish their potential for further applications. Thus, it was demonstrated that nanoparticles could be separated through differential centrifugal speeds, thus allowing nanoparticle populations with a narrower size distribution to be obtained. Therefore, after being prepared by dialysis, nanoparticles were centrifuged under the normal centrifugation conditions (2740 $\times$ g, 20 minutes). The supernatant was recovered and centrifuged at a higher speed (5480 $\times$ g, 20 minutes); the obtained nanoparticles were recovered, and the supernatant was treated in the same way at 8220 and 8768 $\times$ g, for 20 minutes each. The recovered nanoparticle pellets were then suspended in distilled water and analyzed by DLS. The size distributions of the obtained nanoparticles were compared in Fig. 4.

It was observed that with an increasing applied centrifugal force, the mean size decreased from 253.2 nm to 66.18 nm. Also, a decrease of the D_{95} was observed when we compared the D_{95}

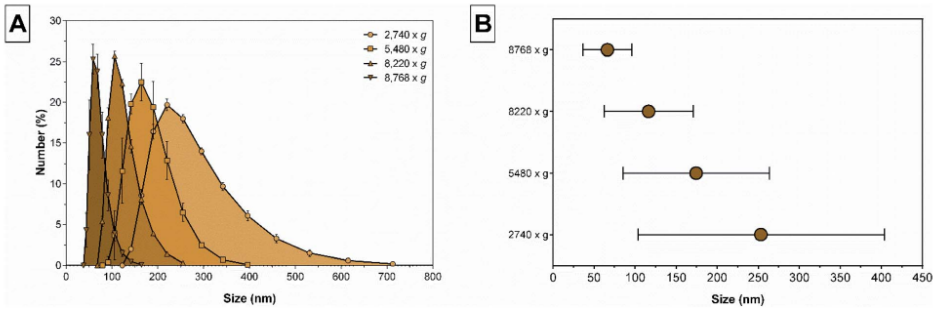

Fig. 4 (A) Distribution curves for the obtained nanoparticles at different centrifugal forces; (B) mean size obtained for nanoparticles at different centrifugal forces.

with an applied centrifugal speed of 2740 × *g* (103.36 nm to 403.4 nm) to that when 8768 × *g* was applied (36.46 to 95.9 nm). These analyses demonstrated that using differential centrifugation speeds allows nanoparticles with decreasing mean size and increasingly tight population distributions to be collected. So, although normally a relatively wide distribution of size of nanoparticles is obtained, smaller fractions can also be obtained by a simple modification of the centrifugation procedure.

Optimization of the preparation by dialysis

To complete the study on this method of preparation, we evaluated various factors that can influence the structure of nanoparticles of acetylated lignins. Herein, we will only focus on **NP-2** nanoparticles.

The influence of the solvent in which the acetylated lignins are initially dissolved was evaluated. The **AcKL-2** material was dissolved at a concentration of 2 g L^{-1} in various organic solvents: acetone, dimethylformamide (DMF) and dimethylsulfoxide (DMSO), all three being water-miscible. Each preparation was made in triplicate. No nanoparticle was formed when **AcKL-2** was initially dissolved in DMF or DMSO, while nanoparticles (**NP-2-Atn**) were obtained with acetone. However, nanoparticles could also be obtained from a mixture of THF and DMSO, at a 8 : 2 proportion. The nanoparticles obtained indicated that the addition of DMSO to the mixture increased the nanoparticles' mean size from 124.7 to 184.6 nm, but a more drastic effect is observed on the width of the D_{95} distribution, going from a basal 54 to 195.4 nm to 12.06 to 357.14 nm when DMSO is added to the mixture. Nevertheless, nanoparticles formed from a starting solution of THF or acetone, and both solutions had similar size distribution profiles (Fig. S6†). These various findings were confirmed by scattering and transmission electron microscopy (Fig. S7 and S8†). SEM analysis also showed that the morphology of nanoparticles prepared with acetone is not different from that prepared using THF, thus making it possible to validate the use of acetone and THF as solvents for the preparation of acetylated lignin nanoparticles. Also, the use of DMSO as a mixture is possible, but the mean size and D_{95} range are increased (Table 2). However, the choice of a more polar solvent, like DMSO, may enable the encapsulation of highly insoluble compounds, such as phthalocyanines and porphyrins.

The influence of the mass concentration of acetylated lignins in the starting solution was also studied. **AcKL-2** was dissolved to obtain concentrations of 1, 2 and 4 g L^{-1} in THF. The size

Table 2 Characteristics of nanoparticles based on acetylated lignins, as a function of the solvent, the starting concentration and the degree of acetylation of lignins

Acetylated lignins	Starting concentration (g L^{-1})	Acetylation rate (%)	Solvent	NP formation	Mean size (nm)	Distribution range with 95% of the nanoparticles (D_{95})
AcKL-2	2	100	THF	Yes	163.3	45.82–268.18
			Acetone	Yes	146.7	56.8–236.6
			DMSO	No	—	—
			DMF	No	—	—
			DMSO : THF 8 : 2	Yes	184.6	12.06–357.14
	1	100	THF	Yes	156.2	42.64–269.76
	4	100	THF	Yes	227.2	79.12–375.28
Ac_7KL-2	2	7	THF	Yes	95.04	45.8–144.28
Ac_{35}KL-2	2	35	THF	Yes	107.1	43.92–170.28
Ac_{59}KL-2	2	59	THF	Yes	102.8	43.76–161.84

distributions of the nanoparticles formed, respectively named **NP-2** (1 g L^{-1}),**NP-2** (2 g L^{-1}) and **NP-2** (4 g L^{-1}), were analyzed by DLS spectroscopy (Fig. S9†) and results are reported in Table 2. Each preparation was made in triplicate.

NP-2 (4 g L^{-1}) exhibited a medium size of around 227.2 nm, which is significantly higher than that of **NP-2** (1 g L^{-1}) and **NP-2** (2 g L^{-1}), which were respectively equal to 156.2 and 163.3 nm. In addition, the particle size distribution of **NP-2** (4 g L^{-1}) extended over a much larger range than **NP-2** (1 g L^{-1}) and **NP-2** (2 g L^{-1}) as the D_{95} of **NP-2** (4 g L^{-1}) is wider (79.12 to 375.28 nm) than the **NP-2** (1 g L^{-1}) and **NP-2** (2 g L^{-1}) distributions (42.64 to 269.76 nm and 52.18 to 274.42 nm, respectively). The results indicated that the nanoparticles obtained, whether with 2 g L^{-1} or 1 g L^{-1}, share the same distribution and mean size. Nevertheless, nanoparticles prepared with a starting solution of 2 g L^{-1} were routinely prepared, as more nanoparticles could be obtained from the same batch and with the same quality.

The effect of the degree of lignin acetylation on nanoparticle formation was also investigated. For this purpose, three partially acetylated lignins, respectively at 7% (**Ac_7KL-2**), 35% (**Ac_{35}KL-2**) and 59% (**Ac_{59}KL-2**), were dissolved in THF to achieve a concentration of 2 g L^{-1}. The size distributions of the nanoparticles formed, respectively named **NP(Ac_7KL-2)**, **NP(Ac_{35}KL-2)** and **NP(Ac_{59}KL-2)**, were measured and compared with that of the fully acetylated **NP-2** nanoparticles (Fig. S10†). As shown in Table 2, the nanoparticles formed from partially acetylated materials have similar mean diameters: 95.04, 107.1 and 102.8 nm for **NP(Ac_7KL-2)**, **NP(Ac_{35}KL-2)** and **NP(Ac_{59}KL-2)**, respectively. These mean diameters appeared to be smaller than the ones obtained for nanoparticles made from totally acetylated lignins. Moreover, the size distributions of nanoparticles prepared from partially acetylated lignins were narrower than that of **NP-2**. Indeed, D_{95} of nanoparticles prepared from partially acetylated lignins ranges between 40 and 170 nm. The incomplete acetylation of the polymers therefore seems to favor the formation of nanoparticles of smaller sizes. These results agreed with those presented by Qian *et al.*[24] whereby the authors obtained particles with similar sizes by preparing them *via* the addition of an anti-solvent to solutions of partially acetylated lignins (82 and 94%) in THF. SEM pictures of **Ac_7KL-2** (Fig. S11†) show that, apart from the size, the nanoparticles prepared from partially acetylated lignins do not show any differences in morphology compared to those prepared from fully acetylated lignins.

THPP encapsulation

In order to validate the feasibility of the encapsulation of hydrophobic bioactive compounds in acetylated lignin nanoparticles, a poorly water-soluble model compound, 5,10,15,20-tetrakis(4-hydroxyphenyl)porphyrin, abbreviated **THPP** (Fig. 5), was encapsulated. This compound also has the advantage of having a distinguishable UV-Visible spectrum, facilitating the monitoring of its encapsulation. The encapsulation of **THPP** was performed *via* dialysis according to the work described by Figueiredo *et al.*,[41] on the encapsulation of sorafenib and capecitabine in lignin and metal-complexed lignin nanoparticles. The obtained nanoparticles (abbreviated **NP-THPP**) were characterized by DLS spectroscopy (Fig. 6A), scattering electron microscopy (Fig. 6B) and transmission electron microscopy (Fig. S12†).

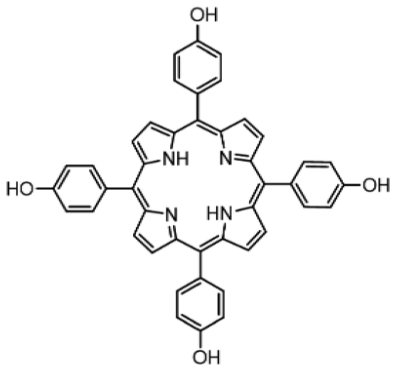

Fig. 5 Chemical structure of 5,10,15,20-tetrakis(4-hydroxyphenyl) porphyrin (THPP).

NP-THPP nanoparticles were smaller (99.17 nm) than **NP-2-Atn** nanoparticles (146.7 nm). Additionally, a narrower distribution is found for **NP-THPP** (43.47 to 154.87 nm) than the distribution observed for **NP-2-Atn** (56.8–236.6 nm). This feature should indicate a strong interaction between nanoparticles and **THPP**. SEM analysis (Fig. 6B) shows that the morphology of **NP-THPP** is not different from that of **NP-2-Atn**. An encapsulation yield of 0.13 (±0.02) mmol of **THPP** per gram of lignin was determined by UV-Vis measurement at 419 nm, a wavelength where lignin light absorption is negligible. This encapsulation level corresponds to an encapsulation of 85 ± 12% of the **THPP** initially introduced. This value is quite similar to those obtained by Figuerido *et al.*,[41] respectively of 75% ± 10% and 68% ± 19% for capecitabine and sorafenib.

The stability of the encapsulation of **NP-THPP** was tested over time. A freshly prepared batch of **NP-THPP** was suspended in phosphate buffer (pH 7.0) and stored away from light. Periodically, a fraction of these nanoparticles was centrifuged (10 000 × *g*, 30 minutes), and both the supernatant and the centrifuged nanoparticles were analyzed through their UV-Vis spectra. Leaking of **THPP** on phosphate buffer is found only after ten days of suspension, but the leaked amount remained the same after 60 days. This leakage can be attributed to **THPP** found on the outermost part of the nanoparticles, where **THPP** is retained by weak interactions with lignins, and so is more susceptible to leaking out (Fig. 6C). Other methods, reported in the literature, where porphyrinic compounds were intended to be transported through lignin[42] or through other biopolymeric matrices,[43] generally involved chemical modification of the porphyrin in order to avoid undesired leaking. Thus, the present formulation seems to be able to encapsulate porphyrinic compounds, without further chemical modifications.

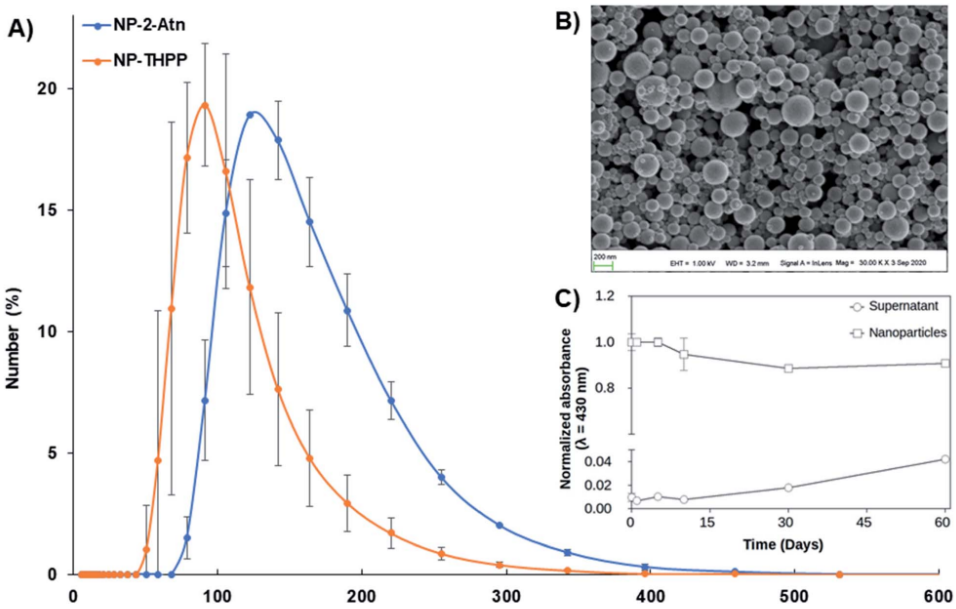

Fig. 6 (A) Size distributions of NP-2Atn and NP-THPP; (B) SEM picture of NP-THPP; (C) release of THPP from NP-2 over time.

Interaction of THPP at the surface of lignin nanoparticles

To evaluate the possible use of acetylated lignin nanoparticles as carriers for hydrophobic compounds, the interaction between **THPP** and lignin nanoparticles was investigated *in silico* by docking and molecular dynamics simulations.

For each lignin model, 1000 structures were taken from the simulated annealing simulations, and **THPP** was docked on these 1000 structures for each lignin model. Docking calculations showed no significant difference of affinity distribution between lignin models (Fig. S13†). No significant difference in average binding affinity was measured when performing time block analysis (10 blocks corresponding to 10 ns of simulated annealing simulation, Table S5†). Small differences were observed for the best docking affinity for each model (from -9.9 kcal mol^{-1} for L6-acetyl to -11.5 kcal mol^{-1} for L0a-acetyl); however these differences are smaller than the reported accuracy of Autodock Vina (2.85 kcal mol^{-1}). Moreover, the proportion of poses with a docking affinity lower than 9.0 kcal mol^{-1} was 0.8%, and these poses correspond to very short-lived lignin structures in the simulated annealing simulations (less than 1 ns). The spatial and temporal repartition of docking poses were visualized by projecting the density of **THPP** atoms on the lignin nanoparticle surface (ESI2, Video S1†). From one lignin conformation to the other, the position of the best docking poses fluctuated widely. Therefore, there is no specific binding site of **THPP** at the surface of lignin nanoparticles, and the interaction is independent of the lignin model used. This non-specificity correlates with the fractal and fluid nature of the lignin surface previously reported.[44]

Docking affinities suggest a strong interaction between **THPP** and lignin nanoparticles. These results were confirmed by MD simulations in water, where **THPP** molecules were initially placed in water, far from the nanoparticles. For every lignin model, all **THPP** molecules moved to the lignin nanoparticle surface in less than 10 ns. The position adopted by **THPP** molecules at the surface of lignin nanoparticles was the closest from the starting position in water. Then they stayed in the same position at the surface for the rest of the 100 ns simulations. This confirms the strong affinity of **THPP** for the lignin nanoparticle surface, and the lack of specific binding sites.

In order to assess whether **THPP** could be encapsulated inside the lignin polymer during dialysis rather than being located at its surface, 2 **THPP** molecules were added at the beginning of the dialysis simulation. These apolar molecules only started to interact with the acetylated lignin surface at around the CWC, *i.e.*, 76% (v/v) water in the solvent. At the end of the dialysis both molecules were located at the surface of the NP, and not encapsulated inside the polymer globules (Fig. 7). Both **THPP** molecules were close to each other on the surface, favoring π–π stacking between them. This suggests that stable **THPP** molecules, that did not leak during experimental measurements, were trapped in between different polymers forming a NP, rather than inside individual polymers.

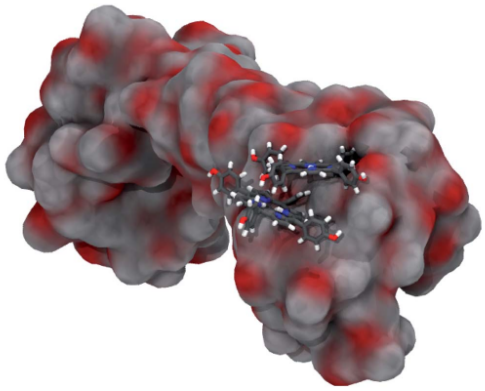

Fig. 7 Position of the THPP molecules at the surface of the L0a-acetyl NP at the end of the dialysis simulation.

Molecular description of the encapsulation in lignin nanoparticles

As the suspensions of **NP-1** and **NP-2** in water were stable over time, we can assume that their density is close to that of water. However, taking into account their respective average diameters (157 nm and 163.3 nm) and the molar weight of the acetylated lignin polymers (13 100 and 9900 g mol^{-1} for **AcKL-1** and **AcKL-2**, respectively), we find that the nanoparticles must consist of 9 $\times$ 10^4 to 1.4 $\times$ 10^5 individual polymers, aggregated during dialysis.

Assuming that these individual lignin polymers are spheres, the sum of their surfaces in one nanoparticle is about 4 μm^2, while the exterior surface of the spherical nanoparticle is about 0.08 μm^2. The ratio of the exterior surface to the total surface is therefore 2%. As the docking and MD simulations showed, **THPP** molecules are located at the surface of these polymers, with no specific binding site. Thus, the uniform repartition of **THPP** molecules at the surface of the polymers while nanoparticles aggregate during dialysis indicates that about 2% of **THPP** is located at the surface of lignin nanoparticles. The remainder is encapsulated inside the nanoparticle, between polymers. This correlates with the 2% increase of absorbance in the supernatant after 30 days (Fig. 6C). Therefore, this suggests that the leakage of **THPP** over time arises from the **THPP** molecules located at the surface of the nanoparticle, while **THPP** that is hidden at the surface of the polymers inside the nanoparticle remains encapsulated.

Conclusions

Acetylated lignin nanoparticles appear to be an economical and easy-to-prepare formulation. The procedure for preparing and obtaining the nanoparticles by dialysis indeed demonstrated its robustness, as we were able to obtain nanoparticles under several solvent conditions and substitutional degrees of lignin. Acetylated lignin nanoparticles seem to be an appropriate vehicle for the delivery of small photosensitizer molecules. Experiments so far had demonstrated the ease of their preparation, being reproducible and quite stable as suspensions. The present experiments and our previous evidence of the photosensitizing activity of acetylated lignins may provide a powerful tool for photodynamic applications. The biological role of nanoparticles loaded with photosensitizing molecules is an interesting topic that is currently being addressed in our research group, as an antibacterial treatment. Future work includes the encapsulation of other porphyrinic compounds, the analysis of their spectrophotometric and photophysical properties, and also a more detailed analysis of their endurance under several conditions. Furthermore, we expect that this formulation will have broader applications, as an oxidant of small molecules in aqueous media, an application with an environmental impact.

Conflicts of interest

There are no conflicts to declare.

Acknowledgements

We thank the "Conseil Régional du Limousin" and European Union for their financial support. Indeed, this work is a part of the ITN-EJD-2017 project POLYTHEA which has received funding from the European Union's Horizon 2020 research and innovation programme under the Marie Sklodowska-Curie grant agreement no. 764837. The authors are indebted to Dr Pierre Carles for TEM analysis, Eloise Hyvernaud for SEM analysis and Dr Yves Champavier for the NMR analysis. The authors thank CALI and its team that supported the molecular modelling calculations; CALI is the calculation center of the University of Limoges, funded by Région Limousin, the European Union, University of Limoges, and XLIM, IPAM, and GEIST research institutes. GF thanks Loukas Petridis for providing the lignin force field. The authors also thank Daire Gibbons for his help in improving the English of this paper.

References

1 F. H. Isikgor and C. Remzi Becer, *Polym. Chem.*, 2015, **6**, 4497–4559.
2 R. A. Sheldon, *Green Chem.*, 2014, **16**, 950–963.
3 A. Corma, S. Iborra and A. Velty, *Chem. Rev.*, 2007, **107**, 2411–2502.
4 G. W. Huber, S. Iborra and A. Corma, *Chem. Rev.*, 2006, **106**, 4044–4098.
5 J. N. Chheda, G. W. Huber and J. A. Dumesic, *Angew. Chem., Int. Ed.*, 2007, **46**, 7164–7183.
6 W. Boerjan, J. Ralph and M. Baucher, *Annu. Rev. Plant Biol.*, 2003, **54**, 519–546.
7 V. K. Thakur, M. K. Thakur, P. Raghavan and M. R. Kessler, *ACS Sustainable Chem. Eng.*, 2014, **2**, 1072–1092.
8 R. Rinaldi, R. Jastrzebski, M. T. Clough, J. Ralph, M. Kennema, P. C. A. Bruijnincx and B. M. Weckhuysen, *Angew. Chem., Int. Ed.*, 2016, **55**, 8164–8215.

9 V. Ugartondo, M. Mitjans and M. P. Vinardell, *Bioresour. Technol.*, 2008, **99**, 6683–6687.
10 A. Barapatre, A. S. Meena, S. Mekala, A. Das and H. Jha, *Int. J. Biol. Macromol.*, 2016, **86**, 443–453.
11 O. Gordobil, R. Herrera, M. Yahyaoui, S. İlk, M. Kaya and J. Labidi, *RSC Adv.*, 2018, **8**, 24525–24533.
12 G. J. Gil-Chávez, S. S. P. Padhi, C. V. Pereira, J. N. Guerreiro, A. A. Matias and I. Smirnova, *Int. J. Biol. Macromol.*, 2019, **136**, 697–703.
13 M. P. Vinardell and M. Mitjans, *Int. J. Mol. Sci.*, 2017, **18**, 1219.
14 M. H. Sipponen, H. Lange, C. Crestini, A. Henn and M. Österberg, *ChemSusChem*, 2019, **12**, 2038.
15 S. Iravani and R. S. Varma, *Green Chem.*, 2020, **22**, 612–636.
16 P. Figueiredo, K. Lintinen, J. T. Hirvonen, M. A. Kostiainen and H. A. Santos, *Prog. Mater. Sci.*, 2018, **93**, 233–269.
17 N. Maldonado-Carmona, T.-S. Ouk, M. J. F. Calvete, M. M. Pereira, N. Villandier and S. Leroy-Lhez, *Photochem. Photobiol. Sci.*, 2020, **19**, 445–461.
18 D. Kai, M. J. Tan, P. L. Chee, Y. K. Chua, Y. L. Yap and X. J. Loh, *Green Chem.*, 2016, **18**, 1175–1200.
19 C. Wang, S. S. Kelley and R. A. Venditti, *ChemSusChem*, 2016, **9**, 770–783.
20 S. Sen, S. Patil and D. S. Argyropoulos, *Green Chem.*, 2015, **17**, 4862–4887.
21 G. Marchand, C. A. Calliste, R. M. Williams, C. McLure, S. Leroy-Lhez and N. Villandier, *ChemistrySelect*, 2018, **3**, 5512–5516.
22 P. Buono, A. Duval, P. Verge, L. Averous and Y. Habibi, *ACS Sustainable Chem. Eng.*, 2016, **4**, 5212–5222.
23 A. Granata and D. S. Argyropoulos, *J. Agric. Food Chem.*, 1995, **43**, 1538–1544.
24 Y. Qian, Y. Deng, X. Qiu, H. Li and D. Yang, *Green Chem.*, 2014, **16**, 2156.
25 S. Salentinig and M. Schubert, *Biomacromolecules*, 2017, **18**, 2649–2653.
26 Y. Qian, Y. Deng, H. Li and X. Qiu, *Ind. Eng. Chem. Res.*, 2014, **53**, 10024–10028.
27 M. Lievonen, J. J. Valle-Delgado, M.-L. Mattinen, E.-L. Hult, K. Lintinen, M. A. Kostiainen, A. Paananen, G. R. Szilvay, H. Setälä and M. Österberg, *Green Chem.*, 2016, **18**, 1416–1422.
28 L. Petridis, R. Schulz and J. C. Smith, *J. Am. Chem. Soc.*, 2011, **133**, 20277–20287.
29 L. Petridis and J. C. Smith, *J. Comput. Chem.*, 2009, **30**, 457–467.
30 J. Huang and A. D. MacKerell, *J. Comput. Chem.*, 2013, **34**, 2135–2145.
31 W. Humphrey, A. Dalke and K. Schulten, *J. Mol. Graphics*, 1996, **14**, 33–38.
32 W. L. Jorgensen, J. Chandrasekhar, J. D. Madura, R. W. Impey and M. L. Klein, *J. Chem. Phys.*, 1983, **79**, 926–935.
33 O. Trott and A. J. Olson, *J. Comput. Chem.*, 2010, **31**, 455–461.
34 M. J. Abraham, T. Murtola, R. Schulz, S. Páll, J. C. Smith, B. Hess and E. Lindahl, *SoftwareX*, 2015, **1–2**, 19–25.
35 B. Hess, H. Bekker, H. J. C. Berendsen and J. G. E. M. Fraaije, *J. Comput. Chem.*, 1997, **18**, 1463–1472.
36 K. Vanommeslaeghe, E. Hatcher, C. Acharya, S. Kundu, S. Zhong, J. Shim, E. Darian, O. Guvench, P. Lopes, I. Vorobyov and A. D. MacKerell, *J. Comput. Chem.*, 2010, **31**, 671–690.
37 K. Vanommeslaeghe and A. D. MacKerell, *J. Chem. Inf. Model.*, 2012, **52**, 3144–3154.
38 K. T. Thomas and R. A. McAllister, *AIChE J.*, 1957, **3**, 161–164.
39 M. D. Smith, B. Mostofian, X. Cheng, L. Petridis, C. M. Cai, C. E. Wyman and J. C. Smith, *Green Chem.*, 2016, **18**, 1268–1277.
40 L. Zhang and A. Eisenberg, *Polym. Adv. Technol.*, 1998, **9**, 677–699.
41 P. Figueiredo, K. Lintinen, A. Kiriazis, V. Hynninen, Z. Liu, T. Bauleth-Ramos, A. Rahikkala, A. Correia, T. Kohout, B. Sarmento, J. Yli-Kauhaluoma, J. Hirvonen, O. Ikkala, M. A. Kostiainen and H. A. Santos, *Biomaterials*, 2017, **121**, 97–108.
42 H.-Y. Tse, S.-C. Cheng, C. S. Yeung, C.-Y. Lau, W.-H. Wong, C. Dong and S.-Y. Leu, *Green Chem.*, 2019, **21**, 1319–1329.
43 C. Ringot, N. Saad, F. Brégier, P. Bressollier, E. Poli, V. Chaleix, T. S. Ouk and V. Sol, *Photochem. Photobiol. Sci.*, 2018, **17**, 1780–1786.
44 L. Petridis, S. V. Pingali, V. Urban, W. T. Heller, H. M. O'Neill, M. Foston, A. Ragauskas and J. C. Smith, *Phys. Rev. E: Stat., Nonlinear, Soft Matter Phys.*, 2011, **83**, 061911.

Electronic Supplementary Material (ESI) for Nanoscale Advances.

Acetylated lignin nanoparticles as a possible vehicle for photosensitizing molecules

Guillaume Marchand[a], Gabin Fabre[b], Nidia Maldonado-Carmona[c], Nicolas Villandier[c], Stéphanie Leroy-Lhez[c]*

a. PEIRENE EA7500, Université de Limoges, Faculté de Pharmacie, 2 rue du Docteur Marcland, 87025 Limoges Cedex, France

b. UMR 1248 INSERM, Université de Limoges, Faculté de Pharmacie, 2 rue du Docteur Marcland, 87025 Limoges Cedex, France

c. PEIRENE EA7500, Université de Limoges, Faculté des Sciences, 123 rue du Albert Thomas, 87025 Limoges Cedex, France.

** Corresponding author: stephanie.lhez@unilim.fr*

ESI - Contents

1. Analysis of partially acetylated lignins Ac_7KL-2, Ac_{35}KL-2 and Ac_{59}KL-2

The IRTF analysis of the products shows clear signs of partial acetylation (Figure S 1). It is especially observed the appearance of bands corresponding to the valence vibrations of the C=O bonds of the aromatic and aliphatic esters (respectively at 1761 and 1739 cm^{-1}) and CO ester bonds (at 1190 cm^{-1}). The intensity of these bands is proportional to the quantity of anhydride used. Similarly, the disappearance of the valence band of the OH bonds between 3100 and 3600 cm^{-1} and the increase of the band located at 1370 cm^{-1}, corresponding to the vibrations of deformation of the CH bonds of the CH_3 is observed.

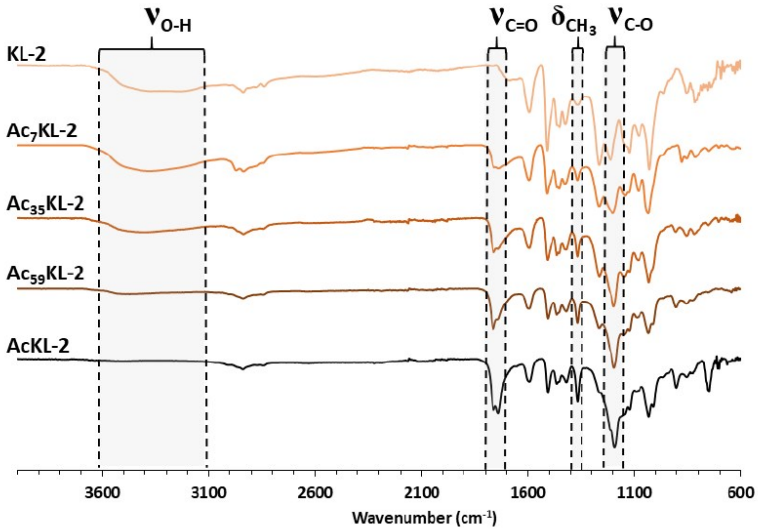

Figure S1. IRTF spectra of **KL-2** lignins before and after total or partial acetylation

^{31}P NMR spectroscopy also made it possible to confirm these previous observations. This analysis technique requires the prior functionalization of lignins with a reagent carrying a phosphorus atom: 2-chloro-4,4',5,5'-tetramethyl-1,3,2-dioxaphospholane (TMDP). The aliphatic alcohol and phenol functions of the polymer, functionalized by TMDP, exhibit different chemical shifts in ^{31}P NMR making it possible to differentiate them from one another. As showing on ^{31}P NMR spectra of partially acetylated products (Figure S 2) a progressive reduction of the signals corresponding to the different alcohol functions functionalized by TMDP is observed. No significant signal was observed in the case of fully acetylated lignin.

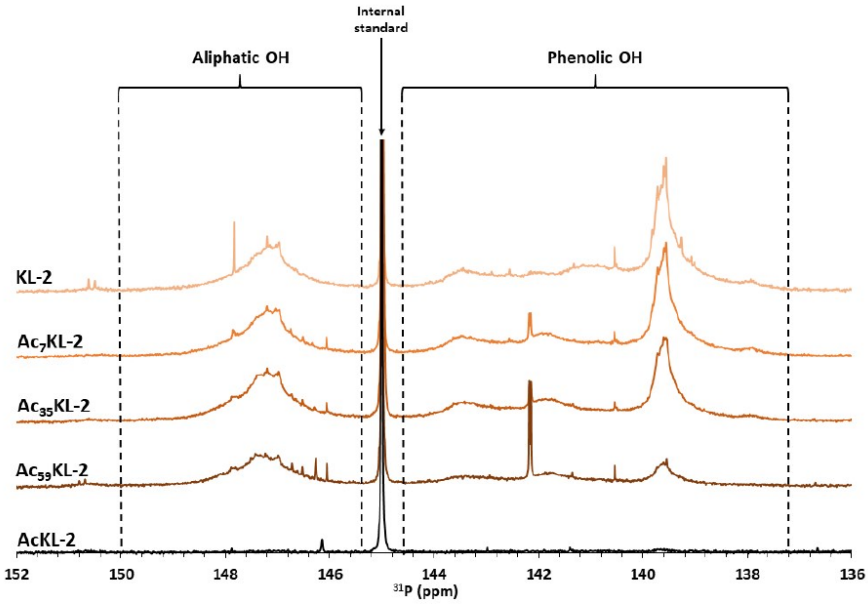

Figure S2. ^{31}P NMR spectra of phosphorylated **KL-2** lignins before and after total or partial acetylation.

^{31}P NMR make also possible to quantify the aliphatic and phenolic alcohols remaining on each material. This quantification method requires the use of an eternal standard. This compound must have a free hydroxyl group capable to react with TMDP. Cyclohexanol, molecule widely describe for this application, is employed. After acquisition, the integral of the signal of TMDP-derivatized alcohol of cyclohexanol is normalized to 1. The amount of hydroxy groups of each partially acetylated lignins are then determined as follow:

$$Number\ of\ OH\ groups\ (mol\ g^{-1}) = \frac{Quantity\ of\ cyclohexanol\ (mol)}{Quantity\ of\ lignins\ (g)} \times Value\ of\ the\ integral\ of\ the\ considered\ signal$$

Each sample (raw, fully and partially acetylated lignins) is analysed in triplicate. Obtained values are presented in the following table (Table S1):

Table S1. NMR data for KL-2 and partially or fully acetalized lignins

	KL-2	**AcKL-2**	**Ac_7KL-2**	**Ac_{35}KL-2**	**Ac_{59}KL-2**	**Integration area (ppm)**
Total aliphatic OH (mol g^{-1})	3.02	-	2.71	1.76	0.95	150.0-145,5
Total phenolic OH (mol g^{-1})	1.32	-	1.34	1.08	0.82	138.2 -144,5
Total OH (mol g^{-1})	4.34	-	4.05	2.83	1.78	-

A total alcohol remaining rate (**KL-2** total OH / partially acetylated lignins total OH) is calculated for each sample from which is deduced an acetylation rate:

Table S2. Acetylation Rate

	Ac_7KL-2	**Ac_{35}KL-2**	**Ac_{59}KL-2**
Total OH remaining	93%	65%	41%
Acetylation rate	7%	35%	59%

It was thus determined that respectively 7, 35 and 59% of the hydroxyl groups of the lignins **Ac_7KL-2**, **Ac_{35}KL-2** and **Ac_{59}KL-2** had been acetylated.

2. Molecular modelling of acetylated lignin nanoparticles formation

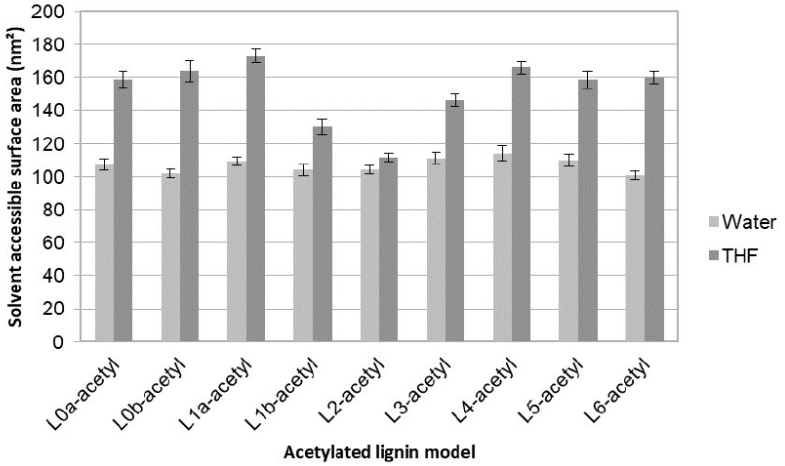

Figure S3. Solvent accessible surface area (SASA) of acetylated lignin models, in water or in THF, averaged over the molecular dynamics simulations (the first 50 ns were discarded for analysis).

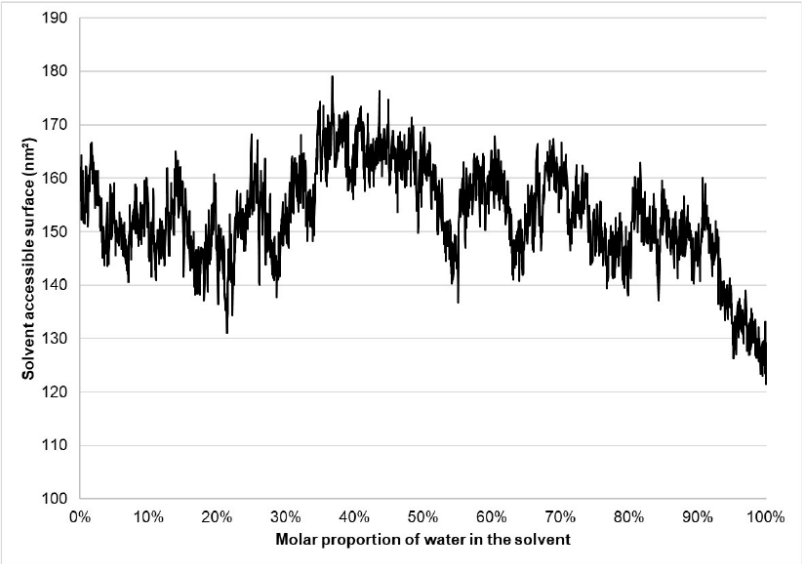

Figure S4. Solvent accessible surface along the dialysis MD simulation. 150 nm² is comparable to the unfolded lignin model. Folding towards 125 nm² started at 93% (mol/mol) water, or 76% (vol/vol) water.

3. DLS data of NP-1; NP-2; NP-1' and NP-2'

Table S3. DLS raw data for **NP-1'**, **NP-2'**, **NP-1** and **NP-2**

Size (nm)	Number (%)				Standard deviation			
	NP-1'	NP-2'	NP-1	NP-2	NP-1'	NP-2'	NP-1	NP-2
0.0	0.0	0.0	0.0	0.0	0.0	0.0	0.0	0.0
6.5	0.0	0.0	0.0	0.0	0.0	0.0	0.0	0.0
7.5	0.0	0.0	0.0	0.0	0.0	0.0	0.0	0.0
8.7	0.0	0.0	0.0	0.0	0.0	0.0	0.0	0.0
10.1	0.0	0.0	0.0	0.0	0.0	0.0	0.0	0.0
11.7	0.0	0.0	0.0	0.0	0.0	0.0	0.0	0.0
13.5	0.0	0.0	0.0	0.0	0.0	0.0	0.0	0.0
15.7	0.0	0.0	0.0	0.0	0.0	0.0	0.0	0.0
18.2	0.0	0.0	0.0	0.0	0.0	0.0	0.0	0.0
21.0	0.0	0.0	0.0	0.0	0.0	0.0	0.0	0.0
24.4	0.0	0.0	0.0	0.0	0.0	0.0	0.0	0.0
28.2	0.0	0.0	0.0	0.0	0.0	0.0	0.0	0.0
32.7	2.3	0.6	0.0	0.0	3.7	0.6	0.0	0.0
37.8	7.8	2.1	0.0	0.0	11.4	2.1	0.0	0.0
43.8	13.7	3.8	0.0	0.0	12.1	4.1	0.0	0.0
50.8	18.0	8.2	0.0	0.0	3.8	6.0	0.0	0.0
58.8	18.8	14.9	0.0	0.0	6.7	6.6	0.0	0.0
68.1	15.5	18.9	0.3	0.0	8.7	4.5	0.5	0.0
78.8	10.5	16.9	2.0	0.2	7.0	3.4	3.2	0.4
91.3	6.2	13.7	6.5	3.1	4.5	4.9	6.6	1.6
105.7	3.4	10.2	12.4	10.0	2.6	6.5	6.3	2.4
122.4	1.8	6.6	16.1	16.3	1.4	5.6	2.9	1.4
141.8	0.9	3.9	16.1	17.8	0.7	3.9	1.6	0.6
164.2	0.5	2.3	14.2	16.2	0.4	2.5	3.2	1.3
190.1	0.3	1.3	11.6	13.4	0.3	1.6	3.9	1.5
220.2	0.2	0.8	8.5	9.7	0.2	1.1	3.6	1.2
255.0	0.1	0.4	5.4	6.2	0.1	0.7	2.8	0.8
295.3	0.1	0.2	3.3	3.6	0.1	0.4	2.0	0.4
342.0	0.0	0.1	1.8	2.0	0.0	0.2	1.4	0.2
396.1	0.0	0.1	1.0	1.0	0.0	0.1	0.9	0.1
458.7	0.0	0.0	0.5	0.4	0.0	0.1	0.5	0.0
531.2	0.0	0.0	0.2	0.1	0.0	0.0	0.3	0.0
615.1	0.0	0.0	0.1	0.0	0.0	0.0	0.1	0.0
712.4	0.0	0.0	0.0	0.0	0.0	0.0	0.1	0.0
825.0	0.0	0.0	0.0	0.0	0.0	0.0	0.0	0.0
955.4	0.0	0.0	0.0	0.0	0.0	0.0	0.0	0.0

4. Measurement of the loss of material during dialysis

Table S4. Measurement of the loss of material during dialysis

	Mass of **KL-2** before dialysis (g)	Mass of **NP-2** obtained after dialysis (g)	Lost mass (%)
Measurement 1	2.016	1.985	1.54
Measurement 2	2.004	1.994	0.50
Measurement 3	1.998	1.989	0.45
Average	2.006	1.989	0.83 +/- 0.61

5. Influence of centrifugation on lignin nanoparticles shape

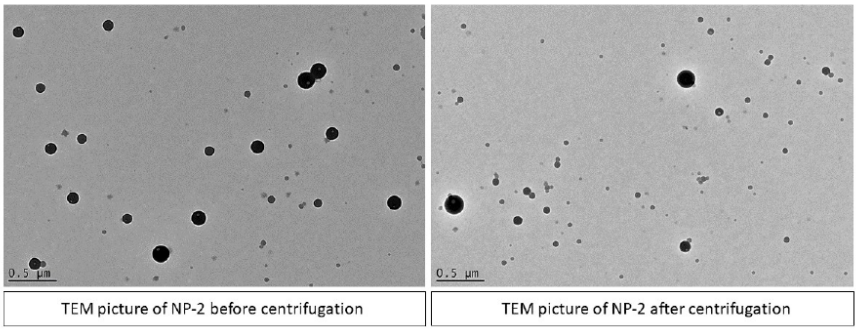

Figure S5.TEM pictures of **NP-2** before and after centrifugation.

6. Influence of the solvent in AcKL-2 nanoparticles preparation

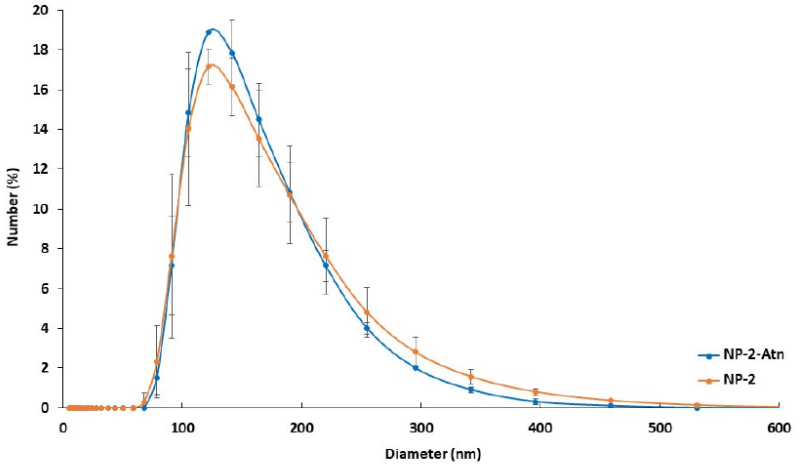

Figure S6. Size distribution of **NP-2** (prepared with THF as solvent) and **NP-2-Atn** prepared with acetone as solvent.

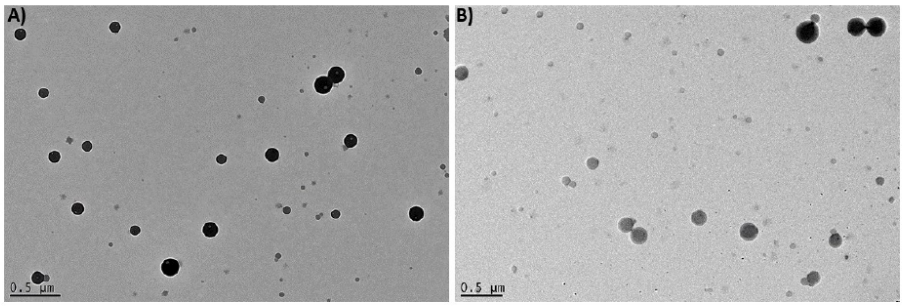

Figure S7. TEM pictures of **NP-2** using **A:** THF or **B:** acetone, as the starting solvent.

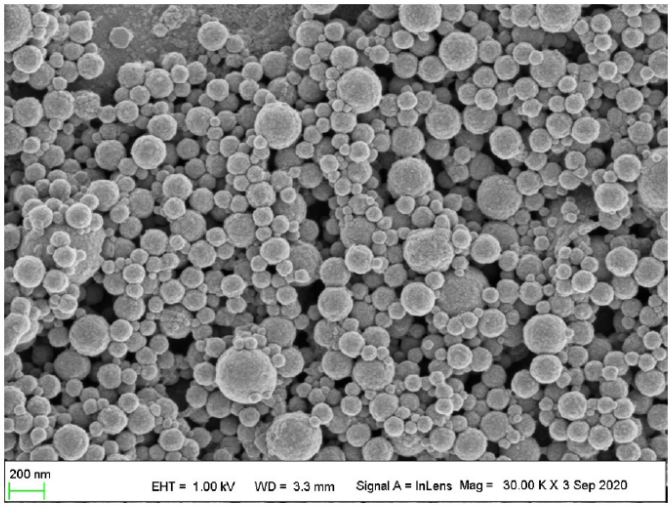

Figure S8. SEM picture of **NP-2Atn**

7. Influence of the initial lignin concentration in AcKL-2 nanoparticles preparation

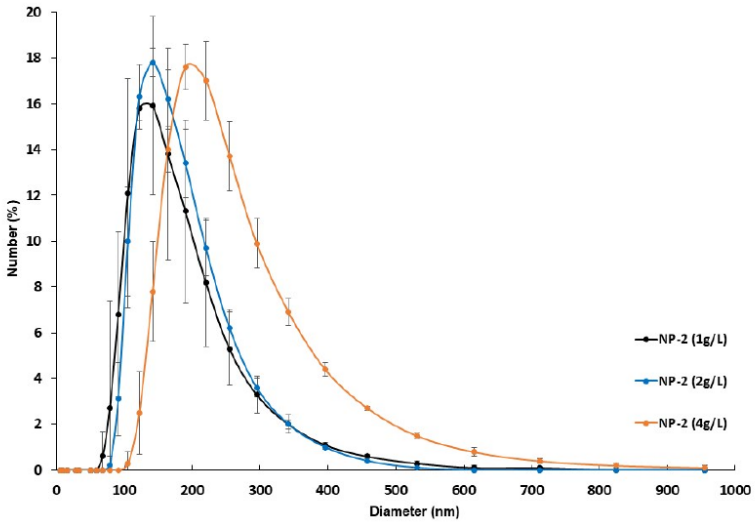

Figure S9. Size distribution of **NP-2(1g L^{-1})** (black lines), **NP-2(2g L^{-1})** (blue lines) and **NP-2(4g L^{-1})** (orange lines) nanoparticles (average over 3 independent measurements).

8. Influence of the degree of acetylation in AcKL-2 nanoparticles preparation

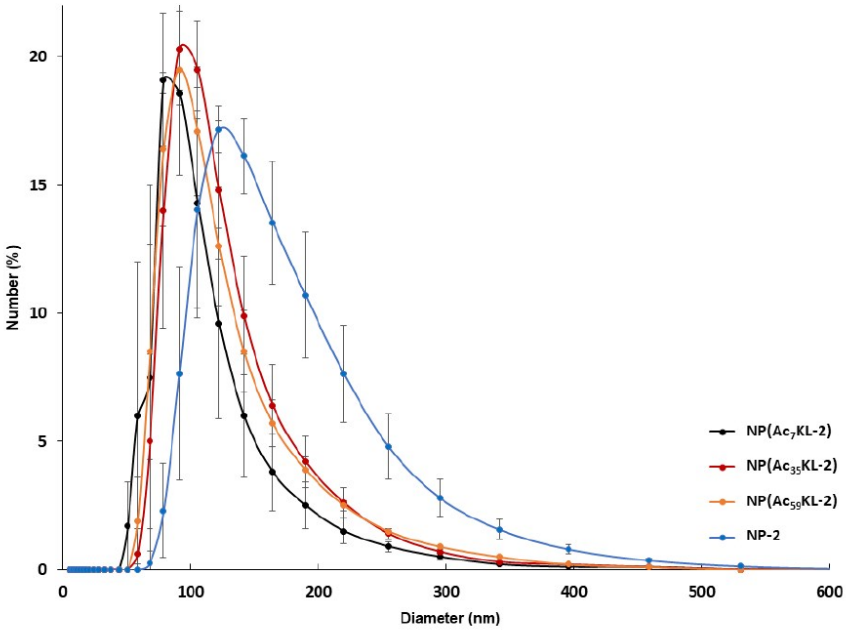

Figure S10. Size distribution of **NP(Ac_{10}KL-2)** (black lines), **NP(Ac_{40}KL-2)** (red lines), **NP(Ac_{60}KL-2)** (orange lines) and **NP-2** nanoparticles (blue lines) (average over 3 independent measurements).

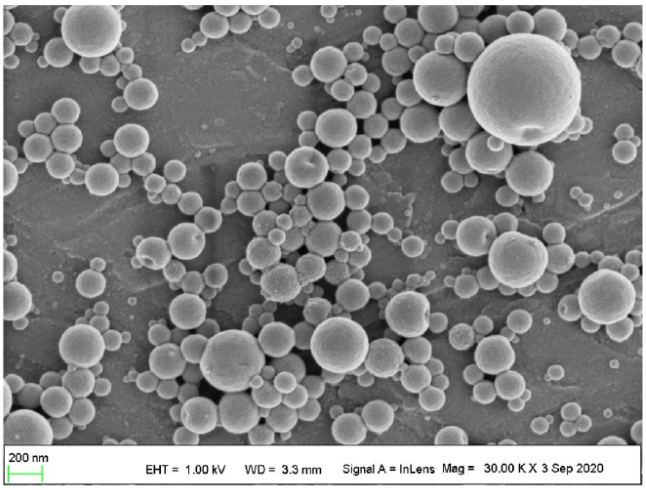

Figure S11. SEM picture of **NP(Ac_7KL-2)**

9. THPP encapsulation

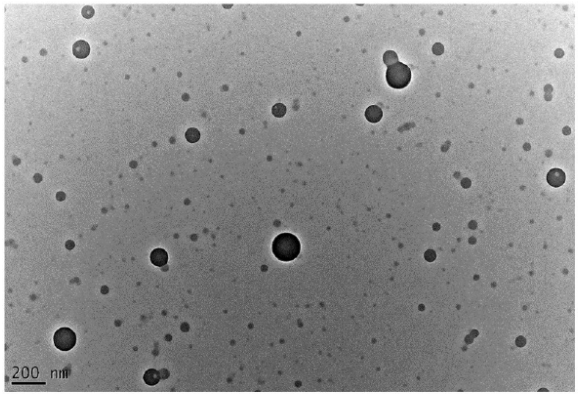

Figure S12. TEM pictures of **NP-THPP.**

10. Docking of THPP in acetylated lignin nanoparticles

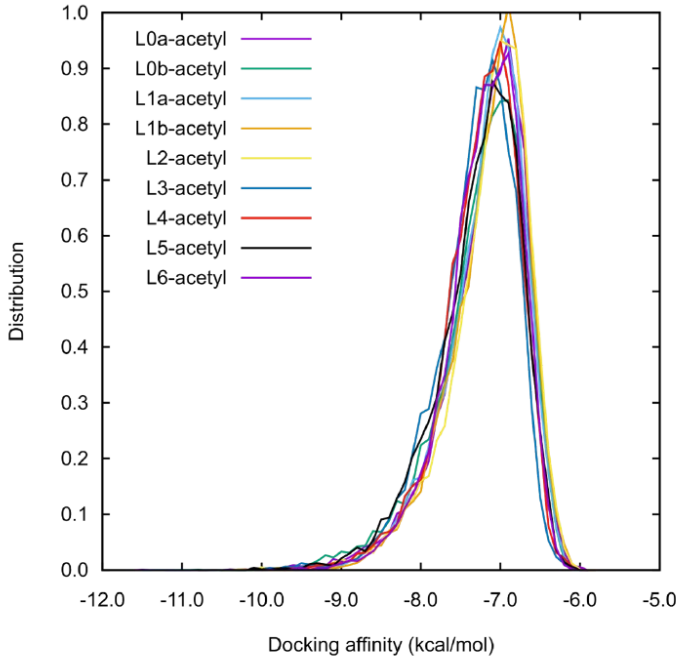

Figure S13. Distribution of docking affinities for each acetylated lignin model

Table S5. Minimum, maximum and average docking affinities for each acetylated lignin model

Lignin model	Minimum docking energy (kcal mol^{-1})	Maximum docking energy (kcal mol^{-1})	Average docking energy (kcal mol^{-1})
L0a-acetyl	-11.5	-6	-7.187
L0b-acetyl	-11	-6.1	-7.241
L1a-acetyl	-10	-6.2	-7.186
L1b-acetyl	-10.4	-6	-7.144
L2-acetyl	-10.3	-6	-7.144
L3-acetyl	-11.3	-6.1	-7.316
L4-acetyl	-9.9	-6.1	-7.25
L5-acetyl	-10.6	-6	-7.277
L6-acetyl	-9.9	-6.1	-7.215

Video S1. Density of **THPP** atoms from docking poses on the lignin nanoparticles surface along the simulated annealing trajectory. Red color indicates high density, and thus best docking poses for a given lignin NP conformation. The instability of the highest density (red spots) suggests that there is no specific binding site for **THPP** at the surface of lignin. Other acetylated lignin model provided similar results.

Page intentionally left in blank

II. Porphyrin-loaded nanoparticles as an antibacterial alternative

THPP is an efficient photosensitizer, which has been widely used for both PDT and PACT. However, although **THPP** is a good singlet oxygen producer in organic solvents, its triplet quantum yield is severely affected in aqueous media. This is due to the porphyrin's tendency to aggregate, forming strong intermolecular π-interactions, in the form of head-to-head aggregates (H-aggregates) or head-to-tail aggregates (J-aggregates) (Figure 5) [19].

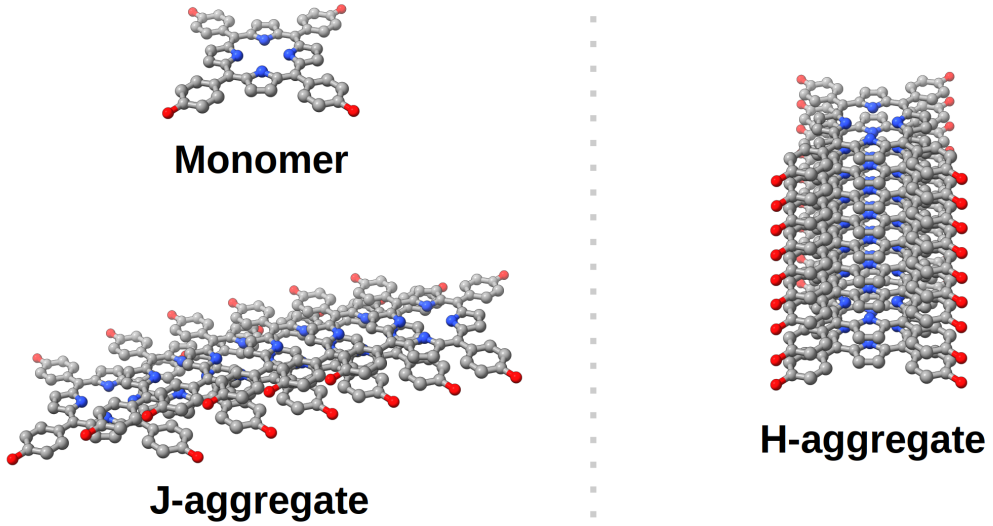

Figure 5: Depiction of porphyrinic monomers and how they aggregate to form J-aggregates (tail-to-head structure) or H-aggregates (head-to-head structure)

In our previous paper it was demonstrated the capacity of acetylated lignin nanoparticles to encapsulate **THPP**, a photosensitizer able to produce ROS through a Type-II mechanism [42]. However, the photophysical characterization of these porphyrin-loaded acetylated lignin nanoparticles was left unexplored, as well as the characterization of its antimicrobial activity.

In **Publication 4**, we present the physical and photophysical characterization of **THPP**-loaded acetylated lignin nanoparticles (**THPP@AcLi**). The characterization included absorption and fluorescence spectroscopy, and singlet oxygen production through electron paramagnetic resonance (EPR). The nanoparticles stability under long-term storage and light irradiation was demonstrated, showing that **THPP** does not leak out from the nanoparticles and that **THPP** does not photobleach under white-LED light irradiation. The **THPP@AcLi** nanoparticles were tested against five bacterial strains, three Gram-positive (*Staphylococcus aureus, Staphylococcus epidermidis* and *Enterococcus faecalis*) and two Gram-negative (*Escherichia coli* and *Pseudomonas aeruginosa*), demonstrating an effective photodynamic bacteriostatic effect against the Gram-positive bacteria, but not against the Gram-negative bacteria. Furthermore, the antibacterial effect was demonstrated solely to be due to the encapsulated porphyrin, with the non-loaded nanoparticles **@AcLi** being innocuous against bacteria, either with or without light irradiation.

Publication 4. "Porphyrin-Loaded Lignin Nanoparticles Against Bacteria: A Photodynamic Antimicrobial Chemotherapy Application" [43]

frontiers in Microbiology

ORIGINAL RESEARCH
published: 17 November 2020
doi: 10.3389/fmicb.2020.606185

Porphyrin-Loaded Lignin Nanoparticles Against Bacteria: A Photodynamic Antimicrobial Chemotherapy Application

*Nidia Maldonado-Carmona[1,2], Guillaume Marchand[3], Nicolas Villandier[1], Tan-Sothea Ouk[1], Mariette M. Pereira[2], Mário J. F. Calvete[2], Claude Alain Calliste[3], Andrzej Żak[4,5], Marta Piksa[5], Krzysztof J. Pawlik[5], Katarzyna Matczyszyn[6] and Stéphanie Leroy-Lhez[1]**

[1] PEIRENE Laboratory, Faculty of Sciences and Techniques, University of Limoges, Limoges, France, [2] Laboratory of Catalysis and Fine Chemistry, Department of Chemistry, University of Coimbra, Coimbra, Portugal, [3] PEIRENE Laboratory, Faculty of Pharmacy, University of Limoges, Limoges, France, [4] Electron Microscopy Laboratory, Wrocław University of Science and Technology, Wrocław, Poland, [5] Institute of Immunology and Experimental Therapy, Polish Academy of Sciences, Wrocław, Poland, [6] Advanced Materials Engineering and Modelling Group, Faculty of Chemistry, Wrocław University of Science and Technology, Wrocław, Poland

OPEN ACCESS

Edited by:
Rodolfo García-Contreras, National Autonomous University of Mexico, Mexico

Reviewed by:
Eliana Alves, University of Aveiro, Portugal
Virginia Aiassa, National University of Córdoba, Argentina

***Correspondence:**
Stéphanie Leroy-Lhez
stephanie.lhez@unilim.fr

Specialty section:
This article was submitted to Antimicrobials, Resistance and Chemotherapy, a section of the journal Frontiers in Microbiology

Received: *14 September 2020*
Accepted: *20 October 2020*
Published: *17 November 2020*

Citation:
Maldonado-Carmona N, Marchand G, Villandier N, Ouk T-S, Pereira MM, Calvete MJF, Calliste CA, Żak A, Piksa M, Pawlik KJ, Matczyszyn K and Leroy-Lhez S (2020) Porphyrin-Loaded Lignin Nanoparticles Against Bacteria: A Photodynamic Antimicrobial Chemotherapy Application. Front. Microbiol. 11:606185. doi: 10.3389/fmicb.2020.606185

The need for alternative strategies to fight bacteria is evident from the emergence of antimicrobial resistance. To that respect, photodynamic antimicrobial chemotherapy steadily rises in bacterial eradication by using light, a photosensitizer and oxygen, which generates reactive oxygen species that may kill bacteria. Herein, we report the encapsulation of 5,10,15,20-tetrakis(4-hydroxyphenyl)-21H,23H-porphyrin into acetylated lignin water-dispersible nanoparticles (**THPP@AcLi**), with characterization of those systems by standard spectroscopic and microscopic techniques. We observed that **THPP@AcLi** retained porphyrin's photophysical/photochemical properties, including singlet oxygen generation and fluorescence. Besides, the nanoparticles demonstrated enhanced stability on storage and light bleaching. **THPP@AcLi** were evaluated as photosensitizers against two Gram-negative bacteria, *Escherichia coli* and *Pseudomonas aeruginosa*, and against three Gram-positive bacteria, *Staphylococcus aureus*, *Staphylococcus epidermidis*, and *Enterococcus faecalis*. **THPP@AcLi** were able to diminish Gram-positive bacterial survival to 0.1% when exposed to low white LED light doses (4.16 J/cm^2), requiring concentrations below 5 μM. Nevertheless, the obtained nanoparticles were unable to diminish the survival of Gram-negative bacteria. Through transmission electron microscopy observations, we could demonstrate that nanoparticles did not penetrate inside the bacterial cell, exerting their destructive effect on the bacterial wall; also, a high affinity between acetylated lignin nanoparticles and bacteria was observed, leading to bacterial flocculation. Altogether, these findings allow to establish a photodynamic antimicrobial chemotherapy alternative that can be used effectively against Gram-positive topic infections using the widely available natural polymeric lignin as a drug carrier. Further research, aimed to inhibit the growth and survival of Gram-negative bacteria, is likely to enhance the wideness of acetylated lignin nanoparticle applications.

Keywords: tetrapyrrolic compounds, valorized lignin, nanoparticles, photodynamic antimicrobial therapy, antimicrobial alternatives

INTRODUCTION

Antimicrobial resistance (AMR) upraise is one of the greatest challenges that modern medicine and chemistry are facing. After the "golden age of antibiotics," the decay on the discovery rate of new and more efficient molecules was conjugated with the appearance of antimicrobial-resistant strains. AMR alone is expected to cause 10 million deaths by 2050, with an accumulative cost of 100 trillion USD (O'Neill, 2016). However, this prediction only accounts for developed countries, and this number is expected to be higher and still to be determined, with the greatest impact on developing countries. The World Health Organization has devised a global action plan (WHO, 2015) emphasizing the necessity to find new antimicrobial alternatives and to improve disinfection processes, while exploring therapeutic approaches that are less prone to generate resistance (Lewis, 2013; Regiel-Futyra et al., 2017).

In that respect, photodynamic therapy (PDT) has revealed to be a suitable alternative. PDT is the conjugation of light and a photosensitizer molecule, generating reactive oxygen species (ROS) from either molecular oxygen in the media (Type II mechanism) or a substrate (Type I mechanism) (Josefsen and Boyle, 2012). When these ROS are directed against microorganisms, the process is addressed as photodynamic antimicrobial chemotherapy (PACT) (Wainwright, 2019). These *in situ*-generated ROS are able to destroy biomacromolecules, including proteins, membrane lipids, and nucleic acids, through a non-specific target mechanism (Wainwright et al., 2017). Commonly in PDT addressed against cancer, desired photosensitizers are molecules with strong absorption bands near the infrared range (700–900 nm), which coincides with the skin transparent wavelengths, and permit light to reach deeper through the skin (Josefsen and Boyle, 2012). In contrast, most of the applications of PACT are at surfaces or topic applications, thus photosensitizing molecules are not limited to absorption in the infrared range. Recent PACT applications have been developed for usage under white light (Nzambe Ta keki et al., 2016; Ringot et al., 2018; Aroso et al., 2019; Khaldi et al., 2019), blue light (Buchovec et al., 2016), and even solar light (Jia et al., 2019). Currently, PACT applications are actively pursued by several research groups, with applications in dentistry as a complement of systemic antibiotic treatments (de Freitas et al., 2016; Bechara Andere et al., 2018), as a non-invasive treatment against *Helicobacter pylori* (Baccani et al., 2019), and even as an environment-friendly alternative for active food packaging (i.e., biodegradable coatings for strawberries disinfection), food disinfection (i.e., curcumin derivatives for lettuce and mung beans disinfection), and other agronomical applications (i.e., porphyrinic insecticides and pesticides) (Riou et al., 2014; Buchovec et al., 2016; Glueck et al., 2017; Martinez et al., 2017).

In parallel, organic matrices (e.g., cellulose, chitosan, cyclodextrin) have been used for the transport and encapsulation of small molecules, with some examples of conjugating photosensitizers, enabling bacterial eradication and, in some cases, demonstrating a synergistic effect with the organic matrix (Hsieh et al., 2019; Maldonado-Carmona et al., 2020). In this regard, an organic matrix that has been neglected is lignin. Lignin is a natural aromatic polymer, representing up to 20–35% of the total lignocellulosic biomass, and it is usually a by-product of the paper industry. It is a polymer of p-coumaryl alcohol, coniferyl alcohol, and sinapyl alcohol units, whose proportions vary according to its botanic origin (Faix, 1991). Due to its chemical nature, it can withstand several chemical modifications, either through the creation of new chemically active sites or through the substitution of the already available ones (Calvo-Flores and Dobado, 2010; Duval and Lawoko, 2014; Wang et al., 2016; Figueiredo et al., 2018; Marchand et al., 2018). In addition to chemical modifications, different methods for the preparation of lignin-based nanomaterials had been developed. One of the main applications given to these nano-objects is the loading and release of active substances.

Understandably, lignin has not been widely used as a photosensitizing molecule's vehicle mainly due to the widely known antioxidant activity of lignin (Ponomarenko et al., 2015; Yang et al., 2016). To the best of our knowledge, only one approach is reported in literature using lignin-coated noble metal nanoparticles for *Staphylococcus aureus* and *Escherichia coli* photo-induced disinfection (Rocca et al., 2018). Another report has been found where lignin was linked to a phenyl porphyrin, resulting in a biopolymer with increased fluorescence, but no photodynamic approach was implied (Tse et al., 2019). Besides, lignin nanoparticles are demonstrated to be innocuous to *Chlamydomonas reinhardtii*, an aquatic microorganism, and to *Saccharomyces cerevisiae*, a eukaryotic cell model (Frangville et al., 2012). Additionally, they are demonstrated to be innocuous against Caco-2 cells (Alqahtani et al., 2019), a human colon carcinoma cell line. Among all the possible lignin modifications, lignin acetylation is widely described in the literature (Qian et al., 2014b). For instance, recent reports have demonstrated that acetylated Kraft and Organosolv lignins (**AcLi**) work as weak photosensitizers (Marchand et al., 2018) and that **AcLi** is also able to form spherical nanoparticles (Qian et al., 2014a,b; Marchand et al., 2020), further demonstrating the capability to transport active molecules (Zhou et al., 2019; Marchand et al., 2020).

Considering all the above, here we report the encapsulation of commercial 5,10,15,20-tetrakis(4-hydroxyphenyl)-21*H*,23*H*-porphyrin (**THPP**) inside acetylated lignin nanoparticles (**@AcLi**). The nanoparticles were characterized through transmission electron microscopy (TEM), dynamic light scattering (DLS), zeta potential, UV-vis absorption and fluorescence, and electron paramagnetic resonance (EPR) in order to evaluate their capacity to generate singlet oxygen. The nanoparticles were tested against three Gram-positive bacteria, *S. aureus* CIP 76.25, *Staphylococcus epidermidis* CIP 109562, and *Enterococcus faecalis* CIP 76.1170, and against two Gram-negative bacteria, *E. coli* CIP 53.126 and *Pseudomonas aeruginosa* CIP 76.110, under white LED light irradiation. Additionally, **THPP**-loaded **@AcLi** (**THPP@AcLi**) were evaluated for their stability over long storage periods, and their properties were assessed at different pH ranges.

MATERIALS AND METHODS

Materials and Microbiological Strains

Kraft lignin was kindly donated by the Université du Québec à Trois-Rivières, Canada. **THPP**, acetic anhydride, dry pyridine, and other reagents were purchased at Sigma-Aldrich (Lyon, France) and used as received, without further purification. *E. coli* CIP 53.126, *E. faecalis* CIP 76.1170, *P. aeruginosa* CIP 76.110, *S. aureus* CIP 76.25, and *S. epidermidis* CIP 109562 were obtained from the Institute Pasteur Collection (Institute Pasteur, Paris, France). All bacterial strains were kept frozen as small aliquots (100 µl), at −78°C, with glycerol 50% as cryopreservant. A whole aliquot was used for each culture, avoiding defrosting of the other samples. *P. aeruginosa* was grown in Luria–Bertani (LB) broth (tryptone 10 g/L, sodium chloride 10 g/L, yeast extract 5 g/L), while all the other bacterial strains were routinely growth at trypto-casein soy medium (TS, Biokar; tryptone 17 g/L, papaic digest of soybean meal 3 g/L, glucose 2.5 g/L, dipotassium phosphate 2.5 g/L, sodium chloride 2 g/L), prepared as a broth (LBB and TSB) or as a solid media (LBA and TSA; 1.7% agar) according to standard procedures. Saline solution (0.9% NaCl) and phosphate buffer pH 7 (PB pH 7, NaH_2PO_4 6.045 g/L, Na_2HPO_4 10.5 g/L) were routinely prepared and sterilized.

Preparation of Acetylated Lignin

AcLi was prepared according to previous publications (Marchand et al., 2018). A kraft lignin solution (50 mg/ml) was prepared in an acetic anhydride/dry pyridine (1:1) mixture and stirred at 25°C, under a calcium chloride ($CaCl_2$) trap, for 48 h. Then, the reaction mixture was poured onto 500 ml distilled water, and the precipitate was filtrated, dissolved on chloroform, and washed three times with distilled water. The organic phase was dried with $MgSO_4$ and evaporated to dryness.

Acetylated Lignin Characterization

Acetylated lignin was dissolved in acetonitrile, and its UV-vis absorption spectrum was recorded on a spectrophotometer Specord 210 Lambda (Analytik Jena) on quartz cells. FT-IR spectrum of materials was obtained using a Frontier PerkinElmer spectrometer in the attenuation total reactance analysis mode. Spectra were collected between 600 and 4,000 cm^{-1} after placing the pure product on a diamond crystal plate.

Preparation and Quantification of Acetylated Lignin Nanoparticles

Nanoparticles were prepared as previously described (Figueiredo et al., 2017). Acetylated lignin nanoparticles were prepared starting from an acetylated lignin solution (2 mg/ml) in acetone. For **THPP** encapsulation, **THPP** (0.2 mg/ml) was added in the acetonic solution. The AcLi solution was dialyzed on a regenerated cellulose membrane rod (Fisherbrand, 12–14 kDa) against distilled water for 24 h. After dialysis, nanoparticles were centrifuged at 10,000 × *g* for 1 h. Then, nanoparticles were washed with distilled water and centrifuged again. Finally, nanoparticles were suspended in distilled water and stored for further use. Routinely, after the harvest of **THPP@AcLi**, a small amount of nanoparticles was dissolved in acetone, and **THPP** quantification was done using the Soret band absorption (λ_{max} 419 nm, ε = 388,500 L/mol cm). Similarly, nanoparticles were dissolved in acetonitrile for AcLi quantification. The volume of dissolved nanoparticles was always below 3%, regarding the final volume on organic solvent. For **THPP@AcLi** analysis in aqueous media, nanoparticles were diluted on an appropriated buffer and their spectra were recorded. Spectra were collected between 200 and 800 nm. The encapsulation rate was calculated, as the ratio of the amount of **THPP** inside the nanoparticles, to the initial amount (Eq. 1):

$$Encapsulation\ rate\,(\%) = \frac{C_{THPP} V_{Np} MW_{THPP}}{THPP_i} \times 100 \qquad (1)$$

where C_{THPP} was the observed concentration of **THPP** in the final volume of nanoparticles (V_{Np}), considering the molecular weight of **THPP** (MW_{THPP}) and the initial mole number of **THPP** (**THPP**$_i$).

Apparent Size and Zeta Potential Analysis

Nanoparticle size was analyzed through DLS on a Zetasizer Nano-ZS (Malvern Instrument). Three measurements were performed on each sample at 20°C using a light scattering angle of 173° and a refractive index of 1.59 for lignins. Nanoparticles were diluted on distilled water for each DLS determination. The obtained DLS raw data were fit to a Gaussian model, excluding the values with less than 1% of presence. The obtained data were validated through the analysis of their R square coefficient and through the analysis of the residuals with a D'Agostino–Pearson Omnibus K2 test. With this statistical approach, we obtained the mean size (geometrical mean) and the standard deviation (σ), which allowed us to approximate the range where 95% of the nanoparticles were found (2σ). Zeta potential was obtained with the same equipment, and nanoparticles were diluted on an appropriated aqueous solution for each determination.

Transmission Electron Microscopy Observations

The samples were observed using the TEM, model H-800 (Hitachi), using an accelerating voltage of 150 kV. For nanoparticle imaging, a dense suspension of nanoparticles in water was used. Two microliters of each sample were deposited on carbon on the copper grid. The excess of liquid was carefully blotted with a filter paper and air-dried for 1 h. For bacterial and interaction observations, an overnight culture of *S. aureus* in TSB was washed with PB pH 7.4 (5,000 × *g*, 5 min) three times. Then, bacteria were carefully suspended on a minimal volume of buffer. After deposition of the 2 µl of the sample on grid and blotting, the samples were fixed and negative stained with 2 µl drop of 2% uranyl acetate deposited on the grid. The stain was blotted after 60 s, and the samples were air-dried for 1 h. For the interaction observations, 150 µl from the bacterial suspension was mixed with 150 µl of the nanoparticle suspension. Light irradiation was done with the 2 µl mixed sample on the TEM grid, under an incandescent lamp, with

light irradiation of around 2,500 lux for 5 min. After that, the samples were blotted and fixed as described above. The scheme of the preparation process is shown in **Supplementary Material 1**. For nanoparticle size determination, ImageJ Fiji (Schindelin et al., 2012; Schneider et al., 2012) software was used (Thresholding default, size 0.01–1.00 μm^2, circularity 0.06–1.00).

Stability of 5,10,15,20-Tetrakis(4-Hydroxyphenyl)-21H,23H-Porphyrin Inside Acetylated Lignin Nanoparticles

The stability of the encapsulation was tested over time. For this, a suspension of **THPP@AcLi** at 100 μM was prepared and divided in small 500-μl fractions, which were stored at 25°C in the dark. When analyzed, samples were centrifuged (10,000 × *g*, 30 min) and the supernatant was retired. The pelleted nanoparticles were resuspended in distilled water, and both nanoparticles and supernatants were analyzed by UV-vis absorption spectroscopy. The stability of the nanoparticles was followed through the changes of the Soret band absorption (λ_{max} 430 nm) over time in both nanoparticles and supernatants.

Singlet Oxygen Detection by Electron Paramagnetic Resonance

Measurements were recorded as described elsewhere (Riou et al., 2014). The samples were exposed to a 20 W halogen lamp, with a light irradiation of 20,000 lux. The intensity of illumination was measured by a lux meter (Digital Lux Tester YF-1065). EPR spectra were recorded with a Bruker Model ESP300E spectrometer operating at room temperature. Routinely, a fresh solution of 25 mM 2,2,6,6-tetramethylpiperidine (**TEMP**) was prepared in phosphate buffer pH 7.4. Acetylated lignin nanoparticle suspension was prepared at a concentration of 4 mg/ml of AcLi, while **THPP@AcLi** suspension was diluted at 120 μM of **THPP** or 0.2 mg/ml of AcLi. For singlet oxygen detection, 50 μl of the fresh **TEMP** solution were mixed with 50 μl of the nanoparticle suspension. The solution obtained was immediately transferred into quartz capillaries (100 μl) and placed at 20 cm from the source of illumination with a light intensity of 270 $\mu E/(s\ m^2)$ during periods of 5 min. A dark control was prepared, and rose Bengal in dimethylformamide (DMF) was used as a standard. EPR spectra were performed under the following conditions: modulation frequency, 100 kHz; microwave frequency, 9.78 GHz; microwave power, 4 mW; modulation amplitude, 0.987 G; time constant, 10.24 ms; scans number, 2.

Fluorescence Quantum Yield

Fluorescence quantum yield was calculated as described elsewhere (Vinagreiro et al., 2020). The fluorescence emission spectra were recorded in a Horiba Scientific Spectrofluorometer Fluoromax-4. The spectra were collected from 550 up to 800 nm using standard quartz cuvettes of 1 cm of optical path. Fluorescence quantum yields (Φ_F) were obtained by comparing the area of integrated fluorescence of the samples (F_s) with that of the reference (F_{ref}) compound, with known Φ_F, corrected by the absorption of sample (A_s) and reference (A_{ref}) at the excitation wavelength and by the refractive index of the solvents used for the sample (η_s) and reference (η_{ref}) solutions (Eq. 2).

$$\Phi_F = \Phi_F^{ref} \frac{F_s A_{ref} \eta_s^2}{F_{ref} A_s \eta_{ref}^2} \quad (2)$$

Tetraphenylporphyrin (**TPP**) in toluene (Φ_F ref = 0.11) was used as standard (Pineiro et al., 1998). The absorbance of the sample at the excitation wavelength was around 0.01.

Photobleaching Quantum Yield

Photobleaching experiments were done at similar conditions as those carried away for the microbiological experiments and following the procedure stated elsewhere (Vinagreiro et al., 2020). **THPP@AcLi** were diluted to a final concentration of 10 μM in PB pH 7. A volume of 200 μl (V_{irr}) was deposited on a flat-bottom 96-well plate (l = 1 cm) and irradiated, ensuring that all the light went through the solution. The samples were irradiated for a time Δ_t using a white LED light with emission (λ_{Em}) at 447 nm and output power P_0 of 1 mW. The actual light power absorbed was determined for each compound and properly taken into account in the calculation of the photobleaching quantum yield, as described in the **Supplementary Material 2** (Schaberle, 2018). Photobleaching quantum yield (Φ_{pb}) is defined as the ratio between the rate of disappearance of photosensitizer molecules (v_d) and the rate of absorption of photons (v_P) (Eq. 3).

$$\Phi_{Pb} = \frac{v_d}{v_p} = \frac{V_{irr} N_A h c \Delta A_{Soret}}{\varepsilon_{Soret} l \lambda_{Em} P (1 - 10^{-A_0}) \Delta_t} \quad (3)$$

where A_0 is the initial absorption at the Soret band. The Soret band absorbance was found to decrease, and its decay was followed during the light exposure.

Photodynamic Antimicrobial Chemotherapy Bacteriostatic Effect

The bacteriostatic effect was evaluated against planktonic bacteria in the middle of the exponential phase of growth. An aliquot of bacteria was inoculated in 5 ml of TSB or LB and incubated for 16 h, 37°C, 100 rpm. The OD_{600} was measured for the resulting culture, and it was diluted at an OD_{600} = 0.05 in 5 ml of fresh TSB or LB. Bacteria subcultures were incubated under the same previous conditions, during 2 h for *E. coli*, and 3 h for the other bacteria. Bacteria were washed with sterile PB pH 7 (5,000 × *g*, 5 min), and 100 μl were diluted in 10 ml of PB pH 7 for a final concentration of $\sim 10^6$ CFU/ml. Onto a 96-well plate, a volume of 50 μl of bacterial suspension was mixed with 50 μl of a solution with **THPP@AcLi** or **@AcLi**, at geometrically decreasing concentrations, ranging from 50 to 0.010 μM and 1.6 mg/ml to 6.25 μg/ml, respectively. The plate was irradiated under white LED light (1.2 mW/cm^2) for 1 h. A volume of 100 μl of TSB media was added to each well, and the initial OD_{595} (S_i) was acquired using an iMark multiplate reader (Bio-Rad). The plate was incubated at 37°C in the dark for 6 h, and then its OD_{595}

was measured again (S_t). Appropriated controls were prepared, a sample without bacteria and treatment (B_0) was used as a blank, while a sample without treatment was used as growth control and addressed as concentration zero (G_i) and followed over time (G_t). Normalized bacterial growth (G_B) was obtained according to Eq. 4.

$$G_B = \frac{S_t - S_i}{G_t - G_i} \quad (4)$$

A second 96-well plate was prepared, with bacteria and nanoparticles at the same concentrations and conditions and kept away from the light. Bacterial growth was allowed and monitored as the light-irradiated plate, becoming the dark control.

Photodynamic Antimicrobial Chemotherapy Bactericidal Effect

The bactericidal effect was evaluated against planktonic bacteria in the middle of the exponential phase of growth. An aliquot of bacteria was inoculated in 5 ml of TSB or LB and incubated for 16 h, 37°C, 100 rpm. The OD_{600} was measured and diluted at an OD_{600} = 0.05 in 5 ml of fresh TSB or LB. Bacteria subcultures were incubated under the same previous conditions for 2 h for *E. coli* and 3 h for the other bacteria. Bacteria were washed with sterile PB pH 7 (5,000 × *g*, 5 min) and suspended in 10 ml of PB pH 7 for a final concentration of $\sim 10^8$ CFU/ml. Onto a 96-well plate, a volume of 50 μl of bacterial suspension was mixed with 50 μl of a solution with **THPP@AcLi**, at geometrically decreasing concentrations, ranging from 2.5 to 0.010 μM, while **@AcLi** was only tested at 1.6 mg/ml, the highest concentration tested at the PACT bacteriostatic effect. Appropriated controls were prepared; a sample without nanoparticle treatment was used as a survival control. The plate was irradiated under white LED light (1.2 mW/cm^2) for 1 h. Besides, a second identical plate was prepared and kept away from light. Then, the solution on the wells was serially diluted on 900 μl of saline solution, and 50 μl were spread on TSA or LBA plates using an automatic plater EasySpiral (Interscience). Petri dishes were incubated at 37°C, in the dark, for 16 h. Colony-forming units (CFUs) were counted using a colony counter Scan 100 (Interscience). Bacterial survival was calculated, comparing the number of viable bacteria after the treatment ($CFU/ml_{Treatment}$) with the number of viable bacteria without treatment ($CFU/ml_{Control}$) (Eq. 5).

$$Bacterial\ survival\,(\%) = \frac{CFU/mL_{Treatment}}{CFU/mL_{Control}} \times 100 \quad (5)$$

Statistical Analysis

Experiments were performed at least in triplicate. The results were analyzed with GraphPad Prism 6.01. Biological data were analyzed with a two-way ANOVA using a Sidak's test for multiple comparisons with 95% of the cohort. The obtained DLS raw data were fit to a Gaussian model, excluding the values with less than 1% of presence. The obtained data were validated through the analysis of their R square coefficient and through the analysis of the residuals with a D'Agostino–Pearson Omnibus K2 test. With this statistical approach, we obtained the mean size (geometrical mean) and the standard deviation (σ), which allowed us to approximate the range of size that have 95% of the nanoparticles (D_{95}).

RESULTS

Preparation of Acetylated Lignin Nanoparticles and Their Physicochemical Characterization

AcLi was prepared as previously described (Marchand et al., 2018), and their chemical properties are discussed in **Supplementary Material 3**. Acetylated lignin nanoparticles were prepared as previously described (Figueiredo et al., 2017; Marchand et al., 2020) from an acetone solution (**Figure 1**). **THPP** encapsulation was done at similar conditions, through the addition of **THPP** into the acetone solution. In both cases, the acetone solution was dialyzed against water. The thereof obtained nanoparticles were centrifuged and suspended in distilled water.

THPP@AcLi suspension was analyzed with UV-vis absorption spectroscopy (**Figure 2**), and the spectroscopic data were summarized in **Table 1**. Due to the low aqueous solubility of **THPP**, the UV-vis spectrum of **THPP@AcLi** was compared with the spectra of **THPP** in dimethylsulfoxide (DMSO) and in a mixture of PB and DMSO (95/5 v/v), with the last simulating biological aqueous conditions. **THPP@AcLi** kept the typical porphyrin UV-vis absorption profile: one intense Soret band and four Q-bands at higher wavelengths. When compared with **THPP**, a red-shift of the Soret band in **THPP@AcLi** (λ = 430.5 nm) was observed compared with the observed Soret band in pure DMSO (λ = 424.5 nm). The observed red-shift and diminished absorbance that occurred were due to a solvatochromic effect and/or π-π interactions with the lignin aromatic core. Additionally, these features could also be due to the formation of **THPP** J-aggregates, as it has been previously described that, in the presence of water, **THPP** aggregates show a red-shifted Soret band with a diminished absorbance (Zannotti et al., 2018). **THPP** proneness to aggregate in aqueous medium was further corroborated with the observed wide and diminished Soret band for **THPP** in 5% DMSO. In addition, the appearance of extra bands at 457 nm (B-band) and at 701.5 nm (Q_c) indicates the presence of protonated **THPP** (**THPPH**$_2^{2+}$) species inside the nanoparticles (Zannotti et al., 2018; Leroy-Lhez et al., 2019). Moreover, it seems that encapsulation of **THPP** inside **AcLi** nanoparticles reduced the aggregated state when compared to **THPP** dissolved in a mixture of aqueous media/organic solvent, where we observed a broad Soret band with diminished absorption.

Given the presence of **THPPH**$_2^{2+}$ species, further investigations on the effect of the pH on the loaded nanoparticles were deemed necessary. Thus, UV-vis absorption spectra of **THPP@AcLi** nanoparticles were recorded at several pH values using different buffers (0.1 M), as displayed in **Figure 3**. The **THPP@AcLi** UV-vis absorption profile remained stable at pH values above 4, as the proportion between the **THPP** and its protonated species **THPPH**$_2^{2+}$ (expressed as ratio A_{457}/A_{430}) remained constant. Upon pH acidification, a change in the

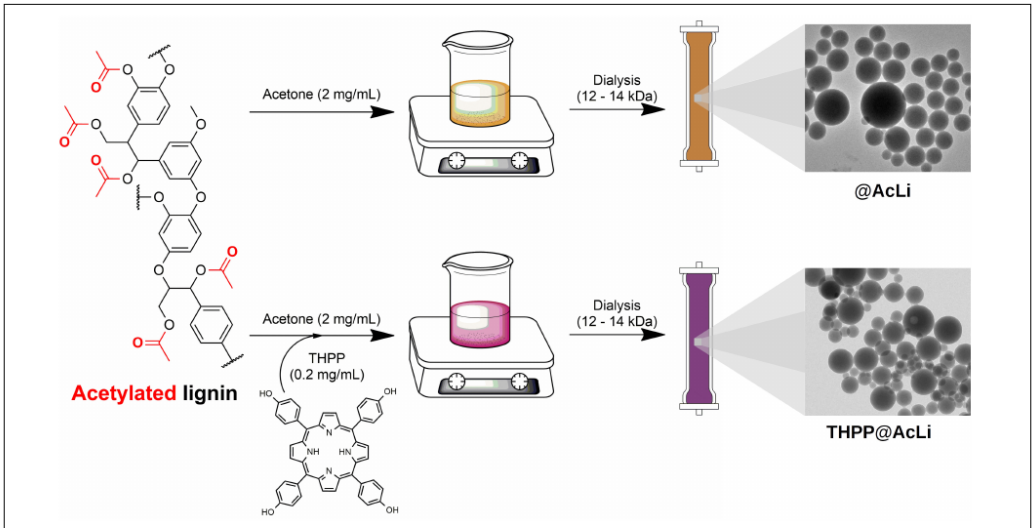

FIGURE 1 | Preparation of acetylated lignin nanoparticles **(@AcLi)** and 5,10,15,20-tetrakis(4-hydroxyphenyl)-21*H*,23*H*-porphyrin (**THPP**)-loaded **@AcLi** (**THPP@AcLi**).

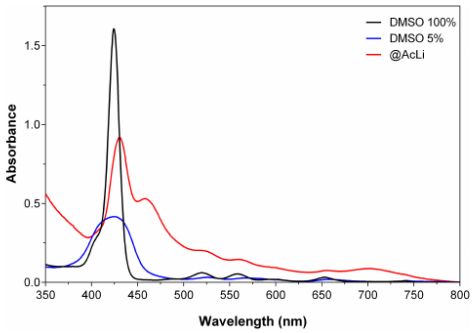

FIGURE 2 | Comparison of the UV-vis spectra of 5,10,15,20-tetrakis (4-hydroxyphenyl)-21*H*,23*H*-porphyrin **(THPP)** 5 μM in DMSO (DMSO 100%) in a mixture of PB pH 7 and DMSO 5% (DMSO 5%) and as **THPP**-loaded acetylated lignin nanoparticles **(THPP@AcLi)**, suspended in PB pH 7.

UV-vis absorption profile can be observed by a decrease of the absorbance at 430 nm with concomitant increase of the absorbance at 457 nm, reaching its maximum at pH 2, as depicted by the evolution of the ratio A_{457}/A_{430} (**Figure 3** inset, left axis). This, along with an increase of the absorbance at 701.5 nm, suggested an increased presence of protonated porphyrin $\mathbf{THPPH_2}^{2+}$ at values below pH 4. This experiment seems to corroborate the presence of both **THPP** and $\mathbf{THPPH_2}^{2+}$ species inside nanoparticles. Interestingly, neither at basic pH do the $\mathbf{THPPH_2}^{2+}$ related bands disappear, which either suggests the stability of the initial mixture or the solvent inaccessibility inside the nanoparticles. The last one has been previously analyzed through computational analysis on **@AcLi** formation, where nanoparticles have a lower solvent accessible surface area than lignin dissolved in organic solvent (Marchand et al., 2020). Nevertheless, **THPP** encapsulated inside **@AcLi** appears to be stable on a wide pH range (ca. 4–10), with its absorbance remaining unaffected by changes in the surrounding media.

Additionally, we could determine the amount of **THPP** encapsulated inside the nanoparticles through UV-vis quantification in acetone, as previously reported (Marchand et al., 2020). Our results demonstrated that up to 87.6% of the initial amount of **THPP** was encapsulated inside **@AcLi**; thus, the encapsulation process is not only sustainable but highly effective, allowing a good recovery of our photosensitizing molecule.

The size and shape of nanoparticles were also analyzed through two different methods, DLS and TEM. DLS indirectly permits to know the hydrodynamic size and the polydispersity index (PDI). The hydrodynamic size takes into account the presence of salts and water molecules surrounding the nanoparticles; thus, the size obtained is apparent and depends on the interaction of nanoparticles with the surrounding media. On the other hand, TEM observations directly analyze the size of opaque nanoparticles without taking into account the influence of the media; however, TEM observations need specialized software for image processing. In order to fully characterize the nanoparticles, both methods were compared for **THPP@AcLi** and **@AcLi** (**Figure 4**), with the results being summarized

TABLE 1 | Absorption bands of **THPP** 5 μM in DMSO 100%, PB and DMSO 5%, and as **THPP@AcLi** suspended in PB pH 7.

	Soret band		λ_{max} B	λ_{max} Q_1	λ_{max} Q_2	λ_{max} Q_3	λ_{max} Q_4	λ_{max} Q_C
	λ_{max}	ε_{max} (L/mol cm)						
DMSO	424.5	3.214×10^5		519.5	558.5	594.5	653	
PB pH 7 DMSO 5%	424.5	8.320×10^4		526	568.5	599.5	657	
PB pH 7 **@AcLi**	430.5	1.836×10^5	457	516.5	559.5	596.5	656	701.5

THPP, *5,10,15,20-tetrakis(4-hydroxyphenyl)-21H,23H-porphyrin;* ***THPP@AcLi, THPP****-loaded acetylated lignin nanoparticles.*

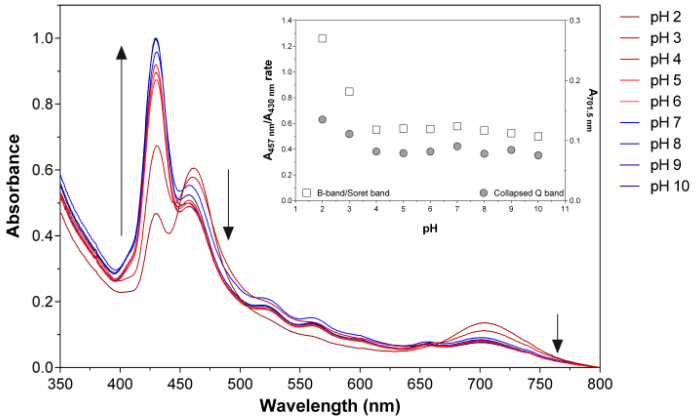

FIGURE 3 | Absorption spectra of 5.87 μM 5,10,15,20-tetrakis(4-hydroxyphenyl)-21*H*,23*H*-porphyrin-loaded acetylated lignin nanoparticles **(THPP@AcLi)** suspensions at different pHs [0.1 M glycine-HCl buffer (pH 2 and pH 3), 0.1 M acetate buffer (pH 4 and pH 5), 0.1 M phosphate buffer (0.1 M pH 6, pH 7, and pH 8), 0.1 M glycine-NaOH buffer (pH 9 and pH 10)]. The black arrows depict the changes found through increasing the pH of the media. Inset, the ratio of absorbance values at 457 and 430.5 nm (squares, left axis) and the absorbance at 701.5 nm (circles, right axis) are depicted as a function of pH.

in **Table 2**. The results obtained were compared under the assumption that the nanoparticle populations follow a Gaussian distribution. DLS and TEM analysis obtained similar size values for both nanoparticles (approximately 200 nm). In both cases, **@AcLi** were slightly smaller than **THPP@AcLi**, by less than 10 nm. When analyzed, the PDI values obtained were below 0.2, which indicates that the degree of size dispersion was in the desired range of reported nanoparticles (Danaei et al., 2018), as high PDI values describe a wide distribution in the size of the population and is associated to flocculation of the samples. The wideness of the size of the nanoparticles was analyzed through the comparison of the range where 95% of the nanoparticles were found (D_{95}). Both TEM and DLS analysis provided evidence that both populations had similar distributions, between 30 and 380 nm. These results were slightly different from those obtained by previous experiences (Marchand et al., 2020), where loaded nanoparticles have a smaller size than non-loaded nanoparticles. However, these differences could be due to differences in the workup of nanoparticles, as in the present work, nanoparticles are centrifuged at 10,000 × *g*.

In addition to size, another important parameter to characterize is the zeta potential. The zeta potential helps to describe both the apparent charge of a nanoparticle, as well as the stability of a colloidal suspension. As the apparent charge of a suspended particle, the zeta potential is deeply related to the presence of ions in the surrounding media and to its pH. Additionally, it allows us to understand the interactions of the particles with themselves and with other nano molecules that may lead to flocculation. Thus, the zeta potentials of **@AcLi** and **THPP@AcLi** were measured in PB pH 7 (-23.42 ± 2.17 and -17.00 ± 1.67, respectively). A negative charge was observed for both nanoparticles, and no significant difference was found between them (two-way ANOVA, Sidak's multiple comparison test, $P > 0.05$). As the values obtained for both nanoparticles were similar, it could be assumed that **THPP** did not exert an effect on the charge of the nanoparticle and in its zeta potential. Thus, for further analysis, nanoparticle zeta potential was measured at different pH values in 0.1 M buffers (**Figure 5**). Interestingly, both types of nanoparticles had a similar behavior, with an increase on the zeta potential value at pH 2, reaching a plateau and then decreasing at basic pH 9 and 10. However, we could observe that the addition of **THPP** into **@AcLi** nanoparticles leads to an increase on the zeta potential (Two-way ANOVA, Sidak's multiple comparison test, $P < 0.05$), excepting pH 7

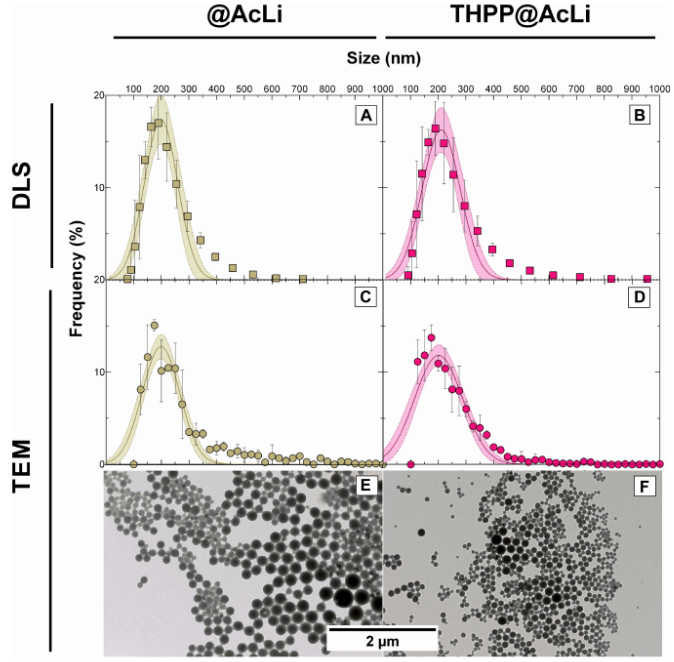

FIGURE 4 | Size distribution of acetylated lignin nanoparticles **(@AcLi)** and 5,10,15,20-tetrakis(4-hydroxyphenyl)-21*H*,23*H*-porphyrin-loaded @AcLi (**THPP@AcLi)** measured through dynamic light scattering (DLS) **(A,B)** and through transmission electron microscopy (TEM) **(C,D)**. Also, the spherical shape of nanoparticles is observed for both **(E,F)**.

and pH 8 (two-way ANOVA, Sidak's multiple comparison test, $P > 0.05$). The magnitude of the zeta potential can predict the stability of a colloidal suspension, being that suspensions with higher magnitudes of zeta potential tend to be more stable and less likely to flocculate (Kumar and Dixit, 2017). Thus, our findings indicate that at acidic pH, **@AcLi** are more likely to flocculate, reaching their highest stability in basic pH. As we found differences between **THPP@AcLi** and **@AcLi**, **THPP** exerts an effect in the apparent charge of the nanoparticles, increasing the likeness of nanoparticle flocculation, when compared with **@AcLi.**

To further demonstrate the viability of our process, we tested the stability of **THPP@AcLi** by monitoring the UV-vis absorption spectra of the nanoparticles suspended in PB pH 7, over 60 days, when stored in the dark at 25°C (**Supplementary Material 4**). **THPP@AcLi** demonstrated a high stability, with negligible **THPP** leaking, after 60 days of storage (9%). Additionally, the UV-vis profile did not change over time. Thus, **THPP@AcLi** withstood suspension in aqueous media in the dark and at 25°C, which makes it suitable for storage, without specific conditions in order to preserve the stability of the formulation.

TABLE 2 | Size of nanoparticles determined by DLS and TEM, expressed as the Gaussian mean and the distribution of 95% of the nanoparticles (D_{95}).

	DLS				TEM		
	Mean size (nm)	Range (D_{95})	R^2 Gaussian model fitting	PDI	Mean size (nm)	Range (D_{95})	R^2 Gaussian model fitting
@AcLi	199.6	79.02–320.18	0.9160	0.189	198.7	130.7–266.7	0.8410
THPP@AcLi	210.8	73.4–348.2	0.9154	0.176	200.6	114.16–287.4	0.8637

***@AcLi**, acetylated lignin nanoparticles; DLS, dynamic light scattering; PDI, polydispersity index; TEM, transmission electron microscopy; **THPP,** 5,10,15,20-tetrakis(4-hydroxyphenyl)-21H,23H-porphyrin; **THPP@AcLi, THPP**-loaded @AcLi.*

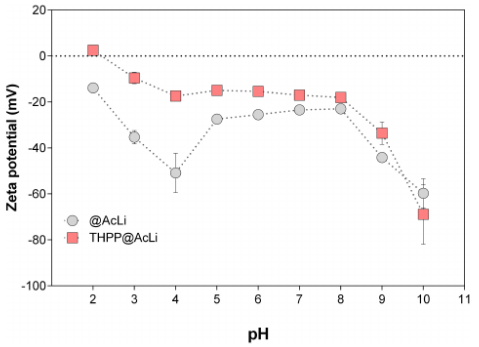

FIGURE 5 | The pH effect on the zeta potential of acetylated lignin nanoparticles **(@AcLi)** and 5,10,15,20-tetrakis(4-hydroxyphenyl)-21*H*,23*H*-porphyrin-loaded @AcLi **(THPP@AcLi)** [0.1 M glycine-HCl buffer (pH 2 and pH 3), 0.1 M acetate buffer (pH 4 and pH 5), 0.1 M phosphate buffer (0.1 M pH 6, pH 7, and pH 8), 0.1 M glycine-NaOH buffer (pH 9 and pH 10)].

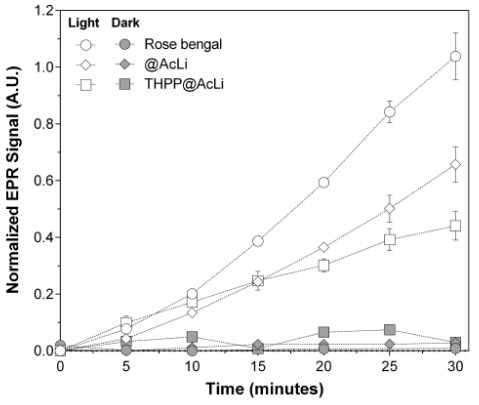

FIGURE 6 | Monitoring of singlet oxygen production, as 2,2,6,6-tetramethylpiperidine-1-oxyl (TEMPO) radical detection through electron paramagnetic resonance (EPR) of acetylated lignin nanoparticles **(@AcLi)** [2 mg/ml] (diamonds) and 5,10,15,20-tetrakis(4-hydroxyphenyl)-21*H*,23*H*-porphyrin-loaded @AcLi **(THPP@AcLi)** [**THPP** 60 μM, **AcLi** 100 μg/ml] (squares). Rose bengal [1.5 μM] (circles) was used as a reference. Singlet oxygen production was measured as a function of time under light irradiation (white symbols) or dark incubation (gray symbols).

Acetylated Lignin Nanoparticles Singlet Oxygen Production

It has been demonstrated that AcLi can produce ROS, specifically, singlet oxygen and superoxide anion (Marchand et al., 2018). We extrapolate these observations to the particular case of **@AcLi**, acting as photosensitizers in aqueous media and producing ROS. The singlet oxygen generated by **@AcLi** and **THPP@AcLi** was monitored by **TEMP** quenching, which easily

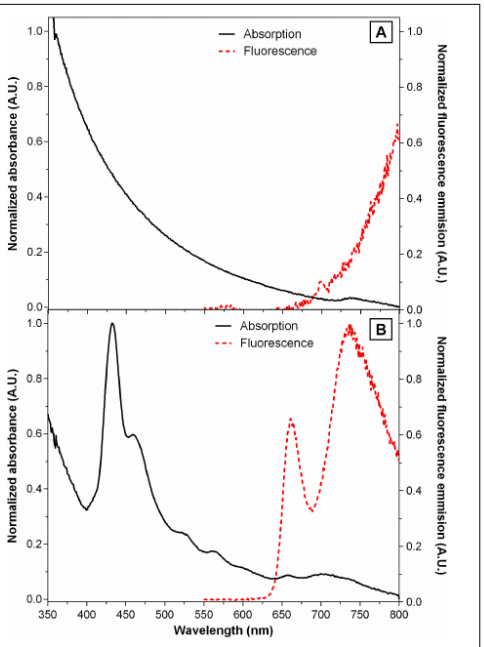

FIGURE 7 | Normalized UV-vis absorption spectra (black lines) and fluorescence emission spectra (red lines) of **(A)** acetylated lignin nanoparticles **(@AcLi)** [30 μg/ml] and **(B)** 5,10,15,20-tetrakis(4-hydroxyphenyl)-21*H*,23*H*-porphyrin-loaded **@AcLi (THPP@AcLi)** [**THPP** 2.5 μM, **AcLi** 30 μg/ml]; recorded in PB 0.1 M pH 7, room temperature, λ_{ex} = 425 nm.

reacts with singlet oxygen to form 2,2,6,6-tetramethylpiperidine-1-oxyl (**TEMPO**), a stable radical that can be detected with EPR spectroscopy (Riou et al., 2014; Marchand et al., 2018). In **Figure 6**, the nanoparticle suspensions in PB pH 7.4 of **@AcLi** (2 mg/ml) and **TPPOH@AcLi** (100 μg/ml lignin, 60 μM **THPP**) were compared, with or without light irradiation [halogen lamp, 270 μE/(s m^2)]. Rose bengal (1.5 μM, DMF), a well-known photosensitizer and singlet oxygen generator, was used as a reference. It is worth mentioning that the concentration of **@AcLi** nanoparticles was 20 times superior to that of **THPP@AcLi** but showed similar singlet oxygen generation, meaning that **THPP@AcLi** is approximately 20 times more efficient at producing singlet oxygen under the tested conditions. Both **@AcLi** and **THPP@AcLi** singlet oxygen was light-driven, corroborated by the differences observed between the dark and light irradiated samples, after 30 min (two-way ANOVA, Sidak's multiple comparison test, $P < 0.01$). The more efficient generation of singlet oxygen of **THPP@AcLi**, compared with **@AcLi**, demonstrated that **THPP** keeps its photosensitizing activity after encapsulation. Remarkably, the singlet oxygen produced by the encapsulated **THPP** is able to diffuse outside the nanoparticles, react with TEMP, and form the more stable TEMPO radical.

Acetylated Lignin Nanoparticle Fluorescence

It has been previously documented that molecular aggregation due to water coordination is a fluorescence quencher for porphyrins (Zannotti et al., 2018), a quantum phenomenon that is competitive with singlet oxygen production. To evaluate the extent of this issue, the fluorescent emission spectra of **@AcLi** (30 μg/ml) and **THPP@AcLi** (**THPP** 2.5 μM, **AcLi** 30 μg/ml) were measured as suspended in PB pH 7, with excitation at 425 nm (**Figure 7**).

Previous reports indicate that different chemical derivatives of lignin are fluorescent (Donaldson and Radotic, 2013). However, most of these observations have been done in organic solvents, where lignin is deployed without aggregation. Reports in the literature indicate that the fluorescence of lignin depends on the degree of aggregation, as the architecture of the nano-objects affects the interaction of the fluorophores (Xue et al., 2020). However, most of the studies on lignin fluorescence have been done with excitation wavelengths on the UV region, where lignin was known to strongly absorb. In our studies, we aimed at exciting the porphyrin, thus using excitation wavelength in the 400–500 nm range, where lignin did not absorb significantly. Thus, it is not surprising that a defined fluorescence band was not found for **@AcLi**; therefore, AcLi contribution to the fluorescence of **THPP@AcLi** was negligible in the tested conditions.

The **THPP@AcLi** emission spectrum, after excitation at 425 nm, showed two main peaks, a defined peak at 663 nm and a stronger less defined peak at around 733 nm. Additional experiments (**Supplementary Material 5**) showed that the peak found at 663 nm corresponds to **THPP** emission, while the peak at 733 nm could correspond to both **THPP** and $\mathbf{THPPH_2}^{2+}$ centered emission, as evidenced by the corresponding excitation spectra. The calculated quantum yield (Φ_F) for **THPP@AcLi** is 0.0016 ± 0.0001, a value that is lower than the one reported for **THPP** (Φ_F = 0.17, DMF) (Ormond and Freeman, 2013). Nevertheless, the obtained fluorescence still represents a success, as previous experiments have demonstrated that the fluorescence of **THPP** in aqueous media (Φ_F = 0.00071, PB pH 7, with 2.5% DMSO) is almost completely quenched. Thus, the encapsulation of **THPP@AcLi** partially prevented the quenching of **THPP** in aqueous medium and additionally avoided the usage of organic solvents to increase the availability of **THPP**.

Porphyrin's fluorescence is sensitive to the medium, especially to the pH (Zannotti et al., 2018; Leroy-Lhez et al., 2019). Previously in this work, we have demonstrated that **THPP@AcLi** were resistant to the fluctuation of pH in the media, according to UV-vis absorption and zeta potential studies. To further corroborate our findings, the fluorescence emission of **THPP@AcLi** was also recorded at different pH values (**Figure 8**). We could observe a pronounced decrease of fluorescence intensity with pH at 663 nm (**Figure 8**, inset), while the intensity of the fluorescence of the second band remained stable. Concomitantly, a red-shift of the wavelength of emission for this second band was also observed (from 733 nm at pH 10 to 745 nm at pH 2). This was not surprising as the peak at 663 nm is related to **THPP**, which in acidic media transforms into the protonated species $\mathbf{THPPH_2}^{2+}$; meanwhile, the second peak was related to both species and was thus affected by the equilibrium between **THPP** and $\mathbf{THPPH_2}^{2+}$ as a function of pH. Therefore, at a low pH value, $\mathbf{THPPH_2}^{2+}$ must be the predominant species, characterized by an emission at higher wavelength than **THPP**. However, when Φ_F was calculated for the whole pH range, it was found that besides variations on the emission profile, Φ_F remained stable (∼0.16) (**Supplementary Material 6**). This is consistent with our previous results, where we observed changes on the absorption spectra at acidic conditions. Nevertheless, the global quantum yield remained stable at different pHs.

Photodynamic Antimicrobial Chemotherapy Effect of Porphyrin-Loaded Nanoparticles Against Bacteria

The nanoparticles were tested against five bacterial strains, three Gram-positive (*S. aureus*, *S. epidermidis*, and *E. faecalis*) and two Gram-negative (*E. coli* and *P. aeruginosa*). The highest concentration of **THPP** encapsulated in **@AcLi** was 50 μM, corresponding to 0.33 mg/ml of **AcLi.** For **@AcLi**, the highest concentration used was 1.6 mg/ml; reports in the literature indicate that at this concentration, lignin nanoparticles were innocuous to human cells (Alqahtani et al., 2019). The results found in this study showed that **@AcLi** have a bacteriostatic effect at 1.6 mg/ml; nevertheless, **@AcLi** do not have a bactericidal effect at the highest concentration tested (**Supplementary Material 7**).

First, **THPP@AcLi** were evaluated as bacteriostatic agents, analyzing its capability to arrest bacterial growth. **THPP@AcLi** demonstrated a high capacity to diminish the growth of Gram-positive bacteria, after 1 h of irradiation, under a white LED light dose (4.16 J/cm^2). For Gram-positive inactivation, concentrations as low as 0.078 μM were enough to diminish growth at around 85% (**Figure 9A**). On the other hand, **THPP@AcLi** was not able to diminish the growth of Gram-negative *E. coli* but seemed to exert a bacteriostatic non-photodynamic effect on *P. aeruginosa* (**Figure 9B**). The most sensitive strain was *S. epidermidis*, followed by *E. faecalis* and, lastly, *S. aureus*. Usually, in PACT, low dark toxicities are desired, as it ensures that the antimicrobial effect is only triggered by light irradiation. Our results fulfill this necessity, as when using 0.640 μM of **THPP@AcLi**, the bacterial growth of *E. faecalis* was less than 10% after light irradiation; meanwhile, at dark incubation, the bacterial growth in the dark was around 85%. Similar results were found with *S. aureus* and *S. epidermidis* (**Supplementary Material 8**).

Although it can be addressed that growth arrest was due to the cellular death, it can also be provoked by a decrease on the bacterial metabolism or due to cellular damage, which may be overcome with enough recovery time. The difference between bacteriostatic and bactericidal effect is dose-dependent. Thus, the bacterial survival was assessed under similar conditions. As previously observed, **THPP@AcLi** was not effective against Gram-negative bacteria (**Supplementary Material 8**). Indeed, **THPP@AcLi** was unable to diminish the Gram-negative bacterial survival rate at 50 μM either at light (white LED light dose,

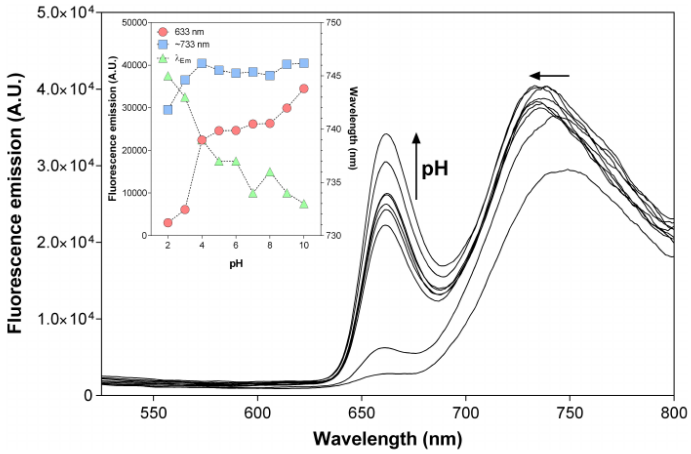

FIGURE 8 | Emission spectra of 5,10,15,20-tetrakis(4-hydroxyphenyl)-21*H*,23*H*-porphyrin-loaded acetylated lignin nanoparticles **(THPP@AcLi)** [3 μM], as a function of pH [0.1 M glycine-HCl buffer (pH 2 and pH 3), 0.1 M acetate buffer (pH 4 and pH 5), 0.1 M phosphate buffer (0.1 M pH 6, pH 7, and pH 8), 0.1 M glycine-NaOH buffer (pH 9 and pH 10)]; recorded at room temperature, λ_{Ex} = 425 nm. Inset: evolution of the fluorescence intensities recorded at 663 nm (red circles), the maximum emission at around 733 (blue squares), and the wavelength for the maximum emission found for the ∼733 nm band (green triangles) as a function of pH.

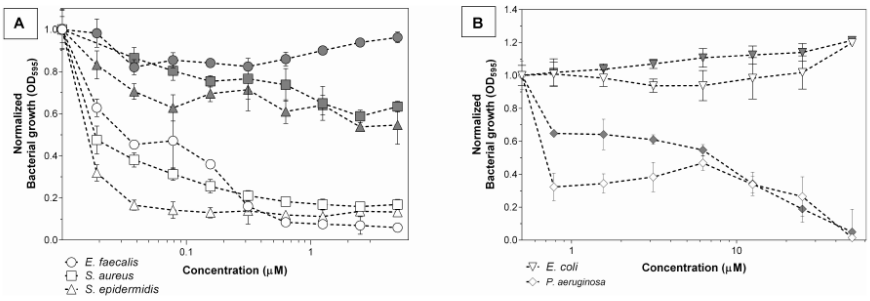

FIGURE 9 | Bacteriostatic effect of 5,10,15,20-tetrakis(4-hydroxyphenyl)-21*H*,23*H*-porphyrin-loaded acetylated lignin nanoparticles **(THPP@AcLi)** after light irradiation (white LED light dose, 4.16 J/cm^2, white symbols) or dark incubation (gray symbols) against **(A)** three Gram-positive bacteria and **(B)** two Gram-negative bacteria.

4.16 J/cm^2) or dark conditions (two-way ANOVA, Sidak's multiple comparisons test, $P > 0.05$).

Otherwise, several concentrations were tested for **THPP@AcLi** against the Gram-positive strains. They demonstrated a great efficiency at killing bacteria, being able to destroy up to 99.9999% of *E. faecalis* (**Figure 10**). Previous experiments (**Figure 9**) demonstrated a low dark chemotoxic effect for **THPP@AcLi**; in agreement, similar results were found on the bacterial survival rate (**Supplementary Material 10**), with differences between the light and dark conditions of several orders of magnitude. We found an efficient bactericidal effect at concentrations as low as 2.5 μM of **THPP@AcLi** and just 4.16 J/cm^2 of white LED light dose.

Our previous experiments had demonstrated that **THPP@AcLi** were stable at a wide range of pH. This is important for antibacterial applications. Usually, bacteria are viable within a limited range of pH values; with pathogenic bacteria being viable at a range between 5.5 and 8 (Madigan et al., 2014). However, bacterial metabolism provokes changes in the pH in different ways. Excretion of organic acids, such as propionic acid and isopropylic acid, can decrease the pH of the surrounding media, while amine compounds, formed through the degradation of amino acids and proteins, can increase the pH of the bacterial surrounding media (MacFaddin, 2000). Additionally, the pH of the medium has been found to influence the efficiency of several antibiotics (Yang et al., 2014). PACT is usually addressed as a

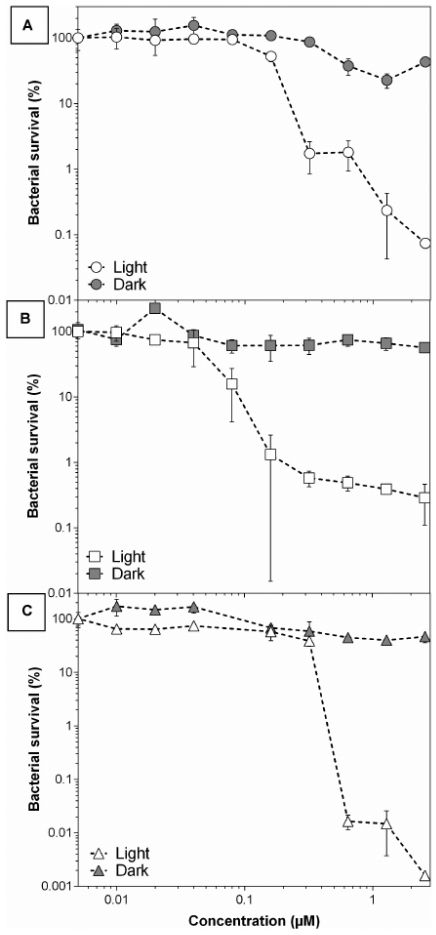

FIGURE 10 | 10 | Bacterial survival of **(A)** *S. aureus*, **(B)** *S. epidermidis*, and **(C)** *E. faecalis*, with 5,10,15,20-tetrakis(4-hydroxyphenyl)-21*H*,23*H*-porphyrin-loaded acetylated lignin nanoparticle **(THPP@AcLi)** treatment at different concentrations after light dose (4.16 J/cm^2) or dark incubation.

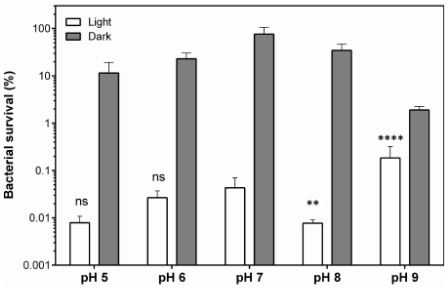

FIGURE 11 | Bacterial survival of *S. aureus*, as a function of pH, when treated with 5,10,15,20-tetrakis(4-hydroxyphenyl)-21*H*,23*H*-porphyrin-loaded acetylated lignin nanoparticles **(THPP@AcLi)** 2.5 μM under light irradiation (white LED light dose, 4.16 J/cm^2) or dark incubation. A two-way ANOVA analysis was made, with a Sidak's multiple comparison test, to analyze the differences found between pH 7 and the other pH conditions tested (ns, non-significant $P > 0.05$; $^{**}P < 0.01$; $^{****}P < 0.0001$). At all pH conditions, a difference was found between the light and dark conditions ($P < 0.0001$).

topical treatment or for surface disinfection due to the difficulty of irradiating the inside of a living being (Wainwright et al., 2017). Thus, a formulation that works on a wide range of pH is desirable, as it can withstand the changes provoked by bacteria or the conditions found on several surfaces.

In that perspective, **THPP@AcLi** was tested against *S. aureus* on aqueous media from pH 5 to pH 9, at a concentration of 2.5 μM, where we had previously observed a decrease of bacterial survival of at least 99.9% (**Figure 11**). Other pH conditions were tested, but as the bacterial controls demonstrated being unviable, these results were not included in the analysis. **THPP@AcLi** was able to diminish bacterial survival at all the pH conditions, through an effective photodynamic effect observed, with differences between light irradiation and dark incubation samples (two-way ANOVA, Sidak's multiple comparisons test, $P < 0.0001$). When compared with the PACT effect obtained at pH 7, no differences were found at pH 5 and pH 6 ($P > 0.05$). Nevertheless, at pH 8, the PACT effect had a slight improvement ($P < 0.01$), while at pH 9, the bacterial survival increased up to 0.184 ($P < 0.0001$). Although statistically there were some differences found, in general, the PACT effect permitted a bacterial survival below 0.2%. The fluctuation of the values found could be attributed to either the pH effect on the cells or the buffer composition, as three buffers with different compositions were used for this experiment. Thus, **THPP@AcLi** PACT effect was stable at a wide range of pH. Their stability corresponded to our previous observations, where their photophysical characteristics remained relatively stable at different pH conditions. This good correlation between the photophysical properties and their biological applications enhanced the applications spectra for **@AcLi** loaded with a photosensitizer.

In order to further demonstrate the stability of **THPP@AcLi**, their resistance to light irradiation was assessed. **THPP@AcLi** were exposed to light irradiation periods before incubation with bacteria under conditions similar to previously done PACT experiments. Afterward, the irradiated nanoparticles were mixed with *S. aureus* bacteria and the PACT irradiation was carried out, as routinely for bacterial eradication. A non-irradiated control was used, and bacterial survival was reported after *S. aureus* photodynamic eradication (**Figure 12A**). The **THPP@AcLi** withstood the light irradiation, remaining as effective as the previously non-irradiated sample (0 J/cm^2). This would allow nanoparticles to remain functional after long irradiation periods or after several cycles of usage. To analyze the effect of light irradiation on **THPP@AcLi**, nanoparticles were irradiated under

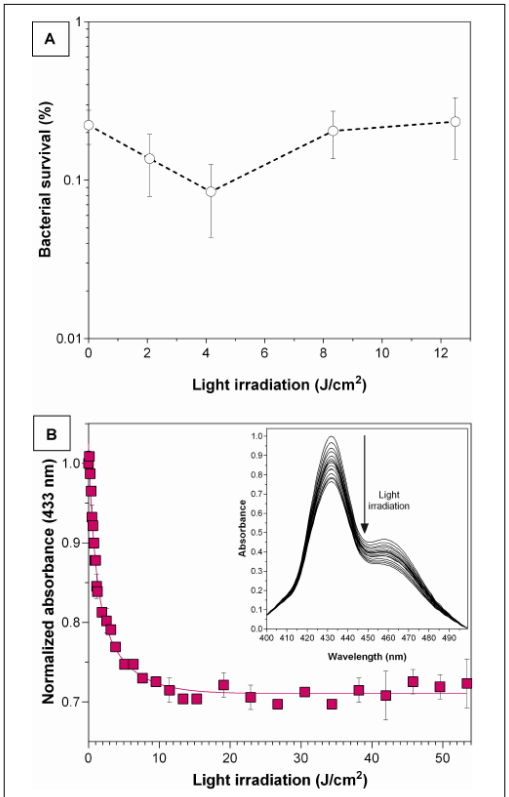

FIGURE 12 | Effect on 5,10,15,20-tetrakis(4-hydroxyphenyl)-21*H*,23*H*-porphyrin-loaded acetylated lignin nanoparticles **(THPP@AcLi)** of previous light irradiation. **(A)** Photoeradication of *S. aureus* (white LED light dose, 4.16 J/cm^2), with nanoparticles previously irradiated with white LED light. As a control, a non-irradiated sample was used (0 J/cm^2). **(B) THPP@AcLi** absorbance at 433 nm was monitored through its irradiation with white LED light (1 mW/cm^2). Inset: the spectra between 400 and 500 nm are observed for the whole irradiation time.

similar conditions and the absorbance at 433 nm was monitored after irradiation in order to evaluate potential degradation due to light-driven self-annihilation (**Figure 12B**). Interestingly, the absorption of the Soret band diminished quickly and then reached a plateau, with around 73.32% of the original absorbance found, even after 7 h of constant irradiation (1 mW/cm^2). By analyzing the UV-vis absorption spectra, a decrease on the B-band intensity at 457 nm was also observed, with changes in the ratio between this and the Soret band (initial A_{437}/A_{452} 0.465, final A_{437}/A_{452} 0.334). As the B-band can be attributed to the protonated molecule **THPPH$_2^{2+}$** according to the literature (Zannotti et al., 2018; Leroy-Lhez et al., 2019), we can conclude that this species was more sensitive to photobleaching than the non-protonated one.

5,10,15,20-Tetrakis(4-Hydroxyphenyl)-21H,23H-Porphyrin Inside Acetylated Lignin Nanoparticle Interaction With Bacteria

In this work, the stability of **THPP@AcLi** photophysical properties has been demonstrated, being effective against Gram-positive bacteria at different pH values, even after previous light irradiation. However, the previous experiments had not clarified how bacteria are eradicated, as is less likely that the photosensitizer gets in direct contact with bacteria. The uptake of porphyrins and other photosensitizers by bacteria had been widely studied (Ferro et al., 2007; Orekhov et al., 2018), but our results suggested that **THPP@AcLi** do not leak out the photosensitizer. In order to have an insight into the interaction between bacteria and **THPP@AcLi**, we made TEM observations over a mixture of bacteria and nanoparticles. *S. aureus* cells were observed without typical chemical fixation (**Figure 13A**). The observed cells did not have the characteristic round shape found for staphylococci bacteria; rather, they had a "squashed" shape likely due to the acidic uranyl acetate fixation/staining. When nanoparticles were mixed, a spontaneous binding was observed, as no incubation time elapsed for the first observation (**Figure 13B**). Interestingly, the amount of observable free nanoparticles was low when compared to the observed bound nanoparticles. Nanoparticles were observed surrounding the surface of bacteria. The attached nanoparticles were observed as spheres, with only a partial merge within the bacterial membrane. This suggested that nanoparticles do not penetrate inside the cell but remained in the outskirts of the membrane. Preparations made from a mixture of bacteria and nanoparticles, done 30 min ahead, still presented this pattern. Thus, the penetration of nanoparticles inside bacteria is not time dependent. The mixture of nanoparticles and bacteria was irradiated *in situ* over the copper grid with an incandescent bulb light (2,500 lux, 5 min) and was observed at TEM. After light irradiation, bacteria were scarce and cellular debris was observed throughout the place. Bacteria were also found surrounded by **THPP@AcLi** (**Figures 13C,D**). In some cases, bacteria were observed while spilling their cellular contents (**Figure 13D**). The cellular contents include proteins and nucleic acids, which are transparent to the TEM, but we were able to observe them after being contrasted with uranyl acetate, observable at TEM, as black debris. The TEM observations suggest that bacteria suffered extensive damage on their cellular wall when exposed to light and **THPP@AcLi**. As presumably nanoparticles were unable to completely penetrate inside the cell, a local ROS production against the cellular wall was likely to trigger the photodynamic effect. Insufficient damage to the bacterial wall may provoke an arrest on the bacterial growth, which corresponds to our previous observations of a large bacteriostatic effect for **THPP@AcLi**.

An interesting observation was the spontaneous binding of THPP@AcLi with bacteria. It had been previously observed that lignin nanoparticles worked as flocculants, capturing

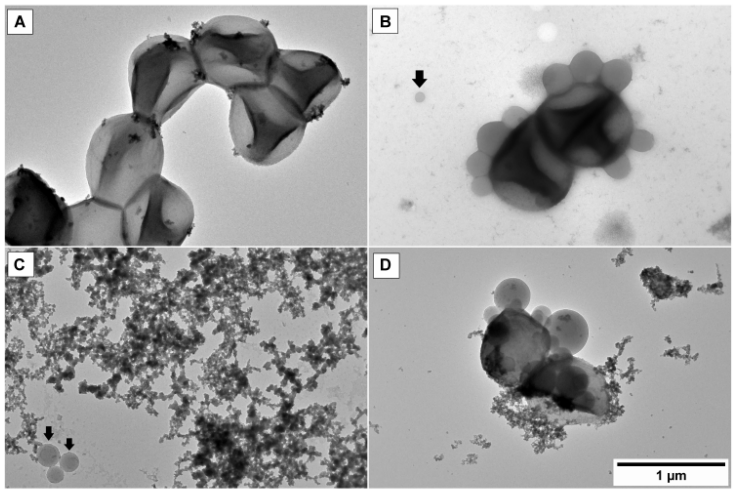

FIGURE 13 | Transmission electron microscopy (TEM) observations of **(A)** *S. aureus* cells *in vivo*; **(B)** *S. aureus* and 5,10,15,20-tetrakis(4-hydroxyphenyl)-21*H*,23*H*-porphyrin-loaded acetylated lignin nanoparticles **(THPP@AcLi)**, the black arrow indicates a non-bound nanoparticle; **(C)** and **(D)** *S. aureus* and **THPP@AcLi** after light irradiation (incandescent bulb, 2,500 luxes, 5 min).

E. coli and *S. aureus* (Yin et al., 2018). This effect was observed in our experiments, where the mixture of bacteria and nanoparticles quickly flocculated to the bottom of the flask. The high affinity of bacteria and THPP@AcLi may work as a synergic system. Although we had observed through EPR a low production of singlet oxygen for THPP@AcLi, the tight interaction between bacteria and nanoparticles results in a higher concentration of ROS at the cellular level. Thus, both flocculant and photodynamic effect could be a promising alternative as a PACT system. Such system could find wide applications in wastewater purification, a complex media with biological and chemical pollutants that require disinfection before release into the environment. Purification of wastewater usually comprises physical methods, involving sedimentation, aeration, and filtration, and at these steps, lignin could be used as an alternative.

DISCUSSION

Our results demonstrate that **THPP** encapsulation into @AcLi is an easy, effective, and reproducible method, increasing the value of lignin as a biopolymer with biomedical applications. Besides, this encapsulation method may be suitable for a wide range of molecules, which are our current subject of study.

The effect of aggregation on porphyrins and tetrapyrrolic compounds has been addressed as one of the main issues for biological applications of both PDT and PACT, as aggregation quenches ROS production, diminishing their efficiency and potential (Liu et al., 2018). The present work has produced a formulation that efficiently delivers **THPP** into an aqueous media, with less aggregation than the non-encapsulated **THPP**. Besides, **THPP** inside **@AcLi** is able to withstand a wide pH range without being affected, as demonstrated by its UV-vis absorption and fluorescence emission properties. Additionally, the pH stability is extended to its physicochemical properties, as its zeta potential, and the changes in the pH of the media do not affect their efficiency against bacteria.

Lignin nanoparticles are currently under research as vehicles for small molecules, with reports of nanoparticles being able to diffuse the small molecules over time or over pH changes (Zhou et al., 2019). Nevertheless, we were able to demonstrate that **THPP@AcLi** are stable over time, releasing less than 10% of **THPP** into the surrounding media after 60 days of observations. However, the stable encapsulation of **THPP** inside nanoparticles leads to the question if ROS generated by **THPP** would be able to escape from the nanoparticles and actually produce an observable macroscopic effect. Through EPR, we detected singlet oxygen generation for **@AcLi** and for **THPP@AcLi**. However, the evidence has demonstrated that **THPP@AcLi** singlet oxygen generation is mostly due to **THPP**, as **THPP@AcLi** is 20 times more efficient at producing singlet oxygen than **@AcLi**. Then, singlet oxygen generated by **THPP** was able to diffuse through the**@AcLi**.

Although it has been indicated that a light dose of 4.16 J/cm^2 is necessary to kill bacteria, recent reports have indicated that the UV-vis absorbance of PACT and PDT molecules need to be taken into account for a corrected light dose (Schaberle, 2018). With this correction done (**Supplementary Material 2**), **THPP@AcLi** is only able to absorb 65% of the white LED light irradiated on it,

resulting in a corrected light dose of 2.71 J/cm^2. Our experiments had demonstrated that the nanoparticles were stable under light doses 20 times higher than the corrected light dose, and thus higher doses could be applied on bacteria, while maintaining their efficiency.

In regard to bacterial eradication, **THPP@AcLi** was only able to diminish the bacterial growth and survival of Gram-positive bacteria. This is not surprising, as PACT has been described as more effective against Gram-positive bacteria than against Gram-negative ones (Huang et al., 2012). The differences in the efficiency were addressed to be due to the impermeability of its double membrane, a common problem with the development of successful antibiotic treatments (Nikaido, 2003). Interestingly, PACT applications on Gram-negative bacteria had overcome this obstacle through the usage of cationic photosensitizers (Ragàs et al., 2010; Cieplik et al., 2018; Aroso et al., 2019) or photosensitizers linked to antimicrobial peptides (Le Guern et al., 2017, 2018), which have a high affinity for the anionic heads of the lipopolysaccharides, facilitating the interaction between bacteria and photosensitizer. Interestingly, in our work, we observed that although nanoparticles have a negative charge, they seem to strongly interact with bacteria, demonstrated by TEM observations. Thus, further investigations are underway with cationic molecules inside **@AcLi**, aiming for Gram-negative bacteria eradication. Additionally, lignin modifications could lead to the construction of cationic lignin nanoparticles. Nevertheless, we had observed strong spontaneous interactions between nanoparticles and bacteria. It has been previously addressed that lignin nanoparticles were prone to act as flocculant agents, working as a physical method for water disinfection (Yin et al., 2018). Our strategy combines physical decontamination and a light-driven chemotoxic effect, a combination that could be ideal for wastewater decontamination. Wastewater is a complex mixture that needs to be purified before being released into the environment. Acetylated lignin nanoparticles could be used for light-driven water purification and, at the same time, for physical removal of bacteria and bacterial debris.

This work represents a cornerstone on lignin applications, as it is the first time it has been used on PACT applications. The present work, although able to eradicate Gram-positive bacteria, was unable to affect the survival of Gram-negative bacteria. Our future work comprises the modification of lignin with "sticky" moieties and the encapsulation of cationic porphyrins, hoping to obtain a wide-range formulation for antibacterial and antibiofilm purposes. Additionally, our future work aims to enhance the comprehension of the mechanism of the interaction between THPP/AcLi/bacteria through porphyrin uptake experiments and flow cytometry.

CONCLUSION

Acetylated lignin nanoparticles were able to encapsulate a porphyrinic compound, **THPP**. Additionally, the encapsulation system was stable at a wide pH range, conserving its physical and photophysical properties, without leaking the encapsulated compound. Furthermore, it was demonstrated that this system was able to produce ROS and exert a photodynamic eradication effect on three Gram-positive strains. The photodynamic eradication could be due to a synergic effect of the flocculant properties of lignin nanoparticles and the light-driven ROS production of **THPP**. The encapsulation of further photosensitizers is likely to improve the presented results, and this strategy is currently under study for water decontamination and other applications.

DATA AVAILABILITY STATEMENT

The raw data supporting the conclusions of this article will be made available by the authors, without undue reservation, to any qualified researcher.

AUTHOR CONTRIBUTIONS

NM-C, GM, and NV participated on the preparation of the raw material and the nanoparticles. NM-C, GM, and SL-L participated on the characterization of the physico-chemical properties of the raw material and the nanoparticles. NM-C and CC measured the singlet oxygen production through EPR. NM-C and T-SO designed and performed the microbiological experiments. NM-C, KP, AŻ, and KM designed and performed the TEM observations. NM-C, MMP, and MC designed and performed the fluorescence spectroscopy experiments. All authors discussed the results and commented on the manuscript.

FUNDING

This project has received funding from the European Union's Horizon 2020 Research and Innovation Program under the Marie Skłodowska-Curie grant agreement no. 764837. The transmission electron microscopy imaging was funded from the National Science Centre (PL) under "Miniatura" grant no. 2019/03/X/NZ3/02100.

ACKNOWLEDGMENTS

NM-C would like to acknowledge the support of Dr. Fábio A. Schaberle regarding the fluorescence spectroscopy and photobleaching experiments.

SUPPLEMENTARY MATERIAL

The Supplementary Material for this article can be found online at: https://www.frontiersin.org/articles/10.3389/fmicb.2020.606185/full#supplementary-material

REFERENCES

Alqahtani, M. S., Alqahtani, A., Al-Thabit, A., Roni, M., and Syed, R. (2019). Novel lignin nanoparticles for oral drug delivery. *J. Mater. Chem. B* 7, 4461–4473. doi: 10.1039/c9tb00594c

Aroso, R. T., Calvete, M. J. F., Pucelik, B., Dubin, G., Arnaut, L. G., Pereira, M. M., et al. (2019). Photoinactivation of microorganisms with sub-micromolar concentrations of imidazolium metallophthalocyanine salts. *Eur. J. Med. Chem.* 184:111740. doi: 10.1016/j.ejmech.2019.111740

Baccani, I., Faraoni, P., Marini, M., Gnerucci, A., Orsini, B., Pecile, P., et al. (2019). Synergistic effect of photodynamic therapy at 400 nm and doxycycline against *Helicobacter pylori*. *Fut. Microbiol.* 14, 1199–1205. doi: 10.2217/fmb-2019-0129

Bechara Andere, N. M. R., Dos Santos, N. C. C., Araujo, C. F., Mathias, I. F., Rossato, A., de Marco, A. C., et al. (2018). Evaluation of the local effect of nonsurgical periodontal treatment with and without systemic antibiotic and photodynamic therapy in generalized aggressive periodontitis. A randomized clinical trial. Photodiagnosis Photodyn. *Ther.* 24, 115–120. doi: 10.1016/j.pdpdt.2018.09.002

Buchovec, I., Lukseviciute, V., Marsalka, A., Reklaitis, I., and Luksiene, Z. (2016). Effective photosensitization-based inactivation of Gram (-) food pathogens and molds using the chlorophyllin–chitosan complex: towards photoactive edible coatings to preserve strawberries. *Photochem. Photobiol. Sci.* 15, 506–516. doi: 10.1039/C5PP00376H

Calvo-Flores, F. G., and Dobado, J. A. (2010). Lignin as renewable raw material. *ChemSusChem* 3, 1227–1235. doi: 10.1002/cssc.201000157

Cieplik, F., Deng, D., Crielaard, W., Buchalla, W., Hellwig, E., Al-Ahmad, A., et al. (2018). Antimicrobial photodynamic therapy–what we know and what we don't. *Crit. Rev. Microbiol.* 44, 571–589. doi: 10.1080/1040841X.2018.1467876

Danaei, M., Dehghankhold, M., Ataei, S., Hasanzadeh Davarani, F., Javanmard, R., Dokhani, A., et al. (2018). Impact of particle size and polydispersity index on the clinical applications of lipidic nanocarrier systems. *Pharmaceutics* 10:57. doi: 10.3390/pharmaceutics10020057

de Freitas, L. M., Calixto, G. M. F., Chorilli, M., Giusti, J. S. M., Bagnato, V. S., Soukos, N. S., et al. (2016). Polymeric nanoparticle-based photodynamic therapy for chronic periodontitis *in Vivo*. *Int. J. Mol. Sci.* 17:769. doi: 10.3390/ijms17050769

Donaldson, L. A., and Radotic, K. (2013). Fluorescence lifetime imaging of lignin autofluorescence in normal and compression wood. *J. Microsc.* 251, 178–187. doi: 10.1111/jmi.12059

Duval, A., and Lawoko, M. (2014). A review on lignin-based polymeric, micro- and nano-structured materials. *React. Funct. Polym.* 85, 78–96. doi: 10.1016/j.reactfunctpolym.2014.09.017

Faix, O. (1991). Classification of lignins from different botanical origins by FT-IR spectroscopy. *Holzforschung* 45, 21–28. doi: 10.1515/hfsg.1991.45.s1.21

Ferro, S., Ricchelli, F., Monti, D., Mancini, G., and Jori, G. (2007). Efficient photoinactivation of methicillin-resistant *Staphylococcus aureus* by a novel porphyrin incorporated into a poly-cationic liposome. *Int. J. Biochem. Cell Biol.* 39, 1026–1034. doi: 10.1016/j.biocel.2007.02.001

Figueiredo, P., Lintinen, K., Hirvonen, J. T., Kostiainen, M. A., and Santos, H. A. (2018). Properties and chemical modifications of lignin: Towards lignin-based nanomaterials for biomedical applications. *Prog. Mater. Sci.* 93, 233–269. doi: 10.1016/j.pmatsci.2017.12.001

Figueiredo, P., Lintinen, K., Kiriazis, A., Hynninen, V., Liu, Z., Bauleth-Ramos, T., et al. (2017). *In vitro* evaluation of biodegradable lignin-based nanoparticles for drug delivery and enhanced antiproliferation effect in cancer cells. *Biomaterials* 121, 97–108. doi: 10.1016/j.biomaterials.2016.12.034

Frangville, C., Rutkevičius, M., Richter, A. P., Velev, O. D., Stoyanov, S. D., and Paunov, V. N. (2012). Fabrication of environmentally biodegradable lignin nanoparticles. *ChemPhysChem* 13, 4235–4243. doi: 10.1002/cphc.201200537

Glueck, M., Schamberger, B., Eckl, P., and Plaetzer, K. (2017). New horizons in microbiological food safety: Photodynamic decontamination based on a curcumin derivative. *Photochem. Photobiol. Sci.* 16, 1784–1791. doi: 10.1039/C7PP00165G

Hsieh, Y. H., Chuang, W. C., Yu, K. H., Jheng, C. P., and Lee, C. I. (2019). Sequential photodynamic therapy with phthalocyanine encapsulated chitosan-tripolyphosphate nanoparticles and flucytosine treatment against *Candida tropicalis*. *Pharmaceutics* 11:16. doi: 10.3390/pharmaceutics11010016

Huang, L., Xuan, Y., Koide, Y., Zhiyentayev, T., Tanaka, M., and Hamblin, M. R. (2012). Type I and Type II mechanisms of antimicrobial photodynamic therapy: An *in vitro* study on Gram-negative and Gram-positive bacteria. *Laser* 44, 490–499. doi: 10.1002/lsm.22045.Type

Jia, R., Tian, W., Bai, H., Zhang, J., Wang, S., and Zhang, J. (2019). Sunlight-driven wearable and robust antibacterial coatings with water-soluble cellulose-based photosensitizers. *Adv. Healthc. Mater.* 8:1801591. doi: 10.1002/adhm.201801591

Josefsen, L. B., and Boyle, R. W. (2012). Unique diagnostic and therapeutic roles of porphyrins and phthalocyanines in photodynamic therapy, imaging and theranostics. *Theranostics* 2, 916–966. doi: 10.7150/thno.4571

Khaldi, Z., Nzambe Takeki, J. K., Ouk, T.-S., Lucas, R., and Zerrouki, R. (2019). Synthesis and photo-bactericidal properties of a cationic porphyrin grafted onto kraft pulp fibers. *J. Porphyr. Phthalocyanines* 23, 489–496. doi: 10.1142/S1088424619500330

Kumar, A., and Dixit, C. K. (2017). "Methods for characterization of nanoparticles," in *Advances in Nanomedicine for the Delivery of Therapeutic Nucleic Acids*, eds C. Ramesh, N. Gupta, and S. Nimesh (Netherlands: Elsevier), 43–58. doi: 10.1016/B978-0-08-100557-6.00003-1

Le Guern, F., Ouk, T. S., Ouk, C., Vanderesse, R., Champavier, Y., Pinault, E., et al. (2018). Lysine analogue of polymyxin B as a significant opportunity for photodynamic antimicrobial chemotherapy. *ACS Med. Chem. Lett.* 9, 11–16. doi: 10.1021/acsmedchemlett.7b00360

Le Guern, F., Sol, V., Ouk, C., Arnoux, P., Frochot, C., and Ouk, T. S. (2017). Enhanced photobactericidal and targeting properties of a cationic porphyrin following the attachment of polymyxin B. *Bioconjug. Chem.* 28, 2493–2506. doi: 10.1021/acs.bioconjchem.7b00516

Leroy-Lhez, S., Rezazgui, O., Issawi, M., Elhabiri, M., Calliste, C. A., and Riou, C. (2019). Why are the anionic porphyrins so efficient to induce plant cell death? A structure-activity relationship study to solve the puzzle. *J. Photochem. Photobiol. A Chem.* 368, 276–289. doi: 10.1016/j.jphotochem.2018.09.050

Lewis, K. (2013). Platforms for antibiotic discovery. *Nat. Rev. Drug Discov.* 12, 371–387. doi: 10.1038/nrd3975

Liu, D., Li, L., Chen, J., Chen, Z., Jiang, L., Yuan, C., et al. (2018). Dissociation of zinc phthalocyanine aggregation on bacterial surface is key for photodynamic antimicrobial effect. *J. Porphyr. Phthalocyanines* 22, 1–10. doi: 10.1142/S1088424618500888

MacFaddin, J. F. (2000). *Biochemical Tests for Identification of Medical Bacteria*, 3rd Edn. Pennsylvania: Williams and Wilkins.

Madigan, M. T., Martinko, J. F., Bender, K. S., Buckley, D. H., Stahl, D. A., and Brock, T. (2014). *Brock Biology of Microorganisms*, 14th Edn. London: Pearson Education Limited.

Maldonado-Carmona, N., Ouk, T. S., Calvete, M. J. F., Pereira, M. M., Villandier, N., and Leroy-Lhez, S. (2020). Conjugating biomaterials with photosensitizers: Advances and perspectives for photodynamic antimicrobial chemotherapy. *Photochem. Photobiol. Sci.* 19, 445–461. doi: 10.1039/c9pp00398c

Marchand, G., Calliste, C. A., Williams, R. M., McLure, C., Leroy-Lhez, S., and Villandier, N. (2018). Acetylated lignins: A potential bio-sourced photosensitizer. *ChemistrySelect* 3, 5512–5516. doi: 10.1002/slct.201801039

Marchand, G., Fabre, G., Maldonado-Carmona, N., Villandier, N., and Leroy-Lhez, S. (2020). Acetylated lignin nanoparticles as a prospective vehicle for photosensitizing molecules. *Nanoscale Adv.* 2020, D0NA00615G. doi: 10.1039/D0NA00615G

Martinez, A. F. C., de Almeida, L. G., Moraes, L. A. B., and Cônsoli, F. L. (2017). Tapping the biotechnological potential of insect microbial symbionts: new insecticidal porphyrins. *BMC Microbiol.* 17:143. doi: 10.1186/s12866-017-1054-y

Nikaido, H. (2003). Molecular basis of bacterial outer membrane permeability revisited. *Microbiol. Mol. Biol. Rev.* 67, 593–656. doi: 10.1128/MMBR.67.4.593-656.2003

Nzambe Ta keki, J. K., Ouk, T.-S., Zerrouki, R., Faugeras, P.-A., Sol, V., and Brouillette, F. (2016). Synthesis and photobactericidal properties of a neutral porphyrin grafted onto lignocellulosic fibers. *Mater. Sci. Eng.* 62, 61–67. doi: 10.1016/j.msec.2016.01.028

O'Neill, J. (2016). *Tackling drug-resistant infections globally: Final report and recommendations*. United Kingdom: Government of the United Kingdom.

Orekhov, P. S., Kholina, E. G., Bozdaganyan, M. E., Nesterenko, A. M., Kovalenko, I. B., and Strakhovskaya, M. G. (2018). Molecular mechanism of uptake of cationic photoantimicrobial phthalocyanine across bacterial membranes revealed by molecular dynamics simulations. *J. Phys. Chem. B* 122, 3711–3722. doi: 10.1021/acs.jpcb.7b11707

Ormond, A. B., and Freeman, H. S. (2013). Effects of substituents on the photophysical properties of symmetrical porphyrins. *Dye. Pigment.* 96, 440–448. doi: 10.1016/j.dyepig.2012.09.011

Pineiro, M., Carvalho, A. L., Pereira, M. M., Gonsalves, A. M. d'A. R, Arnaut, L. G., and Formosinho, S. J. (1998). Photoacoustic measurements of porphyrin triplet-state quantum yields and singlet-oxygen efficiencies. *Chem. A Eur. J.* 4, 2299–2307. doi: 10.1002/(SICI)1521-3765(19981102)4:11<2299::AID-CHEM2299<3.0.CO;2-H

Ponomarenko, J., Lauberts, M., Dizhbite, T., Lauberte, L., Jurkjane, V., and Telysheva, G. (2015). Antioxidant activity of various lignins and lignin-related phenylpropanoid units with high and low molecular weight. *Holzforschung* 69, 795–805. doi: 10.1515/hf-2014-0280

Qian, Y., Deng, Y., Li, H., and Qiu, X. (2014a). Reaction-free lignin whitening via a self-assembly of acetylated lignin. *Ind. Eng. Chem. Res.* 53, 10024–10028. doi: 10.1021/ie5010338

Qian, Y., Deng, Y., Qiu, X., Li, H., and Yang, D. (2014b). Formation of uniform colloidal spheres from lignin, a renewable resource recovered from pulping spent liquor. *Green Chem.* 16, 2156–2163. doi: 10.1039/c3gc42131g

Ragàs, X., Sánchez-García, D., Ruiz-González, R., Dai, T., Agut, M., Hamblin, M. R., et al. (2010). Cationic porphycenes as potential photosensitizers for antimicrobial photodynamic therapy. *J. Med. Chem.* 53, 7796–7803. doi: 10.1021/jm1009555

Regiel-Futyra, A., Dąbrowski, J. M., Mazuryk, O., Śpiewak, K., Kyzioł, A., Pucelik, B., et al. (2017). Bioinorganic antimicrobial strategies in the resistance era. *Coord. Chem. Rev.* 351, 76–117. doi: 10.1016/j.ccr.2017.05.005

Ringot, C., Saad, N., Brégier, F., Bressollier, P., Poli, E., Chaleix, V., et al. (2018). Antibacterial activity of a photosensitive hybrid cellulose fabric. *Photochem. Photobiol. Sci.* 17, 1780–1786. doi: 10.1039/C8PP00212F

Riou, C., Calliste, C. A., Da Silva, A., Guillaumot, D., Rezazgui, O., Sol, V., et al. (2014). Anionic porphyrin as a new powerful cell death inducer of Tobacco Bright Yellow-2 cells. *Photochem. Photobiol. Sci.* 13:621. doi: 10.1039/c3pp50315a

Rocca, D. M., Vanegas, J. P., Fournier, K., Becerra, M. C., Scaiano, J. C., and Lanterna, A. E. (2018). Biocompatibility and photo-induced antibacterial activity of lignin-stabilized noble metal nanoparticles. *RSC Adv.* 8, 40454–40463. doi: 10.1039/C8RA08169G

Schaberle, F. A. (2018). Assessment of the actual light dose in photodynamic therapy. Photodiagnosis Photodyn. *Ther.* 23, 75–77. doi: 10.1016/j.pdpdt.2018.06.009

Schindelin, J., Arganda-Carreras, I., Frise, E., Kaynig, V., Longair, M., Pietzsch, T., et al. (2012). Fiji: an open-source platform for biological-image analysis. *Nat. Methods* 9, 676–682. doi: 10.1038/nmeth.2019

Schneider, C. A., Rasband, W. S., and Eliceiri, K. W. (2012). NIH Image to ImageJ: 25 years of image analysis. *Nat. Methods* 9, 671–675. doi: 10.1038/nmeth.2089

Tse, H.-Y., Cheng, S.-C., Yeung, C. S., Lau, C.-Y., Wong, W.-H., Dong, C., et al. (2019). Development of a waste-derived lignin-porphyrin bio-polymer with enhanced photoluminescence at high water fraction with wide pH range and heavy metal sensitivity investigations. *Green Chem.* 21, 1319–1329. doi: 10.1039/C8GC02904K

Vinagreiro, C. S., Zangirolami, A., Schaberle, F. A., Nunes, S. C. C., Blanco, K. C., Inada, N. M., et al. (2020). Antibacterial photodynamic inactivation of antibiotic-resistant bacteria and biofilms with nanomolar photosensitizer concentrations. *ACS Infect. Dis.* 6, 1517–1526. doi: 10.1021/acsinfecdis.9b00379

Wainwright, M. (2019). Photoantimicrobials and PACT: what's in an abbreviation? *Photochem. Photobiol. Sci.* 18, 12–14. doi: 10.1039/C8PP00390D

Wainwright, M., Maisch, T., Nonell, S., Plaetzer, K., Almeida, A., Tegos, G. P., et al. (2017). Photoantimicrobials—are we afraid of the light? *Lancet Infect. Dis.* 17, 49–55e. doi: 10.1016/S1473-3099(16)30268-7

Wang, C., Kelley, S. S., and Venditti, R. A. (2016). Lignin-based thermoplastic materials. *ChemSusChem* 9, 770–783. doi: 10.1002/cssc.201501531

WHO (2015). *Global action plan on antimicrobial resistance*. Geneva,: World Health. Organnization.

Xue, Y., Qiu, X., and Ouyang, X. (2020). Insights into the effect of aggregation on lignin fluorescence and its application for microstructure analysis. *Int. J. Biol. Macromol.* 154, 981–988. doi: 10.1016/j.ijbiomac.2020.03.056

Yang, L., Wang, K., Li, H., Denstedt, J. D., and Cadieux, P. A. (2014). The influence of urinary pH on antibiotic efficacy against bacterial uropathogens. *Urology* 84:48. doi: 10.1016/j.urology.2014.04.048

Yang, W., Owczarek, J. S., Fortunati, E., Kozanecki, M., Mazzaglia, A., Balestra, G. M., et al. (2016). Antioxidant and antibacterial lignin nanoparticles in polyvinyl alcohol/chitosan films for active packaging. *Ind. Crops Prod.* 94, 800–811. doi: 10.1016/j.indcrop.2016.09.061

Yin, H., Liu, L., Wang, X., Wang, T., Zhou, Y., Liu, B., et al. (2018). A novel flocculant prepared by lignin nanoparticles-gelatin complex from switchgrass for the capture of *Staphylococcus aureus* and *Escherichia coli*. *Colloids Surf. A Physicochem. Eng. Asp.* 545, 51–59. doi: 10.1016/j.colsurfa.2018.02.033

Zannotti, M., Giovannetti, R., Minofar, B., Øeha, D., Plaèková, L., D'Amato, C. A., et al. (2018). Aggregation and metal-complexation behaviour of THPP porphyrin in ethanol/water solutions as function of pH. Spectrochim. *Acta Part A Mol. Biomol. Spectrosc.* 193, 235–248. doi: 10.1016/j.saa.2017.12.021

Zhou, M., Wang, D., Yang, D., Qiu, X., and Li, Y. (2019). Avermectin loaded nanosphere prepared from acylated alkali lignin showed anti-photolysis property and controlled release performance. *Ind. Crops Prod.* 137, 453–459. doi: 10.1016/j.indcrop.2019.04.037

Conflict of Interest: The authors declare that the research was conducted in the absence of any commercial or financial relationships that could be construed as a potential conflict of interest.

frontiers

Supplementary Material

Table of Contents

1. Preparation of samples for transmission electron microscopy observations

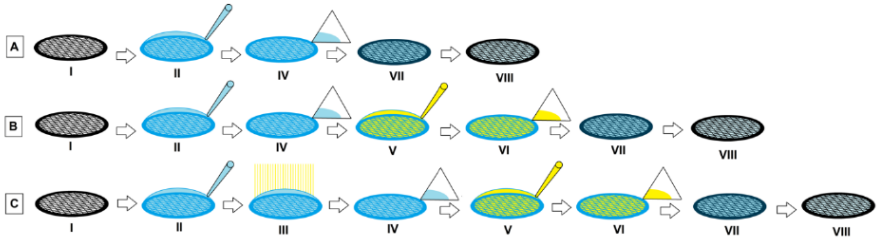

Figure S1. Transmission electron microscopy preparation process for nanoparticles (A), bacteria (B) and nanoparticle-bacteria interaction (C): I - clean and hydrophilic carbon grid, II - sample drop, III - light irradiation, IV - sample blot, V - negative stain drop, VI - negative stain blot after 60s, VII - air-drying, VIII - sample ready for observation.

2. Light Dose correction

Light dose correction was done, accordingly to the literature (Schaberle, 2018). For this, the power of the light emission source was obtained with a handheld power meter (LaserCheck, Coherent), and the light dose calculation was obtained using the equation S1:

$$LDC = \frac{\frac{\sum P(\nu)}{\nu}(1-10^{-A(\nu)})}{\frac{1}{\nu_r}(1-10^{-Ar})} \qquad \text{(Equation S1)}$$

with P(ν) being the emission of the light source at a certain wavenumber (v, cm^{-1}), A(ν) the absorption of **THPP** at a certain wavenumber, ν_r the wavenumber of the Soret band and A_r the absorbance of the Soret band. The obtained light dose correction, is the ratio of light that it is actually absorbed by the compound (Figure S2).

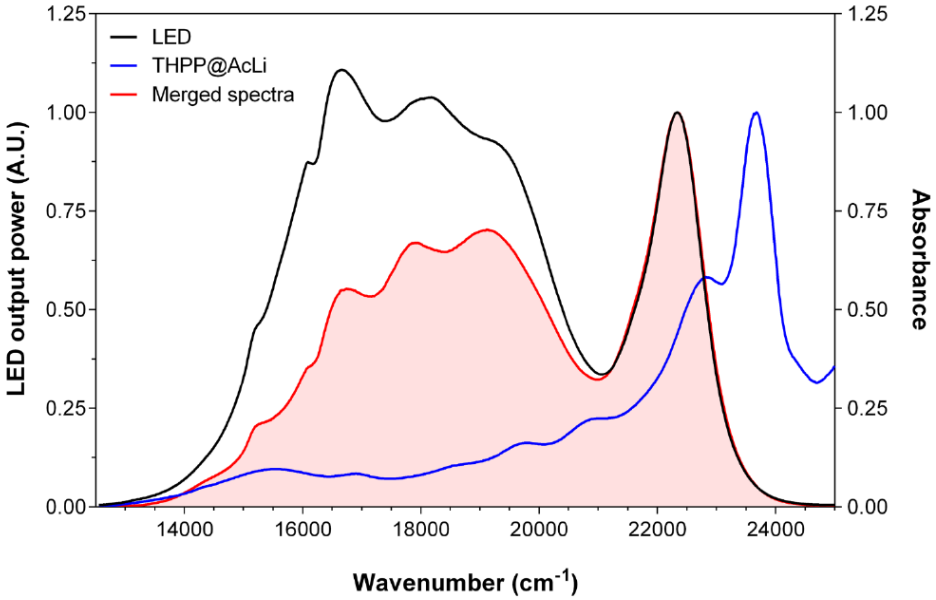

Figure S2. Normalized spectrum of the LED light output power (black line), the absorption spectrum of **THPP@AcLi** in PB pH 7 (blue line), and the merged spectrum (red line), with its area under the curve (light red) corresponding to the light dose correction rate.

3. Acetylated lignin characterization

Lignin acetylation and the photosensitive properties of acetylated lignins have been recently studied on another paper (Marchand *et al.*, 2018). Acetylated lignin (**AcLi**) was prepared as previously described and it was obtained as a crystalline brilliant brown powder. The material was characterized through FTIR (Figure S3.1).

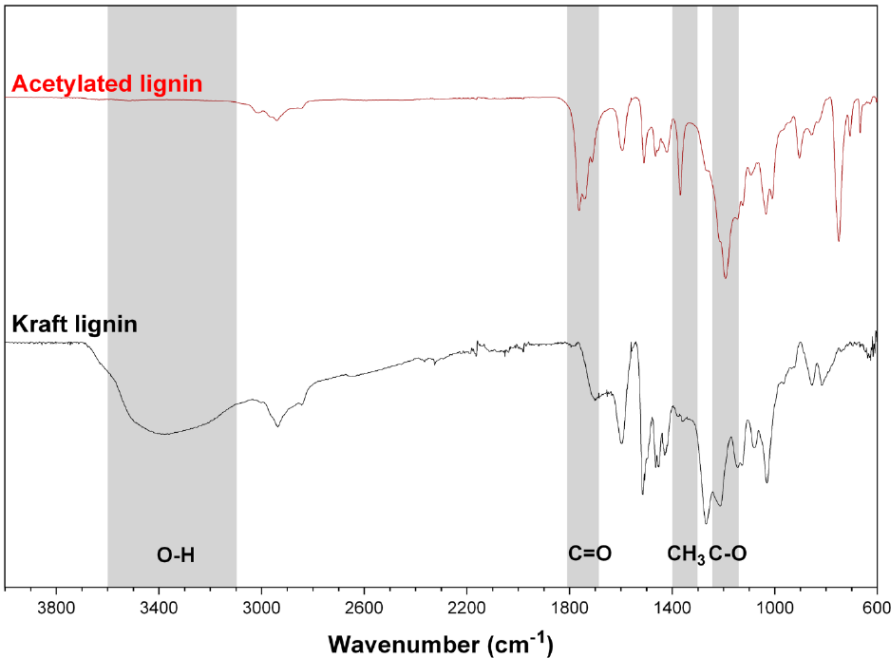

Figure S3.1. FTIR spectra of **AcLi** and raw kraft lignin. Significant absorbance patterns are gray highlighted.

The substitution of the hydroxyl groups at **AcLi** was observed through the disappearance of the wide O-H bond stretching band between 3100 and 3600 cm^{-1}, and with the appearance of a band at 1191 cm^{-1}, corresponding to the C-O ester bond stretch. Additionally, the lignin acetylation was confirmed through the appearance of the bands corresponding to C=O aromatic ester bond stretching and C=O aliphatic ester bond stretching, respectively at 1761 and 1739 cm^{-1}. The CH_3 moiety, corresponding to the acetyl group, appeared at 1464 cm^{-1}, as previously reported (Qian *et al.*, 2014; Marchand *et al.*, 2018).

The UV-vis absorption spectra of **AcLi** was recorded in acetonitrile at increasing concentrations, ranging from 0.010 to 0.400 mg/mL (Figure S3.2).

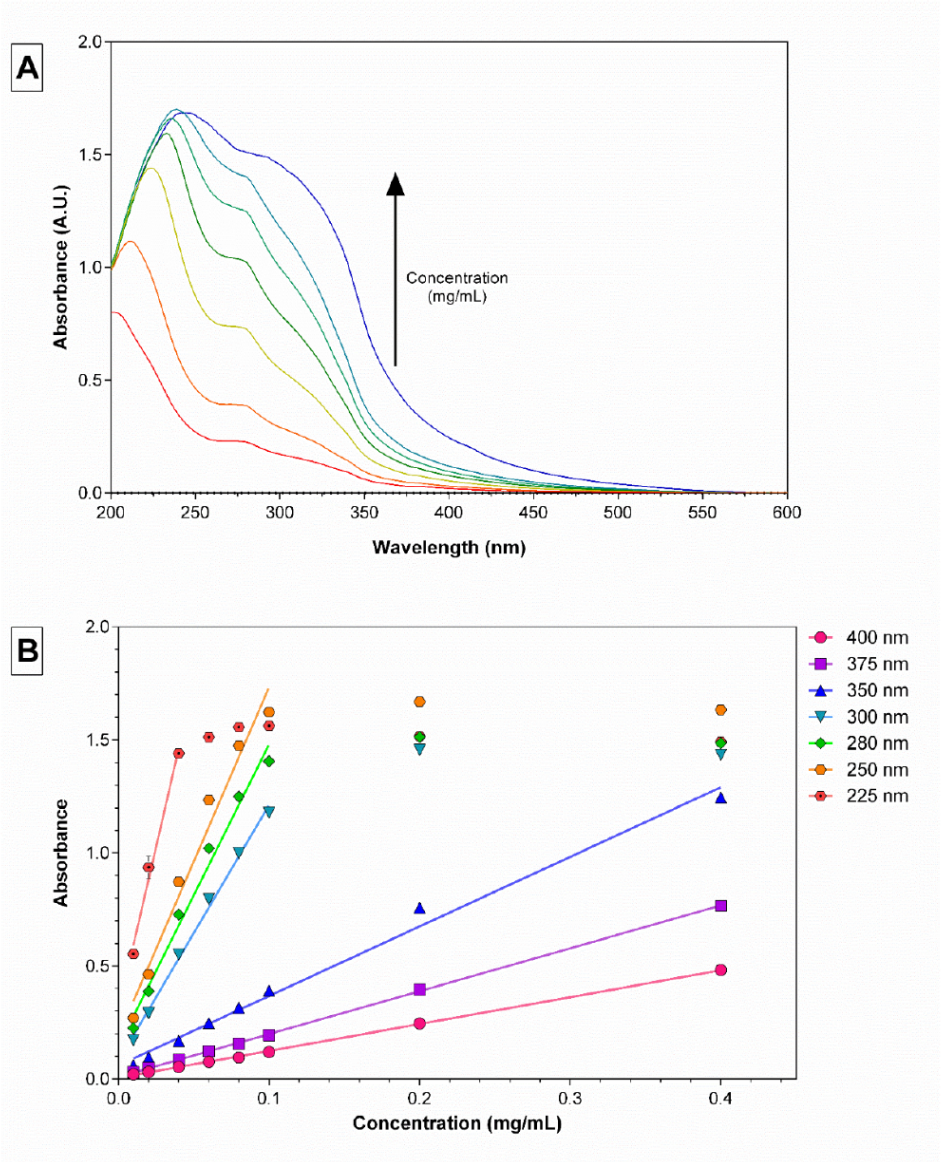

Figure S3.2. UV-vis characterization of **AcLi** in acetonitrile. (A) UV-vis spectra at increasing concentrations. (B) Absorbance of **AcLi** at several wavelengths, as a function of the concentration of the sample.

Interestingly, the **AcLi** UV-vis absorption profile is concentration sensitive; a defined band was observed at around 205 nm at 10 µg/mL, but at increasing concentrations, the band suffered a

progressive red shift from 205.5 to 248 nm, at 400 µg/mL, concomitantly with the appearance of a small peak at 280 and a shoulder at around 325 nm. The characteristics of **AcLi** absorption profile required the test of several random wavelengths to monitorize the changes of absorption as a function of concentration, and calculate its extinction coefficient (Table S3.1). The epsilon was calculated in a range where the increase demonstrated a linear behaviour, with a R square of at least 0.95. The best results were obtained on wavelengths above 350 nm, where the analytical range is bigger (0.01 – 0.4 mg/mL). Nevertheless, it would still be possible to use other wavelengths to determine analyse the **AcLi** concentration, on a smaller range of concentrations. For the present work, 350 nm was routinely monitored for determining the concentration of **AcLi** in nanoparticles samples.

Table S3.1. Epsilon calculated for **AcLi** at different wavelengths.

Wavelength (nm)	Range (mg/mL)	R Square (R^2)	ε (L/g cm)
400	0.01 – 0.4	0.9979	1.189 ± 0.01178
375	0.01 – 0.4	0.9986	1.897 ± 0.01527
350	0.01 – 0.4	0.9896	3.077 ± 0.06898
300	0.01 – 0.1	0.9946	11.33 ± 0.2160
280	0.01 – 0.1	0.9825	13.37 ± 0.4603
250	0.01 – 0.1	0.9724	15.44 ± 0.6713
225	0.01 – 0.03	0.9830	28.92 ± 1.440

4. Stability and leaking of THPP inside acetylated lignin nanoparticles

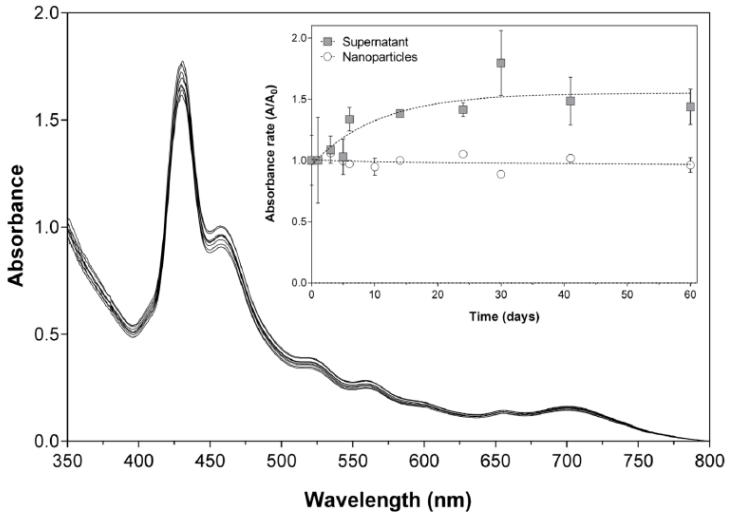

Figure S4. UV-vis absorbance spectra of the **THPP@AcLi** 2.39 µM in PB 0.1 M pH 7, followed up during 60 days. In the insert, the absorbance of the Soret band (430 nm) for the nanoparticles and the supernatants.

5. Excitation spectrum of THPP@AcLi

For further analysis, the excitation spectra recorded for observation wavelengths at 663, 733 and 780 nm were analyzed (Figure S5B). Interestingly, the excitation spectrum at 663 nm corresponds to the spectra of **THPP**, without presence of the protonated **THPP**H_2^{2+}. However, excitation spectrum at 733 and 780 nm showed two main peaks at 426 nm and 453 nm, which correspond to the Soret band and the B-band; the Q bands are observed at 521, 559, 595 and 652 nm for all the excitation spectra. In order to know if the porphyrinic species could be analyzed separately, the emission spectra were recorded at several excitation wavelengths (Figure S5C). Excitation at the B-band (455 nm) lead to a spectrum without the 663 nm band. However, excitation at other wavelengths always showed both emission bands, which is not surprising, as UV-vis absorption spectra of both species, **THPP** and **THPP**H_2^{2+} have spectral overlap in the whole range of wavelength, but between 450 – 475 nm.

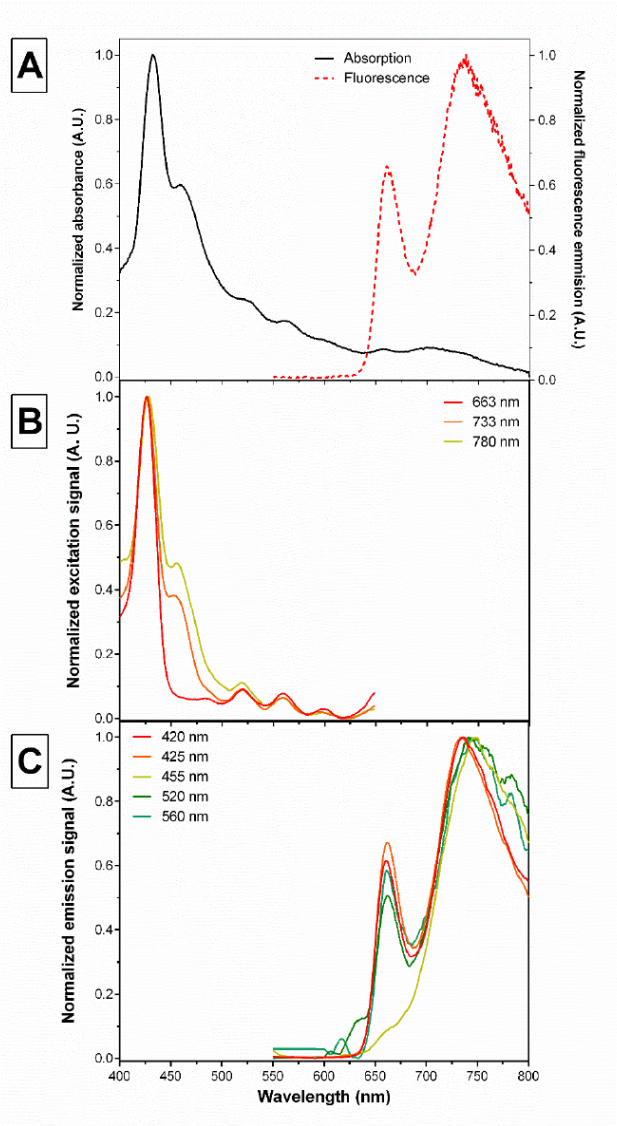

Figure S5. Fluorescent characterization of **THPP@AcLi** 1 µM. (A) UV-vis absorbance (black) and fluorescence emission (red dashed lines) spectra; (B) Excitation spectra at different wavelengths; (C) Emission spectra at different wavelengths. Recorded at PB 0.1 M pH 7, room temperature, λ_{Ex} = 425 nm.

6. Fluorescent quantum yield of THPP@AcLi as a function of pH

Table S6. Φ_F for **THPP@AcLi** 3 µM at different pH, using **TPP** in toluene as a standard ($\Phi_F = 0.11$).

pH	Φ_F
2	0.0016
3	0.0014
4	0.0014
5	0.0014
6	0.0015
7	0.0015
8	0.0014
9	0.0015
10	0.0016

7. PACT effect of @AcLi

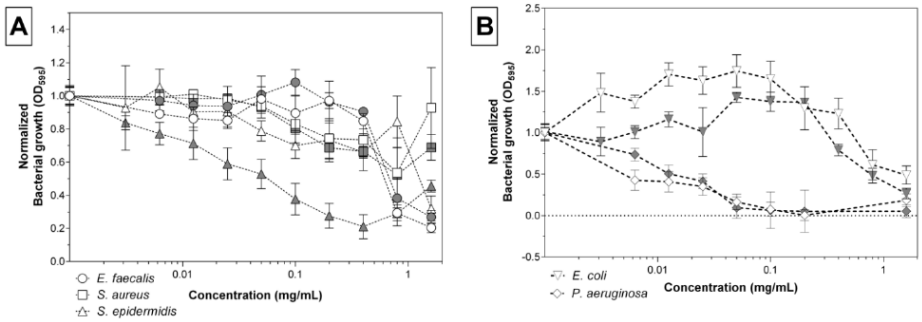

@AcLi nanoparticles were tested against three Gram-positive (*S. aureus, S. epidermidis* and *E. faecalis*) and two Gram-negative bacteria (*E. coli* and *P. aeruginosa*) (Figure S7.1). As the density of nanoparticles was high, results obtained at higher concentrations were difficult to analyze, as nanoparticles, as **@AcLi** also absorb at 600 nm. Nevertheless, the obtained data presents evidence of the lack of photodynamic effect of **@AcLi** against any bacterial strain, as there's not a significant decrease on the bacterial growth when bacteria are exposed to light and **@AcLi** (Table S7.1). However, the presented data seems to indicate that **@AcLi** exerts a non-light-driven bacteriostatic effect, as a decrease on the bacterial growth is observed,in both light and dark conditons. Other researchers have indicated that lignin has an antibacterial effect (Kaur, Uppal and Sharma, 2017; Yang *et al.*, 2018), but no similar evaluations were found in the literature. Interestingly, at some cases (Table S7.1, *S. aureus, E. coli* and *P. aeruginosa)*, the bacteriostatic effect was more evident for the dark controls than for the light irradiated samples. When data was analyzed we found statistical difference between dark and light conditions (P value < 0.05), for *S. aureus* and *E. coli*. Interestingly, in the case of *S. epidermidis* we observed an inversion of the growth tendency at the highest concentrations, while we observe a minor growth in the remaining concentrations (Figure S7.1A). Thus, in general, the presence of lignin into the dark results more toxic than the combination of lignin and light irradiation. As the only difference between the dark and light samples is precisely light irradiation, light seems to be mitigating the bacteriostatic effect of @AcLi. Light irradiation is done at room temperature, with the dark plates covered and away from the light source. As light irradiation is done during one hour, the temperature increases slightly (1 - 2 °C), which may propitiate bacterial growth. Nevertheless, at irradiation time, bacteria are deprived from culture media and thus, bacteria should be able to use lignin as a carbon source in order to continue growing. It has been previously addressed that lignin can be degraded by Proteobacteria, Actinobacteria and Firmicutes, with biodegradation of lignin resulting in a widening research area (Xu *et al.*, 2019). Nevertheless, lignin degrading activity is usually found in lignin-rich environments. Although interesting, the usage of lignin as the sole carbon source is far from the scope of this research but should be noted for future investigations. **Figure S7.1**. Bacteriostatic effect of **@AcLi** under light irradiation (4.16 J/cm^2, white symbols) or dark incubation (dark symbols), against A, three different Gram-positive bacteria and B, two Gram-negative bacteria, *E. coli* and *P. aeruginosa*.

Table S7.1. Comparison of bacterial growth, measured as OD_{600}, after light irradiation (4.16 J/cm^2) or dark incubation, with **@AcLi**. Data was analyzed with a Two-way ANOVA, with a Sidak's multiple comparisons test, statistical differences are considered when the adjusted P value is lower than 0.05.

Strain	Concentration (mg/mL)	Bacterial growth		Adjusted P value
		Light	Dark	
E. faecalis	1.6	0.2027 ± 0.0294	0.2683 ± 0.0405	0.9330
S. aureus	1.6	0.9266 ± 0.2444	0.6883 ± 0.0773	0.0317
S. epidermidis	1.6	0.2850± 0.0356	0.4555 ± 0.0358	0.1911
E. coli	1.6	0.5618 ± 0.0799	0.3182 ± 0.0331	0.0273
P. aeruginosa	1.6	0.1737 ± 0.0886	0.0534 ± 0.0796	0.5298

When bacterial growth results were compared with results from bacterial survival, it was observed that neither a photodynamic or a bactericidal effect was observed when bacteria were exposed to 1.6 mg/mL of **@AcLi**, considering a bactericidal effect when the bacterial survival is lower than 0.1% (Figure S7.2). In conclusion, **@AcLi** may work as a mild bacteriostatic at 1.6 mg/mL, but this effect is not related to the presence of light. There's small evidence that @AcLi could be used as carbon source, but these observations would need further experiments that escape the scope of this study. Is likely that the bacteriostatic effect at 1.6 mg/mL is due to the surfactant properties of lignin. Nevertheless, when loaded with a photosensitizer, as **THPP**, acetylated lignin nanoparticles work as a water-dispersible photosensitizing system, with low chemotoxicity, without any significant contribution of toxicity by @AcLi.

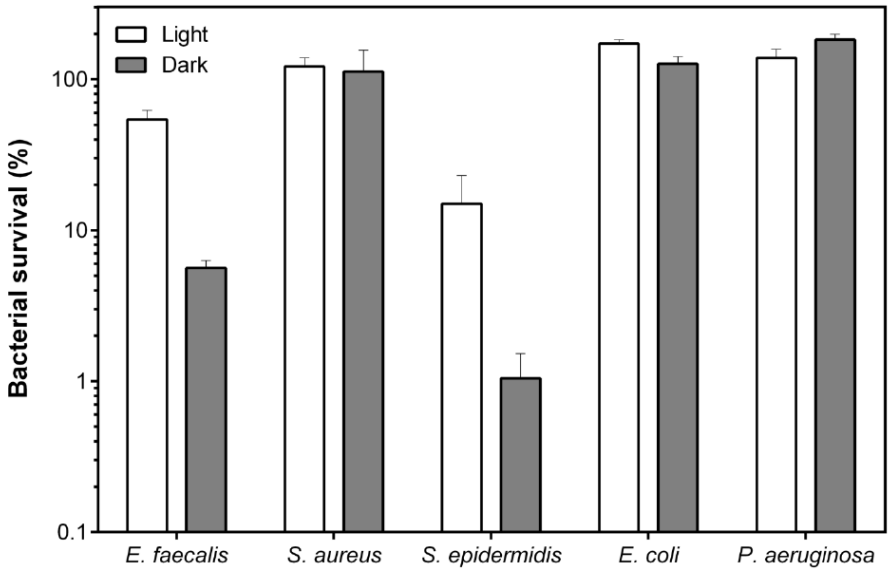

Figure S7.2. Bacterial survival of several bacterial strains with **@AcLi** 1.6 mg/mL treatment, after light irradiation (4.16 J/cm^2) or dark incubation; no differences are found between the light and dark treatment (Two-way ANOVA, Sidak's multiple comparisons test $P > 0.05$).

8. Bacterial growth of five bacterial strains after THPP@AcLi PACT

Table S8. Comparison of bacterial growth, measured as OD_{600}, after light irradiation or dark incubation, with **THPP@AcLi**. Data was analyzed with a Two-way ANOVA, with a Sidak's multiple comparisons test, statistical differences are considered when the adjusted P value is lower than 0.05.

Strain	[**THPP**] in **THPP@AcLi** (μM)	Bacterial growth		Adjusted P value
		Light	Dark	
E. faecalis	0.64	0.0843 ± 0.0094	0.8595 ± 0.0230	< 0.0001
S. aureus	2.56	0.1592 ± 0.0084	0.5874 ± 0.0288	< 0.0001
S. epidermidis	0.078	0.1423 ± 0.0390	0.6274 ± 0.0620	< 0.0001
E. coli	50	1.1981 ± 0.0101	1.2123 ± 0.0111	0.9768
P. aeruginosa	50	0.0247 ± 0.0101	0.0283 ± 0.0122	> 0.9999

9. Bacterial survival of three Gram positive strains after THPP@AcLi PACT

Table S9. Comparison of bacterial survival after light irradiation or dark incubation, with **THPP@AcLi**. Data was analyzed with a Two-way ANOVA, with a Sidak's multiple comparisons test, statistical differences are considered when the adjusted P value is lower than 0.05.

Strain	[**THPP**] in **THPP@AcLi** (μM)	Bacterial survival (%)		Adjusted P value
		Light	Dark	
S. aureus	2.56	0.0739 ± 0.0060	43.0662 ± 3.0837	< 0.0001
S. epidermidis	2.56	0.2874 ± 0.1775	56.65854 ± 4.9189	< 0.0001
E. faecalis	1.28	0.0148 ± 0.0111	39.7717 ± 5.1293	< 0.0001

References

Kaur, R., Uppal, S. K. and Sharma, P. (2017) 'Antioxidant and Antibacterial Activities of Sugarcane Bagasse Lignin and Chemically Modified Lignins', *Sugar Tech*. Springer India, 19(6), pp. 675–680. doi: 10.1007/s12355-017-0513-y.

Marchand, G. *et al.* (2018) 'Acetylated Lignins: A Potential Bio-Sourced Photosensitizer', *ChemistrySelect*, 3(20), pp. 5512–5516. doi: 10.1002/slct.201801039.

Qian, Y. *et al.* (2014) 'Reaction-free lignin whitening via a self-assembly of acetylated lignin', *Industrial and Engineering Chemistry Research*, 53(24), pp. 10024–10028. doi: 10.1021/ie5010338.

Schaberle, F. A. (2018) 'Assessment of the actual light dose in photodynamic therapy', *Photodiagnosis and Photodynamic Therapy*. Elsevier, 23(June), pp. 75–77. doi: 10.1016/j.pdpdt.2018.06.009.

Xu, Z. *et al.* (2019) 'Recent advances in lignin valorization with bacterial cultures: microorganisms, metabolic pathways, and bio-products', *Biotechnology for Biofuels*, 12(1), p. 32. doi: 10.1186/s13068-019-1376-0.

Yang, W. *et al.* (2018) 'Valorization of Acid Isolated High Yield Lignin Nanoparticles as Innovative Antioxidant/Antimicrobial Organic Materials', *ACS Sustainable Chemistry & Engineering*, 6(3), pp. 3502–3514. doi: 10.1021/acssuschemeng.7b03782.

Page intentionally left in blank

III. Porphyrin-loaded nanoparticles: challenging our concept

In **Publication 4** we demonstrated that **THPP,** once encapsulated inside acetylated lignin nanoparticles, kept its photophysical properties, i.e., absorption spectra, fluorescence emission and singlet oxygen production. Furthermore, it was demonstrated that all these properties were due to the presence of **THPP**, without evident contribution of the lignin material. However, in this paper it was left unexplored the comparison between the free porphyrin and the porphyrin-loaded nanoparticles. This was fully explored in **Publication 5**, where **THPP**, as a single molecule, was compared with **THPP@AcLi**. Furthermore, four analogues of **THPP** were synthesized, aiming for a full structure comparison of the single molecules, taking in account a wide variability of structures of porphyrins. Then, a non-polar porphyrin (**T(OAc)PP**), and a zinc-metallated porphyrin (**ZnTHPP**) were prepared. Additionally, two cationic porphyrins were prepared, aiming for disinfection of Gram-negative bacteria, bearing an alkyl (**T(MAP)PP**) or an aromatic (**T(PrOH)PyP**) quaternary ammonium moiety, with **T(PrOH)PyP** also bearing a terminal hydroxyl group (Figure 6).

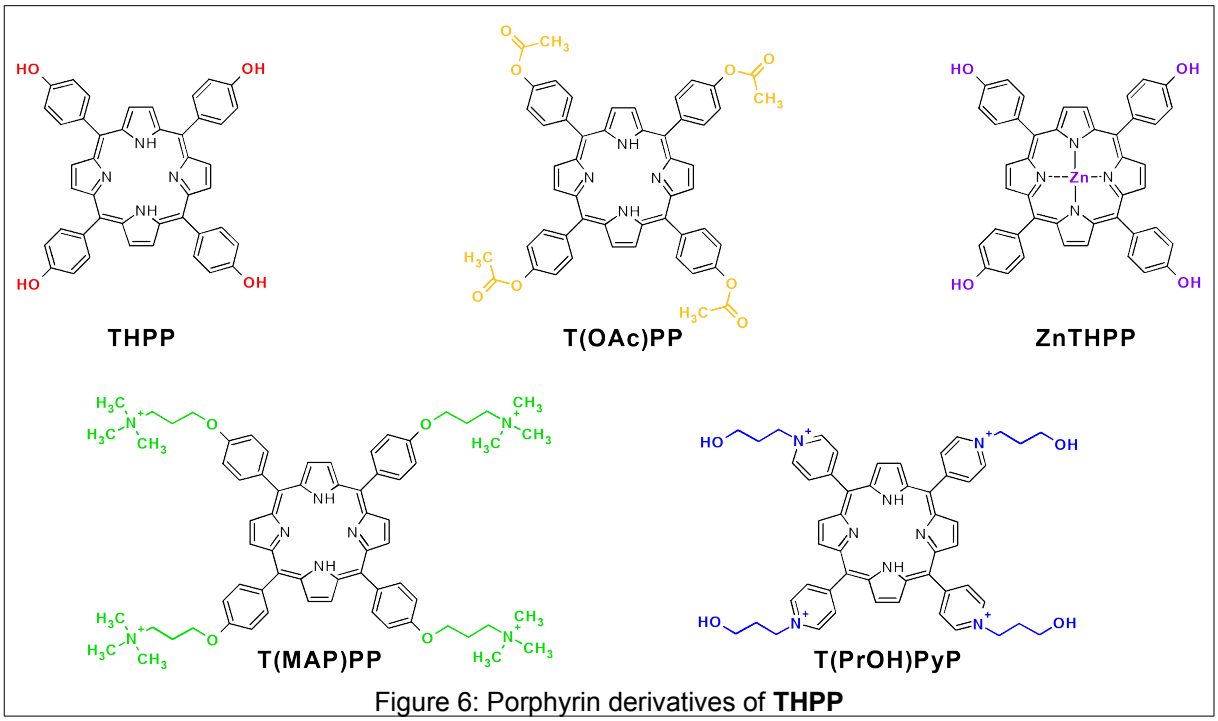

Figure 6: Porphyrin derivatives of **THPP**

The five porphyrin derivatives were encapsulated inside acetylated lignin nanoparticles, and were fully characterized, demonstrating that the encapsulated porphyrins kept their original photophysicial properties. Furthermore, in this research, it was demonstrated that **T(OAc)PP** was able to eradicate *S. aureus* only when encapsulated inside acetylated lignin nanoparticles, which demonstrates the efficiency of our formulation for the delivery of non-polar molecules into biological media. Additionally, it was demonstrated that nanoparticles loaded with **T(PrOH)PyP**, a cationic porphyrin, were able to decrease the bacterial survival of Gram-negative bacteria *E. coli*.

Publication 5. "Photophysical and Antibacterial Properties of Porphyrins Encapsulated inside Acetylated Lignin Nanoparticles" [44]

antibiotics

MDPI

Article

Photophysical and Antibacterial Properties of Porphyrins Encapsulated inside Acetylated Lignin Nanoparticles

Nidia Maldonado-Carmona [1,2], Tan-Sothea Ouk [1], Nicolas Villandier [1], Claude Alain Calliste [3], Mário J. F. Calvete [2], Mariette M. Pereira [2] and Stéphanie Leroy-Lhez [1,*]

[1] PEIRENE Laboratory, Faculty of Sciences and Techniques, University of Limoges, 87060 Limoges, France; nidia.maldonado@etu.unilim.fr (N.M.-C.); tan-sothea.ouk@unilim.fr (T.-S.O.); nicolas.villandier@unilim.fr (N.V.)
[2] Coimbra Chemistry Center, Department of Chemistry, University of Coimbra, 3004-535 Coimbra, Portugal; mcalvete@qui.uc.pt (M.J.F.C.); mmpereira@qui.uc.pt (M.M.P.)
[3] PEIRENE Laboratory, Faculty of Pharmacy, University of Limoges, 87025 Limoges, France; claude.calliste@unilim.fr
* Correspondence: stephanie.lhez@unilim.fr

Abstract: Lignin has recently attracted the attention of the scientific community, as a suitable raw material for biomedical applications. In this work, acetylated lignin was used to encapsulate five different porphyrins, aiming to preserve their photophysical properties, and for further use as antibacterial treatment. The obtained nanoparticles were physically characterized, through dynamic light scattering size measurement, polydispersity index and zeta potential values. Additionally, the photophysical properties of the nanoparticles, namely UV-vis absorption, fluorescence emission, singlet oxygen production and photobleaching, were compared with those of the free porphyrins. It was found that all the porphyrins were susceptible to encapsulation, with an observed decrease in their fluorescence quantum yield and singlet oxygen production. These nanoparticles were able to exert an effective photodynamic bactericide effect (blue-LED light, 450–460 nm, 15 J/cm^2) on *Staphylococcus aureus* and *Escherichia coli*. Furthermore, it was achieved a photodynamic bactericidal activity on an encapsulated lipophillic porphyrin, where the free porphyrin failed to diminish the bacterial survival. In this work it was demonstrated that acetylated lignin encapsulation works as a universal, cheap and green material for the delivery of porphyrins, while preserving their photophysical properties.

Keywords: tetrapyrrolic compounds; photodynamic therapy; lignin valorization

Citation: Maldonado-Carmona, N.; Ouk, T.-S.; Villandier, N.; Calliste, C.A.; Calvete, M.J.F.; Pereira, M.M.; Leroy-Lhez, S. Photophysical and Antibacterial Properties of Porphyrins Encapsulated inside Acetylated Lignin Nanoparticles. *Antibiotics* **2021**, *10*, 513. https://doi.org/10.3390/antibiotics10050513

Academic Editor: Kristjan Plaetzer

Received: 31 March 2021
Accepted: 27 April 2021
Published: 30 April 2021

1. Introduction

Antimicrobial resistance (AMR) is one of major threats to our current way of life, with enduring humanitarian and economic consequences if not addressed assertively [1]. For instance, concerns on the negative influence of the concurrent COVID-19 pandemic over AMR, are arising [2,3], particularly from the extensive use and misuse of mechanical ventilation [4,5]. Moreover, conventional antibiotics' bacterial resistance advocates exploring less resistance-prone therapeutic approaches [6], where photodynamic antimicrobial chemotherapy (PACT) [7] has proved as an efficient alternative in the inactivation of several bacterial strains [8–13]. This therapeutic strategy involves the concomitant use of a light source in appropriate dosage, a photosensitizer molecule and molecular oxygen, generating reactive oxygen species (ROS), namely singlet oxygen ($^1O_2$), super oxide anion ($O_2^{\bullet -}$), and hydroxyl radical ($HO^{\bullet}$). These ROS produce oxidative stress in bacteria through a non-specific molecular target mechanism, which ensures cellular death without risk of antimicrobial resistance [14].

Concurrently, organic matrices (e.g., cellulose, chitosan, cyclodextrin) have been used for the formulation of photosensitizers, aiming for the valorization of biopolymers available

in the nature. Lignin is a natural aromatic polymer, usually obtained as a paper industry by-product, containing p-coumaryl alcohol, coniferyl alcohol, and sinapyl alcohol units, in proportions that vary depending on the botanic origin of the sample [15]. Its aromatic character, easy chemical tuning and low cost of the raw material have paved the way for a current tendency of lignin valorization in biomedical, chemical and environmental applications. Specially, the role of lignin in the preparation of nanomaterials for loading and release of active substances is under growing scientific scrutiny [16].

Justifiably, the use of pristine lignin as a photosensitizer's vehicle is hampered by its known antioxidant activity [17,18]. Consequently, it is not surprising the lack of examples in the literature of lignin as part of a photodynamic treatment [19]. Our latest work reported the use of acetylated lignin nanoparticles as a vehicle for 5,10,15,20-tetrakis (4-hydroxyphenyl)-21H,23H-porphine (THPP), and its efficient antibacterial effect against Gram-positive bacteria [20]. Here, we concluded that the use of acetylated lignin as vehicle might be highly advantageous, for weak and non-hydrophillic photosensitizers. Additionally, improvements were foreseen that would enable the killing of Gram-negative bacteria, which were unaffected by the encapsulated THPP.

Herein, we report the encapsulation inside acetylated lignin nanoparticles of THPP and four derived porphyrins, 5,10,15,20-tetrakis (4-acetyloxyphenyl)-21H,23H-porphine, T(OAc)PP; zinc (II) 5,10,15,20-tetrakis (4-hydroxyphenyl)-21H,23H-porphine, ZnTHPP; 5,10,15,20-tetrakis(4-(3-*N*,*N*,*N*-trimethylammoniumpropoxy)-phenyl)-21H,23H-porphine bromine, T(MAP)PP and 5,10,15,20-tetrakis (4-(3-hydroxy)propyloxypyridyl)-21H,23H-porphine bromine, T(PrOH)PyP. The nanoparticles were characterized through dynamic light scattering (DLS), zeta potential, UV-vis absorption, fluorescence, and singlet oxygen production through electron paramagnetic resonance (EPR). The nanoparticles were tested against *Staphylococcus aureus* and *Escherichia coli*, under blue-LED light irradiation (450–460 nm, 15 J/cm^2).

2. Results and Discussion

2.1. Porphyrins Synthesis

Different porphyrins were synthesized, accordingly to already published methods, as shown in Scheme 1. These porphyrins were intended to be structural derivatives of 5,10,15,20-tetrakis (4-hydroxyphenyl)-21H,23H-porphine (THPP), by blocking the hydroxyl moiety with an acetyl group (5,10,15,20-tetrakis (4-acetyloxyphenyl)-21H,23H-porphine, T(OAc)PP) [21,22], through its metallation with a divalent metal (zinc (II) 5,10,15,20-tetrakis (4-hydroxyphenyl)-21H,23H-porphine, ZnTHPP) [23–25], and through the formation of a cationic porphyrin (5,10,15,20-tetrakis(4-(3-*N*,*N*,*N*-trimethylammoniumpropoxy)-phenyl)-21H,23H-porphine bromine, T(MAP)PP) [12,26]. Additionally, a cationic porphyrin with four free hydroxyl moieties was synthesized (5,10,15,20-tetrakis (4-(3-hydroxy) propyloxypyridyl)-21H,23H-porphine bromine, T(PrOH)PyP) [12], allowing a comparison between two cationic porphyrins with or without free hydroxyl moieties. The role of hydroxyl seems to be important for their hydrophilic character, as solubility and encapsulation efficiency, as well as for their possible antioxidant properties [27]. These targeted compounds have been designed for the sake of comparison and for a better understanding of the hydroxyl group role in the whole studied system.

2.2. Preparation of Acetylated Lignin Nanoparticles

Porphyrin-loaded acetylated lignin nanoparticles were prepared as previously reported [20], and as described in detail in Materials and Methods 4.3. Nanoparticles were obtained and kept as suspensions in distilled water, during the whole characterization and evaluation process.

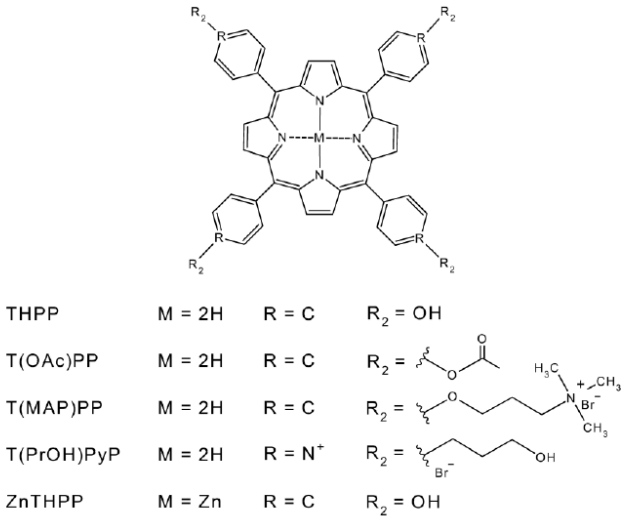

Scheme 1. Structure of the porphyrins used along the present work.

2.3. Physical Properties of Acetylated Lignin Nanoparticles

The obtained nanoparticles suspensions were physically characterized. The size distribution was analyzed through dynamic light scattering (DLS), which provides the hydrodynamic size of any particle. Usually, the hydrodynamic size takes into account the ions that may surround a particle, so can differ from the size obtained through other methods, such as microscopic observations. Previous research has demonstrated that the hydrodynamic size correlates with the size measured through transmission electron microscopy (TEM) observations, for acetylated lignin nanoparticles [20]. The obtained size, the polydispersity index (PDI) and the zeta potential (Table 1) provide information of the stability and the way that nanoparticles interact.

Table 1. Physical characteristics of nanoparticles.

Nanoparticles	DLS				PDI	Zeta Potential (mV) [b]
	Mean Size (nm)	Range (D_{95}) [a]	R^2 Gaussian Model Fitting	Normality of Residuals (*p* Value)		
@AcLi	184.3	57.16–311.44	0.7517	0.2232	0.183 ± 0.026	−22.1 ± 2.041
THPP@AcLi	160.4	51.29–262.98	0.8112	0.4243	0.126 ± 0.028	−20.8 ± 0.474
T(OAc)PP@AcLi	199.6	78.92–320.28	0.8535	0.1327	0.122 ± 0.117	−21.180 ± 0.887
T(MAP)PP@AcLi	886.2	597.8–1174.6	0.8931	0.8561	0.653 ± 0.145	−2.808 ± 1.461
T(PrOH)PyP@AcLi	1348	880.6–1815.4	0.6612	0.9621	0.457 ± 0.016	−9.962 ± 1.301
ZnTHPP@AcLi	208.2	77.88–338.52	0.8721	0.2714	0.117 ± 0.020	−24.140 ± 1.618

[a] The range denotes the distribution of 95% of the nanoparticles in suspension, calculated as ±2σ obtained from the Gaussian fitting. [b] Zeta potential measured in phosphate buffer 0.01 M, pH 7.0.

The obtained values were compared with the empty acetylated lignin nanoparticles (@AcLi). We could observe that the presence of the porphyrins affects the size of the obtained nanoparticles, this being more evident for the cationic porphyrins, which have a size of around 1 µm, with a wide D_{95} distribution. The resulting size of the cationic porphyrins

nanoparticles could be due to the rejection between the cationic charges, preventing the formation of tight nanoparticles. Furthermore, the encapsulation of cationic porphyrins affected the PDI and the zeta potential. Normally, suspensions with a PDI below 0.2 and zeta potentials above ±20 mV are desirable, which ensure that the suspension preserves its efficiency and its proper dosage. Both nanoparticles obtained with the cationic porphyrins have PDI above 0.2 and zeta potentials close to zero, resulting in suspensions that quickly sediment over time (Figure 1), with T(PrOH)PyP@AcLi being the quickest to sediment, as these nanoparticles are also the largest, with a size difference of 462 nm with respect to T(MAP)PP@AcLi nanoparticles. The difference of size seems to overweight the observed values of PDI and zeta potential, which indicated that T(MAP)PP@AcLi would tend to sediment faster than T(PrOH)PyP@AcLi [28]. In all cases, a gentle shake was enough to suspend the nanoparticles again.

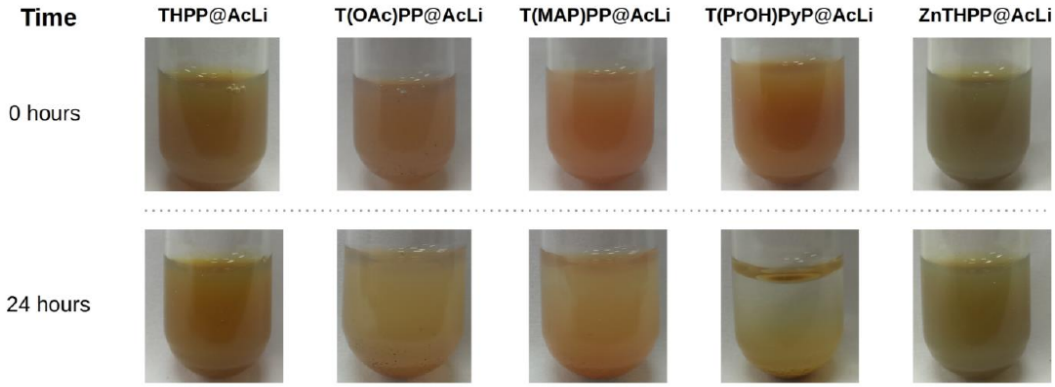

Figure 1. Sedimentation of the acetylated lignin nanoparticles, as a function of time.

2.4. Photophysical Properties

Previous studies [20] have demonstrated that THPP encapsulated inside acetylated lignin nanoparticles conserved their main photophysical features (i.e., absorption and emission spectra), as well as their capacity to generate singlet oxygen under light irradiation. In order to investigate the impact of the metallation, the blockage of the hydroxyl moieties, and the presence of positive charges in the porphyrins, the nanoparticles library, as well as the free porphyrins, were characterized on these different parameters.

2.4.1. UV-Vis Absorption Characterization

Nanoparticles absorption spectra was measured on phosphate buffer 0.01 M pH 7 and compared with the absorption spectra of the single porphyrins in DMF or in PB pH 7 (Table 2). The obtained raw spectra for the nanoparticles were blanked from the light dispersion effect of nanoparticles. Similar treatment was used for all UV-vis spectra presented in this work. An example of the nanoparticles original raw spectra compared with the treated spectra and the spectra of the free porphyrin are presented as Supplementary Figure S1.

In all cases, the absorbance profile of the porphyrin remained distinctive, with a Soret band between 400 and 450 nm and Q bands observable in the 500–700 nm range. The absorbance of their Soret bands was analyzed through their intensity and their wavelength of maximum absorbance (Table 2). As previously described, except for T(PrOH)PyP, the Soret band of the porphyrins in PB pH 7 showed a red shift, between 3 and 16 nm, when compared with the free porphyrins in DMF. Additionally, a decrease in the absorption coefficient was observed, showing between 12 and 78% of their original absorbance, with all the neutral porphyrins, namely THPP, T(OAc)PP and ZnTHPP, being below 20%.

Meanwhile, T(MAP)PP, a cationic porphyrin, conserved the intensity of its Soret band, with 78% of the original value. The decrease in absorbance and the red-shift observed could be due to the difference of solvent, as well as the consequence of the formation of J-aggregates because of π–π stacking between porphyrins [29,30]. As the case of the cationic porphyrins, especially for T(PrOH)PyP, their solubility in aqueous media is superior than for the other porphyrins, supporting the hypothesis of aggregates formation for the neutral compounds.

Table 2. Absorption spectra properties at the Soret band wavelength of different porphyrins dissolved in DMF or PB pH 7, or encapsulated in acetylated lignin nanoparticles, and suspended in PB pH 7. The effect of encapsulation on the absorption capacity of the porphyrins is described as the ratio of absorption coefficients of the encapsulated porphyrins and of the free porphyrins ($\varepsilon/\varepsilon_{Free}$). Additionally, the shift of the observed Soret bands wavelength upon encapsulation is given (Δ_λ).

Porphyrin	Free in DMF		Free in PB pH 7 [a]		Free in PB pH 7 vs. Free in DMF		Encapsulated in PB pH 7		Encapsulated vs. Free in DMF		Encapsulated vs. Free in PB	
	ε (M^{-1} cm^{-1})	λ (nm)	ε (M^{-1} cm^{-1})	λ (nm)	$\varepsilon_{PB}/\varepsilon_{DMF}$	Δ_λ (nm)	ε (M^{-1} cm^{-1})	λ (nm)	$\varepsilon/\varepsilon_{Free}$	Δ_λ (nm)	$\varepsilon/\varepsilon_{Free}$	Δ_λ (nm)
THPP	35.0668×10^4	424	5.9361×10^4	440	0.169	16	12.9984×10^4	434	0.3707	10	2.1897	−6
T(OAc)PP	36.1354×10^4	419	4.4123×10^4	429	0.122	10	12.0609×10^4	426	0.3338	7	2.7335	−3
T(MAP)PP	20.1871×10^4	422	15.7138×10^4	425	0.778	3	20.7684×10^4	432	1.0288	10	1.3217	−7
T(PrOH)PyP	13.2376×10^4	427	13.2908×10^4	419	1.004	−8	1.3472×10^4	448	0.1018	21	0.1014	−19
ZnTHPP	47.7749×10^4	430	5.9163×10^4	426	0.124	−4	18.5219×10^4	435	0.3877	5	3.1307	−9

[a] Free porphyrins in PB pH = 7, 5% DMF.

When the absorption coefficient of the Soret band of the free porphyrins in aqueous media was compared with their respective value for encapsulated porphyrins, it was generally observed that the encapsulation presents an advantage over the delivery of the free porphyrin, as encapsulated porphyrins have higher absorption coefficients than the free porphyrins in aqueous media. The exception for this rule is, once again, T(PrOH)PyP, as this cationic porphyrin has a better absorption coefficient in aqueous media, possibly due to the presence of the four hydroxyl moieties that enable the formation of hydrogen bonds with water. The Soret band wavelength of encapsulated porphyrins, suspended in PB pH 7, were neither the same than the free porphyrin in DMF nor in PB pH 7 with 5% of DMF. This suggests that aggregation of porphyrins is not the sole factor that affects the absorption of porphyrins, but also the encapsulation process modifies the absorption of the porphyrins.

In silico simulations of nanoparticles formation suggest that, when water content reaches a threshold concentration, it triggers the spontaneous formation of acetylated lignin nanoparticles [31]. However, the effect that water introduction has over the porphyrin aggregation and how it correlates with nanoparticles formation has been unexplored. In order to gain further insight into this process, acetylated lignin and porphyrins were dissolved in the solvent or solvents mixtures routinely used for the formation of loaded-porphyrin acetylated lignin nanoparticles (Table 7). Acetylated lignin aggregation, as increase in corrected scattered light, and porphyrin aggregation, as diminishment of Soret band's absorption, were followed up as a function of water addition into the solvent mixture (Figure 2).

These observations showed that the acetylated lignin nanoparticles formation starts at a critical water concentration (CWC) of around 30%, an inflexion point where corrected scattered light increases, which correlates with previous reports [31]. On the other hand, porphyrin aggregation was assumed to be indicated by a decrease in absorbance in the Soret band upon water addition (Supplementary Figure S2). In the case of non-cationic porphyrins THPP, T(OAc)PP and ZnTHPP, water addition into the starting solution led to a widening of the Soret band, in addition to a decrease in absorbance. Meanwhile cationic porphyrins solutions showed an unaltered profile. Similarly to AcLi collapsing, non-cationic porphyrins reached a critical water concentration, as the inflexion point where absorbance suddenly decreases, indicating the aggregation point of porphyrins. The CWC

for each porphyrin was different and structure-dependent. As an example, for T(OAc)PP, a porphyrin without hydroxyl moieties, its CWC was found at around 10%, while THPP and ZnTHPP, both with four free hydroxyl moieties, CWC is found at 70 and 75%, respectively. The increase in the aggregation tolerance is likely due to the presence of the hydroxyl moieties, which favors their partial solubility in aqueous media. The blockage of their hydroxyl moieties seems to provoke the rapid aggregation of T(OAc)PP in the presence of water. Meanwhile, cationic porphyrins do not aggregate upon water addition. This was expected, as both porphyrins are water-soluble, but, while absorbance of T(PrOH)PyP is not altered by water addition, T(MA)PP doubles its absorbance when water is added, suggesting that the mixture of acetone and DMSO does not favor its proper solubility. These observations suggest that encapsulation of porphyrins can happen either with the molecules as monomers (cationic porphyrins) or when porphyrins are aggregated polymers (T(OAc)PP). As result, porphyrins with a higher tolerance for water addition (T(MAP)PP > T(PrOH)PyP > ZnTHPP > THPP > T(OAc)PP) also have a better absorbance ratio, when compared to the encapsulated and free porphyrins (T(MAP)PP > ZnTHPP > THPP > T(OAc)PP) > T(PrOH)PyP). The exception of this observation is T(PrOH)PyP, as their absorbance diminishes to only 15% of its original absorbance (Table 2).

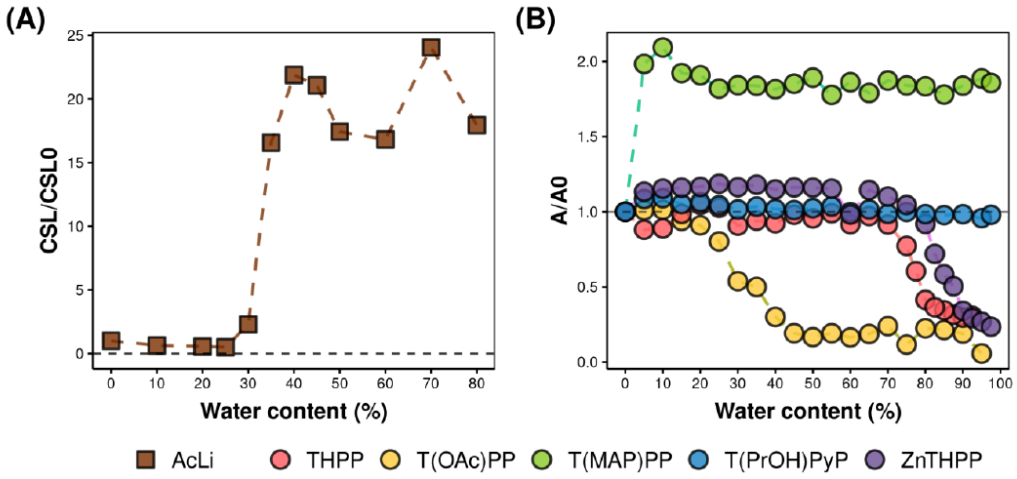

Figure 2. Simulation of nanoparticles formation. (**A**) Corrected scattered light (CSL) of an acetylated lignin solution (acetone, 2 mg/mL) as a function of water addition. (**B**) Porphyrin aggregation as a function of water addition. Porphyrins were dissolved in the organic solvent or solvents mixture used as the starting solution for nanoparticles formation, at a final concentration of 5 µM. Porphyrin aggregation was monitored through the maximum absorbance of the Soret band in their respective solvent: THPP, acetone; T(OAc)PP, acetone:DMF 9:1; T(MAP)PP, acetone:DMSO; T(PrOH)PyP, acetone:DMSO 9:1; ZnTHPP, THF.

Although aggregation of porphyrins has an important role in the diminishing of light absorption, it appears that the encapsulation process per se affects the porphyrins' ability to absorb light, with the most evident effect being light dispersion of the nanoparticles suspension. In the literature, there are several reports where formulations of photosensitizers present affected photophysical properties [32], representing a challenge for the formulation of photosensitizers.

2.4.2. Fluorescence Quantum Yield

Fluorescence of porphyrins was analyzed as a function of their encapsulation. Emission spectra were obtained upon excitement at 425 nm (Supplementary Figure S3), using

tetraphenyl porphyrin (TPP) in toluene as a reference [33] to calculate the fluorescent quantum yield Φ_F (Table 3).

Table 3. Fluorescent quantum yields for porphyrins dissolved in DMF, in PB pH 7 0.5% DMF or encapsulated in acetylated lignin nanoparticles and suspended in PB pH 7. Fluorescent emission was measured at a porphyrin concentration of 0.5 μM, upon excitation at 425 nm, at 25 °C, and using TPP as a standard (Φ_F = 0.11 in toluene).

Porphyrin	Fluorescent Quantum Yield (Φ_F)			$\Phi_{F\ encapsulated}/\Phi_{F\ free\ in\ PB}$ (PB pH 7)
	Free Porphyrin (DMF)	Free Porphyrin (PB pH 7)	Encapsulated Porphyrin (PB pH 7)	
THPP	0.1696	0.0034	0.0103	3.029
T(OAc)PP	0.1176	0.0089	0.0690	7.753
T(MAP)PP	0.1341	0.1349	0.0310	0.230
T(PrOH)PyP [a]	0.1933	0.4219	3.5835 [a]	8.494 [a]
ZnTHPP	0.0648	0.0063	0.0101	1.603

[a] The obtained value of the T(PrOH)PyP@AcLi fluorescence is a result of low fluorescence and low absorbance obtained after the light scattering correction, resulting in an extremely high value that is unlikely to have any relevance.

In all cases, once porphyrins were encapsulated, they kept their distinctive emission spectra, with two main emission bands between 600 and 800 nm (Supplementary Figure S3). As previously explored, porphyrins in aqueous media greatly aggregated, leading to fluorescence quenching. Aggregation of porphyrins, due to high concentrations or due to water presence, is a common issue that leads to quenching of fluorescence emission and, most importantly, singlet oxygen production. The encapsulated porphyrins succeeded at delivering the porphyrins in an aqueous media, while improving their fluorescence, when compared with obtained values of the free porphyrins in PB pH 7. Thus, the encapsulation inside acetylated lignin nanoparticles aids in delivering non-cationic porphyrins into aqueous media, while preserving their fluorescence.

Although all the porphyrins kept their emission spectra bands, in some cases, there were changes in their profiles. The most relevant changes were monitored for THPP emission, which in DMF presents a major band at 663 nm, and a secondary band at 733 nm. Indeed, when THPP is encapsulated, its relative intensity of the two emission bands inverted, with a higher emission band at 733 nm, instead of 663 nm, for the encapsulated porphyrin. This has been explained by the formation of the protonated species $THPPH_2^{2+}$ [29], which suggests that the microenvironment inside acetylated lignin nanoparticles is acidic [20]. Further analysis (Supplementary Figure S4) revealed that encapsulated ZnTHPP and T(PrOH)PyP have similar emission profiles, with the principal emission band was found after 700 nm; this profile does not fluctuate even upon pH change in the media. Furthermore, a red-shift was observed for the excitation spectra of the "acidic" bands, when compared with the excitation spectra of the free porphyrins in DMF, and corresponding to the excitation spectra of the free porphyrins in acidic pH. Interestingly, this behavior was not found for T(OAc)PP and T(MAP)PP, as their principal emission bands were found at around 650 nm, as found in the emission spectra for the free porphyrins in DMF. These observations are structure-dependent, as THPP, T(PrOH)PyP and ZnTHPP have four free hydroxyl groups, susceptible to changes upon pH change. As a contrast, both T(OAc)PP and T(MAP)PP have blocked their hydroxyl moieties and seem to be less prone to structural changes upon pH alteration. Consequently, the structural differences between the porphyrins used in this study has permitted the elucidation of the internal environment of acetylated lignin nanoparticles, an environment that seems slightly acidic, confirming our previous observations [20].

2.4.3. Singlet Oxygen Production

Fluorescence emission is not the only photophysical feature of importance for those porphyrins, as these molecules work as excellent photosensitizers, producing singlet oxygen upon light irradiation [34]. Singlet oxygen production of porphyrin-loaded nanoparticles was monitored through electron paramagnetic spectroscopy (EPR), in combination with the use of a singlet oxygen trap, 2,2,6,6-pyperidine (TEMP), as already reported in the literature [20,35]. TEMP easily reacts with singlet oxygen to form 2,2,6,6-tetramethyl-1-piperidinyloxy (TEMPO), a stable radical that can be detected through EPR. Singlet oxygen production was driven through irradiation of the samples with blue LED-light (450–460 nm, 60 mW/cm^2) through increasing light doses (Figure 3). The tendencies of the singlet oxygen production were compared with the singlet oxygen quantum yield of the free porphyrins (Table 4), obtained through measuring the singlet oxygen phosphorescence decay with near-infrared spectroscopy (NIRS), using phenalenone as standard (Φ_Δ = 1.0 [36]) and excitation at 355 nm (Supplementary Figure S5).

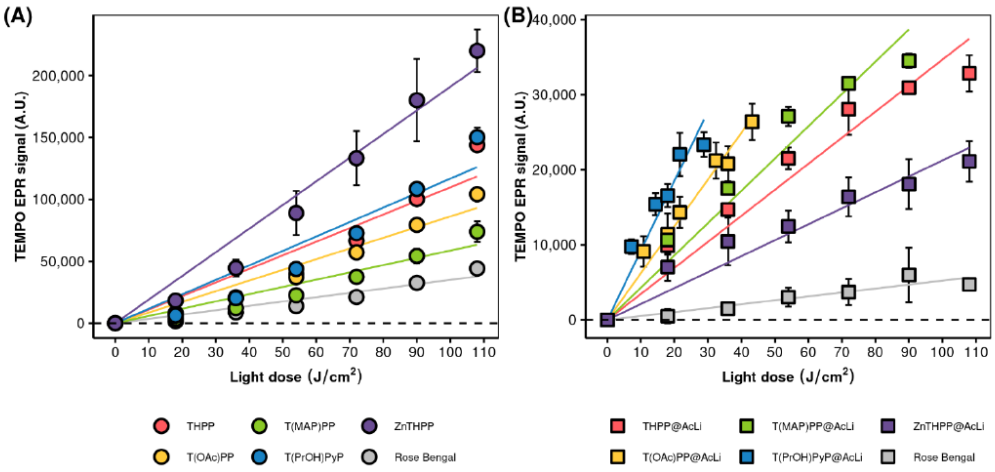

Figure 3. Singlet oxygen production, detected as TEMPO formation through EPR for (**A**) free porphyrins and (**B**) encapsulated porphyrins, using 12.5 mM of TEMP, either in DMF or in PB pH 7. Free porphyrins were dissolved in DMF, for a final concentration of 1.5 μM, while encapsulated porphyrins were suspended in PB pH 7, at 25 μM of their corresponding porphyrin. Rose Bengal was used as a standard, at (**A**) 1.5 μM and (**B**) 5 μM. The samples were irradiated with blue LED-light (450–460 nm, 60 mW/cm^2), at different light doses. The results shown are the average of three independent experiments.

Table 4. Singlet oxygen quantum yield for the free porphyrins, calculated through the decay of singlet oxygen phosphorescence at 1270 nm.

Porphyrin	Singlet Oxygen Quantum (Φ_Δ)		
	Free Porphyrin [a]	Literature [b]	
THPP	0.5900	0.57 (DMA oxidation, DMF, air, λ_{Ex} = 401 nm)	[37]
T(OAc)PP	0.6560		
T(MAP)PP	0.6321	0.51 (DMA oxidation, DMF, air, λ_{Ex} = 420 nm)	[38]
T(PrOH)PyP	0.5804		
ZnTHPP	0.7320		

[a] Porphyrins dissolved in DMF, with an optical density of around 0.18 at the excitation wavelength (355 nm), using phenalenone as standard (Φ_Δ = 1 [36]). [b] The reported values found in the literature are presented with the method used, the solvent, the kind of aeration and the wavelength of excitation.

Singlet oxygen quantum yields for the free porphyrins in DMF showed that our most efficient photosensitizer is ZnTHPP (Φ_Δ = 0.7320), followed by T(OAc)PP and T(MAP)PP and lastly by THPP and T(PrOH)PyP. The results obtained with EPR for the free porphyrins dissolved in DMF contrast with the results obtained through NIRS, as the singlet oxygen production efficiency is shown as ZnTHPP > T(PrOH)PyP > THPP > T(OAc)PP > T(MAP)PP. These discrepancies between EPR and NIRS obtained values have been previously explored [39], and it has been demonstrated that TEMP can act as a quencher of the excited triplet state of certain photosensitizers, leading to an overestimation of the production of singlet oxygen. Nevertheless, NIRS could not be used for the detection of singlet oxygen quantum production for the encapsulated porphyrins, not even in deuterated water. Thus, EPR was used for the detection of singlet oxygen production of encapsulated porphyrins, and the results show that singlet oxygen production tendency goes T(PrOH)PyP@AcLi > T(OAc)PP@AcLi > T(MAP)PP@AcLi > THPP@AcLi > ZnTHPP@AcLi. Interestingly, these results coincide with the fluorescent quantum yield of the encapsulated porphyrins, with T(PrOH)PyP@AcLi and ZnTHPP@AcLi having the highest and lowest fluorescent quantum yield, respectively (Table 3). This suggests that encapsulation affects both singlet oxygen and fluorescence in the same magnitude, as could be expected.

Something remarkable is that we were able to find singlet oxygen production at all our nanoparticles, similarly to our previous report [20]. Lignin has been rarely used as a material on PDT and PACT applications, due to its well-known antioxidant activity, but a report indicates that esterified lignin is able to produce singlet oxygen upon light irradiation [40]. However, other reports also specify that, even if lignin is able to produce singlet oxygen, the amount produced by the non-loaded nanoparticles @AcLi is insignificant when compared with the singlet oxygen produced by the porphyrins [20]. Here, we provide evidence that several types of porphyrins, once encapsulated inside acetylated lignin nanoparticles, are still able to generate singlet oxygen. Additionally, it has been hypothesized that porphyrins remain inside the nanoparticles and that only the singlet oxygen is diffusing through and towards the outside of the nanoparticle

2.4.4. Photobleaching

The production of reactive oxygen species can lead to the self-destruction of the photosensitizer. Previous reports indicate that THPP encapsulated inside acetylated lignin nanoparticles does not photobleach over white-LED light irradiation [20]. In order to deepen insight into the behavior of porphyrins encapsulated into acetylated lignin nanoparticles, the destruction of the porphyrins, as a loss of absorbance at the Soret band, was followed up for both free porphyrins (Supplementary Figure S6) and their encapsulated formulations (Supplementary Figure S7), under blue-LED light irradiation, at several light dosages (Figure 4).

In most cases, porphyrin degradation was easily followed up at the Soret band, with porphyrins profile remaining similar through the whole irradiation process. However, in the case of T(PrOH)PyP and T(PrOH)PyP@AcLi, since the beginning of irradiation, there was a blue shift of the Soret and Q bands, leading to a fast disruption, followed up by a slower degradation. This could be indicative of the destruction of aggregates of porphyrins, as it has been previously observed that T(PrOH)PyP solubility is not favored in DMF (Table 2). Nevertheless, when the spectra of T(PrOH)PyP is compared with the spectra of THPyP, the starting porphyrin for T(PrOH)PyP, a match was found between the photobleached T(PrOH)PyP and THPyP (Supplementary Figure S8). Then, blue light irradiation could be led to the fast degradation of T(PrOH)PyP to THPyP, which has a slower rate of photodegradation and worst solubility in DMF (Scheme 2). This is similarly observed in T(PrOH)PyP nanoparticles.

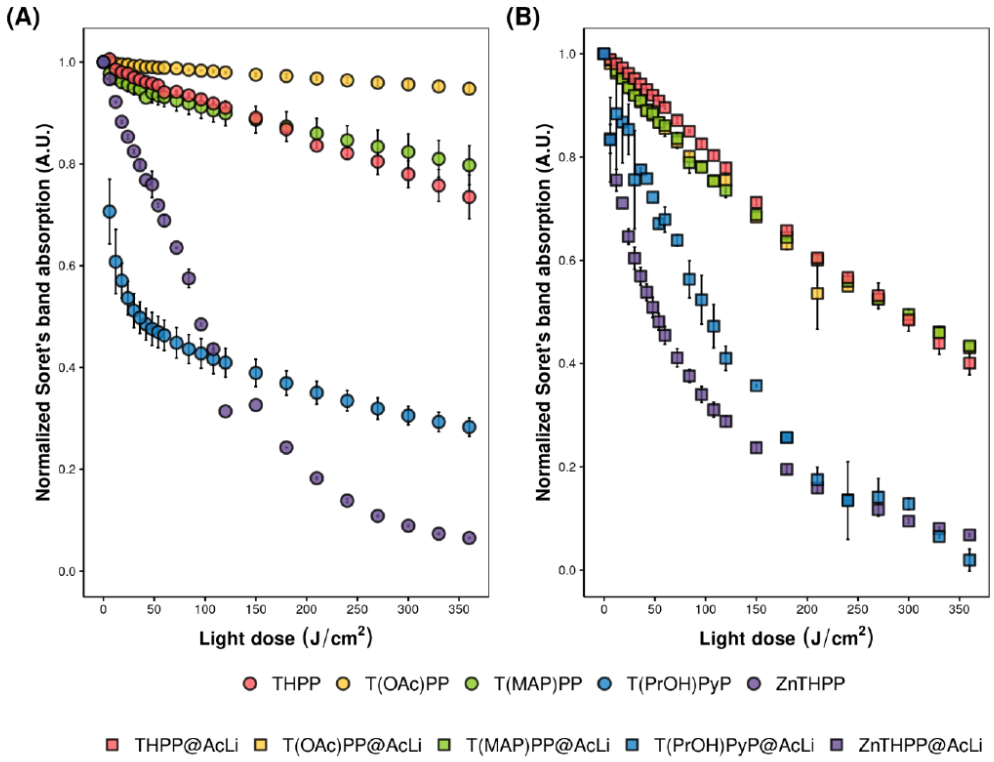

Figure 4. Photobleaching of (**A**) free porphyrins and (**B**) encapsulated porphyrins. Free porphyrins were dissolved in DMF at 5 μM, while nanoparticles were suspended in PB pH 7, at 5 μM of their respective porphyrin. Three milliliters of both solutions were deposited in an open quartz square cell of 1 cm width, with constant stirring, under blue-LED light irradiation (100 mW/cm^2), under several lapses. The normalized absorbance is presented and the results presented are the average of two independent experiments.

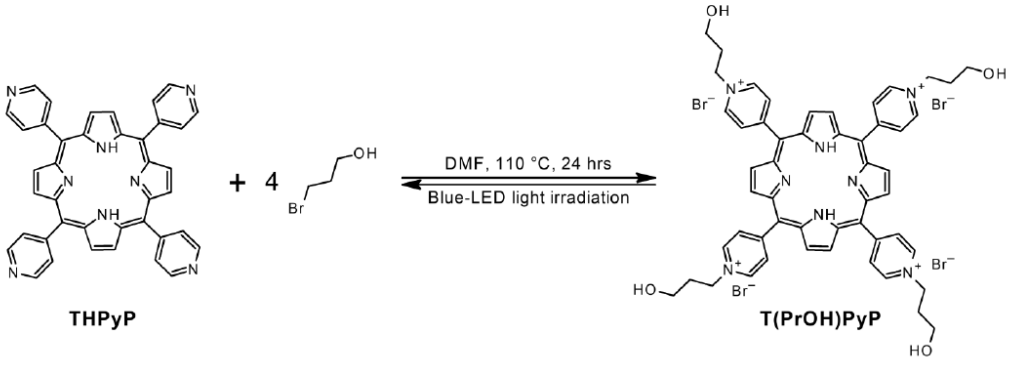

Scheme 2. Synthesis of T(PrOH)PyP, from THPyP. When T(PrOH)PyP is irradiated with blue light, it seems to be destroyed back to THPyP.

Previous reports indicated that THPP@AcLi, when exposed to white light in static conditions, withstood photodegradation [20]. In this report, we present data with a different experimental approach, as light irradiation is five times higher, using a narrow-band light source and with constant stirring that ensures both aeration and prevents nanoparticles precipitation. Under these conditions, it was found that encapsulated porphyrins degrade at a similar or higher speed than the free porphyrins. This could be due to the high concentration of porphyrins in the nanoparticles volume, leading to an easier self-destruction. Interestingly, THPP@AcLi, T(OAc)PP@AcLi and T(MAP)PP@AcLi have similar photobleaching rates when encapsulated, unlike when they are dissolved in organic solvent. This is interesting, as the singlet oxygen production is greatly reduced for the encapsulated porphyrins, and then a lower photobleaching would be expected. This finding corroborates our hypothesis of a singlet oxygen diffusion through the nanoparticle, creating a high concentration of singlet oxygen inside the nanoparticles and leading to an accelerated rate of photobleaching for the encapsulated porphyrins.

On the other hand, it was previously described that THPP@AcLi presents a Soret band and a B-band, which corresponds to the protonated form of THPP, $THPPH_2^{2+}$. This B-band was described to degrade at a faster pace than the main Soret band and to have a great contribution on the fluorescence of the nanoparticles [20]. Our results so far indicate a similar trend, with the B-band degrading at a faster pace than the Soret band, until reaching the base of the peak of THPP (Figure 5). This suggest that $THPPH_2^{2+}$ could have an important role on ROS production, as it does in fluorescence, even though it has a short half-life.

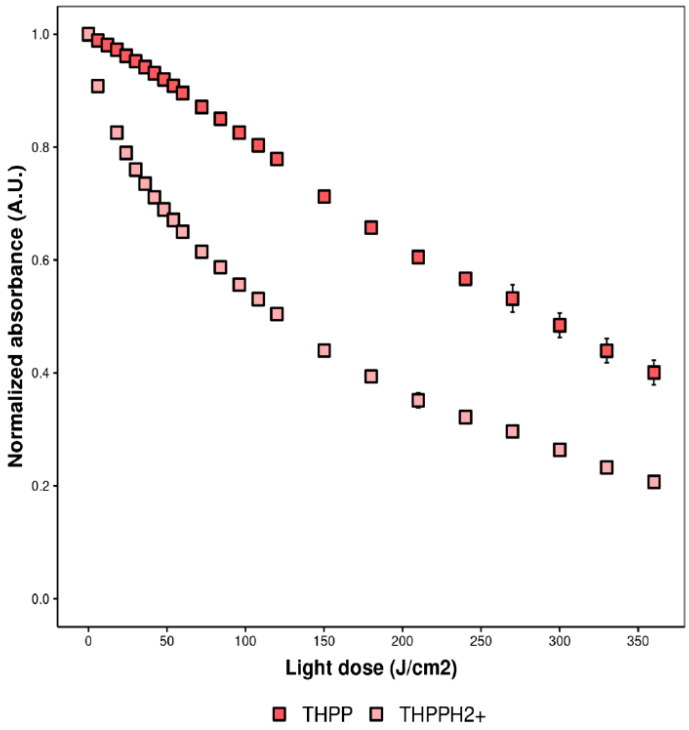

Figure 5. Compared photodegradation of THPP and $THPPH_2^{2+}$, as both co-exist inside acetylated lignin nanoparticles, with the cationic species degrading faster upon blue-LED light irradiation.

2.5. Effect of the Aqueous Media on Porphyrins and Porphyrin Loaded Nanoparticles

Through all the present work, the pH of the medium has played an important role at the different photophysical parameters of our nanoparticles. To corroborate and elaborate this aspect, the influence of the pH on the medium for the free porphyrins and the encapsulated porphyrins was analyzed. In the literature, there are some examples where drug-loaded lignin nanoparticles are able to release their cargo into the media, in acidic pH [41–44]. However, porphyrins loaded into acetylated lignin nanoparticles seem to be unaltered when the pH of the media fluctuates [20], and this could be due to a diminishing of the accessibility of the solvent during acetylated lignin nanoparticles formation [40], which could eventually lead to the permanent entrapment of porphyrins inside nanoparticles.

2.5.1. Effect of Fluctuations of pH into the Medium

It has been hypothesized that, inside the nanoparticles, an acidic media permits the formation of $THPPH_2^{2+}$, the protonated derivative of THPP, which appears to have an important role on the fluorescence, singlet oxygen formation and photobleaching. To demonstrate if these observations are extensive to other porphyrins encapsulated inside nanoparticles, the influence of pH in the media for both free and encapsulated porphyrins was analyzed (Figure 6).

As previously reported, encapsulation of porphyrins inside acetylated lignin nanoparticles prevents changes of the porphyrins, as a result of pH changes. This is particularly evident when comparing the spectra of the free and encapsulated porphyrins, with the latest remaining unaltered through the pH changes (Supplementary Figure S9). This corroborates our previous reports, supporting our hypothesis of diminished solvent accessibility for the porphyrins, once inside the nanoparticles.

2.5.2. pH Driven Release

The lack of interaction between the medium and the encapsulated porphyrins could mean that the porphyrins are not released into the media, even when a pH change occurs. In the literature, there are reports that indicate that lignin nanoparticles loaded with benzazulene [41,42], sorafenib [42], 10-hydroxycamptothecin [43] and emamectin benzoate [44] are able to release their cargo in acidic pH. Furthermore, some reports indicate that release happens even at neutral pH, but is enhanced in acidic pH [41]. However, none of these reports were done in acetylated lignin, but in lignin chemically modified with functional groups that are susceptible to pH changes, as carboxyl and histidine moieties. Nevertheless, the capacity of our nanoparticles to leak the compound in response to an acidic pH was analyzed (Figure 7).

Nanoparticles were suspended either at pH 3 or pH 7 buffer and at each time a sample was taken and centrifuged, sampling over the supernatant obtained. The supernatants were analyzed through fluorescence and reported as free porphyrin, with respect to the initial amount of porphyrins (20 μM). Interestingly, we could observe differences between the amount of free porphyrin at time zero as a function of pH, for THPP and ZnTHPP. Both samples showed a higher amount of free porphyrin when suspended in pH 7. Nevertheless, this namely free porphyrin quickly degrades and at the final time of observation there could be no distinguishable differences as a function of pH.

For most of the cases, the amount of free porphyrin remained stable from the beginning to the end of the experiment (Supplementary Table S1). Remarkably, besides the decrease in free porphyrin found for THPP and ZnTHPP, it was found that the amount of free T(MAP)PP increased significantly from 9.38 to 16.4% when the nanoparticles were suspended in pH 3 buffer. Furthermore, this effect was not found for the same nanoparticles when suspended in pH 7. Similar behavior could not be found in the other porphyrins, not even in T(PrOH)PyP, which shares T(MAP)PP's cationic nature. Our previous report has indicated that THPP@AcLi would keep its porphyrin for up to 60 days, with minimal leaking (9%). Although the present approach lasted a shorter time, this was a more dynamic experiment, as nanoparticles suspensions were under constant stirring, ensuring a better

interaction with the media. Nevertheless, we were not able to observe leaking in any other than for T(MAP)PP in acidic pH.

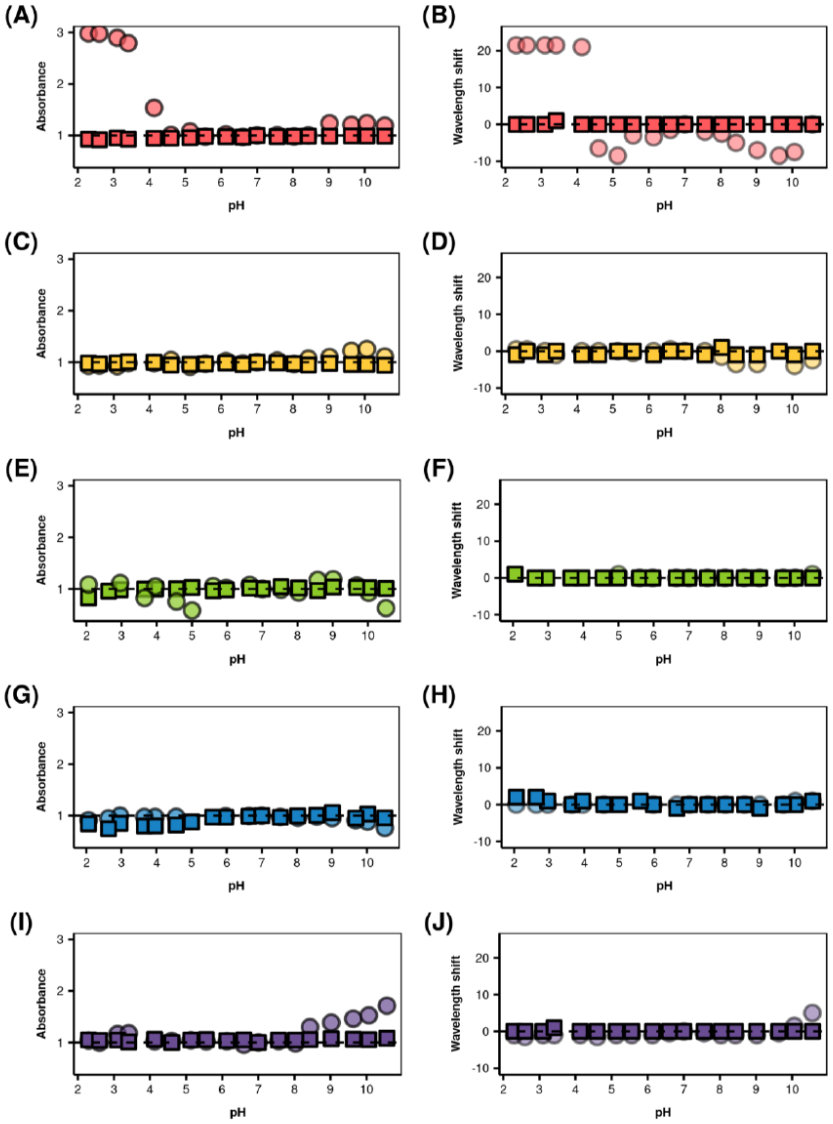

Figure 6. Effect of pH on the UV-vis absorption of (**A**) THPP, (**C**) T(OAc)PP, (**E**) T(MAP)PP, (**G**) T(PrOH)PyP and (**I**) ZnTHPP, as free porphyrins (circles) or as encapsulated poprhyrins (squares). The effect on the Soret band maximum wavelength was also analyzed, for (**B**) THPP, (**D**) T(OAc)PP, (**F**) T(MAP)PP, (**H**) T(PrOH)PyP and (**J**) ZnTHPP, as free porphyrins (circles) or as encapsulated porphyrins (squares). Free porphyrins were dissolved in DMF and diluted in aqueous media to a final concentration of 5 μM and 5% DMF; encapsulated porphyrins were suspended in aqueous media, for a final concentration of 5 μM, of their corresponding porphyrin. Data were normalized, as based on the obtained absorbance and Soret's band wavelength at pH 7.

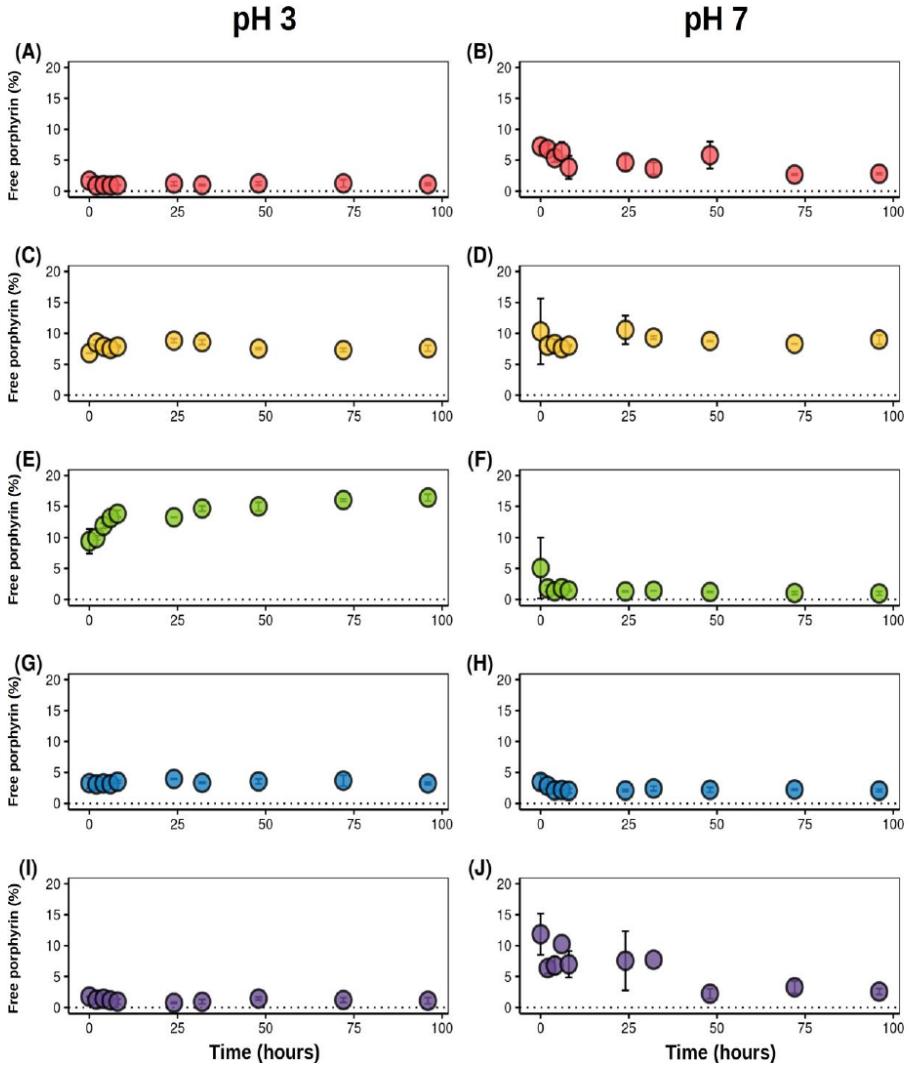

Figure 7. Leaking of porphyrins over time, as a function of pH. Porphyrin leakage was evaluated in pH 3 and pH 7 for THPP (**A**,**B**), T(OAc)PP (**C**,**D**), T(MAP)PP (**E**,**F**), T(PrOH)PyP (**G**,**H**) and ZnTHPP (**I**,**J**), respectively. The leakage is presented as free porphyrin, with respect to the initial amount of porphyrin, 20 μM.

The tight entrapment of porphyrins inside nanoparticles is interesting as an immobilization vehicle for porphyrins. Normally, to ensure such a tight interaction with a material, covalent bonds are used, increasing the cost of the developed technology, but ensuring their lasting, and even providing molecular targeting [45]. Our nanoparticles then provide an effective and endurable strategy, without the nuisance of chemical modifications to prevent leakage from the material.

2.6. Photodynamic Antimicrobial Chemotherapy Effect

Our latest report indicated that THPP@AcLi was able to eradicate three strains of Gram-positive bacteria, while remaining ineffective against Gram-negative bacteria, using white-LED light irradiation as a light source. This was a breakthrough, as it was demonstrated that nanoparticles with low apparent singlet oxygen production were able to kill bacteria using concentrations below 1 μM. The challenge was set then to eradicate Gram-negative bacteria as well, bacteria which are normally impermeable to porphyrins, but which are sensitive to cationic photosensitizers.

2.6.1. Bacteriostatic Effect

The bacteriostatic effect of both free and encapsulated porphyrins was tested against *Staphylococcus aureus* and *Escherichia coli*, as Gram-positive and Gram-negative models, respectively. The minimal inhibitory concentrations (MIC) for the light and dark conditions are shown in Table 5, while the obtained graphs of growth as a function of concentration can be found in Supplementary Figures S10 and S11.

Table 5. Minimal inhibitory concentrations found for *S. aureus* and *E. coli*, when treated with the free or encapsulated porphyrins. Irradiated bacteria were incubated with the treatment for 30 min, before irradiation under blue-LED light (15 J/cm^2).

Porphyrin	*S. aureus*		*E. coli*	
	Light	**Dark**	**Light**	**Dark**
THPP	0.78 μM	>50 μM	>50 μM	>50 μM
THPP@AcLi	>25 μM	>50 μM	>50 μM	>50 μM
T(OAc)PP	>50 μM	>50 μM	>50 μM	>50 μM
T(OAc)PP@AcLi	>50 μM	>50 μM	>50 μM	>50 μM
T(MAP)PP	1.56 μM	3.13 μM	1.56 μM	>50 μM
T(MAP)PP@AcLi	>50 μM	>50 μM	50 μM	50 μM
T(PrOH)PyP	6.25 μM	50 μM	1.56 μM	>50 μM
T(PrOH)PyP@AcLi	>50 μM	>50 μM	50 μM	50 μM
ZnTHPP	0.78 μM	3.13 μM	>50 μM	>50 μM
ZnTHPP@AcLi	50 μM	50 μM	50 μM	50 μM

In the conditions tested, only the free porphyrin T(OAc)PP was unable to arrest the growth of *S. aureus*, while only the free cationic porphyrins were able to arrest the growth of *E. coli*. However, all the encapsulated porphyrins seemed to be unable to inhibit the growth of both *S. aureus* and *E. coli*. Nevertheless, these results, which contrast with our previous report, could be due to a methodological difference. In our last report, bacteria were grown for 6 h at 37 °C after the light treatment, before measuring the resultant growth. However, experimental limitations due to COVID-19 restrictions prevented from observing bacterial growth in a narrower time window, monitoring bacteria growth at 16 h after light irradiation. Then, any lack of growth can be due a total annihilation of bacteria due to a photodynamic effect, or due to a slow, dark chemotoxic effect. Our previous observations indicated that THPP@AcLi were unable to produce dark toxicity in Gram-positive bacteria strains [20], and thus the high MIC values for the nanoparticles could be camouflaged by a bacterial recovery and low dark toxicity.

2.6.2. Bactericidal Effect

The obtained MIC results were complemented with the minimal bactericidal concentration (MBC), understood as the concentration with at least three logarithmic orders of

magnitude reduction in the bacterial counting. When compared, MBC are expected to be several orders of magnitude lower than MIC. Normally, in chemotherapy, this is the other way around, with MBC > MIC, but this is considering that the chemotoxic effect is always present and rarely disappears over time. In the case of photodynamic compounds, normally after light irradiation, bacteria cells are cultured and able to recover after the ROS production driven by light, so it is not surprising that obtained MIC values are overestimations of the actual concentrations needed to kill bacteria. Here, we present the MBC values obtained for *S. aureus* (Supplementary Figure S12) and *E. coli* (Supplementary Figure S13), after blue-LED light irradiation (Table 6).

Table 6. Minimal bactericidal concentrations found for *S. aureus* and *E. coli*, when treated with the free or encapsulated porphyrins. Irradiated bacteria were incubated with the treatment for 30 min, before irradiation under blue-LED light (15 J/cm^2). In parenthesis is indicated the rate MIC/MBC for the concentrations where MBC could be precisely determined.

Porphyrin	*S. aureus*		*E. coli*	
	Light	**Dark**	**Light**	**Dark**
THPP	0.0488 µM (16)	0.1953 µM	>50 µM	>50 µM
THPP@AcLi	0.7813 µM (32)	>1.5625 µM	>50 µM	>50 µM
T(OAc)PP	>50 µM	>50 µM	>50 µM	>50 µM
T(OAc)PP@AcLi	>50 µM	>50 µM	>50 µM	>50 µM
T(MAP)PP	0.0500 µM (32)	>0.2 µM	0.4 µM (4)	>0.4 µM
T(MAP)PP@AcLi	>50 µM	>50 µM	>50 µM	>50 µM
T(PrOH)PyP	0.200 µM (32)	>0.2 µM	0.2 µM (8)	>0.2 µM
T(PrOH)PyP@AcLi	1.0 µM (50)	>2 µM	6.25 µM (8)	>50 µM
ZnTHPP	0.0977 µM (8)	>0.1953 µM	>50 µM	>50 µM
ZnTHPP@AcLi	6.25 µM (8)	>50 µM	>50 µM	>50 µM

As expected, the MBC values found were lower than the MIC values, indicating that most of the bacteriostatic effect observed in the MIC values are due to the light-driven bactericide effect. Additionally, the MBC values for all the treatments were lower for the irradiated samples than for the non-irradiated bacteria, and then bacterial death results in a photodynamic effect.

Interestingly, while free T(OAc)PP fails to diminish the bacterial concentration of *S. aureus*, the nanoparticles T(OAc)PP@AcLi were able to diminish in ~2.5 log the bacterial concentration of *S. aureus* with 12.5 µM of the porphyrin. Surprisingly, this was the best result obtained, with an increase in concentration failing to further diminish the bacterial concentration of *S. aureus*. Similar results were observed for T(MAP)PP@AcLi and ZnTHPP@AcLi with an increase in bacterial survival on the highest concentrations tested, 50 µM. This effect is likely to be due to the high concentration of nanoparticles, which may provoke light diffraction, preventing nanoparticles and bacteria from the bottom being reached by the light. Consequently, it is likely that this problem could be overcome with stirring of the sample, which was not done due to the short irradiation times and the small volume of the samples (30 s and 100 µL). This effect is not observed for THPP@AcLi and T(PrOH)PyP@AcLi, as their MIC values are 0.7813 and 1 µM, respectively, and the presence of lignin and light dispersion is neglected. Nevertheless, it is remarkable that T(OAc)PP@AcLi was able to diminish the bacterial concentration, where the free T(OAc)PP failed to do so. As previously explored throughout this report, T(OAc)PP is the most lipophilic porphyrin, and greatly aggregates in aqueous media. Then, through our approach we were able to deliver a lipophilic porphyrin and provide it with an antibacterial activity against Gram-positive bacteria.

In general, the encapsulation of porphyrins diminished their efficiency, when compared with the free porphyrins in aqueous media, despite its aggregated character. Nevertheless, encapsulated porphyrins were unable to diminish the bacterial concentration when incubated in the dark. This was previously observed for THPP@AcLi, where null dark toxicity was found for several Gram-positive strains [20]. In this report, it was shown that THPP and ZnTHPP, are able to diminish the bacterial viability after light irradiation (MBC 0.0488 and 0.0977 μM, respectively), but they also diminish the bacterial viability in the dark, with reductions of 2.5 and 1.4, respectively, at the same concentrations. One of the most appreciated characteristics of PACT is its activation upon light irradiation, which permits modulation and control of the bactericidal effect, keeping at bay any antibacterial resistance which may arise. Thus, the presence of dark toxicity is pernicious to any research related to PACT. Our formulation presents an advantage over the use of the free porphyrins, as our formulation requires a precise light dose to exert their antibacterial activity. As an example, in the dark against *S. aureus*, ZnTHPP@AcLi is unable to diminish the bacterial survival at 50 μM, the highest concentration tested, while ZnTHPP diminishes in 3-log the bacterial survival at around 0.3 μM. Consequently, encapsulation of porphyrins prevents dark toxicity, with the latest being a consequence of chemotoxicity and likely to be unrelated to ROS production. It is remarkable that the free cationic porphyrins did not present dark toxicity for *S. aureus* or *E. coli*.

The lack of dark toxicity from our formulation also suggests that porphyrins, once entrapped inside the acetylated lignin nanoparticles, are unable to enter the cell and provoke chemotoxic damage in the absence of light, which is supported by the stability of our formulation at pH 7. This gives an insight into their killing mechanism, and it can be hypothesized that nanoparticles interact with the bacterial wall or membrane, with the resulting death being due to the localized production of singlet oxygen from the entrapped porphyrins, without requiring the entry of the porphyrins into the cell.

While most of the free porphyrins and nanoparticles were able to diminish the bacterial count of *S. aureus*, only the free cationic porphyrins were able to kill *E. coli*, as thoroughly explored in the literature [38,46,47]. Interestingly, T(MAP)PP@AcLi was unable to diminish the bacterial counts of *E. coli*. This corresponds with the results presented for *S. aureus*, where we observed a decrease of approximately 2-log, at its best. Interestingly, T(PrOH)PyP@AcLi was able to diminish 3-log of bacterial survival at 6.25 μM, and so the lack of effect of T(MAP)PP@AcLi is not due to its cationic charges, but is a consequence of another factor.

3. Conclusions

In this work the encapsulation of five porphyrins was analyzed, with different chemical characteristics, inside acetylated lignin nanoparticles. It was demonstrated that acetylated lignin nanoparticles are a suitable vehicle for several kinds of porphyrins, preserving their photochemical and antibacterial properties. Here, the stability of the nanoparticles was demonstrated, which seem to be unable to leak the porphyrins once encapsulated. Furthermore, it was demonstrated that, through the increase in bioavailability, a lipophilic porphyrin as T(OAc)PP was able to diminish bacterial survival. This observation is a fundamental stone for easy, cheap and green encapsulation of lipophilic tetrapyrrolic compounds, which in aqueous media greatly aggregate, quenching the production of singlet oxygen.

Although the mechanisms of cellular death driven by porphyrin-loaded acetylated lignin nanoparticles are still unclear, these observations are likely to push forward the research on lignin and lignin nanoparticles, as suitable materials for the formulation of photosensitizers against bacterial proliferation.

4. Materials and Methods

4.1. Materials, Equipment and Microbiological Strains

Kraft lignin was kindly donated by the Université du Québec à Trois-Rivières, Canada. 5,10,15,20-tetrakis(4-hydroxyphenyl)-21H,23H-porphine (THPP), 5,10,15,20-tetrakisphenyl-

21H,23H-porphine (TPP), 2,2,6,6-tetramethylpiperidine (TEMP), and Rose Bengal, were purchased at Sigma-Aldrich (Lyon, France). THPyP was purchased at Porphychem (Dijon, France). Other solvents and reagents were bought at Fluorochem (Hadfield, UK), Alfa Aesar (Haverhill, MA, USA), TCI (Paris, France), Carlo Erba (Barcelona, Spain), Fisher Chemicals (Hampton, VA, USA) and VWR Chemicals (Radnor, PA, USA). All chemicals were used as received, without further purification.

The ^{1}H spectra were recorded on a 400 Bruker Advance spectrophotometer or a Bruker DPX500 NMR spectrophotometer, using tetramethylsilane as an internal standard.

E. coli CIP 53.126 and *S. aureus* CIP 76.25 were obtained from the Institute Pasteur Collection (Institute Pasteur, Paris, France). All bacterial strains were kept frozen as small aliquots (200 µL), at −78 °C, with glycerol 50% as cryopreservant. A whole aliquot was used for each culture, avoiding defrosting of the other samples. *E. coli* was grown in Luria Bertani (LB) broth (Biokar, Allone, France; tryptone 10 g/L, sodium chloride 10 g/L, yeast extract 5 g/L), while *S. aureus* was routinely grown in trypto-casein soy medium (Biokar, Allone, France; tryptone 17 g/L, papaic digest of soybean meal 3 g/L, glucose 2.5 g/L, dipotassium phosphate 2.5 g/L, sodium chloride 2 g/L), prepared as a broth (LBB and TSB) or as a solid media (TSA; 1.7% agar) according to standard procedures. Saline solution (0.9% NaCl) and phosphate buffer pH 7 (PB pH 7, $NaH_2PO_4 \bullet 2H_2O$ 0.964 g/L, $Na_2HPO_4 \bullet 2H_2O$ 3.463 g/L) were routinely prepared and sterilized.

4.2. Synthesis of Porphyrins

4.2.1. 5,10,15,20-Tetrakis (4-acetyloxyphenyl)-21H,23H-porphine

Freshly distilled pyrrole (1.2210 g, 18.2 mmol, 1 eq.) was added dropwise to a refluxing solution of propionic acid (68.5 mL) containing 4-acetoxybenzaldehyde (2.987 g, 18.2 mmol, 1 eq). The mixture was stirred under reflux for 30 min and cooled to room temperature. The reaction mixture was filtered and washed with MeOH. The crude product was purified by silica gel column chromatography ($CHCl_3$/MeOH 9/1, *v*/*v*) to afford T(OAc)PP as a purple solid (yield 12.3%). ^{1}H NMR (500 MHz, $CDCl_3$): δ (ppm) = 8.88 (s, 8H, Hpyrr), 8.21 (d, *J* = 11.0 Hz, 8H, H-Ar), 7.52 (d, *J* = 11.0 Hz, 8H, H-Ar), 2.5 (s, 12H, CH_3), −2.81 (s, 2H, NH).

4.2.2. 5,10,15,20-Tetrakis(4-(3-*N*,*N*,*N*-trimethylammoniumpropoxy)-phenyl)-21H,23H-porphine bromine

Previously dried commercial THPP (150 mg, 0.2652 mmol, 1 eq.) were dissolved in dry DMF (5 mL), with further addition of cesium carbonate (753.1 mg, 2.3114 mmol, 8.7 eq.), under constant stirring and nitrogen atmosphere. Then, (3-bromopropyl)trimethylammonium bromide (583.1 mg, 2.2337 mmol, 8.4 eq.) was added and the reaction was heated at 100 °C for 24 h. The reaction was cooled to room temperature and precipitated with CH_2Cl_2 (100 mL). The obtained solid was filtrated and evaporated. The solid was dissolved in water (50 mL) and extracted with 50 mL of CH_2Cl_2 three times. The aqueous phase was recovered and evaporated, to afford T(PrOH)PyP as a crystalline violet solid (yield 72%). ^{1}H NMR (400 MHz, DMSO-d_6): δ (ppm) = 9.59 (d, *J* = 6.68 Hz, 8H, H-Ar), 9.23 (s, 8H, Hpyrr), 9.02 (d, *J* = 6.68 Hz, 8H, Har), 5.07 (m, 8H, CH_2-N), 3.80 (m, 8H, CH_2-O), 2.46 (m, 8H, CH_3), −3.08 (s, 2H, NH).

4.2.3. 5,10,15,20-Tetrakis (4-(3-hydroxy)propyloxypyridyl)-21H,23H-porphine bromine

Previously dried commercial THPyP (101.2 mg, 0.1636 mmol, 1 eq.) were dissolved in dry DMF (8 mL), under constant stirring and nitrogen atmosphere. Then, 3-bromopropanol (922 mg, 6.6350 mmol, 40 eq.) were added dropwise and the reaction was heated at 100 °C over 24 h. The reaction was cooled to room temperature and precipitated with CH_2Cl_2 (50 mL). The obtained solid was filtrated and evaporated. The solid was dissolved in MeOH and purified by silica gel flash column chromatography (Acetonitrile/MeOH/Water 6/2/2), to afford a T(MAP)PP as a violet powder (yield 62%). ^{1}H NMR (400 MHz, DMSO-d_6): δ (ppm) = 8.92 (s, 8H, Hpyrr), 8.21 (d, *J* = 8 Hz, 8H, H-Ar), 7.42 (d, *J* = 8 Hz, 8H, H-Ar), 4.45 (m, 8H, CH_2-O), 3.76 (m, 8H, CH_2-N), 3.29 (s, 36H, CH_3), 2.36 (m, 8H, CH_2), −2.83 (s, 2H, NH).

4.2.4. Zinc (II) 5,10,15,20-Tetrakis (4-hydroxyphenyl)-21H,23H-porphine

Commercial THPP (60 mg, 0.09 mmol, 1 eq.) was dissolved in DMF anhydre (10 mL), with further addition of zinc acetate (0.1 g, 0.44 mmol, 5 eq.). The mixture was stirred under reflux under a nitrogen atmosphere, over 1.5 h and cooled to room temperature. The reaction mixture was then precipitated in distilled water over 12 h, at 4 °C. The solid was filtrated, obtaining ZnTHPP as a violet powder solid (yield 84%). ^{1}H NMR (500 MHz, DMSO-d_6): δ (ppm) = 9.81 (s, 4H, Ar-OH), 8.88 (s, 8H, Hpyrr), 7.95 (d, J = 8.28 Hz, 8H, H-Ar), 7.17 (d, J = 8.36, 8H, H-Ar).

4.3. Preparation and Quantification of Porphyrin-Loaded Acetylated Lignin Nanoparticles

Nanoparticles were prepared using acetylated lignin [30]. Acetylated lignin (2 mg/mL) and porphyrins (0.2 mg/mL) were dissolved in a solvent or mixture solvent, accordingly to the porphyrins' solubility (Table 7). The starting solutions were dialyzed on a regenerated cellulose membrane rod (Fisherbrand, Ottawa, Canada; 12–14 KDa), against distilled water, at room temperature and without stirring, for 24 h. After dialysis, nanoparticles were centrifuged at 10,000× g for 30 min and washed twice with distilled water. Nanoparticles were suspended in distilled water and kept in the dark at room temperature until further use. For quantification, nanoparticles were diluted and quantified, using their absorption coefficients, in acetone (THPP ($\varepsilon_{419\ nm}$ = 388,500 $M^{-1}cm^{-1}$) and ZnTHPP ($\varepsilon_{425\ nm}$ = 485,914 $M^{-1}cm^{-1}$)), DMSO (T(MAP)PP ($\varepsilon_{423\ nm}$ = 242,207 $M^{-1}cm^{-1}$)) or DMF (T(OAc)PP ($\varepsilon_{418\ nm}$ = 388,725 $M^{-1}cm^{-1}$) and T(PrOH)PyP ($\varepsilon_{426\ nm}$ = 132,376 $M^{-1}cm^{-1}$)).

Table 7. Solvents used for the starting solution of each type of nanoparticle analyzed in the present work.

Porphyrin	Solvent or Solvents Mixtures
THPP	Acetone
T(OAc)PP	Acetone:DMF 9:1
T(MAP)PP	Acetone:DMSO 9:1
T(PrOH)PyP	Acetone:DMSO 9:1
ZnTHPP	THF

4.4. Physical Characterization

Nanoparticles size was analyzed through DLS on a Zetasizer Nano-ZS (Malvern Instrument, Malvern, UK). For each sample, three measurements were performed on each sample, using a disposable plastic cuvette, at 20 °C and using a light scattering angle of 173° and a refractive index of 1.61, for lignin materials [48]. The obtained DLS raw data were fitted to a Gaussian distribution model, excluding the values with less than 1% of frequency. The normality of the obtained model was evaluated through its R square coefficient and through the analysis of the residuals, with a D'Agostino-Pearson Omnibus K2 test, affording the mean size (geometrical mean) and the standard deviation (σ), which allowed us to approximate the range where 95% of the nanoparticles were found (2σ).

Zeta potential was measured using a DTS1070 cuvette (Malvern Instrument, Malvern, UK), in a Zetasizer Nano-ZS (Malvern Instrument, Malvern, UK), obtaining five measurements for each sample.

4.5. Photophysical Characterization

UV-vis spectra were recorded on a Hitachi U-2001 (Tokyo, Japan) or Analytic Jena Specord 210 (Jena, Germany). Spectra were collected from 350 up to 800 nm, using standard quartz cuvettes of 1 cm of optical path.

The fluorescence quantum yield was calculated as described elsewhere [11,20]. Fluorescence spectra were recorded in a Horiba Scientific Spectrofluorometer Fluoromax-4 (Potsdam, Germany) or in an Edinburgh Instruments FLS980 (Edinburgh, UK). Spectra

were collected from 550 up to 800 nm, using standard quartz cuvettes of 1 cm of optical path, at room temperature. Fluorescence quantum yields (Φ_F) were calculated using TPP dissolved toluene in a reference (Φ_F = 0.11), by comparing the area of the integrated fluorescence of the samples (F_s) with the fluorescence of the reference (F_{ref}) and corrected by the absorption of the sample (A_s) and the reference (A_{ref}) at the excitation wavelength and by the refractive index of the solvents used for the sample (η_s) and reference (η_{ref}) solutions (Equation (1)).

$$\Phi_F = \Phi_F^{ref} \frac{F_s A_{ref} \eta_s^2}{F_{ref} A_s \eta_{ref}^2} \quad (1)$$

Singlet oxygen phosphorescence decay was monitored at room temperature, according to previously described procedures [11]. Porphyrins were dissolved in DMF, until they reached an optical density of 0.18. The porphyrins solutions were excited at 355 nm, using an Nd-YAG laser Spectra-Physics Quanta-Ray GRC-130 (Stahnsdorf, Germany). The singlet oxygen phosphorescence was collected at 1270 nm, in a Hamamatsu R5509-42 (Hamamatsu, Japan) photomultiplier, cooled to 193 K in a liquid nitrogen chamber, after selection of the wavelength with a monochromator with 600 lines grading. A Newport filter model 10LWF-1000-B was used in the emission to prevent light scattering and fluorescence. As a reference for the singlet oxygen production, phenalenone was used ($\Phi_\delta{}^{ref}$ = 1.0) [35]. The decays obtained were extrapolated to time-zero, obtaining the initial emission intensities as a function of laser intensity. The singlet oxygen quantum yields were obtained by comparing the linear dependence of the singlet oxygen emission and the energy of the laser pulse for the sample (S_s) and the reference (S_{ref}), corrected by the absorption of the sample (A_s) and reference (A_{ref}) at the excitation wavelength, considering the singlet oxygen quantum yield of the reference (Equation (2)).

$$\Phi_\Delta = \Phi_\Delta^{ref} \frac{S_s 1 - 10^{-A_{ref}}}{S_{ref} 1 - 10^{-A_s}} \quad (2)$$

Singlet oxygen production detected through EPR were recorded as described elsewhere [20,35]. The samples were exposed to a blue-LED light (LED-Illuminator, Luzchem, Gluocester, Canada); light irradiation was measured with a handheld powermeter (Lasercheck, Coherent, Santa Clara, CA, USA), centered at 455 nm. EPR spectra were recorded with a Bruker Model ESP300E spectrometer (Berlin, Germany) operating at room temperature. Routinely, a fresh solution of 25 mM 2,2,6,6- tetramethylpiperidine (TEMP) was prepared in DMF or PB pH 7. Free porphyrins were dissolved in DMF and diluted in DMF until they reached 3 µM. Nanoparticles suspensions were diluted at 50 µM in PB pH 7. For singlet oxygen detection, 50 µL of the fresh TEMP solution were mixed with 50 µL sample to analyze. The solution obtained was immediately transferred into quartz capillaries (100 µL) and placed at 14.5 cm from the source of illumination with a light intensity irradiation of 60 mW/cm^2, for appropriate periods of time. A dark control was prepared, and Rose Bengal in DMF or PB pH 7 was used as a standard. EPR spectra were performed under the following conditions: modulation frequency, 100 kHz; microwave frequency, 9.78 GHz; microwave power, 4 mW; modulation amplitude, 0.987 G; time constant, 10.24 ms; scans number, 2.

Photobleaching experiments were done as stated elsewhere [11]. Free porphyrins were dissolved in DMF, while the encapsulated porphyrins were suspended in PB pH 7, both at a final concentration of 5 µM. A volume of 3 mL was deposited in a standard quartz cuvette of 1 cm of optical path. The sample was stirred and irradiated with a blue-LED light (LED-Illuminator, Luzchem, Gluocester, Canada), with emission at 450–460 nm and an output power of 100 mW/cm^2. The Soret band absorbance was followed for the light irradiation, and its decay was followed through UV-vis absorption (350–800 nm).

4.6. Influence of pH for the Nanoparticles Behaviour and Stability

4.6.1. pH Buffers

Aqueous buffer solutions prepared for the pH analysis were prepared using appropriated acid–base pairs, at the same molarity. Namely, glycine–HCl 0.01 M was used for buffers at pH 2.0, 2.6, 3.0 and 3.6. Sodium acetate–acetic acid 0.01 M was used for buffers at pH 4.0, 4.6, 5.0 and 5.6. Sodium phosphate–sodium biphosphate 0.01 M was used for buffers at pH 6.0, 6.6, 7.0, 7.6 and 8.0. Glycine–NaOH 0.01 M was used for buffers at pH 8.6, 9.0, 9.6, 10.0 and 10.6. The pH of all buffers was verified and adjusted, using a pH meter (Mettler Toledo, Columbus, OH, USA).

The influence of pH was analyzed through UV-vis absorption, measured between 350 and 800 nm. Free porphyrins were dissolved in DMF at a concentration of 1 mM and then diluted to 5 μM in the buffer for analysis, resulting in a final concentration of 5% DMF v/v. Nanoparticles suspensions were diluted in the buffer to analyze at a final concentration of 5 μM. The Soret band absorption and maximum wavelength were followed up, and the values were normalized according to the values obtained at pH 7.

4.6.2. pH Driven Release

Porphyrin-loaded nanoparticles were suspended either in buffer glycine–HCl 0.01 M pH 3 or phosphate buffer 0.01 M pH 7, at a final concentration of 20 μM. The nanoparticles suspensions were stirred on an orbital shaker, at 200 rpm. For analysis, 500 μL of the nanoparticles suspension were taken and immediately centrifuged (10,000× g, 10 min). Afterwards, 200 μL of the supernatant were carefully taken and stored at 4 °C until analysis. For analysis, the samples were diluted with 1.8 mL of methanol, and excited at the porphyrin's wavelength of the Soret's band in methanol, for monitoring at the maximum emission wavelength, according to Table 8.

Table 8. Wavelengths for excitation and emission, for the porphyrins dissolved in methanol with 10% aqueous buffer.

Porphyrin	Excitation Wavelength	Emission Wavelength
THPP	419 nm	652 nm
T(OAc)PP	415 nm	648 nm
T(MAP)PP	418 nm	652 nm
T(PrOH)PyP	427 nm	650 nm
ZnTHPP	424 nm	607 nm

4.7. Photodynamic Antimicrobial Chemotherapy

All experiments used planktonic bacteria in the middle of the exponential phase of growth. For this, an aliquot of frozen bacteria was inoculated in 5 mL of culture media and incubated overnight, at 37 °C and constant stirring at 100 rpm. The optical density at 600 nm (OD_{600}) was measured for the resulting culture, and further diluted at an OD_{600} = 0.1 in 5 mL of fresh culture media. This subculture was incubated for two hours, at 37 °C and constant stirring. Bacteria were collected, centrifuged (4000× g, 10 min), washed with sterile PB pH 7 and resuspended in 1 mL of PB pH 7, resulting in a bacterial suspension with around 10^8 CFU/mL.

Free porphyrins were dissolved in DMSO, for a stock concentration of 1 mM. Then, the DMSO solution was geometrically diluted in DMSO, obtaining solutions ranging from 1000 to 7.8125 μM. Then, each dilution was diluted 1:10 in PB pH 7, resulting in a solution with 10% DMSO and concentrations of porphyrins ranging between 100 and 0.78125 μM. Porphyrin-loaded nanoparticles were diluted in PB pH 7, at a stock concentration of 100 μM and geometrically diluted until 0.78125 μM.

For the bacteriostatic effect analysis, bacteria were diluted to ~10^5 CFU/mL in PB pH 7. Bacteria aliquots (50 µL) were delivered in a 96-well plate (Corning, Corning, NY, USA) and mixed with 50 µL of the treatment solution, for a final range of concentrations of 50 to 0.35625 µM. Bacteria and the treatment were incubated in the dark for 30 min. Afterwards, each well was irradiated with a vertical array of blue-LED light (LED-Illumintor, Luzchem, Gluocester, Canada) at 1.4 cm from the plate and with an intensity of 500 mW/cm^2 for 30 s, resulting in a light dosage of 15 J/cm^2. Light irradiance was routinely verified using a handheld powermeter (Lasercheck, Coherent, Santa Clara, CA, USA), centered at 455 nm. During the irradiation of each well, the rest of the plaque was protected from light with a black cardboard mold. A similar plaque was prepared, kept in the dark during the irradiation and worked as dark control. Without further incubation, 100 µL of culture media were added into each well and the initial optical density at 595 nm (OD_{595}) was measured on a multiplate reader (iMark, Bio-Rad, Marnes-la-Coquette, France) as time-zero ($OD_{595}{}^0$). Each plate was incubated in the dark, at 37 °C, and its optical density was measured again ($OD_{595}{}^{16}$). Appropriated controls were prepared: a sample without bacteria and without treatment was used as a blank (G_B), while a bacterial sample with PB pH 7 or PB pH 7 5% DMSO was used as growth control (G_C). Growth was obtained as the difference between $OD_{595}{}^{16}$ and $OD_{595}{}^0$, while the normalized growth (G_N) for each sample was obtained according to the Equation (3), where G_S is the growth of the sample. The MIC was considered to be the lowest concentration where the normalized growth was below 0.1.

$$G_N = \frac{G_S - G_B}{G_C - G_B} \quad (3)$$

For the bactericidal effect analysis, bacteria were diluted to ~10^7 CFU/mL in PB pH 7. Bacteria aliquots (50 µL) were delivered in a 96-well plate (Corning, Corning, NY, USA) and mixed with 50 µL of the treatment solution, descending from the MIC concentration values. Bacteria and the treatment were incubated in the dark for 30 min. Afterwards, each well was irradiated with a vertical array of blue-LED light (LED-Illumintor, Luzchem, Gluocester, Canada) at 1.4 cm from the plate and with an intensity of 500 mW/cm^2 for 30 s, resulting in a light dosage of 15 J/cm^2. Light irradiance was routinely verified using a handheld powermeter (Lasercheck, Coherent, Santa Clara, CA, USA), centered at 455 nm. During the irradiation of each well, the rest of the plaque was protected from light with a black cardboard mold. A similar plaque was prepared and kept in the dark during the irradiation and worked as a dark control. A bacterial control with PB pH 7 or PB pH 7 5% DMSO was used as growth control (G_C). Without further incubation, bacterial suspensions were recovered and serially diluted in saline solution. Afterwards, 50 µL of the diluted bacterial suspension were plated into TSA culture media, using an automatic plater (EasySpyral, Interscience, Mourjou, France). Colony-forming units were counted using a colony counter (Scan100, Interscience, Mourjou, France). Bacterial survival was expressed as the logarithm of the concentration (log(CFU/mL)). The MBC was considered to be the lowest concentration where a reduction of 3-log was observed.

4.8. Statistical Analysis

Physical and photophysical experiments were performed at least in duplicate. Microbiological experiments were performed at least in triplicate. The obtained DLS raw data were analyzed with GraphPad Prism 6.01, and data were fit to a Gaussian model, excluding the values with less than 1% of presence. The obtained data were validated through the analysis of their R square coefficient and through the analysis of the residuals with a D'Agostino–Pearson Omnibus K2 test. Statistical significance was determined using a Two-Way ANOVA and a Tukey's test for multiple comparisons, with 95% of the cohort.

Graphs presented throughout this work were prepared with RStudio (R version 4.0.4), using ggplot and diplyr libraries.

Supplementary Materials: The following are available online at https://www.mdpi.com/article/10.3390/antibiotics10050513/s1. Figure S1. Comparison of the spectra of (A) THPP, (B) T(MAP)PP, (C) T(OAc)PP, (D) T(PrOH)PyP and (E) ZnTHPP as free porphyrins (black), or as the encapsulated porphyrins before (blue) and after (red) the correction of the baseline. Figure S2. Spectra of (A) THPP, (B) T(OAc)PP, (C) T(MAP)PP, (D) T(PrOH)PyP, and (E) ZnTHPP upon water addition. Porphyrins were initially dissolved in (A) acetone, (B) acetone:DMF 9:1, (C) acetone:DMSO 9:1, (D) acetone:DMSO 9:1, and (E) THF, at a concentration of 5 μM (black line), through increasing water addition. Figure S3. Normalized absorbance (solid lines) and emission (dashed lines) spectra of (A) THPP, (B) T(MAP)PP, (C) T(OAc)PP, (D) T(PrOH)PyP and (E) ZnTHPP, dissolved in DMF (black), in PB pH 7, 0.5% DMF (blue), or as encapsulated porphyrins (red). Emission spectra were collected from a solution at 0.5 μM, at 25 ºC, with excitation at 425 nm. Figure S4. Fluorescence emission (black solid lines) and excitation (black and blue dashed lines) spectra of the free porphyrins in DMF (A, B, C, D, E) or in aqueous buffer at pH 2 (F, G, H, I, J); or as encapsulated porphyrins suspended in pH 7 (K, L, M, N, O) or in pH 2 (P, Q, R, S, T). The black horizontal line indicates the wavelength of the Soret band of each porphyrin in DMF, while the dashed horizontal lines indicate the peak of the emission bands of each porphyrin in DMF, also indicating as well the emission wavelength monitored in the excitation spectra. Emission spectra were after excitation at 425 nm; all spectra were measured at 25 °C, from a solution 0.5 μM of the corresponding porphyrin. Figure S5. Slopes of the decay of singlet oxygen phosphorescence, detected at 1270 nm, measured through near infrared spectroscopy, as a function of laser energy. Porphyrins were dissolved in DMF, with an absorption of around 0.18 at 355 nm, the excitation wavelength. Phenalenone in DMF was used as a standard ($\Phi\Delta = 1$). Figure S6. Absorption spectra of free porphyrins (A) THPP, (B) T(OAc)PP, (C) T(MAP)PP, (D) T(PrOH)PyP and (E) ZnTHPP, after irradiation under blue LED light (100 mW/cm^2). Porphyrins were dissolved in DMF, 5 μM, with constant stirring on an open quartz cell. Shown spectra are the average of two individual experiments. Figure S7. Absorption spectra of encapsulated porphyrins (A) **THPP@AcLi**, (B) T(OAc)PP@AcLi, (C) T(MAP)PP@AcLi, (D) T(PrOH)PyP@AcLi and (E) ZnTHPP@AcLi, after irradiation under blue-LED light (100 mW/cm^2). Nanoparticles were suspended in PB pH 7, at 5 μM of their corresponding porphyrin, with constant stirring on an open quartz cell. Shown spectra are the average of two individual experiments. Figure S8. Comparison of spectra for T(PrOH)PyP before light irradiation (black), after light irradiation (blue), and the raw porphyrin, THPyP in DMF (red). Figure S9. Effect of pH on the UV-vis absorbance profile of the free porphyrins (A) THPP, (C) T(OAc)PP, (E) T(MAP)PP, (G) T(PrOH)PyP, (I) ZnTHPP, or as encapsulated porphyrins (B) THPP@AcLi, (D) T(OAc)PP@AcLi, (F) T(MAP)PP@AcLi, (H) T(PrOH)PyP@AcLi, (J) ZnTHPP@AcLi. Red lines represent the pH below 7, while blue lines represent the pH above 7. Both free and encapsulated porphyrins were set in a final concentration of 5 μM of their corresponding porphyrin, in an adequate aqueous buffer. Free porphyrins were dissolved in DMF and diluted into an aqueous buffer, for a final DMF concentration of 5%. Table S1. Free porphyrin observed at initial and final observation times, expressed as percent of free porphyrin, with respect to the global amount of encapsulated porphyrins (20 μM). Similar superscript letters indicate the pairs that have differences with a statistical significance, found as $p < 0.05$ with a two-way ANOVA, and a multiple comparisons Tukey's test. Figure S10. Growth inhibition of Staphylococcus aureus, after treatment with (A) THPP, (B) THPP@AcLi, (C) T(OAc)PP, (D) T(Oac)PP@AcLi, I T(MAP)PP, (F) T(MAP)PP@AcLi, (G) T(PrOH)PyP, (H) T(PrOH)PyP@AcLi, (I) ZnTHPP and (J) ZnTHPP@AcLi. Bacteria were incubated for 30 min and then irradiated with blue-LED light (15 J/cm^2, white symbols) or incubated in the dark (grey symbols). Afterwards, culture medium was added and bacteria were incubated at 37 °C, in the dark for 16 h. Results shown are the average of three independent experiments. Figure S11. Growth inhibition of Escherichia coli, after treatment with (A) THPP, (B) THPP@AcLi, (C) t(OAc)PP, (D) t(OAc)PP@AcLI, (E) T(MAP)PP, (F) T(MAP)PP@AcLi, (G) T(PrOH)PyP, (H) T(PrOH)PyP@AcLi, (I) ZnTHPP and (J) ZnTHPP@AcLi. Bacteria were incubated for 30 min and then irradiated with blue-LED light (15 J/cm^2, white symbols) or incubated in the dark (grey symbols). Afterwards, culture medium was added and bacteria were incubated at 37 °C, in the dark for 16 h. Results shown are the average of three independent experiments. Figure S12. Bacterial survival of S. aureus, after treatment with (A) THPP, (B) THPP@AcLi, (c) T(OAc)PP, (d) T(OAc)PP@Ii, (E) T(MAP)PP, (F) T(MAP)PP@AcLi, (G) T(PrOH)PyP, (H) T(PrOH)PyP@AcLi, (I) ZnTHPP and (J) ZnTHPP@AcLi. Bacteria were incubated for 30 min and then irradiated with blue-LED light (15 J/cm^2, white symbols) or incubated in the dark (grey symbols). Afterwards, bacteria were diluted and plated in Petri dishes, which were incubated in the dark 16 h, before counting colonies. The dotted line indicates the limit of quantification (2.9 log),

while the dashed line indicates a diminish of at least 3 log. Figure S13. Bacterial survival of *E. coli*, after treatment with (A) THPP, (B) THPP@AcLi, (C) T(OAc)PP, (D) T(OAc)IAcLi, (E) T(MAP)PP, (F) T(MAP)PP@AcLi, (G) T(PrOH)PyP, (H) T(PrOH)PyP@AcLi, (I) ZnTHPP and (J) ZnTHPP@AcLi. Bacteria were incubated for 30 min and then irradiated with blue-LED light (15 J/cm^2, white symbols) or incubated in the dark (grey symbols). Afterwards, bacteria were diluted and plated in Petri dishes, which were incubated in the dark for 16 h, before counting colonies. The dotted line indicates the limit of quantification (2.9 log), while the dashed line indicates a decrease of at least 3 log.

Author Contributions: Conceptualization, N.M.-C., T.-S.O., N.V., S.L.-L.; methodology, N.M.-C., T.-S.O., N.V., S.L.-L., M.J.F.C.; software, N.M.-C.; validation, T.-S.O., N.V., S.L.-L.; formal analysis, N.M.-C.; investigation, N.M.-C., C.A.C., S.L.-L.; resources, T.-S.O., M.J.F.C., S.L.-L.; data curation, N.M.-C.; writing—original draft preparation, N.M.-C.; writing—review and editing, T.-S.O., N.V., C.A.C., M.J.F.C., S.L.-L.; visualization, N.M.-C.; supervision, T.-S.O., N.V., C.A.C., M.J.F.C., S.L.-L.; project administration, M.J.F.C., M.M.P., S.L.-L.; funding acquisition, S.L.-L. All authors have read and agreed to the published version of the manuscript.

Funding: This project has received funding from the European Union's Horizon 2020 Research and Innovation Programme under the Marie Skłodowska-Curie grant agreement no. 764837.

Institutional Review Board Statement: Not applicable.

Informed Consent Statement: Not applicable.

Data Availability Statement: No datasets were generated.

Acknowledgments: The authors would like to acknowledge Fábio A. Schaberle, for his kind support on the photophysical characterization, Yves Champavier (BISCEm, Limoges University, France) for some of the NMR experiments, Johann Bouclé (XLIM, Limoges University, France) for allowing us to use the fluorometer Edinburgh Instrument FLS980, and Marie Lopez, Romain Le Digabel, Victor Blonder and Andrea Onestas for the synthesis of T(OAc)PP and ZnTHPP as part of their bachelor's training. NMR data of the cationic porphyrins was collected at the UC-NMR facility which is supported in part by FEDER—European Regional Development Fund through the COMPETE Programme (Operational Programme for Competitiveness) and by National Funds through FCT—Fundação para a Ciência e a Tecnologia (Portuguese Foundation for Science and Technology) through grants RECI/QEQ-QFI/0168/2012, CENTRO-07-CT62-FEDER-002012, and also through support to Rede Nacional de Ressonância Magnética Nuclear (RNRMN) and to Coimbra Chemistry Centre through grant UID/QUI/00313/2019.

Conflicts of Interest: The authors declare no conflict of interest.

References

1. World Health Organization. Global Antimicrobial Resistance Surveillance System (GLASS) Report: Early Implementation 2020. Available online: https://apps.who.int/iris/bitstream/handle/10665/332081/9789240005587-eng.pdf (accessed on 15 March 2021).
2. Rawson, T.M.; Moore, L.S.P.; Castro-Sanchez, E.; Charani, E.; Davies, F.; Satta, G.; Ellington, M.J.; Holmes, A.H. COVID-19 and the potential long-term impact on antimicrobial resistance. *J. Antimicrob. Chemother.* **2020**, *75*, 1681–1684. [CrossRef]
3. Murray, A.K. The Novel Coronavirus COVID-19 Outbreak: Global Implications for Antimicrobial Resistance. *Front. Microbiol.* **2020**, *11*, 1–4. [CrossRef] [PubMed]
4. Khoshfetrat, M.; Keykha, A.; Sedaghatkia, M.; Farahmandrad, R.; Behnampour, M. Determination of Antibiotic Resistance Pattern of Organisms Isolated from Endotracheal Tube Cultures of Patients Admitted to Intensive Care Unit. *Arch. Anesth. Crit. Care* **2020**, *6*, 125–132. [CrossRef]
5. Sarda, C.; Fazal, F.; Rello, J. Management of ventilator-associated pneumonia (VAP) caused by resistant gram-negative bacteria: Which is the best strategy to treat? *Expert Rev. Respir. Med.* **2019**, *13*, 787–798. [CrossRef] [PubMed]
6. Ribeiro da Cunha, B.; Fonseca, L.P.; Calado, C.R. Antibiotic Discovery: Where Have We Come from, Where Do We Go? *Antibiotics* **2019**, *8*, 45. [CrossRef] [PubMed]
7. Wainwright, M. Photoantimicrobials and PACT: What's in an abbreviation? *Photochem. Photobiol. Sci.* **2019**, *18*, 12–14. [CrossRef]
8. Mahmoudi, H.; Bahador, A.; Pourhajibagher, M.; Alikhani, M.Y. Antimicrobial Photodynamic Therapy: An Effective Alternative Approach to Control Bacterial Infections. *J. Lasers Med. Sci.* **2018**, *9*, 154–160. [CrossRef] [PubMed]
9. Wainwright, M.; Maisch, T.; Nonell, S.; Plaetzer, K.; Almeida, A.; Tegos, G.P.; Hamblin, M.R. Photoantimicrobials—Are we afraid of the light? *Lancet Infect. Dis.* **2017**, *17*, e49–e55. [CrossRef]
10. Hamblin, M.R. Antimicrobial photodynamic inactivation: A bright new technique to kill resistant microbes. *Curr. Opin. Microbiol.* **2016**, *33*, 67–73. [CrossRef]

11. Vinagreiro, C.S.; Zangirolami, A.; Schaberle, F.A.; Nunes, S.C.C.; Blanco, K.C.; Inada, N.M.; da Silva, G.J.; Pais, A.A.C.C.; Bagnato, V.S.; Arnaut, L.G.; et al. Antibacterial Photodynamic Inactivation of Antibiotic-Resistant Bacteria and Biofilms with Nanomolar Photosensitizer Concentrations. *ACS Infect. Dis.* **2020**, *6*, 1517–1526. [CrossRef] [PubMed]
12. Aroso, R.T.; Calvete, M.J.F.; Pucelik, B.; Dubin, G.; Arnaut, L.G.; Pereira, M.M.; Dąbrowski, J.M. Photoinactivation of microorganisms with sub-micromolar concentrations of imidazolium metallophthalocyanine salts. *Eur. J. Med. Chem.* **2019**, *184*, 111740. [CrossRef]
13. Khaldi, Z.; Nzambe Takeki, J.K.; Ouk, T.-S.; Lucas, R.; Zerrouki, R. Synthesis and photo-bactericidal properties of a cationic porphyrin grafted onto kraft pulp fibers. *J. Porphyr. Phthalocyanines* **2019**, *23*, 489–496. [CrossRef]
14. Kashef, N.; Hamblin, M.R. Can microbial cells develop resistance to oxidative stress in antimicrobial photodynamic inactivation? *Drug Resist. Updat.* **2017**, *31*, 31–42. [CrossRef]
15. Faix, O. Classification of Lignins from Different Botanical Origins by FT-IR Spectroscopy. *Holzforschung* **1991**, *45*, 21–28. [CrossRef]
16. Sipponen, M.H.; Lange, H.; Crestini, C.; Henn, A.; Österberg, M. Lignin for Nano- and Microscaled Carrier Systems: Applications, Trends, and Challenges. *ChemSusChem* **2019**, *12*, 2039–2054. [CrossRef]
17. Yang, W.; Owczarek, J.S.; Fortunati, E.; Kozanecki, M.; Mazzaglia, A.; Balestra, G.M.; Kenny, J.M.; Torre, L.; Puglia, D. Antioxidant and antibacterial lignin nanoparticles in polyvinyl alcohol/chitosan films for active packaging. *Ind. Crops. Prod.* **2016**, *94*, 800–811. [CrossRef]
18. Ponomarenko, J.; Lauberts, M.; Dizhbite, T.; Lauberte, L.; Jurkjane, V.; Telysheva, G. Antioxidant activity of various lignins and lignin-related phenylpropanoid units with high and low molecular weight. *Holzforschung* **2015**, *69*, 795–805. [CrossRef]
19. Rocca, D.M.; Vanegas, J.P.; Fournier, K.; Becerra, M.C.; Scaiano, J.C.; Lanterna, A.E. Biocompatibility and photo-induced antibacterial activity of lignin-stabilized noble metal nanoparticles. *RSC Adv.* **2018**, *8*, 40454–40463. [CrossRef]
20. Maldonado-Carmona, N.; Marchand, G.; Villandier, N.; Ouk, T.-S.; Pereira, M.M.; Calvete, M.J.F.; Calliste, C.A.; Žak, A.; Piksa, M.; Pawlik, K.J.; et al. Porphyrin-Loaded Lignin Nanoparticles Against Bacteria: A Photodynamic Antimicrobial Chemotherapy Application. *Front. Microbiol.* **2020**, *11*. [CrossRef] [PubMed]
21. Ellis, A.; Twyman, L.J. Probing Dense Packed Limits of a Hyperbranched Polymer through Ligand Binding and Size Selective Catalysis. *Macromolecules* **2013**, *46*, 7055–7074. [CrossRef]
22. Majumder, R.; Roy, S.; Okamoto, K.; Nagao, S.; Matsuo, T.; Parui, P.P. Porphyrin-Based Probe for Simultaneous Detection of Interface Acidity and Polarity during Lipid-Phase Transition of Vesicles. *Langmuir* **2020**, *36*, 426–434. [CrossRef] [PubMed]
23. Zhao, H.; Wang, H.; Chang, H.; Qiu, S.; Deng, B.; Liao, J. Covalent and Non-covalent Chemical Modification of Multi-walled Carbon Nanotubes with Tetra-(4-hydroxylphenyl)porphyrin and Its Complexes. *Chin. J. Chem.* **2011**, *29*, 1901–1905. [CrossRef]
24. Qiu, N.; Li, Y.; Li, Y.; Wang, H.; Duan, Q.; Kakuchi, T. A photo- and thermo-responsive star-shaped diblock copolymer with a porphyrin core prepared via consecutive ATRPs. *RSC Adv.* **2016**, *6*, 47912–47918. [CrossRef]
25. Tesakova, M.V.; Semeikin, A.S.; Parfenyuk, V.I. Electrochemical determination of antioxidant properties of a series of tetraphenylporphyrin derivatives and their zinc complexes. *J. Porphyr. Phthalocyanines* **2015**, *19*, 1032–1038. [CrossRef]
26. Caminos, D.A.; Durantini, E.N. Synthesis of asymmetrically *meso*-substituted porphyrins bearing amino groups as potential cationic photodynamic agents. *J. Porphyr. Phthalocyanines* **2005**, *9*, 334–342. [CrossRef]
27. Poli, E.; Ouk, T.S.; Barrière, G.; Lévèque, G.; Sol, V.; Denes, E. Does low hydroxyl group surface density explain less bacterial adhesion on porous alumina? *Orthop. Traumatol. Surg. Res.* **2019**, *105*, 473–477. [CrossRef]
28. Beyle, A. Physical and Biochemical Risk Phenomena in Nanotechnology. In *Nanotechnolgy Safety*; Elsevier: Amsterdam, The Netherlands, 2013; pp. 219–231.
29. Zannotti, M.; Giovannetti, R.; Minofar, B.; Řeha, D.; Plačková, L.; D'Amato, C.A.; Rommozzi, E.; Dudko, H.V.; Kari, N.; Minicucci, M. Aggregation and metal-complexation behaviour of THPP porphyrin in ethanol/water solutions as function of pH. *Spectrochim. Acta Part A Mol. Biomol. Spectrosc.* **2018**, *193*, 235–248. [CrossRef]
30. Leroy-Lhez, S.; Rezazgui, O.; Issawi, M.; Elhabiri, M.; Calliste, C.A.; Riou, C. Why are the anionic porphyrins so efficient to induce plant cell death? A structure-activity relationship study to solve the puzzle. *J. Photochem. Photobiol. A Chem.* **2019**, *368*, 276–289. [CrossRef]
31. Marchand, G.; Fabre, G.; Maldonado-Carmona, N.; Villandier, N.; Leroy-Lhez, S. Acetylated lignin nanoparticles as a possible vehicle for photosensitizing molecules. *Nanoscale Adv.* **2020**, *2*, 5648–5658. [CrossRef]
32. Maldonado-Carmona, N.; Ouk, T.-S.S.; Calvete, M.J.F.F.; Pereira, M.M.; Villandier, N.; Leroy-Lhez, S. Conjugating biomaterials with photosensitizers: Advances and perspectives for photodynamic antimicrobial chemotherapy. *Photochem. Photobiol. Sci.* **2020**, *19*, 445–461. [CrossRef]
33. Pineiro, M.; Carvalho, A.L.; Pereira, M.M.; Gonsalves, A.D.; Arnaut, L.G.; Formosinho, S.J. Photoacoustic Measurements of Porphyrin Triplet-State Quantum Yields and Singlet-Oxygen Efficiencies. *Chem. A Eur. J.* **1998**, *4*, 2299–2307. [CrossRef]
34. Callaghan, S.; Senge, M.O. The good, the bad, and the ugly—Controlling singlet oxygen through design of photosensitizers and delivery systems for photodynamic therapy. *Photochem. Photobiol. Sci.* **2018**, *17*, 1490–1514. [CrossRef]
35. Riou, C.; Calliste, C.A.; Da Silva, A.; Guillaumot, D.; Rezazgui, O.; Sol, V.; Leroy-Lhez, S. Anionic porphyrin as a new powerful cell death inducer of Tobacco Bright Yellow-2 cells. *Photochem. Photobiol. Sci.* **2014**, *13*, 621. [CrossRef] [PubMed]
36. Schmidt, R.; Tanielian, C.; Dunsbach, R.; Wolff, C. Phenalenone, a universal reference compound for the determination of quantum yields of singlet oxygen O2(1Δg) sensitization. *J. Photochem. Photobiol. A Chem.* **1994**, *79*, 11–17. [CrossRef]

37. Ormond, A.B.; Freeman, H.S. Effects of substituents on the photophysical properties of symmetrical porphyrins. *Dyes Pigments* **2013**, *96*, 440–448. [CrossRef]
38. Caminos, D.A.; Spesia, M.B.; Durantini, E.N. Photodynamic inactivation of Escherichia coli by novel meso-substituted porphyrins by 4-(3-*N*,*N*,*N*-trimethylammoniumpropoxy)phenyl and 4-(trifluoromethyl)phenyl groups. *Photochem. Photobiol. Sci.* **2006**, *5*, 56–65. [CrossRef]
39. Nardi, G.; Manet, I.; Monti, S.; Miranda, M.A.; Lhiaubet-Vallet, V. Scope and limitations of the TEMPO/EPR method for singlet oxygen detection: The misleading role of electron transfer. *Free Radic. Biol. Med.* **2014**, *77*, 64–70. [CrossRef] [PubMed]
40. Marchand, G.; Calliste, C.A.; Williams, R.M.; McLure, C.; Leroy-Lhez, S.; Villandier, N. Acetylated Lignins: A Potential Bio-Sourced Photosensitizer. *Chem. Select.* **2018**, *3*, 5512–5516. [CrossRef]
41. Figueiredo, P.; Ferro, C.; Kemell, M.; Liu, Z.; Kiriazis, A.; Lintinen, K.; Florindo, H.F.; Yli-Kauhaluoma, J.; Hirvonen, J.; Kostiainen, M.A.; et al. Functionalization of carboxylated lignin nanoparticles for targeted and pH-responsive delivery of anti-cancer drugs. *Nanomedicine* **2017**, *12*, 2581–2596. [CrossRef] [PubMed]
42. Figueiredo, P.; Lintinen, K.; Kiriazis, A.; Hynninen, V.; Liu, Z.; Bauleth-Ramos, T.; Rahikkala, A.; Correia, A.; Kohout, T.; Sarmento, B.; et al. In vitro evaluation of biodegradable lignin-based nanoparticles for drug delivery and enhanced antiproliferation effect in cancer cells. *Biomaterials* **2017**, *121*, 97–108. [CrossRef]
43. Zhao, J.; Zheng, D.; Tao, Y.; Li, Y.; Wang, L.; Liu, J.; He, J.; Lei, J. Self-assembled pH-responsive polymeric nanoparticles based on lignin-histidine conjugate with small particle size for efficient delivery of anti-tumor drugs. *Biochem. Eng. J.* **2020**, *156*, 107526. [CrossRef]
44. Cui, J.-G.; Mo, D.-M.; Jiang, Y.; Gan, C.-F.; Li, W.-G.; Wu, A.; Li, X.-Y.; Xiao, J.-A.; Hu, Q.; Yuan, H.-Y.; et al. Fabrication, Characterization, and Insecticidal Activity Evaluation of Emamectin Benzoate–Sodium Lignosulfonate Nanoformulation with pH-Responsivity. *Ind. Eng. Chem. Res.* **2019**, *58*, 19741–19751. [CrossRef]
45. Godard, J.; Chapron, D.; Bregier, F.; Rosilio, V.; Sol, V. Synthesis and supramolecular arrangement of new stearoyl acid-based phenalenone derivatives. *Colloids Surf. A Physicochem. Eng. Asp.* **2021**, *612*, 125988. [CrossRef]
46. Vatansever, F.; de Melo, W.C.M.A.; Avci, P.; Vecchio, D.; Sadasivam, M.; Gupta, A.; Chandran, R.; Karimi, M.; Parizotto, N.A.; Yin, R.; et al. Antimicrobial strategies centered around reactive oxygen species—Bactericidal antibiotics, photodynamic therapy, and beyond. *FEMS Microbiol. Rev.* **2013**, *37*, 955–989. [CrossRef] [PubMed]
47. Le Guern, F.; Ouk, T.-S.; Yerzhan, I.; Nurlykyz, Y.; Arnoux, P.; Frochot, C.; Leroy-Lhez, S.; Sol, V. Photophysical and Bactericidal Properties of Pyridinium and Imidazolium Porphyrins for Photodynamic Antimicrobial Chemotherapy. *Molecules* **2021**, *26*, 1122. [CrossRef] [PubMed]
48. Li, Y.; Fu, Q.; Yu, S.; Yan, M.; Berglund, L. Optically Transparent Wood from a Nanoporous Cellulosic Template: Combining Functional and Structural Performance. *Biomacromolecules* **2016**, *17*, 1358–1364. [CrossRef] [PubMed]

Supplementary Data

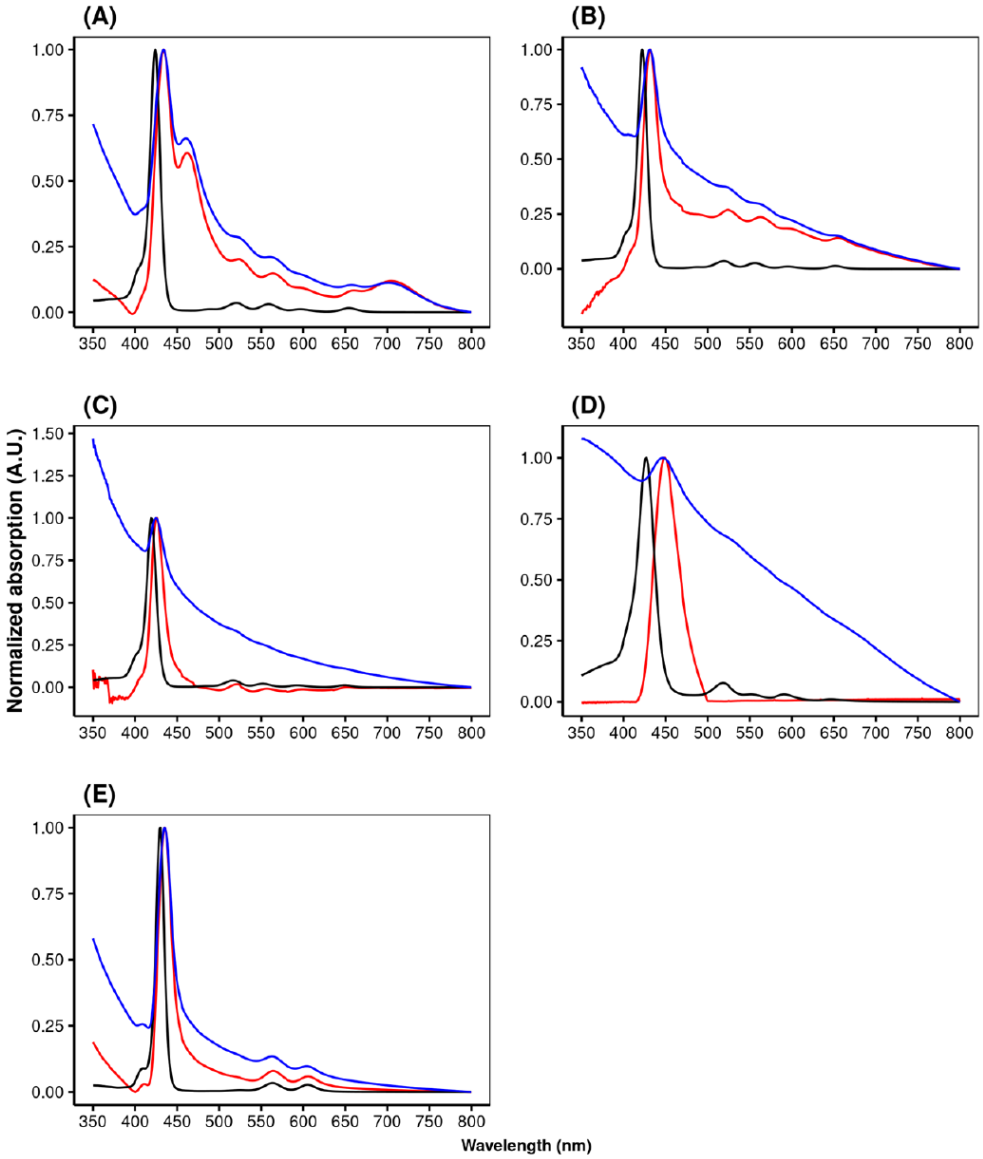

Supplementary Figure S1. Comparison of the spectra of (A) **THPP**, (B) **T(MAP)PP**, (C) **T(OAc)PP**, (D) **T(PrOH)PyP** and (E) **ZnTHPP** as free porphyrins (black), or as the encapsulated porphyrins before (blue) and after (red) the correction of the baseline.

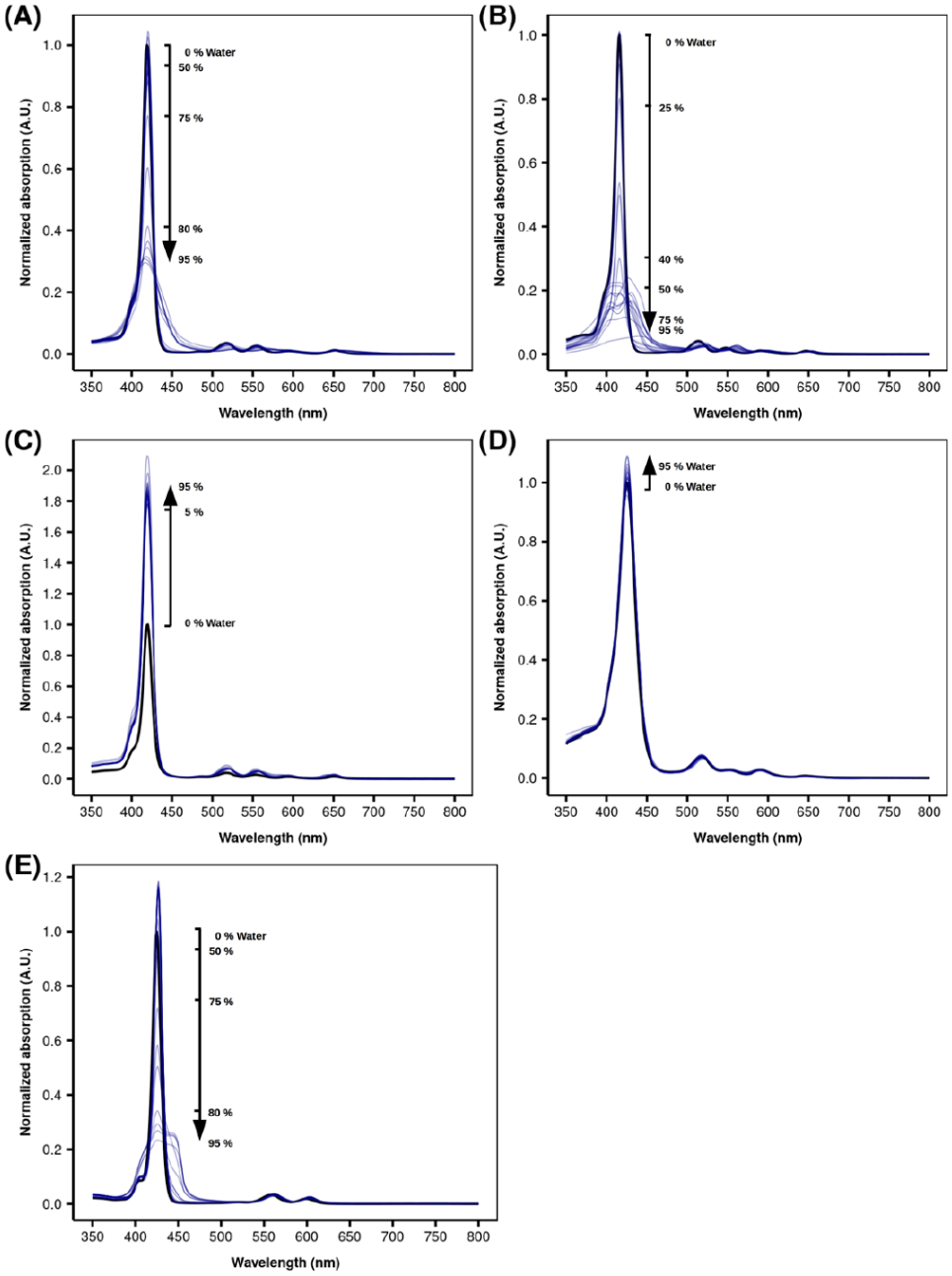

Supplementary Figure S2. Spectra of (A) **THPP**, (B) **T(OAc)PP**, (C) **T(MAP)PP**, (D) **T(PrOH)PyP**, and (E) **ZnTHPP** upon water addition. Porphyrins were initially dissolved in (A) acetone, (B) acetone:DMF 9:1, (C) acetone:DMSO 9:1, (D) acetone:DMSO 9:1, and (E) THF, at a concentration of 5 µM (black line), through increasing water addition.

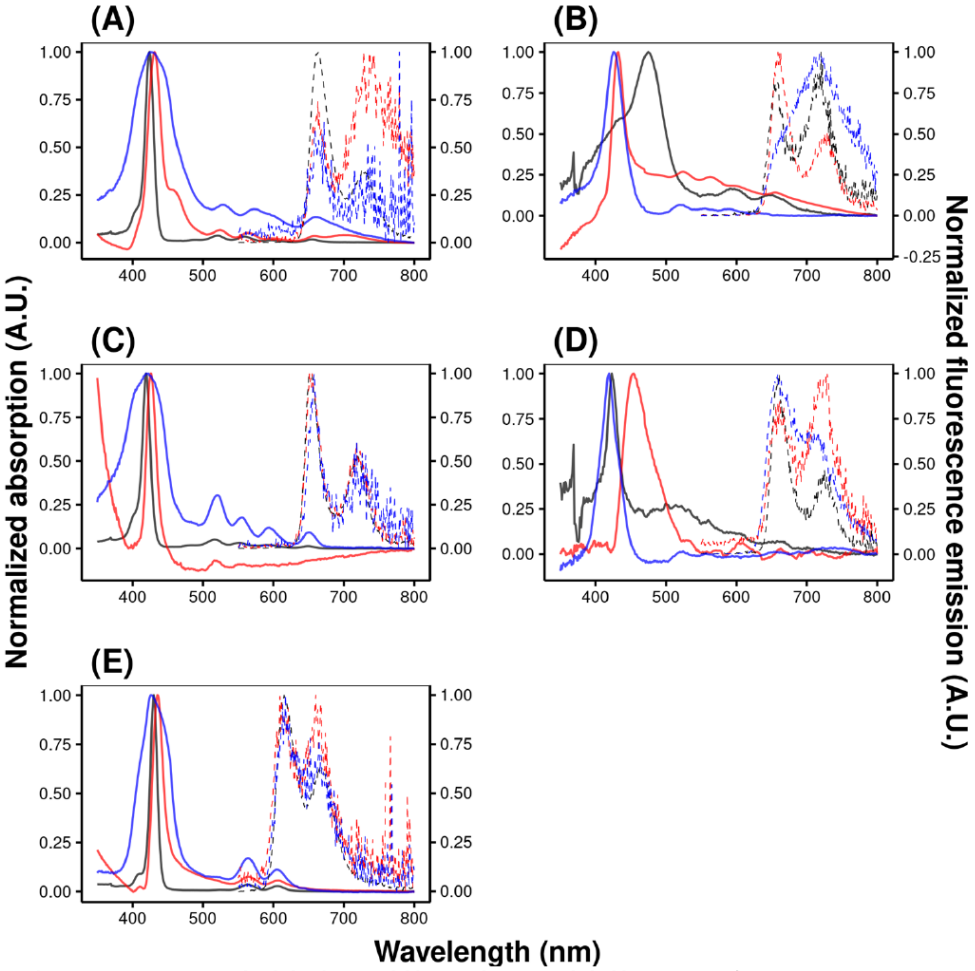

Supplementary Figure S3. Normalized absorbance (solid lines) and emission (dashed lines) spectra of (A) **THPP**, (B) **T(MAP)PP**, (C) **T(OAc)PP**, (D) **T(PrOH)PyP** and (E) **ZnTHPP**, dissolved in DMF (black), in PB pH 7, 0.5% DMF (blue), or as encapsulated porphyrins (red). Emission spectra were collected from a solution at 0.5 µM, at 25 ºC, with excitation at 425 nm.

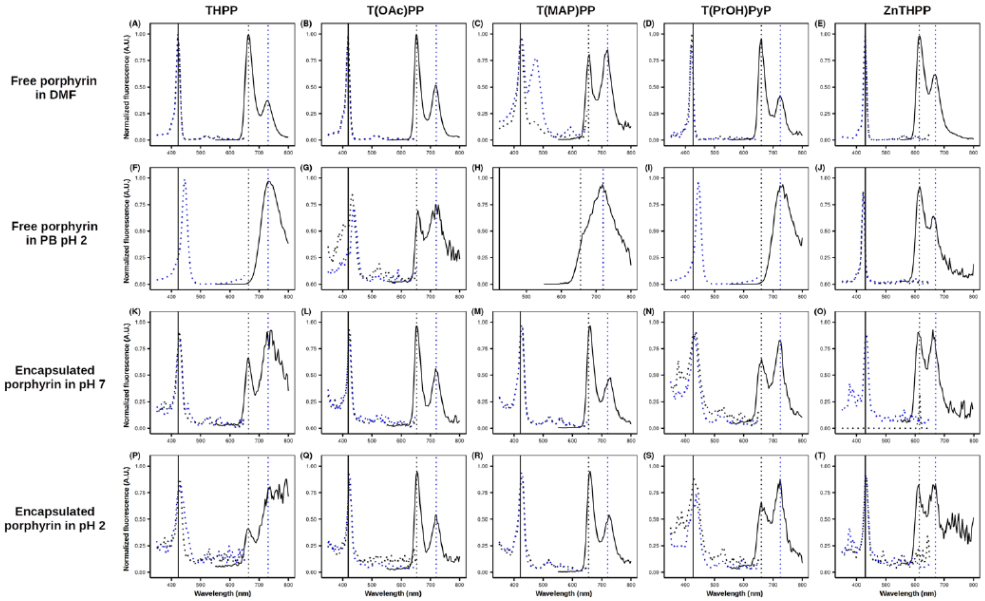

Supplementary Figure S4. Fluorescence emission (black solid lines) and excitation (black and blue dashed lines) spectra of the free porphyrins in DMF (A, B, C, D, E) or in aqueous buffer at pH 2 (F, G, H, I, J); or as encapsulated porphyrins suspended in pH 7 (K, L, M, N, O) or in pH 2 (P, Q, R, S, T). The black horizontal line indicates the wavelength of the Soret band of each porphyrin in DMF, while the dashed horizontal lines, indicate the peak of the emission bands of each porphyrin in DMF, indicating as well the emission wavelength monitored in the excitation spectra. Emission spectra were after excitation at 425 nm; all spectra were measured at 25 ºC, from a solution 0.5 µM of the corresponding porphyrin.

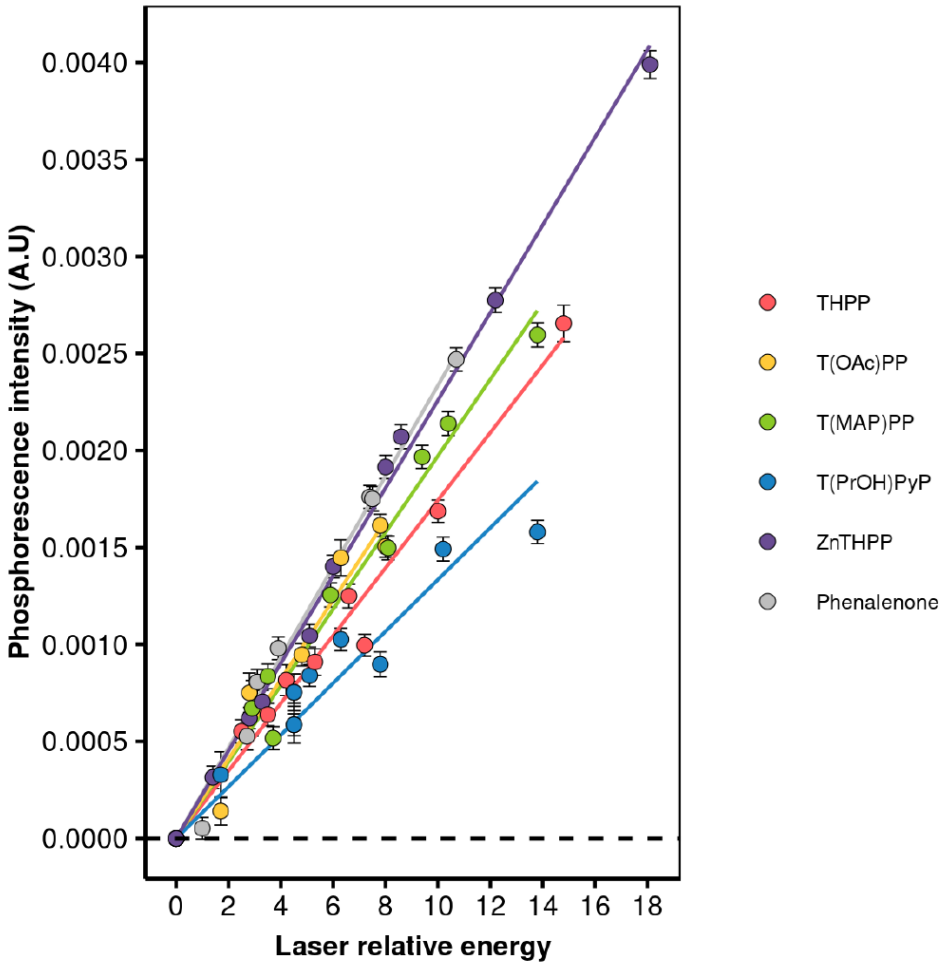

Supplementary Figure S5. Slopes of the decay of singlet oxygen phosphorescence, detected at 1270 nm, measured through near infrared spectroscopy, as a function of laser energy. Porphyrins were dissolved in DMF, with an absorption of around 0.18 at 355 nm, the excitation wavelength. Phenalenone in DMF was used as a standard ($\Phi_\Delta = 1$).

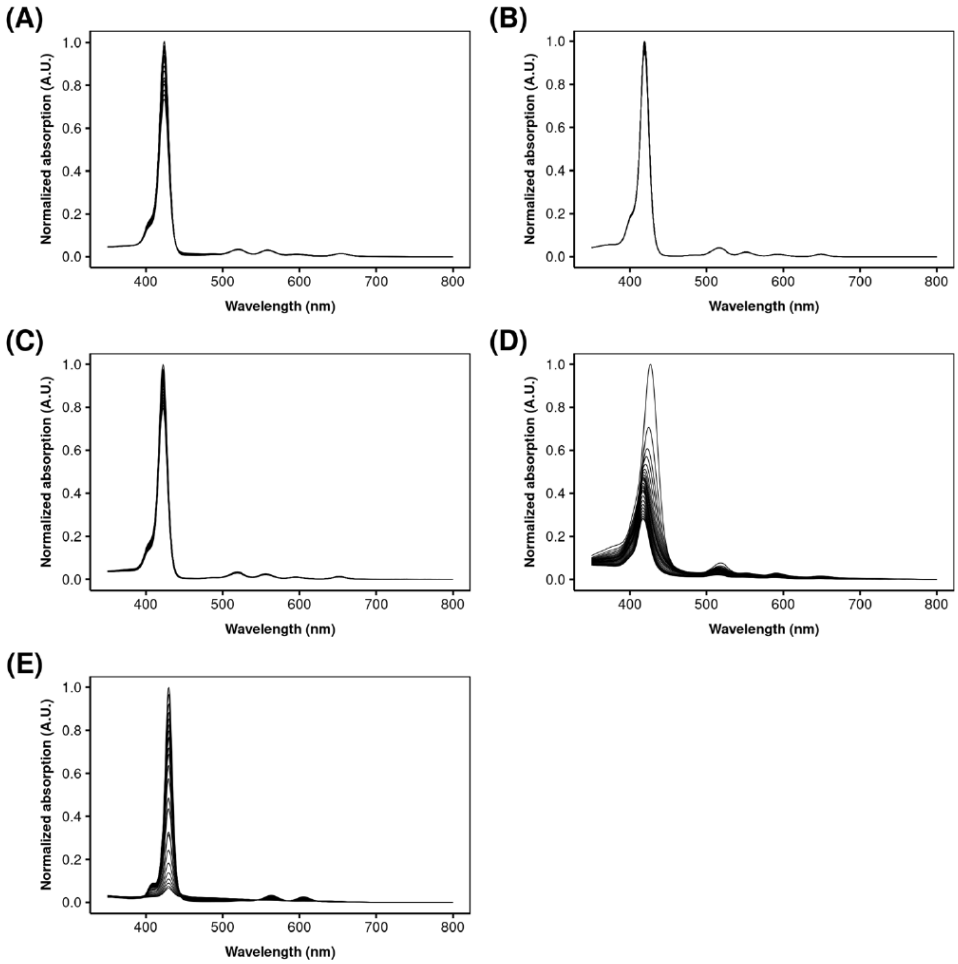

Supplementary Figure S6. Absorption spectra of free porphyrins (A) **THPP**, (B) **T(OAc)PP**, (C) **T(MAP)PP**, (D) **T(PrOH)PyP** and (E) **ZnTHPP**, after irradiation under blue LED light (100 mW/cm^2). Porphyrins were dissolved in DMF, 5 µM, with constant stirring on an open quartz cell. Shown spectra are the average of two individual experiments.

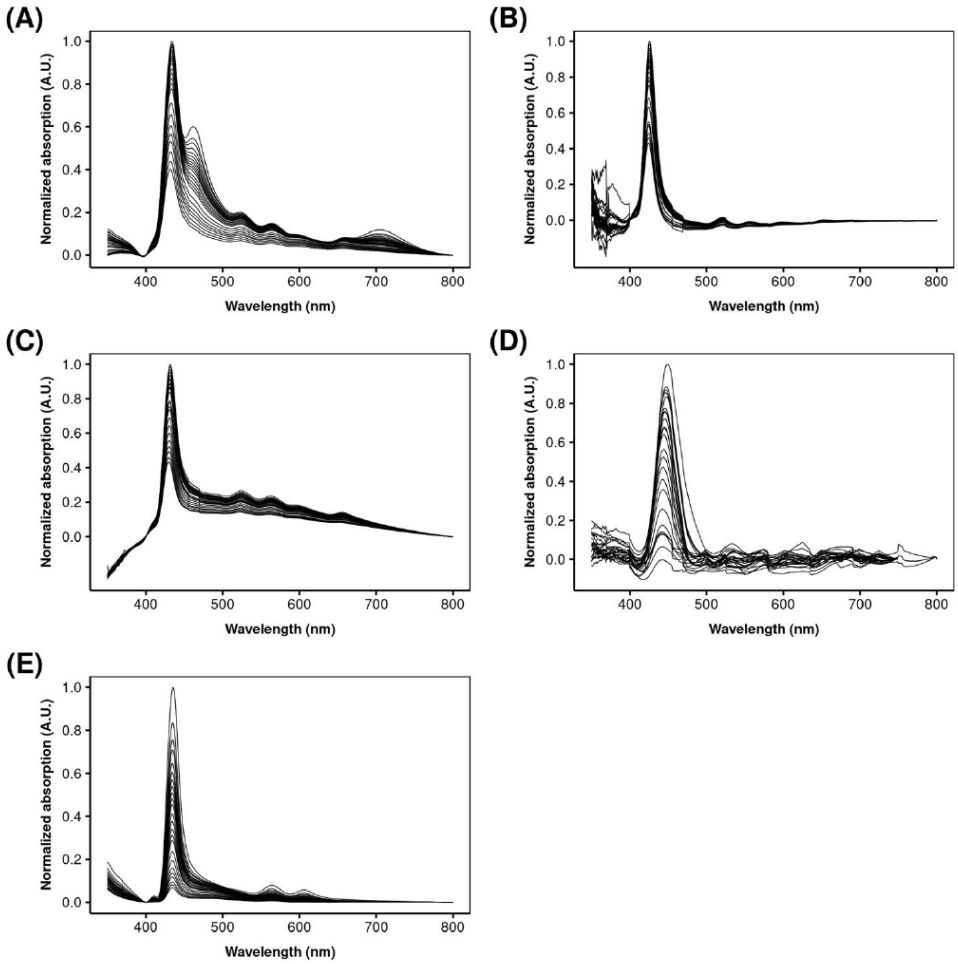

Supplementary Figure S7. Absorption spectra of encapsulated porphyrins (A) **THPP@AcLi**, (B) **T(OAc)PP@AcLi**, (C) **T(MAP)PP@AcLi**, (D) **T(PrOH)PyP@AcLi** and (E) **ZnTHPP@AcLi**, after irradiation under blue LED light (100 mW/cm^2). Nanoparticles were suspended in PB pH 7, at 5 µM of their corresponding porphyrin, with constant stirring on an open quartz cell. Shown spectra are the average of two individual experiments.

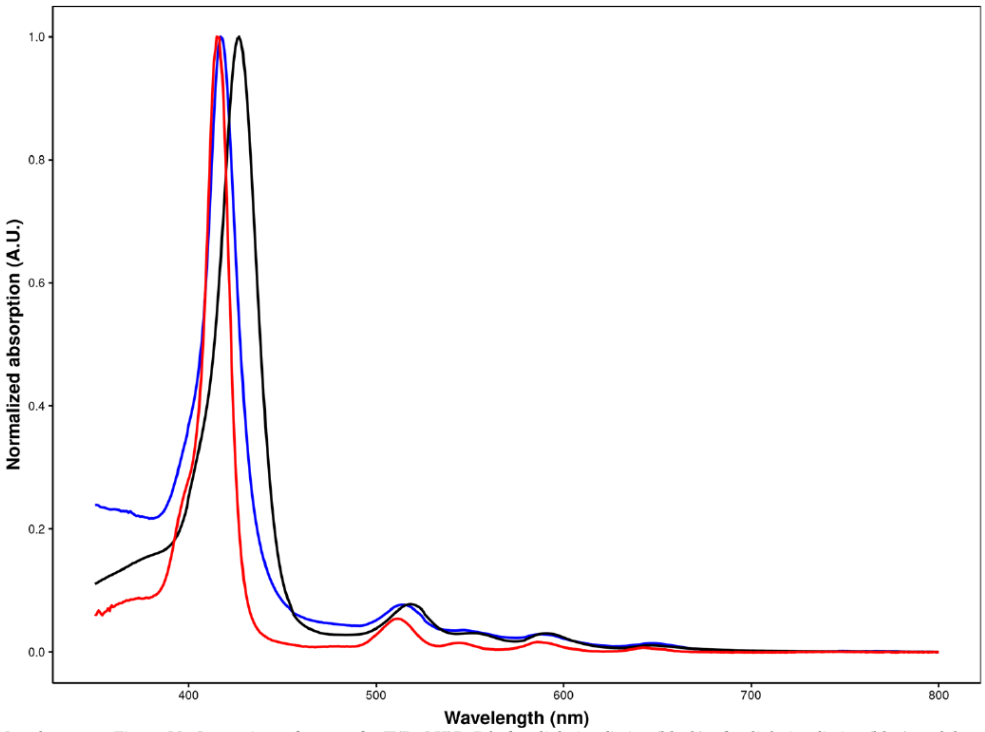

Supplementary Figure S8. Comparison of spectra for **T(PrOH)PyP** before light irradiation (black), after light irradiation (blue), and the raw porphyrin, THPyP in DMF (red).

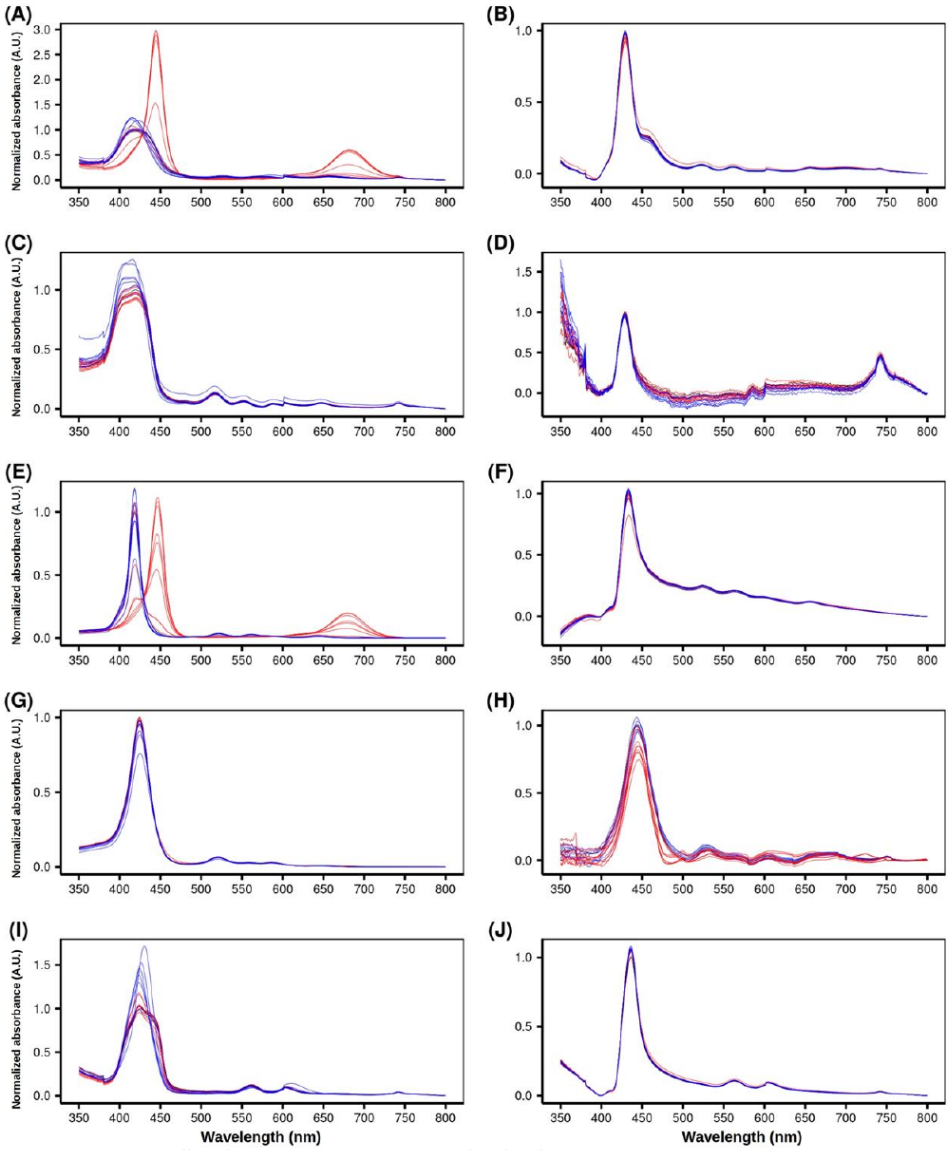

Supplementary Figure S9. Effect of pH on the UV-vis absorbance profile of the free porphyrins (A) **THPP**, (C) **T(OAc)PP**, (E) **T(MAP)PP**, (G) **T(PrOH)PyP**, (I) **ZnTHPP**, or as encapsulated porphyrins (B) **THPP@AcLi**, (D) **T(OAc)PP@AcLi**, (F) **T(MAP)PP@AcLi**, (H) **T(PrOH)PyP@AcLi**, (J) **ZnTHPP@AcLi**. Red lines represent the pH below 7, while blue lines represent the pH above 7. Both free and encapsulated porphyrins were set in a final concentration of 5 µM of their corresponding porphyrin, in an adequate aqueous buffer. Free porphyrins were dissolved in DMF and diluted into an aqueous buffer, for a final DMF concentration of 5%.

Supplementary Table S1. Free porphyrin observed at initial and final observation times, expressed as percent of free porphyrin, with respect to the global amount of encapsulated porphyrins (20 µM). Similar superscript letters indicate the pairs that have differences with a statistical significance, found as $P < 0.05$ with a Two-way ANOVA, and a multiple comparisons Tukey's test.

Porphyrin	pH 3		pH 7	
	0 hours	96 hours	0 hours	96 hours
THPP	1.67 ± 0.63^{a}	1.11 ± 0.17	7.23 ± 0.73^{a}	2.81 ± 0.16
T(OAc)PP	16.82 ± 0.02	7.58 ± 0.49	10.32 ± 5.30	9.00 ± 0.75
T(MAP)PP	9.38 ± 1.96^{b}	$16.4 \pm 0.55^{b,c}$	5.07 ± 4.94	0.97 ± 0.32^{c}
T(PrOH)PyP	3.25 ± 0.87	3.22 ± 0.17	3.46 ± 1.12	2.07 ± 0.21
ZnTHPP	1.76 ± 0.04^{d}	1.09 ± 0.50	$11.86 \pm 3.34^{d,e}$	2.56 ± 0.47^{e}

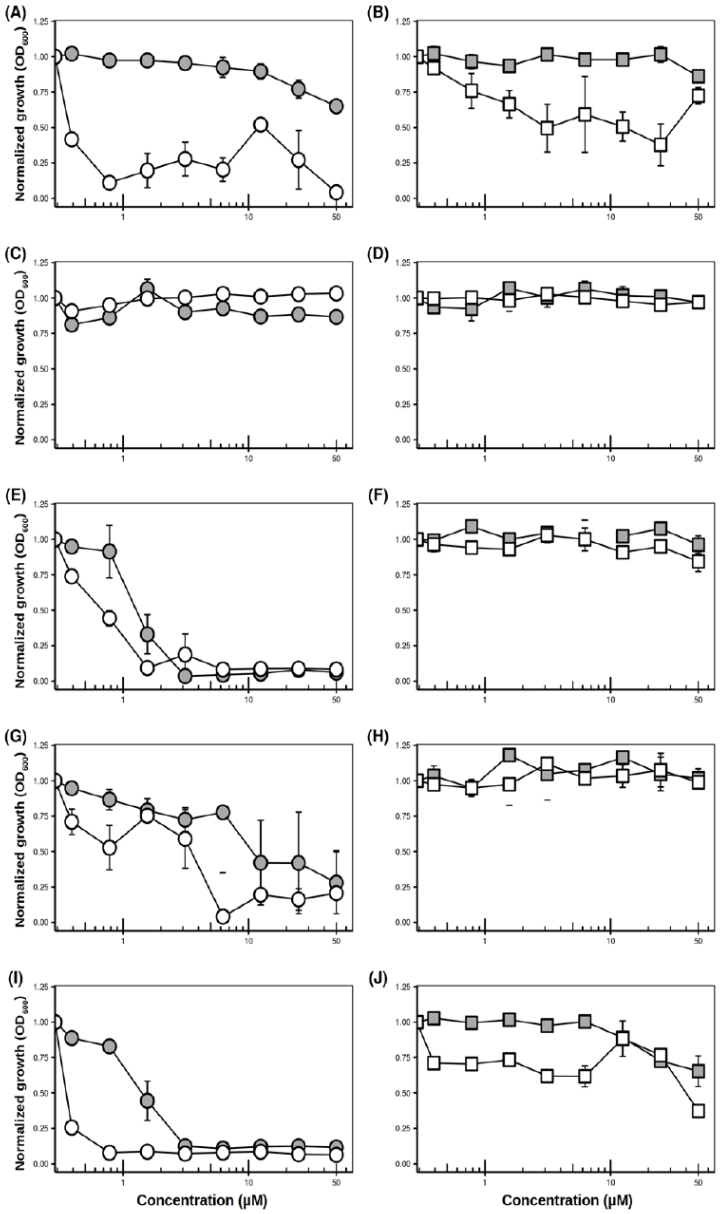

Supplementary Figure S10. Growth inhibition of *Staphylococcus aureus*, after treatment with (A) **THPP**, (B) **THPP@AcLi**, (C) **T(OAc)PP**, (D) **T(OAc)PP@AcLi**, (E) **T(MAP)PP**, (F) **T(MAP)PP@AcLi**, (G) **T(PrOH)PyP**, (H) **T(PrOH)PyP@AcLi**, (I) **ZnTHPP** and (J) **ZnTHPP@AcLi**. Bacteria were incubated for 30 minutes and then irradiated with blue-LED light (15 J/cm^2, white symbols) or incubated in the dark (grey symbols). Afterwards, culture medium was added and bacteria were incubated at 37 ººC, in the dark for 16 hours. Results shown are the average of three independent experiments.

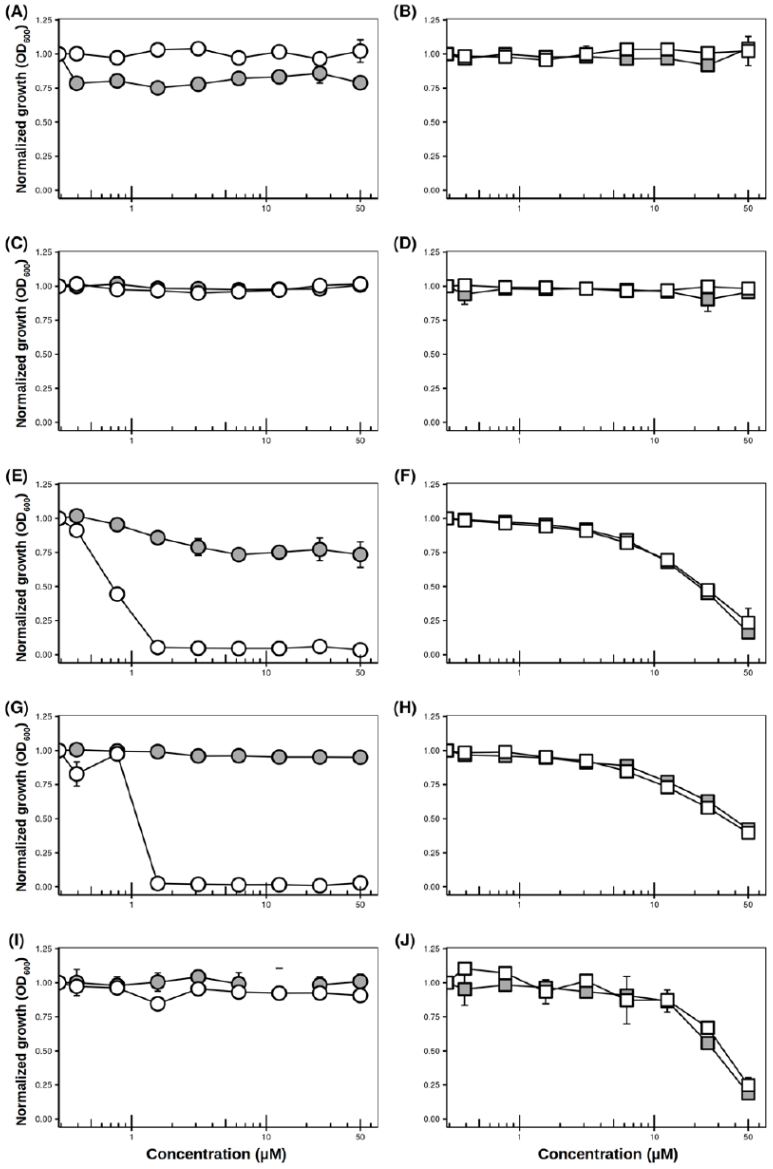

Supplementary Figure S11. Growth inhibition of *Escherichia coli*, after treatment with (A) **THPP**, (B) **THPP@AcLi**, (C) **T(OAc)PP**, (D) **T(OAc)PP@AcLi**, (E) **T(MAP)PP**, (F) **T(MAP)PP@AcLi**, (G) **T(PrOH)PyP**, (H) **T(PrOH)PyP@AcLi**, (I) **ZnTHPP** and (J) **ZnTHPP@AcLi**. Bacteria were incubated for 30 minutes and then irradiated with blue-LED light (15 J/cm^2, white symbols) or incubated in the dark (grey symbols). Afterwards, culture medium was added and bacteria were incubated at 37 °°C, in the dark for 16 hours. Results shown are the average of three independent experiments.

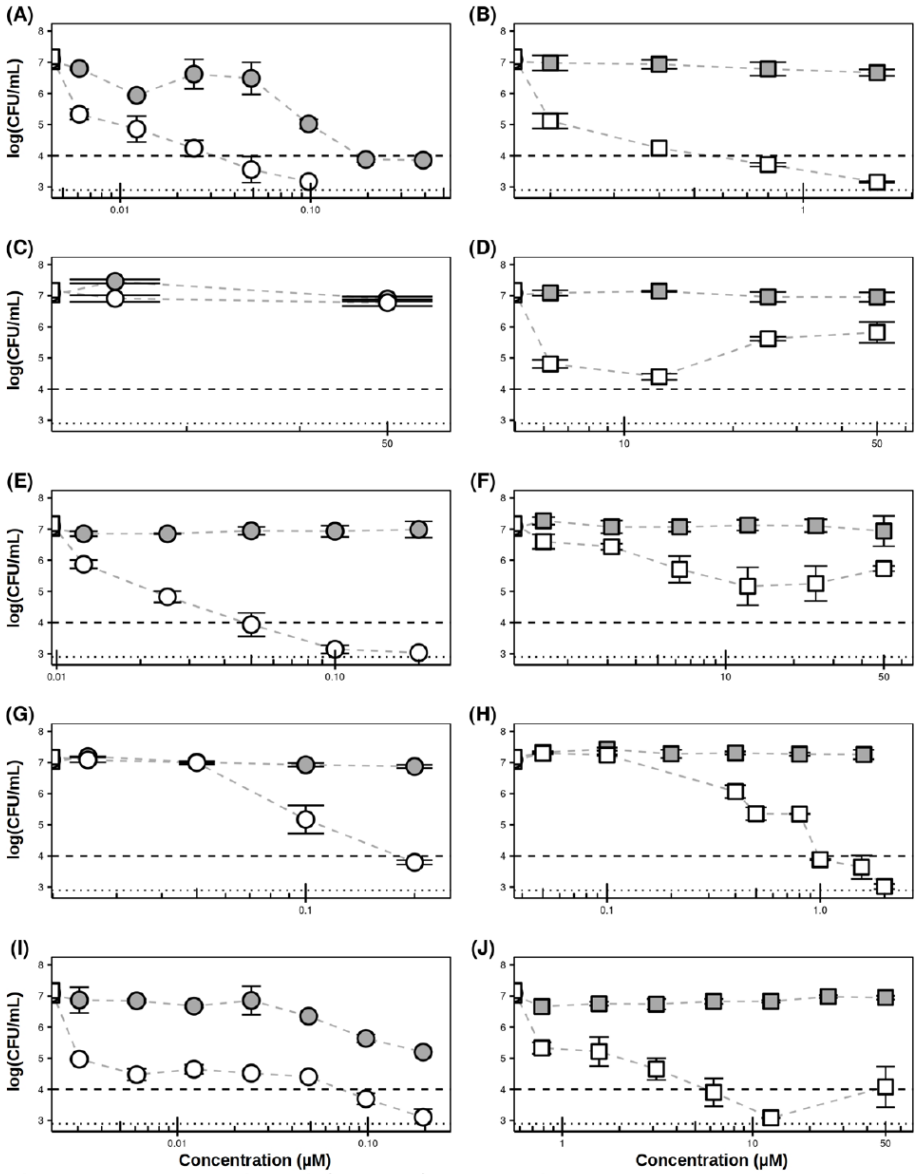

Supplementary Figure S12. Bacterial survival of *S. aureus*, after treatment with (A) **THPP**, (B) **THPP@AcLi**, (C) **T(OAc)PP**, (D) **T(OAc)PP@AcLi**, (E) **T(MAP)PP**, (F) **T(MAP)PP@AcLi**, (G) **T(PrOH)PyP**, (H) **T(PrOH)PyP@AcLi**, (I) **ZnTHPP** and (J) **ZnTHPP@AcLi**. Bacteria were incubated for 30 minutes and then irradiated with blue-LED light (15 J/cm^2, white symbols) or incubated in the dark (grey symbols). Afterwards, bacteria were diluted and plated in petri dishes, which were incubated in the dark 16 hours, before counting colonies. The dotted line indicates the limit of quantification (2.9 log), while the dashed line indicates a diminish of at least 3 log.

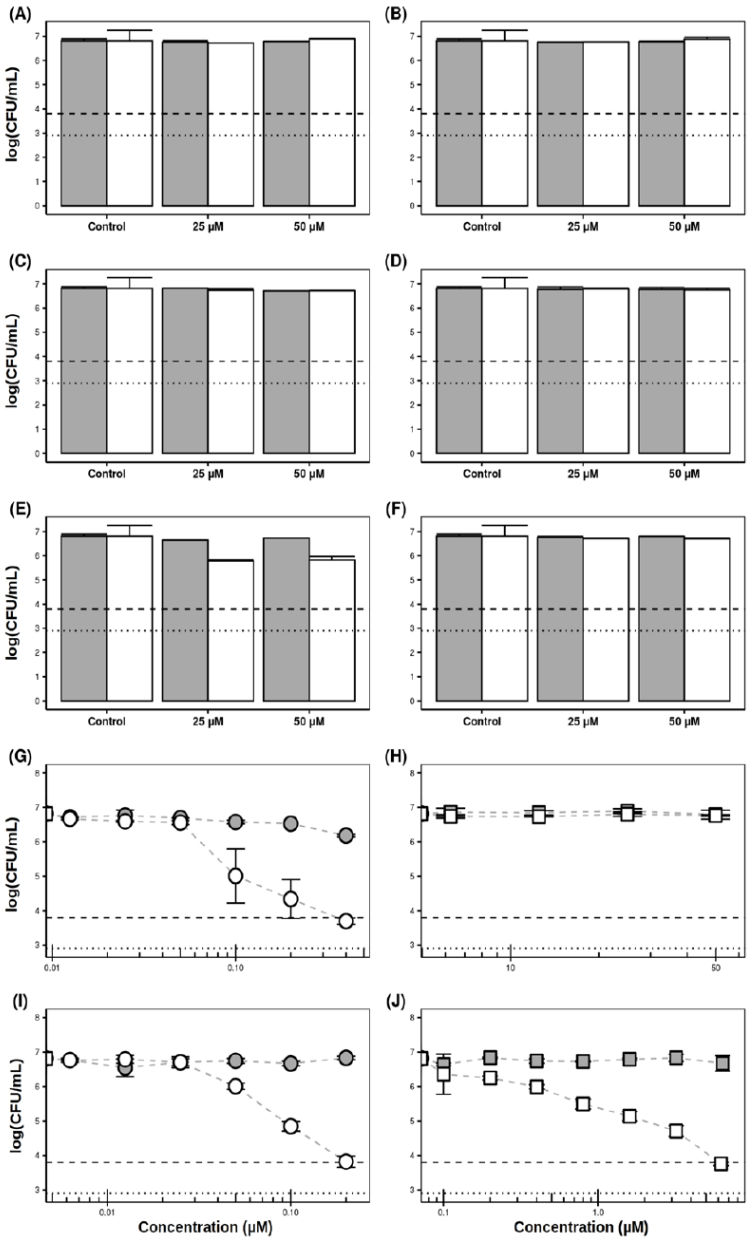

Supplementary Figure S13. Bacterial survival of *E. coli*, after treatment with (A) **THPP**, (B) **THPP@AcLi**, (C) **T(OAc)PP**, (D) **T(OAc)PP@AcLi**, (E) **T(MAP)PP**, (F) **T(MAP)PP@AcLi**, (G) **T(PrOH)PyP**, (H) **T(PrOH)PyP@AcLi**, (I) **ZnTHPP** and (J) **ZnTHPP@AcLi**. Bacteria were incubated for 30 minutes and then irradiated with blue-LED light (15 J/cm^2, white symbols) or incubated in the dark (grey symbols). Afterwards, bacteria were diluted and plated in petri dishes, which were incubated in the dark 16 hours, before counting colonies. The dotted line indicates the limit of quantification (2.9 log), while the dashed line indicates a diminish of at least 3 log.

Page intentionally left in blank

General Conclusions and Perspectives

The exhausted pipeline of antibiotic drugs waiting for FDA approval is a concern that has been aggravated by the COVID-19 pandemic, a reminder that microorganisms can shape the future of mankind. This urgent need of antibacterial alternatives has promoted the use of alternative therapies, as PACT. In this work, it was intended to create an alternative for bacterial disinfection, while increasing the value of a biosourced polymer, as lignin.

Then, along this project, we were able to prepare acetylated lignin nanoparticles and load them with a porphyrinic compound. These nanoparticles were fully characterized and it was demonstrated that they were able to transport the porphyrin in aqueous solvent, preserving the porphyrin's photochemical properties. The obtained nanoparticles were able to efficiently disinfect Gram-positive bacteria, while the disinfection of Gram-negative bacteria was only achieved when the nanoparticles were loaded with a cationic porphyrin. Remarkably, only one of the candidate cationic porphyrins was able to achieve *E. coli* eradication.

This work has thoroughly described this novel delivery system, while also demonstrating its universality towards porphyrinic compounds. Although there are some hints that this system could also be used for other kinds of photosensitizers (i.e., chlorins, BODIPY, phenalenone derivatives, curcumin, hypericin), this was left unexplored. Also, this work was only able to explore one modification of lignin, while other modifications of lignin, and its effects on the photosensitizer's photophysical properties and its interaction with bacteria, is still left to be explored. Finally, although we were able to demonstrate the efficiency of our system towards model bacteria, its efficiency towards multi-drug resistant bacteria is to be analyzed.

Then, this work could be the first step for designing better lignin-based photosensitizers vehicles, while modifying lignin to achieve better interaction with bacteria, and preserving the photophysical properties of the photosensitizers. Then, the implemented methodologies and analysis that were thoroughly used along this work could settle the bases for future research.

References

1. World Health Organization Global antimicrobial resistance surveillance system (GLASS) report: early implementation 2020. Available online: https://apps.who.int/iris/bitstream/handle/10665/332081/9789240005587-eng.pdf.
2. O'Neill Commission; O'Neill Commission Tackling Drug-Resistant Infections Globally: Final Report and Recommendations the Review on Antimicrobial Resistance Chaired By Jim O'Neill. **2016**.
3. Bartoloni, A.; Pallecchi, L.; Rodríguez, H.; Fernandez, C.; Mantella, A.; Bartalesi, F.; Strohmeyer, M.; Kristiansson, C.; Gotuzzo, E.; Paradisi, F.; et al. Antibiotic resistance in a very remote Amazonas community. *Int. J. Antimicrob. Agents* **2009**, *33*, 125–129, doi:10.1016/j.ijantimicag.2008.07.029.
4. McCann, C.M.; Christgen, B.; Roberts, J.A.; Su, J.-Q.; Arnold, K.E.; Gray, N.D.; Zhu, Y.-G.; Graham, D.W. Understanding drivers of antibiotic resistance genes in High Arctic soil ecosystems. *Environ. Int.* **2019**, *125*, 497–504, doi:10.1016/j.envint.2019.01.034.
5. Wang, R.; van Dorp, L.; Shaw, L.P.; Bradley, P.; Wang, Q.; Wang, X.; Jin, L.; Zhang, Q.; Liu, Y.; Rieux, A.; et al. The global distribution and spread of the mobilized colistin resistance gene mcr-1. *Nat. Commun.* **2018**, *9*, 1179, doi:10.1038/s41467-018-03205-z.
6. The PEW Charitable Trusts Antibiotics Currently in Global Clinical Development Available online: https://www.pewtrusts.org/en/research-and-analysis/data-visualizations/2014/antibiotics-currently-in-clinical-development (accessed on Mar 23, 2021).
7. Belete, T.M. Novel targets to develop new antibacterial agents and novel alternatives to antibacterial agents. *Hum. Microbiome J.* **2019**, *11*, 100052, doi:10.1016/j.humic.2019.01.001.
8. Donohoe, C.; Senge, M.O.; Arnaut, L.G.; Gomes-da-Silva, L.C. Cell death in photodynamic therapy: From oxidative stress to anti-tumor immunity. *Biochim. Biophys. Acta - Rev. Cancer* **2019**, *1872*, 188308, doi:10.1016/j.bbcan.2019.07.003.
9. Simões, J.C.S.; Sarpaki, S.; Papadimitroulas, P.; Therrien, B.; Loudos, G. Conjugated Photosensitizers for Imaging and PDT in Cancer Research. *J. Med. Chem.* **2020**, *63*, 14119–14150, doi:10.1021/acs.jmedchem.0c00047.
10. Gallardo-Villagrán, M.; Leger, D.Y.; Liagre, B.; Therrien, B. Photosensitizers used in the photodynamic therapy of rheumatoid arthritis. *Int. J. Mol. Sci.* **2019**, *20*, doi:10.3390/ijms20133339.
11. Khaldi, Z.; Nzambe Takeki, J.K.; Ouk, T.-S.; Lucas, R.; Zerrouki, R. Synthesis and photo-bactericidal properties of a cationic porphyrin grafted onto kraft pulp fibers. *J. Porphyr. Phthalocyanines* **2019**, *23*, 489–496, doi:10.1142/S1088424619500330.

12. Maldonado Alvarado, E.; Osorio Peralta, M.O.; Moreno Vázquez, A.; Martínez Guzmán, A.; Melo Petrone, M.E.; Enriquez Mar, Z.I.; Jovel Galdamez, D.E.; Carrión Solana, B.; Balderas Martínez, G.; Parra, E.; et al. Effectiveness of Photodynamic Therapy in Elimination of HPV-16 and HPV-18 Associated with CIN I in Mexican Women. *Photochem. Photobiol.* **2017**, *93*, 1269–1275, doi:0.1111/php.12769.

13. Güzel Tunccan, Ö.; Kalkanci, A.; Unal, E.A.; Abdulmajed, O.; Erdoğan, M.; Dizbay, M.; Çaglar, K. The in vitro effect of antimicrobial photodynamic therapy on Candida and Staphylococcus biofilms. *Turkish J. Med. Sci.* **2018**, *48*, 873–879, doi:10.3906/sag-1803-44.

14. Akilov, O.E.; Kosaka, S.; O'Riordan, K.; Hasan, T. Photodynamic therapy for cutaneous leishmaniasis: The effectiveness of topical phenothiaziniums in parasite eradication and Th1 immune response stimulation. *Photochem. Photobiol. Sci.* **2007**, *6*, 1067–1075, doi:10.1039/b703521g.

15. Jia, R.; Tian, W.; Bai, H.; Zhang, J.; Wang, S.; Zhang, J. Sunlight-Driven Wearable and Robust Antibacterial Coatings with Water-Soluble Cellulose-Based Photosensitizers. *Adv. Healthc. Mater.* **2019**, *8*, 1801591, doi:10.1002/adhm.201801591.

16. Pourhajibagher, M.; Chiniforush, N.; Monzavi, A.; Barikani, H.; Monzavi, M.M.; Sobhani, S.; Shahabi, S.; Bahador, A. Inhibitory Effects of Antimicrobial Photodynamic Therapy with Curcumin on Biofilm-Associated Gene Expression Profile of Aggregatibacter actinomycetemcomitans. *J. Dent. (Tehran).* **2018**, *15*, 169–177.

17. Josefsen, L.B.; Boyle, R.W. Photodynamic Therapy and the Development of Metal-Based Photosensitisers. *Met. Based. Drugs* **2008**, *2008*, 1–23, doi:10.1155/2008/276109.

18. Abrahamse, H.; Hamblin, M.R. New photosensitizers for photodynamic therapy. *Biochem. J.* **2016**, *473*, 347–364, doi:10.1042/BJ20150942.

19. Zannotti, M.; Giovannetti, R.; Minofar, B.; Řeha, D.; Plačková, L.; D'Amato, C.A.; Rommozzi, E.; Dudko, H. V.; Kari, N.; Minicucci, M. Aggregation and metal-complexation behaviour of THPP porphyrin in ethanol/water solutions as function of pH. *Spectrochim. Acta - Part A Mol. Biomol. Spectrosc.* **2018**, *193*, 235–248, doi:10.1016/j.saa.2017.12.021.

20. Gierlich, P.; Mata, A.I.; Donohoe, C.; Brito, R.M.M.; Senge, M.O.; Gomes-da-Silva, L.C. Ligand-Targeted Delivery of Photosensitizers for Cancer Treatment. *Molecules* **2020**, *25*, doi:10.3390/molecules25225317.

21. Q. Mesquita, M.; J. Dias, C.; P. M. S. Neves, M.; Almeida, A.; F. Faustino, M. Revisiting Current Photoactive Materials for Antimicrobial Photodynamic Therapy. *Molecules* **2018**, *23*, 2424, doi:10.3390/molecules23102424.

22. Jori, G.; Magaraggia, M.; Fabris, C.; Soncin, M.; Camerin, M.; Tallandini, L.; Coppellotti, O.; Guidolin, L. Photodynamic Inactivation of Microbial Pathogens: Disinfection of Water and Prevention of Water-Borne Diseases. *J. Environ. Pathol. Toxicol. Oncol.* **2011**, *30*, 261–271, doi:10.1615/JEnvironPatholToxicolOncol.v30.i3.90.

23. Alvarenga, V.O.; Brancini, G.T.P.; Silva, E.K.; da Pia, A.K.R.; Campagnollo, F.B.; Braga, G.Ú.L.; Hubinger, M.D.; Sant'Ana, A.S. Survival variability of 12 strains of Bacillus cereus yielded to spray drying of whole milk. *Int. J. Food Microbiol.* **2018**, *286*, 80–89, doi:10.1016/j.ijfoodmicro.2018.07.020.

24. Wang, J.; Wu, H.; Yang, Y.; Yan, R.; Zhao, Y.; Wang, Y.; Chen, A.; Shao, S.; Jiang, P.; Li, Y.Q. Bacterial species-identifiable magnetic nanosystems for early sepsis diagnosis and extracorporeal photodynamic blood disinfection. *Nanoscale* **2018**, *10*, 132–141, doi:10.1039/c7nr06373c.

25. Bulhões Portapilla, G.; Pereira, L.M.; Bronzon da Costa, C.M.; Voltarelli Providello, M.; Sampaio Oliveira, P.A.; Goulart, A.; Ferreira Anchieta, N.; Wainwright, M.; Leite Braga, G.Ú.; de Albuquerque, S. Phenothiazinium Dyes Are Active against Trypanosoma cruzi In Vitro. *Biomed Res. Int.* **2019**, *2019*, 1–9, doi:10.1155/2019/8301569.

26. Preis, E.; Baghdan, E.; Agel, M.R.; Anders, T.; Pourasghar, M.; Schneider, M.; Bakowsky, U. Spray dried curcumin loaded nanoparticles for antimicrobial photodynamic therapy. *Eur. J. Pharm. Biopharm.* **2019**, *142*, 531–539, doi:10.1016/j.ejpb.2019.07.023.

27. Buchovec, I.; Lukseviciute, V.; Marsalka, A.; Reklaitis, I.; Luksiene, Z. Effective photosensitization-based inactivation of Gram (−) food pathogens and molds using the chlorophyllin–chitosan complex: towards photoactive edible coatings to preserve strawberries. *Photochem. Photobiol. Sci.* **2016**, *15*, 506–516, doi:10.1039/C5PP00376H.

28. van Raamsdonk, L.W.D.; van der Zande, M.; Koelmans, A.A.; Hoogenboom, R.L.A.P.; Peters, R.J.B.; Groot, M.J.; Peijnenburg, A.A.C.M.; Weesepoel, Y.J.A. Current Insights into Monitoring, Bioaccumulation, and Potential Health Effects of Microplastics Present in the Food Chain. *Foods* **2020**, *9*, 72, doi:10.3390/foods9010072.

29. Ragusa, A.; Svelato, A.; Santacroce, C.; Catalano, P.; Notarstefano, V.; Carnevali, O.; Papa, F.; Rongioletti, M.C.A.; Baiocco, F.; Draghi, S.; et al. Plasticenta: First evidence of microplastics in human placenta. *Environ. Int.* **2021**, *146*, 106274, doi:10.1016/j.envint.2020.106274.

30. Patrício Silva, A.L.; Prata, J.C.; Walker, T.R.; Campos, D.; Duarte, A.C.; Soares, A.M.V.M.; Barcelò, D.; Rocha-Santos, T. Rethinking and optimising plastic waste management under COVID-19 pandemic: Policy solutions based on redesign and reduction of single-use plastics and personal protective equipment. *Sci. Total Environ.* **2020**, *742*, 140565, doi:10.1016/j.scitotenv.2020.140565.

31. Maldonado-Carmona, N.; Ouk, T.-S.S.; Calvete, M.J.F.F.; Pereira, M.M.; Villandier, N.; Leroy-Lhez, S. Conjugating biomaterials with photosensitizers: advances and perspectives for photodynamic antimicrobial chemotherapy. *Photochem. Photobiol. Sci.* **2020**, *19*, 445–461, doi:10.1039/c9pp00398c.

32. Marchand, G.; Calliste, C.A.; Williams, R.M.; McLure, C.; Leroy-Lhez, S.; Villandier, N. Acetylated Lignins: A Potential Bio-Sourced Photosensitizer. *ChemistrySelect* **2018**, *3*, 5512–5516, doi:10.1002/slct.201801039.

33. Calvo-Flores, F.G.; Dobado, J.A. Lignin as Renewable Raw Material. *ChemSusChem* **2010**, *3*, 1227–1235, doi:10.1002/cssc.201000157.

34. Sipponen, M.H.; Lange, H.; Crestini, C.; Henn, A.; Österberg, M. Lignin for Nano- and Microscaled Carrier Systems: Applications, Trends, and Challenges. *ChemSusChem* **2019**, *12*, 2038–2038, doi:10.1002/cssc.201901218.

35. Zhao, J.; Zheng, D.; Tao, Y.; Li, Y.; Wang, L.; Liu, J.; He, J.; Lei, J. Self-assembled pH-responsive polymeric nanoparticles based on lignin-histidine conjugate with small particle size for efficient delivery of anti-tumor drugs. *Biochem. Eng. J.* **2020**, *156*, 107526, doi:10.1016/j.bej.2020.107526.

36. Figueiredo, P.; Ferro, C.; Kemell, M.; Liu, Z.; Kiriazis, A.; Lintinen, K.; Florindo, H.F.; Yli-Kauhaluoma, J.; Hirvonen, J.; Kostiainen, M.A.; et al. Functionalization of carboxylated lignin nanoparticles for targeted and pH-responsive delivery of anticancer drugs. *Nanomedicine* **2017**, *12*, 2581–2596, doi:10.2217/nnm-2017-0219.

37. Yang, W.; Owczarek, J.S.; Fortunati, E.; Kozanecki, M.; Mazzaglia, A.; Balestra, G.M.; Kenny, J.M.; Torre, L.; Puglia, D. Antioxidant and antibacterial lignin nanoparticles in polyvinyl alcohol/chitosan films for active packaging. *Ind. Crops Prod.* **2016**, *94*, 800–811, doi:10.1016/j.indcrop.2016.09.061.

38. Wahlström, R.; Kalliola, A.; Heikkinen, J.; Kyllönen, H.; Tamminen, T. Lignin cationization with glycidyltrimethylammonium chloride aiming at water purification applications. *Ind. Crops Prod.* **2017**, *104*, 188–194, doi:10.1016/j.indcrop.2017.04.026.

39. Matsushita, Y.; Yasuda, S. Preparation of anion-exchange resins from pine sulfuric acid lignin, one of the acid hydrolysis lignins. *J. Wood Sci.* **2003**, *49*, 423–429, doi:10.1007/s10086-002-0489-3.

40. Zhou, M.; Wang, D.; Yang, D.; Qiu, X.; Li, Y. Avermectin loaded nanosphere prepared from acylated alkali lignin showed anti-photolysis property and controlled release performance. *Ind. Crops Prod.* **2019**, *137*, 453–459, doi:10.1016/j.indcrop.2019.04.037.

41. Barapatre, A.; Meena, A.S.; Mekala, S.; Das, A.; Jha, H. In vitro evaluation of antioxidant and cytotoxic activities of lignin fractions extracted from Acacia nilotica. *Int. J. Biol. Macromol.* **2016**, *86*, 443–453, doi:10.1016/j.ijbiomac.2016.01.109.

42. Marchand, G.; Fabre, G.; Maldonado-Carmona, N.; Villandier, N.; Leroy-Lhez, S. Acetylated lignin nanoparticles as a possible vehicle for photosensitizing molecules. *Nanoscale Adv.* **2020**, *2*, 5648–5658, doi:10.1039/D0NA00615G.

43. Maldonado-Carmona, N.; Marchand, G.; Villandier, N.; Ouk, T.-S.; Pereira, M.M.; Calvete, M.J.F.; Calliste, C.A.; Żak, A.; Piksa, M.; Pawlik, K.J.; et al. Porphyrin-Loaded Lignin Nanoparticles Against Bacteria: A Photodynamic Antimicrobial Chemotherapy Application. *Front. Microbiol.* **2020**, *11*, doi:10.3389/fmicb.2020.606185.

44. Maldonado-Carmona, N.; Ouk, T.; Villandier, N.; Calliste, C.A.; Calvete, M.J.F.; Pereira, M.M.; Leroy-Lhez, S. Photophysical and Antibacterial Properties of Porphyrins Encapsulated inside Acetylated Lignin Nanoparticles. *Antibiotics* **2021**, *10*, 513, doi:10.3390/antibiotics10050513.

Nanoparticules de lignine acétylée comme nouveau véhicule photosensibilisant pour la Chimiothérapie Antimicrobienne Photodynamique

La résistance aux antibactériens est une menace pour les développements de la médecine moderne, représentant un fardeau économique et social dans les années à venir. Cette crise est aggravée par un pipeline déprécié de nouveaux médicaments antibactériens, en raison des coûts de recherche élevés et de la faible rentabilité. De plus, le développement de nouvelles molécules spécifiques ne garantit pas l'absence de résistance antibactérienne contre une nouvelle molécule, et il existe alors une tendance croissante à rechercher des alternatives antibactériennes avec des cibles moléculaires non spécifiques. Dans cet aspect, la Chimiothérapie Antimicrobienne Photodynamique réalise une désinfection bactérienne grâce à l'utilisation d'une molécule photosensibilisante qui n'est active que lors d'une irradiation lumineuse, ajoutant un autre niveau de contrôle au processus. Dans ce travail, nous présentons un système de livraison biopolymère pour les molécules photosensibilisantes, sous forme de nanoparticules de lignine acétylée. La préparation, la caractérisation physique et la caractérisation photophysique sont discutées tout au long de ce projet, en explorant les effets de l'encapsulation vis-à-vis du photosensibilisateur. Enfin, ces nanoparticules ont été testées contre les bactéries, constatant qu'elles n'étaient capables de les éradiquer efficacement que par irradiation lumineuse, démontrant une faible toxicité dans l'obscurité et une stabilité dans le temps et l'exposition à la lumière. Ensuite, cette formulation pour molécules photosensibilisantes s'est avérée être une formulation antibactérienne efficace, remplissant sa fonction, tout en s'attaquant à la désinfection antibactérienne et en valorisant un biopolymère très abondant.

Mots-clés: valorisation de la lignine, formulation antibactérienne, désinfection par la lumière

Acetylated lignin nanoparticles as a new photosensitizer’s vehicle for Photodynamic Antimicrobial Chemotherapy

Antibacterial resistance is a threat to the developments of modern medicine, representing an economic, and social burden in years to come. This crisis is enhanced by a belittled pipeline of novel antibacterial drugs, due to the high research costs and low profitability. Furthermore, the development of new, specific molecules is not guarantee that antibacterial resistance will not arise against any new molecule, and then there is a growing tendency to look for antibacterial alternatives with unspecific molecular targets. In this aspect, Photodynamic Antimicrobial ChemoTherapy achieves bacterial disinfection through the use of a photosensitizing molecule which is only active upon light irradiation, adding another level of control to the process. In this work, we present a biopolymeric delivery system for photosensitizing molecules, as acetylated lignin nanoparticles. The preparation, physical characterization and photophysical characterization are discussed along this project, exploring the effects of the encapsulation towards the photosensitizer. Finally, these nanoparticles were tested against bacteria, finding that they were able to efficiently eradicate them only upon light irradiation, demonstrating low dark toxicity, and stability over time and light exposure. Then, this formulation for photosensitizing molecules has proven to be an efficient antibacterial formulation, fulfilling its purpose, while tackling antibacterial disinfection and valorizing a highly abundant biopolymer.

Keywords: lignin valorization, antibacterial formulation, light-driven disinfection

Nanopartículas de lignina acetilada como um novo veículo fotossensibilizador para quimioterapia antimicrobiana fotodinâmica

A resistência antibacteriana é uma ameaça ao desenvolvimento da medicina moderna, representando um fardo econômico e social nos próximos anos. Esta crise é agravada por um reduzido portfólio de novos medicamentos antibacterianos, devido aos altos custos de investigação e baixa lucratividade. Além disso, o desenvolvimento de novas moléculas específicas não é garantia de que não surja resistência antibacteriana contra qualquer nova molécula, e há uma tendência crescente de buscar alternativas antibacterianas com alvos moleculares inespecíficos. Nesse aspecto, a Quimioterapia Antimicrobiana Fotodinâmica realiza a desinfecção bacteriana por meio do uso de uma molécula fotossensibilizadora que só é ativa sob irradiação de luz, adicionando outro nível de controle ao processo. Neste trabalho, apresentamos um sistema de transporte biopolimérico para moléculas fotossensibilizantes, como nanopartículas de lignina acetilada. A preparação, caracterização física e caracterização fotofísica são discutidas ao longo deste projeto, explorando os efeitos do encapsulamento para o fotossensibilizador. Finalmente, essas nanopartículas foram testadas contra bactérias, descobrindo que eram capazes de erradicá-las de forma eficiente apenas após irradiação de luz, demonstrando baixa toxicidade no escuro e estabilidade ao longo do tempo e exposição à luz. Então, essa formulação para moléculas fotossensibilizantes tem se mostrado uma formulação antibacteriana eficiente, cumprindo seu propósito, ao mesmo tempo em que atua na desinfecção antibacteriana e valoriza um biopolímero altamente abundante.

Palavras-chave: valorização da lignina, formulação antibacteriana, desinfecção por luz